Cape Peninsula
University of Technology

IN-SITU CHARACTERISATION OF THE INSULATOR LEAKAGE CURRENT OF HIGH VOLTAGE DIRECT CURRENT TRANSMISSION LINES

by

MORNÉ ROMAN

Thesis submitted in fulfilment of the requirements for the degree

Doctor of Engineering: ELECTRICAL ENGINEERING

in the Faculty of Engineering

at the Cape Peninsula University of Technology

Supervisor: Prof. R.R. van Zyl

Bellville

January 2021

CPUT copyright information

The dissertation/thesis may not be published either in part (in scholarly, scientific or technical journals), or as a whole (as a monograph), unless permission has been obtained from the University

DECLARATION

I, Morné Roman, declare that the contents of this dissertation/thesis represent my own unaided work, and that the thesis has not previously been submitted for academic examination towards any qualification. Furthermore, it represents my own opinions and not necessarily those of the Cape Peninsula University of Technology.

Signed

18 January 2021

Date

ABSTRACT

Leakage current (LC) monitoring of high voltage transmission line insulators is of interest as it is indicative of the degradation of the insulators, as well as the potential for flashover. Several high voltage direct current (HVDC) transmission schemes are being constructed worldwide, and issues of dimensioning and specification of the transmission line insulators are an area of debate. Further, advancements in composite insulator materials are touted to offer a better pollution performance; however, *there is little operational information available in the literature to understand the benefits completely*. This research addresses topics that relate to the characterisation of the LC under HVDC conditions. There is ample experience with LC under HVAC conditions, *but far less so for HVDC*. HVDC lines are harder to monitor than alternating current (ac) lines, since the conventional current transformers cannot be used to measure dc. Presently, there is no commercially available, non-intrusive, clamp-on type device for HVDC transmission line insulator LC measurements. Power utilities, like South Africa's Eskom, have operational requirements for such a device for two critical applications. First, for continuous real-time monitoring of HVDC line insulators, and second, for use by live line workers to determine if it is safe to work on energised insulators. This thesis investigates various LC sensing techniques as well as their respective advantages and disadvantages. Commercially-off-the-shelf (COTS) sensors are used to perform initial LC measurements on insulators. The author subsequently developed a new dc LC sensor for HVDC transmission lines, which determines the current indirectly by measuring the magnetic field associated with it. The sensor was deployed in the Cahora Bassa HVDC transmission line scheme for an extended period. Such results are rare, and not readily available in the public domain. The results show that this sensor can measure LC across the full anticipated range non-intrusively; hence, it can be readily used by live line workers to determine the probability of flashovers.

Two case studies have also been performed at Eskom's corona cage high voltage testing facility on HVDC glass insulators. The first case study investigates the relationship between current and increased pollution layer conductivity of a glass insulator. The measurement results show that the LC increases with an increase in contamination level when the voltage level is kept constant, but also that flashover will occur for LC exceeding a critical threshold of 1.4 mA, irrespective of the conductivity layer applied to the insulator.

The second case study investigates the probability of flashover occurring as a function of LC at a constant equivalent salt deposit density (ESDD) level of 0.03 mg/cm^2. The results show that for currents exceeding 0.6 mA there exists a possibility of flashover occurring. This quantification of the LC that can lead to flashover is important as it indicates safe scenarios when live line workers can perform maintenance on energised HVDC transmission line insulators.

In order to better understand LC behaviour on insulators, finite element method (FEM) simulations have been performed on dc insulators, and compared with that of ac insulators. Voltage, electric field and current density distributions are simulated in COMSOL Multiphysics for clean and uniformly polluted ac and dc energised insulators with layer thickness of 0.02 mm and conductivity of 0.07 S/m. To the best of the author's knowledge, no voltage, electric field and current density distribution simulations have been conducted for glass dc insulators in literature. When insulators are polluted, a dramatic increase in current density for both the ac and dc insulators are observed, with the ac and dc insulator exhibiting current densities of 4.81 x 10^3 A/m^2 and 5.34 x 10^3 A/m^2, respectively. It is observed that the electric field on the surface of a polluted insulator is higher on an energised dc insulator compared to that on an energised ac insulator. This can lead to a dc insulator having a higher flashover probability than the ac insulator under the same excitation voltage. It is expected that arcs (that will lead to eventual flashover) will first emanate from the energised end of the insulator, since that is where the highest electric field occurs for both types of insulator. From the electric field simulations, it is also observed that interim maxima exist on the sheds of a polluted ac and dc insulator. These higher electric fields on the polluted insulator surface can lead to heating on the insulator surface and to the formation of dry bands, which increases the probably of a flashover occurring. These interim maxima are not observed on the clean insulator case. The simulations further show that the LC leakage current on ac energised insulators is purely resistive (conduction current) and that the contribution of capacitive currents on the current density is negligible. Various conductivities of air have been studied to emulate different altitudes and ambient humidity conditions. It is concluded that an increase in the air's conductivity has a negligible effect on an insulator's performance. The simulated current in COMSOL Multiphysics are compared with the laboratory LC measurements and the results agree well.

The research concludes with in-situ measurements to characterise the behaviour of LC on the Cahora Bassa HVDC transmission lines, as representative of HVDC schemes at large. For this purpose, a glass and composite insulator have been installed on the terminal tower of the transmission line located at the Apollo Converter Station in Johannesburg, South Africa. Shunt resistors have been installed on both insulators, and the prototype sensor on the glass insulator, to measure the LC activity. (The prototype sensor measurements have not been used during the analyses of the data, but agreement with the shunt resistor measurements are shown.) Insulator LC measurements have been performed over an 11-month period. The influence of temperature, humidity, dew, rain and the HVDC line's voltage and current on the behaviour of LC have been investigated. The measurements show that the composite and glass insulator LC behaviour is similar, except in cases of high humidity or rain. At the onset of rainfall and humidity (>90%), elevated LC levels are observed on glass insulators, while composite insulators demonstrate lower LC levels under the same conditions. LC activity is observed in the presence of continuous rain as well, but with low magnitude. A statistical analysis of all data shows the following correlation coefficients between LC and climatic and line conditions over the 11-month period for the two types of insulator:

- LC and temperature: 0.40 (composite) and -0.12 (glass);
- LC and humidity: -0.28 (composite) and 0.13 (glass);
- LC and rain: -0.03 (composite) and 0.43 (glass)
- LC and line voltage: 0.06 (composite) and -0.07 (glass)
- LC and line current: 0.01 (composite) and 0.11 (glass)

It is evident that the glass insulator's LC increases when rain is present, but that rain has little effect on LC composite insulators. This may be the result of self-cleaning of the insulator that occurs due to its hydrophobicity properties. The HVDC transmission line current and voltage fluctuations have been found to have negligible influence on the LC levels. Overall, during the 11-month LC monitoring period, it has been evident that elevated LC activity occurs more frequently in the spring-summer period, which is the rainy season for Johannesburg, than in winter. Interestingly, under nominal weather conditions of no rain and low humidity, the LC measurements for both types of insulators exhibit an almost square-wave behaviour with LC switching between ≈ 20 μA and ≈ 60 μA with short transitions on a daily basis. These swift transitions can be attributed to condensation on

the insulators, which has been found to be the primary determinant of the LC levels on these contaminated insulators.

The field tests show that the line is working better than first anticipated by Eskom engineers, as higher levels of LC had been expected.

A novel, linear approximation has also been determined between LC measured during laboratory tests and actual HVDC field tests. It was observed that by using the initial developed equation, the LC calculated for the field measurements agrees well with the actual LC measurements conducted on the HVDC line. This approximation can be especially helpful to support the design of new HVDC lines

In conclusion, a novel dc LC sensor prototype has been designed, tested, calibrated and validated for the measuring of HVDC LC non-intrusively on HVDC transmission lines. Furthermore, the insulator LC of the Cahora Bassa transmission line has now been quantified and analysed over an extended period for both glass and composite insulators. These measurements have not previously been documented to this extent in the literature. Finally, a satisfactory correspondence between laboratory and live line LC measurements has also been established, which aids future research and development in this field.

ACKNOWLEDGEMENTS

I wish to thank:

- The Almighty God for blessing me with wisdom and understanding.
- My parents for being there for me, for encouraging me to give only my best.
- Prof. Robert van Zyl for his supervision and his guidance during my studies.
- Nishanth Parus and Nishal Mahatho from Eskom for their technical expertise on insulators and high voltage engineering.
- Stephen Cupido, Craig Olivier and Ben Dixon for the fabrication of PCBs.
- Etnard Louw and Enrico Louw for assisting with soldering.
- Electdom Matandirotya, Elda Saunderson and Danie Gouws for sharing their knowledge on magnetic field sensors and measurement techniques.
- Shane Martin for assisting in creating CAD models for the COMSOL Multiphysics simulations.

The financial assistance of the French South African Institute of Technology (F'SATI), the National Research Foundation (NRF) and Eskom towards this research is acknowledged. Opinions expressed in this thesis and the conclusions arrived at, are those of the author, and are not necessarily to be attributed to the F'SATI or the NRF.

RESEARCH OUTPUTS

1) Peer-reviewed scientific journal paper(s)

- Roman, M. van Zyl, R., Parus, N., Mahatho, N. **2019**. In-situ monitoring of leakage current on composite and glass insulators of the Cahora Bassa HVDC transmission line. *SAIEE African Research Journal*, 110(1):1-7.

2) Peer-reviewed conference paper(s)

- Parus, N., Mathebula M, Roman, M., Mahatho, N., Motsei, L., van Zyl, R. **2019**. Leakage current monitoring on in-service composite and glass insulators of the Cahora Bassa HVDC transmission line. Proceedings for the joint 9th CIGRE Southern Africa Regional Conference & CIGRE B4 International Colloquium, Muldersdrift, 1-5 October, 1-8.

- Roman, M., van Zyl, R., Parus, N., Mahatho, N. **2018**. Design of a Hand-Held, Clamp-on, Leakage Current Sensor for High Voltage Direct Current Insulators. *The 20th International Conference on High Voltage Engineering*, London, United Kingdom, 19-20 November, 1-6.

- Roman, M., van Zyl, R., Parus, N., Mahatho, N. **2017**. Experimental study of LC and flashover onset with various conductivities on HVDC glass insulators. *The 20th International Symposium on High Voltage Engineering (ISH), https://e-cigre.org/publication/ISH2017_577-leakage-current-and-flashover-onset-with-various-conductivities-on-hvdc-glass-insulators,* Buenos Aires, Argentina, 28 August - 1 September, 1-6.

- Roman, M., van Zyl, R., Parus, N., Mahatho, N. Nalomo, B. **2016**. The measurement of HVDC insulator LC using magnetic field sensors. *The Southern African Universities Power Engineering Conference*, http://www0.sun.ac.za/saupec2017/Papers/PaperView.php?%20PublicationID%20=%201554, Vereeniging, South Africa, 26-28 January, 1-6.

- Roman, M., van Zyl, R.R. Parus, N. Mahatho, N. **2015**. A novel technique for measuring HVDC insulator leakage current using magnetic field sensors. *The 19th*

International Symposium on High Voltage Engineering, http://www.zcu.cz/pracoviste/vyd/online/FEL_ISH_2015_Proceedings.zip, Pilsen, Czech Republic, 23 - 28 August, 1-6.

- *Obtained the young researcher award for the outstanding and excellent paper presented at the 2015 ISH.*

- Roman, M., van Zyl, R., Parus, P., Mahatho, N. **2014**. Insulator leakage current monitoring: Challenges for high voltage direct current transmission lines. The *International Conference on the Industrial and Commercial Use of Energy (ICUE),* Cape Town, South Africa, 19-20 August, 1-7.

3) Artefact

- Hand-held leakage current sensor for HVDC glass insulators.

GLOSSARY

AC	Alternating Current
CIGRE	International Council on Large Electric Systems
COTS	Commercially-Off-The-Shelf
CPUT	Cape Peninsula University of Technology
CT	Current Transformer
DC	Direct Current
ESDD	Equivalent Salt Deposit Density
FEMM	Finite Element Method Magnetics
FOV	Flashover Voltage
F'SATI	French South African Institute of Technology
GIC	Geomagnetically Induced Current
HVAC	High Voltage Alternating Current
HVDC	High Voltage Direct Current
LC	Leakage Current
LCC	Line Commutated Converter
LCPR	Leakage Current Prototype
LED	Light Emitting Diode
N.D	No Date
OLCA	Online Leakage Current Analyzer
OP-AMP	Operational Amplifier
USCD	Unified Specific Creepage Distance
WITS	University of the Witwatersrand

TABLE OF CONTENTS

LIST OF FIGURES

LIST OF TABLES

1: INTRODUCTION

1.1 Introduction

Leakage current (LC) monitoring of high voltage transmission line insulators is of interest as it is an indicator of insulator condition and performance. This research focuses on high voltage direct current (HVDC) schemes, with particular reference to the complexities of measuring LC of in-situ (online) insulators. Little information is available in literature on how to measure LC on energised HVDC insulators in the field. Also, some of the conventional methods used for measuring ac LC, such as a current transformer (CT), will not work for dc as there are no alternating fields to couple into the device. Thus, a clamp-on type, non-intrusive device for HVDC line insulator LC measurements is investigated. Insulator LC case studies on glass insulators are performed at Eskom's (the South African power utility) corona cage high voltage test facility. Subsequently, in-situ measurements of LC on composite and glass insulators of the Cahora Bassa HVDC transmission line in South Africa have been performed between August 2016 and June 2017. This research deepens our understanding of LC behaviour on insulators under operational HVDC conditions, at least at high altitudes (although altitude is shown to have a negligible effect on LC behaviour). The influence of temperature, humidity, dew, rain and the HVDC line's voltage and current on LC are investigated.

1.2 Statement of the research problem

LC on insulators can, if not mitigated, lead to line faults, which occur as flashover of the insulator and the degradation of the insulator material (Sudalai Shunmugam *et al*., 2017). These flashovers can cause tripping and malfunction of an HV transmission line, which are very costly to power utilities. LC exists on insulators because of insulator ageing, damage to the fibreglass core of composite insulators and pollution of glass insulators (Holtzhausen *et al*., 2010; Pylarinos *et al*., 2011). The magnitude of LC can be used as a good indicator of the ability of the insulator to perform under high voltage stress. The LC on HVDC insulators is of much interest to power utilities, such as South Africa's Eskom, as little information is available in the public domain on the magnitude and behaviour of LC that one can expect on an in-service HVDC insulator. It is critical to understand insulator performance if new transmission line projects are being envisaged, as stated by Zhang *et al*. (2013) when China was in the process of developing their 800 kV UHV dc transmission lines, to guarantee the safety of the HVDC scheme. This information is, therefore, critical as South Africa also plans to construct a new HVDC scheme. The data will assist in designing an improved and more efficient HVDC scheme. Measurement of LC for ac conditions is usually carried out with the use of a conventional CT. CTs are available as clamp-on devices, but

for insulator implementation, it becomes quite difficult due to the size of insulators. For dc, however, CTs cannot be used as there are no alternating fields to couple into the CT device. Currently, to the best of the author's knowledge, there is no non-intrusive, in-situ technology solution that can be clamped around the cap of a glass insulator to measure the LC flowing through HVDC transmission lines' insulators. A study of the LC in real-time may be used as a condition-based monitoring system for early detection of possible line faults and may also be used to classify safe and unsafe conditions for live line workers.

1.3 Research questions

The research questions guiding the research are stated below.

Finite element method simulations of a glass insulator

- What is the comparison between the voltage, electric field and current density distributions of clean and polluted HVAC and HVDC glass insulators, respectively?
- What can be derived from the simulations in terms of LC behaviour?
- How reliable is the finite element method models compared to the real-life performance of insulators?

Development of LC measurement technology

- Which sensors can measure small currents (mA) or small magnetic fields (nT) in the vicinity of HVDC line currents (kA) and associated magnetic fields (mT)?
- How can the sensor be modified to perform non-intrusive measurements of LC on HVDC insulators?
- How do HVDC transmission lines affect measurements from the LC sensor and how can those affects be mitigated?

Empirical characterisation of LC on HVDC transmission lines, with Cahora Bassa HVDC transmission lines as case study

- What is the relationship between contamination and insulator LC?
- What is the probability of a flashover occurring as a function of LC?
- What is the behaviour of LC of the Cahora Bassa transmission lines?
- What is the impact of temperature, humidity, rain and the Cahora Bassa HVDC line voltage and current on the insulators' LC?
- How do the LC characteristics differ for composite and glass insulators under the same environmental conditions?

- What is the relationship between LC measured at the corona cage and that of the Cahora Bassa HVDC line?

1.4 Objectives of the research project

The specific objectives of the research are listed below:

- Design and implement an LC sensor capable of measuring small magnetic fields non-intrusively around in-situ energised HVDC insulators. This device should also be stand-alone, and which can be left out in the field to monitor LC over an extended period of time. The specific requirements for the sensor are given below:
    - a hand-held, clamp-on type device that can be carried around by live line workers;
    - performing in-situ measurements on energised insulators and in the vicinity of an HVDC transmission line (the 1800 A Cahora Bassa HVDC transmission line as case study);
    - measuring LC from 1 mA to 100 mA within an average error of 5%; and
    - withstanding flashovers that might occur during measurements.
- Determine the relationship between LC and increased insulator pollution levels.
- Determine the probability of flashover occurring as a function of LC at a constant equivalent salt deposit density (ESDD) level.
- Characterise the LC found on the Cahora Bassa HVDC insulators under various weather conditions. The measured LC will also be correlated with the HVDC line voltage and current.
- Determine the correspondence between laboratory LC measurements and actual live line LC measurements with the Cahora Bassa HVDC transmission line as case study.

1.5 Research design and methodology

The research is conducted in four stages to achieve the research objectives.

First, finite element method (FEM) physics-based simulations are conducted of the electric field, voltage and current distributions on glass insulators to gain insight into what may occur during laboratory measurements and when in-situ insulator LC measurements are eventually performed on the Cahora Bassa HVDC insulators. Knowledge of the voltage and electric field distributions are vital to the design and development of insulators (Kontargyri *et al.*, 2004).

Second, a suitable monitoring and measurement tool is developed, tested, calibrated and verified to gather empirical LC data. It also serves as technology validation for future sensor designs for in-situ monitoring of LC of HVDC transmission line schemes.

Third, case studies are performed on HVDC glass insulators under controlled laboratory conditions to contribute to the limited publicly available empirical body of knowledge regarding LC and flashover occurrences on these insulators under HVDC conditions.

Fourth, in-situ LC measurements in an operational HVDC scheme, namely the Cahora Bassa transmission line, are performed.

The research and design methodology followed in each of these stages are summarised below:

FEM physics-based simulations of electric field, voltage and current distributions on glass insulators

- Build FEM models in COMSOL Multiphysics (COMSOL Multiphysics, 2019) of clean and contaminated glass insulators under ac and dc excitation.
- Simulate and compare the voltage, electric field and current density distributions that can be found on and near glass insulators under ac and dc excitation.
- Determine where the peak dc LC can be expected for glass insulators as only ac composite insulators current densities have been reported in the literature thus far (Netravati *et al*., 2016).
- Perform simulations for ac energised insulators to study the differences in the voltage, electric field and current density distributions between the ac and dc energised insulators as no comprehensive literature exists comparing these parameters for ac and dc conditions.

Design of LC sensor:

- Review existing LC measurement techniques for HVDC insulators.
- Use shortlisted sensors to perform initial LC measurements on glass insulators.
- Develop a non-intrusive LC sensor prototype and conduct measurements.
- Compare results with existing LC measurement techniques to validate the prototype sensor.

Empirical LC case studies performed on HVDC glass insulators under controlled conditions:

- Determine the relationship between LC and insulator pollution.
- Determine the probability of flashover as a function of LC.
- Determine the relationship between insulator length and LC.

Empirical in-situ characterisation of LC on Cahora Bassa HVDC transmission lines:

- Perform in-situ LC measurements on energised insulators of the Cahora Bassa scheme.

- Correlate the LC behaviour with climatic conditions, HVDC line voltage and current.

1.6 Delineation of the research

In line with the requirements of a Doctor of Engineering (DEng) degree, the research is an *original investigation*, based on *empirical methods* and of an *applied nature*.

This research is limited to studying the LC behaviour on HVDC insulators, and not of HVAC insulators, as the ultimate objective is to characterise the LC of HVDC transmission lines, with the Cahora Bassa scheme as a case study. The work done will focus more on glass insulators as they are prominent on Eskom's side of the Cahora Bassa and most faults on the transmission line have been linked to them. Field tests will only be performed at the Apollo converter station in Johannesburg, on the South African side of the Cahora Bassa transmission line, and compared to environmental conditions, such as temperature, humidity, rain and dew. The LC measurements are conducted with an LC prototype sensor and not an industrial device.

1.7 Significance of the research

Generally, and specifically for the Cahora Bassa HVDC scheme, there is minimal data available on the nominal behaviour of LC on HVDC insulators. The principal significance of this research is to obtain and contribute sought-after empirical data to the body of knowledge concerning LC behaviour on glass and composite insulators on HVDC transmission lines in general, but specifically applied to the Cahora Bassa scheme as a case study. It also validates novel technology for non-intrusive LC measurements on HVDC lines.

1.8 Outcomes and contribution

The research has resulted in the following broad outcomes and contributions:

- A hand-held LC sensor capable of measuring LC from 1 - 100 mA in the vicinity of higher current (1800 A).
- The characterisation of LC on contaminated HVDC glass insulators.
- In-situ LC measurements on the Cahora Bassa HVDC insulators, which will be the first of its kind on this specific transmission line. These LC measurements will be correlated with ambient weather conditions and the Cahora Bassa's line voltage and current.
- Correspondence between simulated, laboratory and live line LC behaviour has been established, which will aid future research and development in this field.

- The results and analyses contribute significantly to the knowledge and understanding of the leakage current behaviour on composite and glass HVDC insulators, based on a real-line application.

1.9 Structure of thesis

Chapter Two presents a technical literature review of HVDC transmission schemes. Discussions on insulators, contamination, live line work and the benefits of monitoring LC are presented. It also discusses available methods for measuring LC.

Chapter Three presents the finite element method results for an ac and dc insulator's voltage, electric field and current density distributions.

Chapter Four discusses commercial-off-the-shelf (COTS) LC sensors for dc insulators and the development of an LC sensor prototype that can measure LC of HVDC schemes non-intrusively.

Chapter Five presents the case studies conducted on glass insulators at Eskom's corona cage high voltage test facility in Johannesburg, South Africa, to ascertain the relationship between contamination and insulator LC. This chapter also determines the probability of flashover occurring as a function of LC.

Chapter Six reports on the in-situ LC measurements performed on the Cahora Bassa transmission line's insulators over an 11-month period.

Chapter Seven concludes the thesis with a summary of the findings and recommendations for future work.

2: TECHNICAL LITERATURE REVIEW

2.1 Introduction

This chapter reviews literature related to insulators on HVAC and HVDC schemes. Specifically, insulator types, contamination of insulators, insulator leakage current (LC) monitoring and different LC sensing techniques for HVAC and HVDC schemes are reviewed.

2.1.1 Background

Composite and glass insulators have been used for decades in HV transmission networks and have been published on widely. Composite insulators generally offer more cost-effective solutions than glass, but in terms of reliability, glass insulators are superior. Composite and glass insulators also behave differently in the environment; thus, careful consideration has to be taken upon selecting an appropriate insulator. Elevated LC levels on insulators can represent degraded performance of an insulator string, and may lead to faults, such as flashover (Schwardt *et al.,* 2004; HoltzHausen, 2010; Mavrikakis, 2015). Dry-band arcs and possible flashover on insulators are a consequence of light rain and high humidity conditions (Zchariades *et al.,* 2013; Meyer *et al*., 2011; Suwarno & Parhusip, 2010). Transmission line faults involving insulator flashover pose a great financial risk to power utilities as well as to the safety of their live line workers, especially along coastal areas. Studying LC in real-time can be used as an early warning tool against line faults caused by insulators (Zhengfa *et al*., 2018). Also, measurements can be used to classify safe and unsafe working conditions for live line workers. Therefore, the measuring of insulator LC on high voltage transmission lines has become relevant. Monitoring the LC of HVDC schemes in real-time is even more important as little has been published on the typical LC behaviour of these schemes, especially at high altitudes. Laboratory measurements have been performed on insulators in high altitude conditions and it was seen that lower pressure affects the arc development phenomenon and insulator flashover voltage (Jiaqi *et al.,* 1988*;* Zhang *et al.,* 2010; Zhang *et al*., 2013). However, it is shown in this thesis that altitude has negligible influence on LC behaviour per say.

2.1.2 HVAC and HVDC technologies

HVDC technology is well-established across the world. HVDC transmission lines offer economic and environmental advantages for the transport of power over long distances (Jeroense, 2011; Ildstad, 2013). The first commissioning of an HVDC transmission line was in 1882 (Siemens, 2011:4). This was a 50 km long 2 kV line between Miesbach and Munich. However, the first commercial transmission scheme was only commissioned in 1954. It was a submarine cable

linking the island of Gotland with the Swedish mainland (Limbo, 2009:18-19). The longest HVDC line in operation is the Inga-Kolwezi in the Democratic Republic of Congo, which is 1 700 km long. The HVDC link with the highest capacity is the Changji-Guquan in China, harnessing a capacity of 12 000 MW (Lempriere, 2019). The Cahora Bassa HVDC transmission line running through South Africa and Mozambique carries ±533 kV/1800 A over a distance of 1 420 km.

There are several advantages of HVDC technology when compared to HVAC. One of the most significant benefits is cost over distance. The longer the transmission line is, the more cost-effective the HVDC technology becomes (Reddy & Verma, 2014). Figure 2.1 shows the relationship between cost and length of the HVAC and HVDC transmission lines. Further advantages are (i) HVDC technology makes undersea connections feasible, and (ii) power transmission and stabilisation between unsynchronised ac distribution systems are enabled (Drobik, n.d:3; Bahrman & Johnson, 2007:32-44; Limbo, 2009:18-19). In HVDC links, rectifiers are always required to connect to their ac counterparts (Heyman *et al*.,2012:3). These rectifiers allow for the conversion of ac to dc power. The commercialisation of the fully-static mercury arc valve in the 1940s aided the development of HVDC technology tremendously. The mercury arc valve was replaced by thyristors from the 1970s in the conventional line commutated converter (LCC) schemes (Heyman *et al*., 2012:3; Siemens, 2011:4).

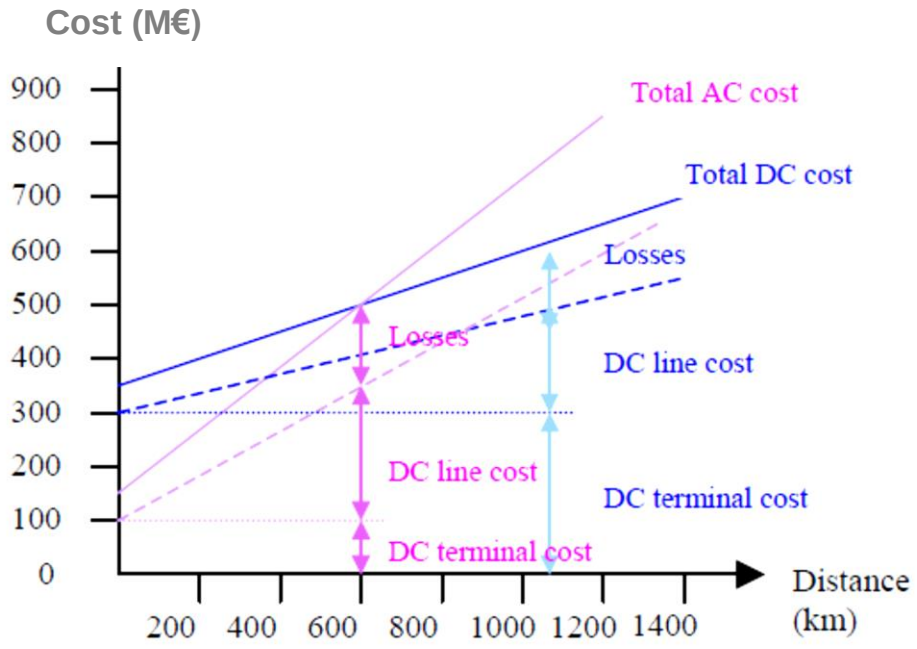

Figure 2.1: Relation between length of line and costs in ac and dc transmission lines (From Larruskain *et al*., n.d:4)

2.2 High voltage insulators

Insulators are vital components of overhead transmission lines and substations. They also provide mechanical support between the conductor bundle and the tower in power systems (Douar, *et al*., 2010). Insulator and transmission line faults caused by birds, pollution, contamination and lightning largely determine the performance of HV transmission lines. These conditions can lead to the occurrence of flashovers, which are discussed in later sections. In fact, most transmission line faults are caused by insulator malfunction due to flashover (Glossop, 2008:3). Flashover causes severe damage to insulators, such as the degradation of composite insulator sheds and cracking of porcelain insulators (Schwardt *et al.,* 2004). Thejane *et al*. (2015) state that an insulator's material has a huge impact on its LC performance, followed by its profile.

In HV transmission lines, composite and glass insulators fall under polymeric and ceramic insulators, respectively (Holtzhausen, 2010). The different types of insulators are presented in Figure 2.2. The lengths of the insulators are determined by leakage distance (also known as creepage distance). The leakage distance is dependent on the anticipated contamination in the surrounding environment of the insulator string (Phillips & Engelbrecht, 2005).

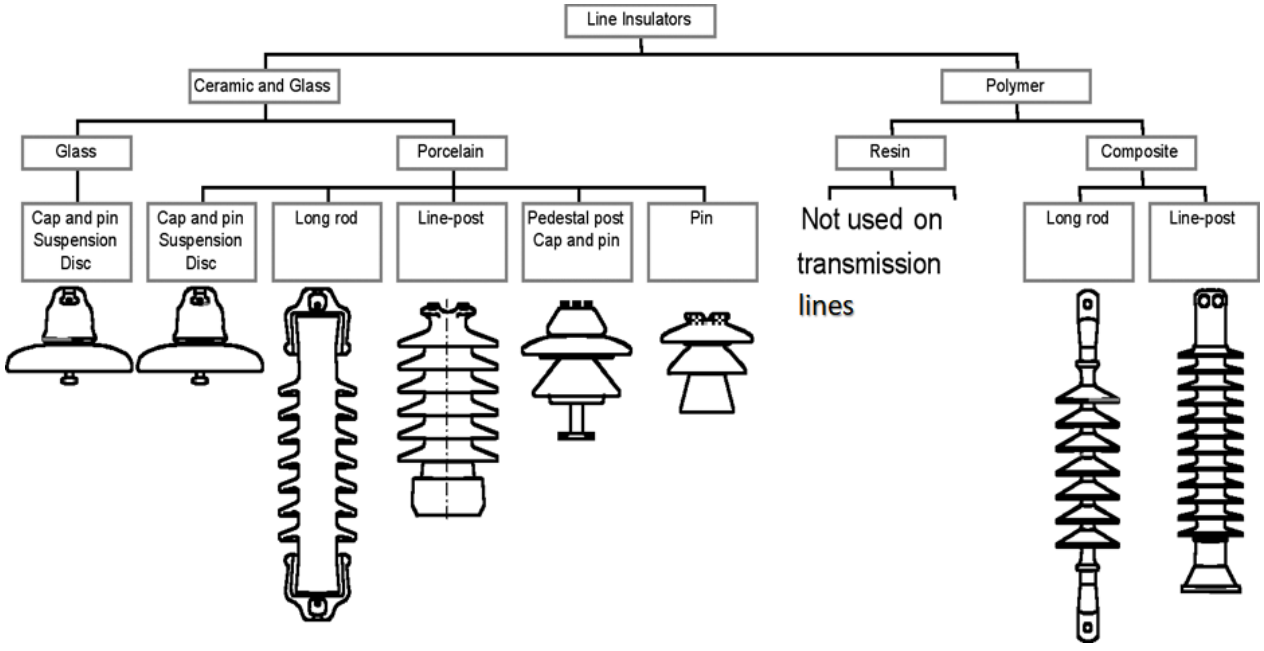

Figure 2.2: Types of insulators used on transmission overhead lines (From Phillips & Engelbrecht, 2005)

2.2.1 Glass insulators

Glass insulators consist of glass and steel with cement separating the steel caps from the pins. The individual units of glass insulators are connected by the steel caps and pins to form one insulator string (Holtzhausen, 2010). The conical shape of the glass insulator fittings allows for high mechanical strength. Glass insulators can have an operational lifetime of more than 50 years in the field due to their robustness, which is a major operational and cost advantage (Costea & Baran, 2012). Figure 2.3 shows the cross-section of a standard glass insulator. Glass insulators are more expensive than composite insulators due to their mechanical design and they weigh more (Nobrega *et al*., 2017).

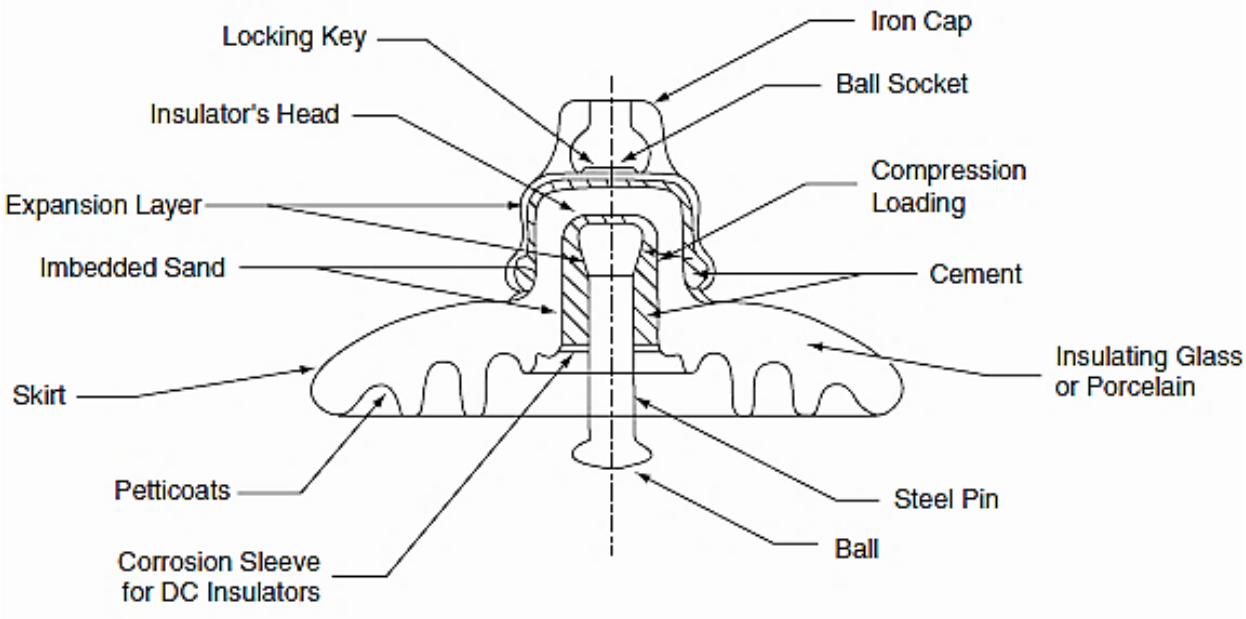

Figure 2.3: Cross-section of a standard glass insulator (From Edvard, 2012)

2.2.2 Composite insulators

Composite insulators are normally made of glass fibre reinforced, resin bonded rods to which metal end fittings are attached (Gencoglu, 2007). The benefits of composite insulators are its cost-effectiveness, enhanced imperviousness to vandalism and its light weight (Gencoglu, 2007; Sunitha *et al*., 2015). Composite insulators also have hydrophobicity properties, which are advantageous in polluted environments (Sunitha *et al.,* 2015; Zhengfa *et al*., 2018). A drawback of composite insulators is that its rods can become brittle and break. Also, since its diameter is smaller than porcelain insulators, it is more susceptible to lighting strikes since the minimum

electric arc distance is less compared to a porcelain insulator string of the same length (Hu & Liu, 2017). Figure 2.4 shows the basic components of a polymer insulator.

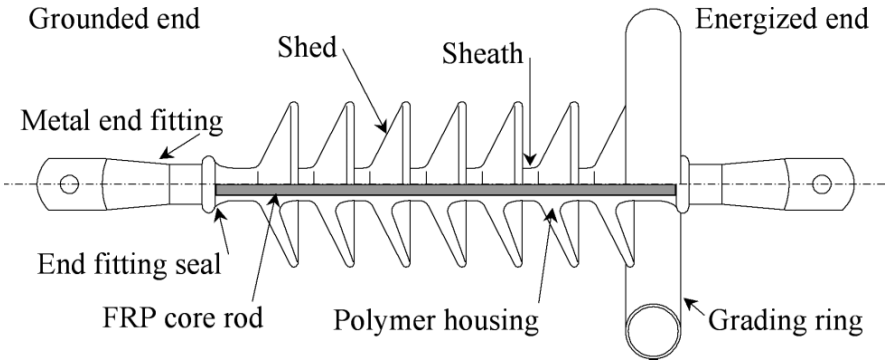

Figure 2.4: Basic components of a polymer insulator (From Phillips & Engelbrecht, 2005)

2.2.3 Damage to insulators

Damage to insulators affect its electrical and mechanical properties. Electrical discharge can weaken the insulator's mechanical strength. This effect can be mitigated by equipping the insulator with arching devices. Punctures can also occur, which lead to water seeping into the composite insulator's fibreglass rod and weakening it. This is called the *brittle fracture* phenomenon (Cheng *et al*., 1981). Research has shown that if shattered glass disks are present on insulator strings, there will be a definite reduction in insulation strength (Parus *et al*., 2011). The insulation strength further deteriorates when these glass fragments are closer to the live end of the insulator string (as will be shown in Chapter 3, this is also the region of highest electric field and surface current density for HVDC insulators). Optical devices can be used on the ground or on top of the tower to inspect if mechanical weakening of the insulator has taken place (Valagussa *et al*., 2009).

Figure 2.5 shows a flashover event when two broken glass disks are placed at the live end of the insulator.

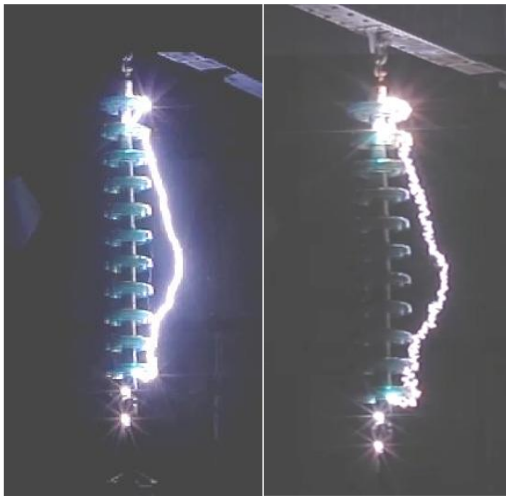

Figure 2.5: Flashover event sequence with 2 broken discs at live end (From Parus *et al*., 2011)

Electrical damage causes the loss of hydrophobic features and weakening of the composite insulator's dielectric strength. It usually has an influence in highly polluted, moist and rainy environments. Insulator dielectric strength may also be weakened by conductive defects in the insulator (Valagussa *et al*., 2009). An insulator surface becomes a conductive electrolyte when it is polluted. This enhances the flow of LC on the insulator surface, which decreases the insulators' electrical withstand voltage (Schwardt *et al*., 2004).

Methods for inspecting insulators include:

- thermovision acquired from the ground;
- ultraviolet (UV) images from the ground; and
- electric field distribution analysis from the tower by using an electric field probe.

Limbo (2009) performed insulator aging tests on various insulators under HVAC, positive HVDC and negative HVDC and noted that there is a change in the appearance and hydrophobicity due to the different excitations. For a porcelain insulator, Limbo (2009) observed a slight discolouration after HVAC, a brownish discolouration after positive HVDC and a reddish discolouration after negative HVDC excitation as seen in Figure 2.6. For a High Temperature Vulcanized Silicone Rubber (HTV SR) insulator, Limbo (2009) observed punctures, discoloration and tracks after HVAC, partial shedding of its material for positive HVDC and a burned rod after negative HVDC excitation as seen in Figure 2.7.

Figure 2.6: Comparison of material aging of a porcelain insulator under HVAC, positive HVDC and negative HVDC excitation, respectively (From Limbo, 2009)

Figure 2.7: Comparison of material aging of an HTV SR insulator under HVAC, positive HVDC and negative HVDC excitation, respectively (From Limbo, 2009)

2.3 Contamination of insulators

Pollution on insulator surfaces is one of the primary causes of failure on transmission lines (Nobrega *et al*., 2017). Pollution causes conductive deposits in heavily polluted areas to form conductive tracks on insulators, which allows LC to flow. This happens over an extended period of time and is called *tracking*, which can eventually lead to flashover (Shaohua *et al*., 2015). The effects of contamination can be mitigated by selecting the correct type and length of insulator. The environment in which the insulator is situated, plays a major role in the selection process. If excessive contamination is present, the simplest way to decrease the effect of the contamination would be to add more insulator disks. This, however, is not always practical due to tower configurations and the cost involved (Glossop, 2008:25). High LCs are indicative of contamination by pollution and loss of insulating properties.

A good insulator would normally have LC in the micro-Ampère (μA) range (Ferreira *et al.*, 2010:1). Measuring such small currents, in what can be termed a hostile electromagnetic environment around HVDC transmission lines, poses metrology challenges. Mitigation of the influence of the external line current, for example, is discussed in Chapter 4 where calibration and a differential

measurement methodology are incorporated in the design and validation of the prototype sensor presented in this work.

Insulator site pollution severity

By determining the pollution severity of a site, one can properly dimension an insulator to perform under those polluted conditions. Insulator dimensioning is dependent on the contamination conditions an insulator will be under and should be selected to obtain an acceptable level of flashover performance at the site where it will be in service (Engelbrecht *et al*., 2005). One of the most common methods of determining site pollution severity is to perform equivalent salt deposit density (ESDD) measurements over a long period of time (months to years). The artificial variation of ESDD can also be used to test how an insulator would behave in the field.

LC will increase (and flashover withstand voltage will decrease) when there is an increase in ESDD (Zhengfa *et al*., 2018). Jiang *et al.* (2010) and Abbasi *et al.* (2014) performed HVDC pollution measurements on porcelain and polymer insulators, and observed that the average flashover voltage decreases with an increase in ESDD. Zhang *et al.* (2007) and Zhang *et al.* (2010) performed HVDC tests under high altitudes for glass insulators and various long string insulators, and observed the same trend by Jiang *et al.* (2010) and Abbasi *et al.* (2014). Jiaqi *et al.* (1988) also notes that flashover withstand voltage decreases with an increase in altitude, as seen in Figure 2.8.

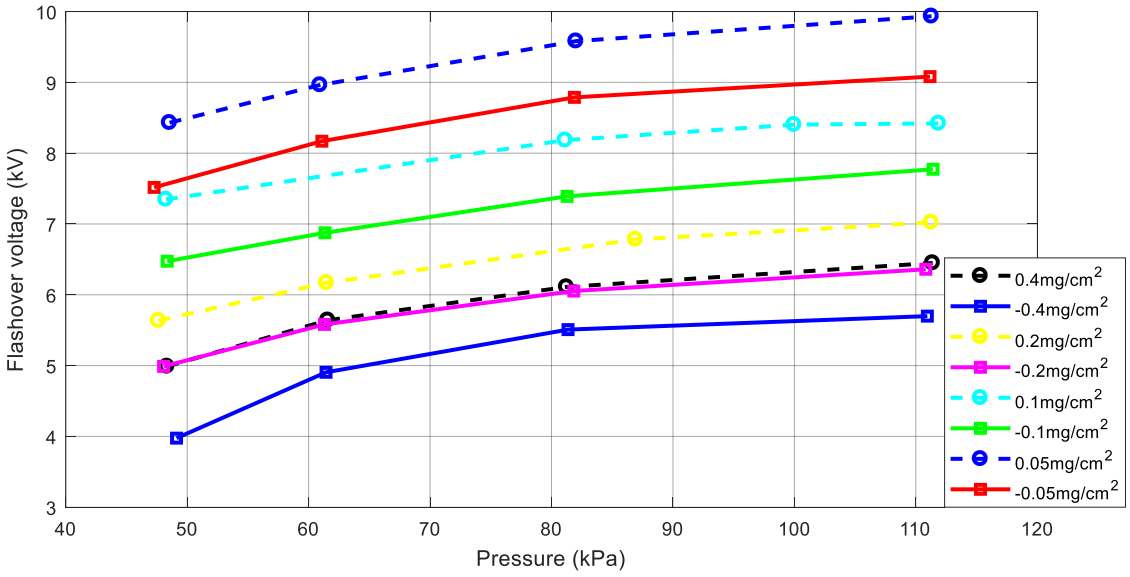

Figure 2.8: Pollution flashover voltage (positive and negative) versus pressure for a dc glass insulator (Adapted from Jiaqi *et al*., 1988)

Jayabal & Vijayarekha (2017) tested porcelain and polymeric insulators with an ac excitation and also found that the flashover voltage decreases with an increase in contamination. Jun *et al.* (2003) and Guo *et al.* (2015) performed ac voltage pollution tests for various insulators at high altitudes and observed that the withstand voltage decreases with an increase in ESDD. Also, Guo *et al.* (2015) tested various insulators (as seen in the legend) and observed that the voltage gradient decreases with an increase in altitude (decrease in atmospheric pressure) as seen in Figure 2.9.

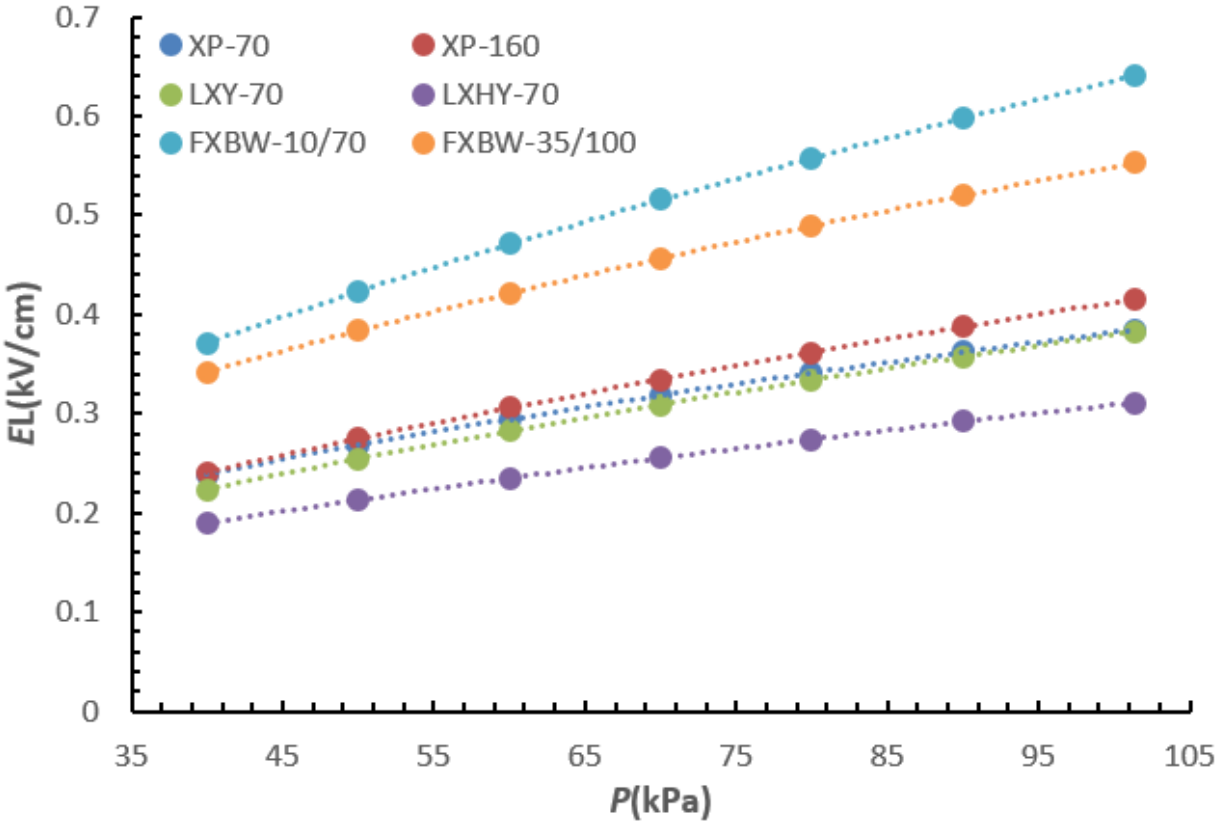

Figure 2.9: Relationships between voltage gradient *E*L and atmospheric pressure when ESDD = 0.05 mg/cm^2, Non-Soluble Deposit Density *NSDD* = 0.50 mg/cm^2 and temperature *t* = 15 °C (From Guo *et al.*, 2015)

Thus, it is safe to state that an increase in ESDD will lead to increased LC activity, irrespective of altitude or whether the transmission line is HVAC or HVDC. However, it can be seen that a change in altitude has an impact on an insulator's flashover performance.

The contamination flashover characteristic of ac insulators can be determined in terms of a power-law relationship, which is derived from the physics of the pollution mechanism. This is expressed by the following formula (Engelbrecht *et al*., 2005):

$$\frac{CD}{V} = B \cdot \gamma^{\alpha} \qquad \textbf{Equation 2.1}$$

Where CD is the insulator's creepage distance in mm, V is the insulator's flashover voltage in kV and γ is the contamination severity in mg/cm^2. B and α are unitless constants that characterise the contamination performance of an insulator and are determined empirically. Artificial contamination tests performed on glass insulators show that the average withstand characteristic voltage, V_{10}, which is 10% of the flashover voltage, can be determined by the following expression (Engelbrecht *et al*., 2005):

$$\frac{CD}{V_{10}} = 49.0 \cdot \gamma^{0.22} \qquad \textbf{Equation 2.2}$$

Figure 2.10 shows that the probability of an insulator flashover occurring is both a function of applied voltage and contamination severity. Along line 1 (in Figure 2.10), which represents a constant contamination severity, the flashover probability increases with an increase in applied voltage (meaning a reduction in the creepage distance per kV of the applied voltage) with a constant contamination severity. This probability function is usually determined through laboratory experiments. The normalised standard deviation 'c', expressed in per unit of the 50% flashover voltage, typically varies between 0.06 and 0.10 in artificial contamination tests (Engelbrecht *et al*., 2005). An insulator should not have a flashover probability of more than 10% at a certain withstand severity. This aspect of a particular insulator can be determined in laboratory experiments.

Line 2 in Figure 2.10 represents the actual service conditions where an HVAC insulator is energised to its maximum operating voltage but the level of contamination varies over time. For this case, the probability of flashover increases with an increase in contamination severity. Figure 2.11 shows the probability of flashover as a function of applied voltage for a contamination severity of 0.056 mg/cm^2 and a creepage distance of 2484 mm (Engelbrecht *et al*., 2007). It is observed that choosing a lower standard deviation for the contamination severity leads to a higher flashover probability as the applied voltage is increased.

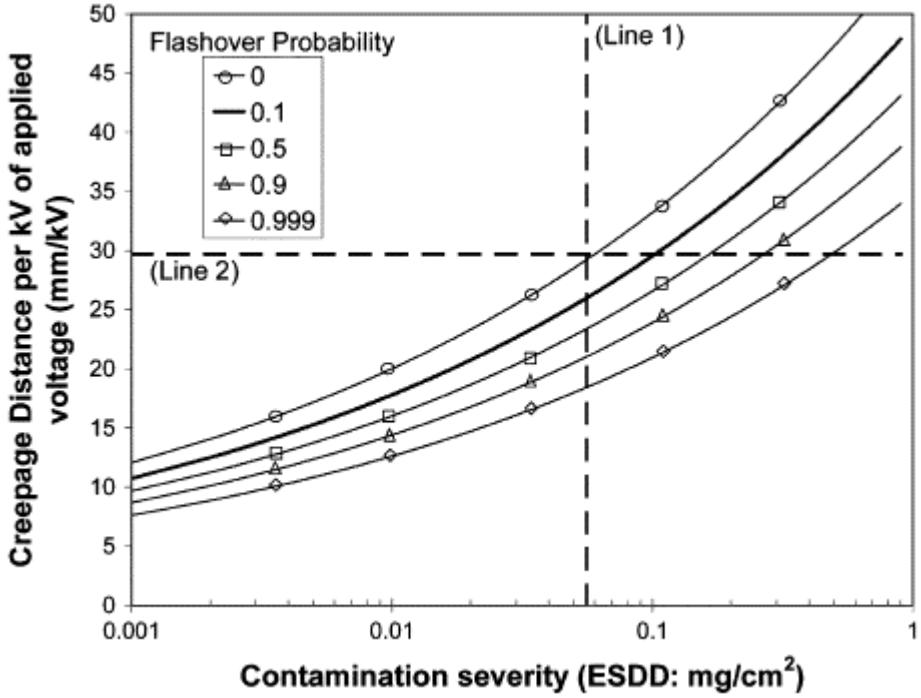

Figure 2.10: Flashover probability for an ac insulator as a function of applied voltage and the contamination severity. A standard deviation of 8% is assumed for the contamination severity (From Engelbrecht *et al*., 2007)

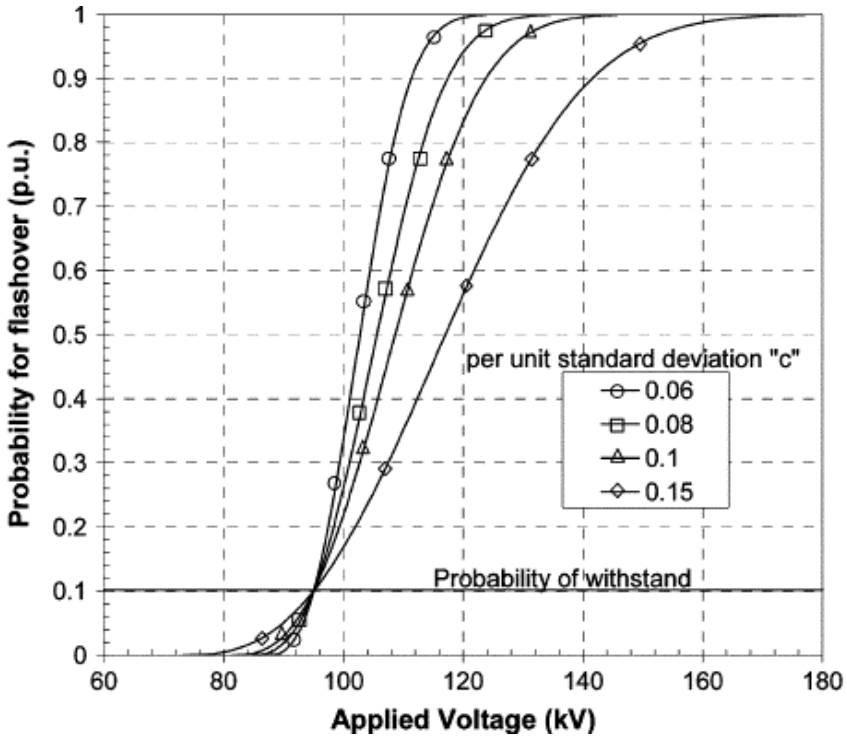

Figure 2.11: The probability for flashover as a function of applied voltage for an ac insulator with a creepage distance of 2484 mm and at a contamination severity of 0,056 mg/cm^2 (From Engelbrecht *et al*., 2007)

Pigini & Cortina (2011) used a statistical approach for the design of HVDC insulators. They compared HVDC ceramic insulators and composite insulators to display the influence of the insulator type on the insulation design for an HVDC transmission line. The simulation results (not experimental data) in Figure 2.12 (a) show that there is a higher flashover risk on ceramic insulators with the same unified specific creepage distance (USCD) when compared to composite insulators with the same USCD. The USCD is defined as the creepage distance of the insulator divided by the root mean square value of the maximum operating voltage across the insulator (Mouton, 2012). Figure 2.12 (b) shows that an increase in insulator string length will decrease flashover risk but the HVDC line would require a much longer ceramic insulator string to decrease the risk of flashover.

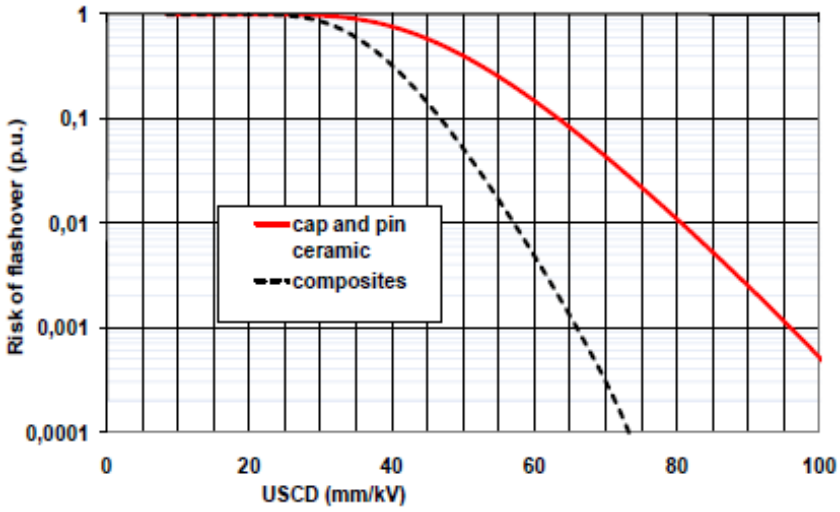

a)

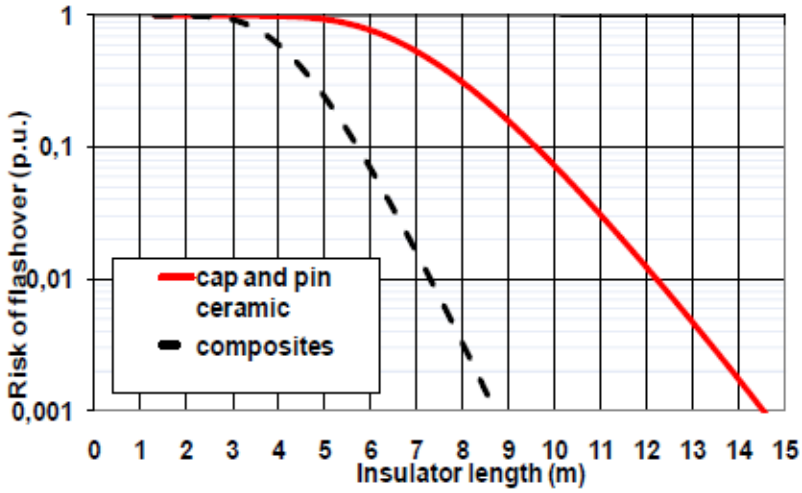

b)

Figure 2.12: Comparison between ceramic and composite insulator requirements for a 500 kV dc line with ESSD of 0.3 mg/cm^2 and Non-Soluble Deposit Density (NSDD) of 0.1 mg/cm^2. Risk of flashover as a function of a) USCD and b) insulator length (From Pigini & Cortina, 2011)

Zhang *et al*. (2010) mentions that the dc insulator flashover withstand voltage is approximately 20% lower than the ac insulator flashover withstand voltage under the same contamination conditions. This statement agrees well with Jiang *et al*. (2010) who states that the accumulation of contaminants is 1.2 to 1.5 times higher for dc than ac. The flashover withstand voltage is also higher (~ 4%) for a positively charged dc insulator compared to a negatively charged dc insulator (Abbasi *et al.,* 2014).

The conductance of an insulator is related to the LC that is flowing in the contamination layer on its surface due to the applied voltage. The conductivity of the pollution layer σ is determined by multiplying the form factor F of the test insulator with the measured surface conductance G_s of the insulator (Schwardt, 2005):

$$\sigma_s = FG_s \qquad \textbf{Equation 2.3}$$

The insulator surface conductivity can be related to the ESDD (see section 4.3.2), which is expressed as the equivalent Sodium Chloride (NaCl) on the insulator surface that will have the same electrical conductance as that of the actual deposit when dissolved in the same amount of water. Banik *et al*. (2015) performed studies on how two different salts, namely, NaCl and Potassium Chloride (KCl), affect insulator LC when mixed with Kaolin. Kaolin is mostly found in Asia and is also known as China clay. They observed that KCl had a greater impact on the formation of LC.

A formula for ac insulators that calculates the maximum value of leakage current, I_{max}, before an insulator flashover occurs, has been defined by Verma in the late 1970's (Verma *et al*., 1978). The formula is stated below (Schwardt *et al*., 2004):

$$I_{\max} = \left[\frac{\text{USCD}}{15.32}\right]^2 \qquad \textbf{Equation 2.4}$$

where I_{max} is in Ampère. I_{max} is not dependant on an insulator's geometry, pollutant or test procedure. The only variable of importance is the insulator's USCD in mm/kV. I_{max} can predict the flashover of any insulator in real-time. However, $I_{highest}$ is presently used as the standard definition of the minimum LC where flashover can occur (Schwardt *et al*., 2005):

$$I_{highest} = 0.25 \cdot \left[\frac{\text{USCD}}{15.32} \right]^2$$ **Equation 2.5**

This definition is preferred, since the calculated I_{max} value is too close to the actual flashover value. Thus, the $I_{highest}$ value gives an indication of excessive LC that can lead to flashover.

It is informative to reflect here on similar expressions for the dc case that have been empirically determined through two case studies at the corona cage as reported in Section 5.3. From those case studies that were conducted on glass insulators, it has been found that for the corona cage setup with an USCD = 9.6 mm/kV, flashover occurs at all contamination levels for currents of the order 1.4 mA and higher (case study 1). At 2 mA for the case of 0.07 S/m conductivity (case study 2), the LC with 100% probability of flashover is of the order 2 mA. Also, for the 0.07 S/m case, it is found that the probability of flashover is non-zero for currents of the order 0.4 mA and higher.

From these results, it can be deduced that $I_{highest}$ is also of the order 0.25 I_{max}, similar to the ac case.

However, the dc equivalent to Equation 2.5 is determined as:

$$I_{highest} = 0.25 \cdot \left[\frac{\text{USCD}}{258} \right]^2$$ **Equation 2.6**

which indicates that dc insulators have much lower LC thresholds for flashover than their ac counterparts.

A mathematical relationship between flashover voltage (FOV) and ESDD for HVDC schemes has been developed by Abdus Salam *et al*. (2000). An energised HVDC glass insulator was used during measurements. The results from the analytical expression were verified with experimental results and a close agreement between the results had been found. Length, mass, time (incorporated in the dimensional constant *dim*) and current values were used to develop the analytical expression that relates the HVDC FOV and ESDD of an insulator, as given in the following equation:

$$FOV = dim\left(ESDD\right)^{-0.4} L^{-0.3}$$ **Equation 2.7**

where dim is the dimensional constant and L is the leakage distance (the shortest distance between two conductive parts along the insulator's surface). The contaminants were created by mixing various percentages of NaCl in 100 ml distilled water. After the glass insulator had been tested for minimum and maximum FOV, it was dried out and the remaining NaCl granules were collected and dissolved into 100 ml of distilled water. Afterwards, a test cell was filled with the solution and the resistivity (in Ω-cm) of the salt solution calculated by the following formula:

$$\rho = \frac{V_t A_t}{I_t l_t} \qquad \textbf{Equation 2.8}$$

Where ρ is the solution restivity, I_t is the current of the test cell in Ampère, V_t is the voltage across the test cell in Volt, l_t is the length of the test cell in cm and A_t is the area of the test cell in cm^2. A relation between ESDD and the solution resistivity is expressed as:

$$ESDD = \frac{\rho^{-1.0143}}{A_i} 65650 \qquad \textbf{Equation 2.9}$$

where A_i is the area of the insulator under test (in cm^2). The calculated FOV from the analytical expression and the measured FOV obtained from the experiments are shown in Figure 2.13. The model of Akbar *et al.* (1991) is also included in Figure 2.13.

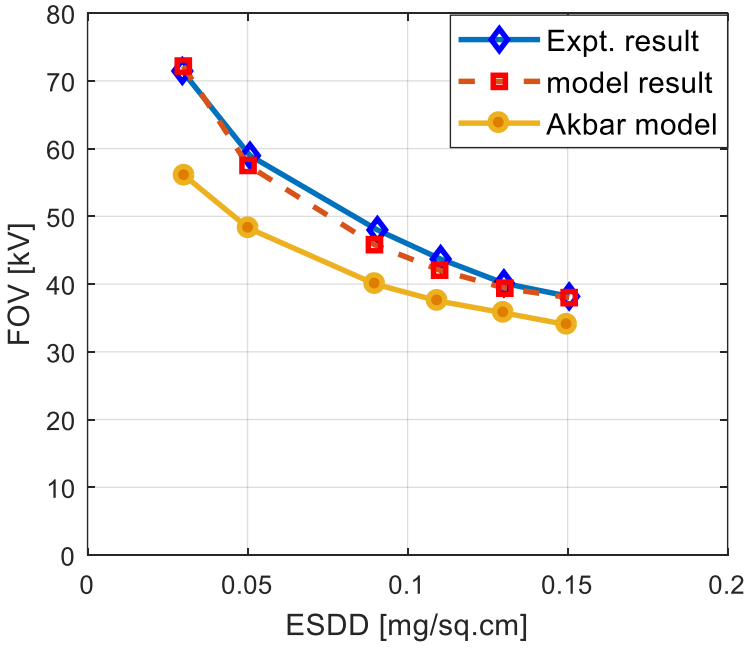

Figure 2.13: Variation of dc *FOV* with ESDD (Adapted from Abdus Salam *et al.*, 2000)

The work presented in this thesis also addresses a gap in the literature, i.e. laboratory testing of the probability of flashover versus LC for HVDC insulators. This is presented in Figure 5.14 and serves as valuable data for the determination of safe operational levels for live line workers. For the glass insulator investigated, and for a surface layer conductivity of 0.07 S/m, it is found that LC exceeding 0.6 mA can indicate the onset of flashover. The results are presented in detail in Section 5.3.2.2.

Contamination on an insulator's surface, as shown in Figure 2.14, is caused by the pollution in industrial areas, ambient salt content in coastal areas and dust in agricultural and rural areas (Farzaneh *et al.,* 2003; Thejane *et al*., 2013; Sierra *et al*., 2015; Sudalai Shunmugam *et al*., 2017). LC usually occurs when the insulator string is operated under high humidity conditions and where it is contaminated with bird excreta. The insulator will start to heat up at the energised end of the HV line. This leads to a dry-band forming on the insulator. As the sizes of these dry-bands increase, the frequency of flashovers occurring increases as well. For HVAC lines, the insulation design is primarily based on its overvoltage switching performance, which determines the arcing distance. Adequate pollution performance of an HVAC line can be obtained by selecting an appropriate creepage factor (Pigini & Cortina, 2011). However, in the case of HVDC lines, the pollution performance of dc insulators and the pollution severity in the areas where an HVDC transmission line passes through affects the HVDC insulator scheme more (Long *et al*., n.d).

Figure 2.14: Examples of surface contamination of glass insulators

2.4 Leakage current on high voltage insulators

From the previous section, it is clear that LC on HV insulators is a phenomenon that can have dire consequences, such as insulator flashover, if left unattended. The level of LC on an insulator's surface is affected by weather and pollution on an insulator's surface.

2.4.1 Influence of weather on LC

Strong winds decrease LCs on insulators because they sweep away deposits and also dry the insulator from dew or rain droplets. However, wind can also deposit pollutants on the surface of an insulator (Sudalai Shunmugam *et al*., 2017).

A cooler insulator surface will suppress the formation of LCs on ac and dc insulators since it reduces the solubility of most salts, and therefore, decreases the conductivity of the salts. This is indeed supported by experimental data presented in the work presented here, where a correlation coefficient of +0.37 has been calculated between LC and temperature for composite HVDC insulators in the Cahora Bassa case study (refer to Chapter 6). Interestingly, for glass insulators, no correlation has been determined between LC and temperature over the same extended time period.

Studies on HVDC insulators have also revealed that an insulator's flashover voltage decreases at higher altitudes due to low air pressure (Liang *et al.*, 2011; Yang *et al*., 2012; Yu *et al*., 2016). Air density is one of the primary factors affecting the dielectric strength of an insulator. Air density increases with an increase in air pressure and a decrease in temperature. The effect of air density on an insulator's dielectric strength is given in Equation 2.10 (Engelbrecht *et al*., 2012):

$$\frac{V}{V_0} = \left(\frac{\delta}{\delta_0} \right)^m \qquad \textbf{Equation 2.10}$$

where V is the insulator's breakdown voltage at air density δ, V_0 is the breakdown voltage, m is the arc index and δ_0 is the air density at sea level.

In the presence of light rain, but otherwise calm conditions, the rain dissolves existing contaminants on the insulator, which produces an increasingly large current (Muniraj & Chandrasekar, 2009; Dias *et al*., 2017). The LC itself causes ohmic heating in continuous but light rainfall and at the same time dissolving of contaminants take place, which causes the LC level to fluctuate. However, if the rainfall is very heavy, it will wash away contaminants and, hence, lower the LC level. LC is directly proportional to the humidity if the level of humidity is around 90%. Insulators closest to the energised end experience more contamination than insulators at the dead-end (near ground) due to the higher electric fields that exists at the energised end. The dc insulators also accumulate more pollution on its surfaces due to the electrostatic force acting on the contaminants (Zhang *et al*., 2013).

2.4.2 Relationship between LC and flashovers

Leakage current can be hazardous. Even a 1 mA LC can lead to pole-top fires in wooden pole distribution line structures. An insulator's surface layer resistance, which is affected by pollution and weather conditions, is the primary factor in determining the magnitude of the LC (Thejane *et al.*, 2013).

LC monitoring can also be used as an early warning flashover detection system (Engelbrecht *et al*., 2007; Phillips *et al.,* 2009). This detection system will allow for greater safety when deploying live line workers to perform maintenance on energised transmission lines. Referring to Figure 2.15, an acceptable LC must be defined for use in insulator monitoring, which will act as an alarm to commence maintenance of the insulators. This alarm level can be determined by combining the current characteristics of the insulator with the statistical flashover data.

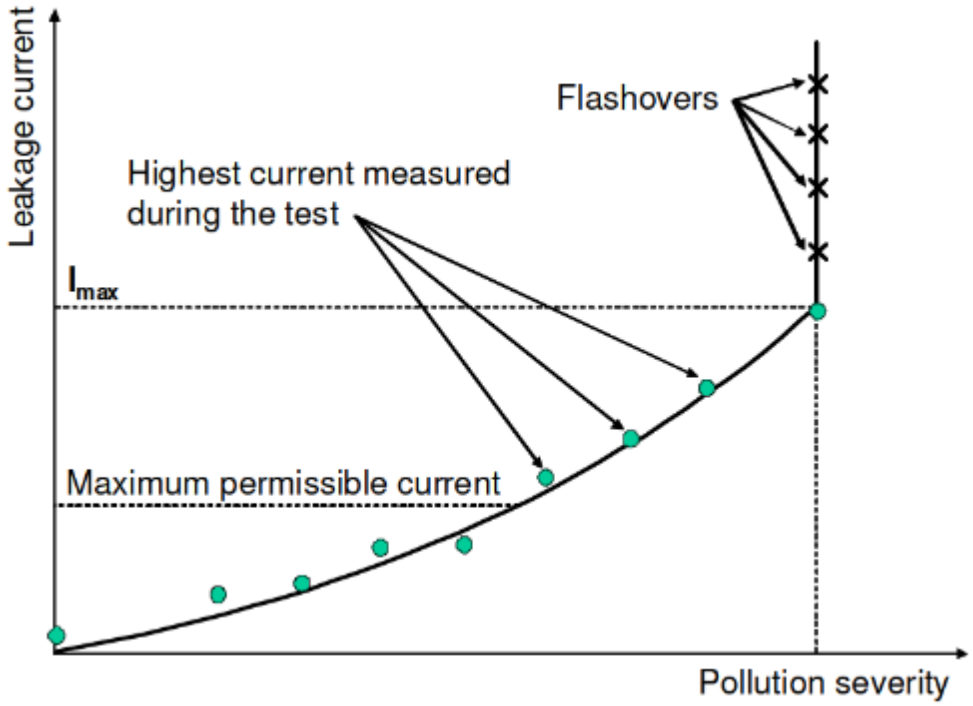

Figure 2.15: Relationship between LC and the pollution severity as determined through laboratory testing for HVAC insulators (From Phillips *et al.,* 2009)

An example of how this principle is applied to an ac insulator is given by Phillips *et al.* (2009). Laboratory experiments were conducted on a 69 kV post insulator with a USCD of 46 mm/kV. The experiments showed that the maximum LC on the insulator can be expressed in terms of pollution severity by the following formula:

$$I_{highest\_Phillips} = 1.45 \cdot \gamma^{0.77}$$ **Equation 2.11**

where $I_{highest\_Phillips}$ is expressed in Ampère and γ by the ESDD in mg/cm^2, respectively. Figure 2.16 shows the relationship between LC and contamination severity for this particular insulator. For other insulators, this characteristic has to be determined via laboratory testing.

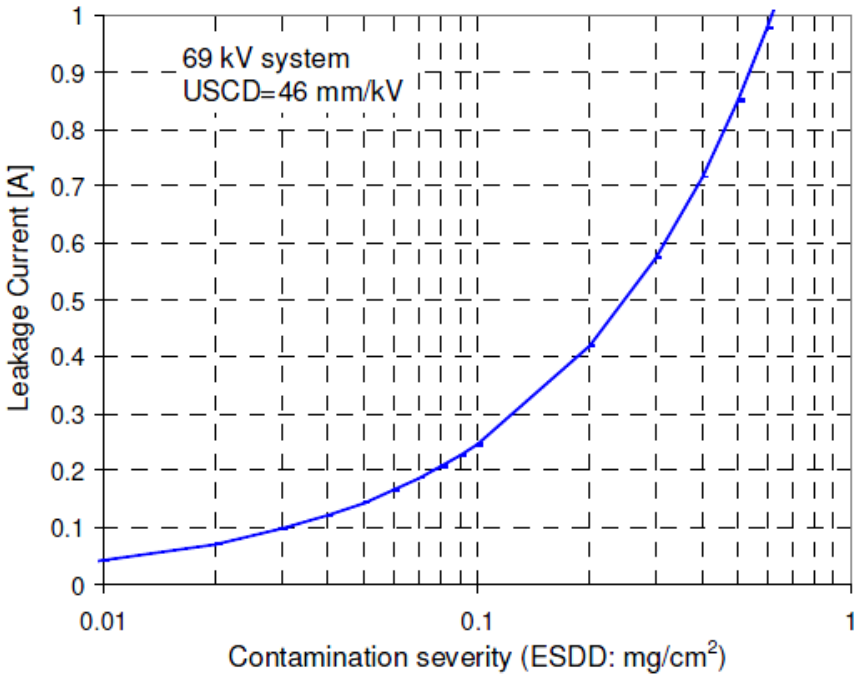

Figure 2.16: The highest LC measured during laboratory testing for an ac insulator (From Phillips *et al.*, 2009)

Flashover testing on this ac insulator showed that the *USCD* can be expressed in terms of the pollution severity by:

$$USCD = 72.8 \cdot \gamma^{0.47}$$ **Equation 2.12**

The flashover probably as a function of pollution severity for this ac insulator was also calculated and the results presented in Figure 2.17. Figure 2.17 is generated by incorporating the methodology of Engelbrecht *et al.* (2004) and assuming a normalised standard deviation of 0.08 for flashover probability of an insulator with an USCD of 46 mm/kV. Figure 2.18 shows the probability of flashover as a function of the maximum LC measured. Combining the data presented

in Figure 2.16 and Figure 2.17 yields the probability of flashover occurring as a function of highest peak current as presented in Figure 2.18.

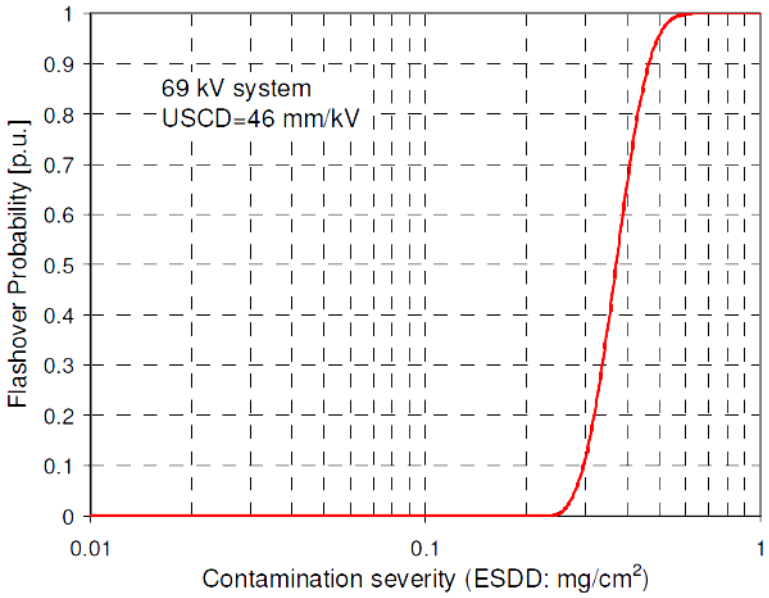

Figure 2.17: Calculated flashover probability as a function of pollution severity for a 69 kV ac insulator (From Phillips *et al.*, 2009)

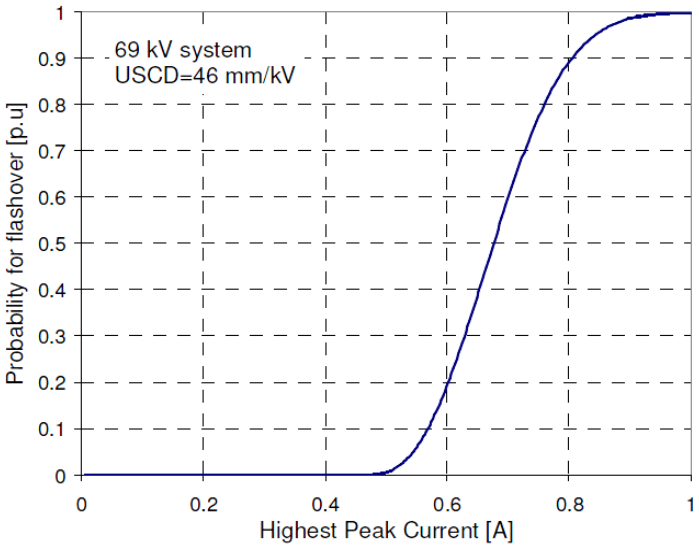

Figure 2.18: Probability of a flashover occurring as a function of highest peak current for a 69 kV ac insulator (From Phillips *et al.*, 2009)

Flashovers are present in both HVAC and HVDC transmission line systems, but in some respects, their mechanisms are fundamentally different. Cheng *et al.* (1981) and Engelbrecht *et al*. (2012) mention some reasons for the different responses:

- The accumulation process of contaminants is different. HVDC insulators attract more pollution than its HVAC counterpart in similar weather conditions.
- HVDC outputs a constant voltage or current, which further increases the flashover problem on its insulators. Scintillations are therefore harder to extinguish on HVDC insulators. Under ac conditions, an arc tends to travel along the surface of the insulator, while the dc arc is prone to leave the surface of the insulator and propagate in the air, as shown in Figure 2.19. (Also refer to Section 2.4.3.)
- Literature also states that insulators with the same pollution level will have a lower flashover voltage under dc than ac (Kimoto *et al*.,1973; Baker *et al*., 1989; de Decker *et al*.,1992).

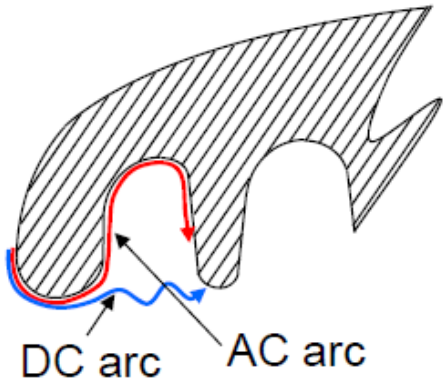

Figure 2.19: Schematic representation of a dry band arc propagating under ac and dc excitation (From Engelbrecht *et al*., 2012)

Use of LC to describe the flashover process on polluted insulators

LC can be used to fully describe the different stages that lead up to insulator flashover, namely the security stage, forecast stage and danger stage (Li *et al*., 2009). All these stages can be used as a pre-warning tool for insulator flashover, but the security stage is most important as it precedes the flashover event. Figure 2.20 shows an example of the three different forecast stages (Li *et al*., 2009). The ceramic insulators were energised to 20.2 kV RMS and had an ESDD of 0.1 mg/cm^2. The LC was calculated for each minute up to when flashover occurred. The change in LC shows the characteristics of the stages. This test was performed on ac insulators.

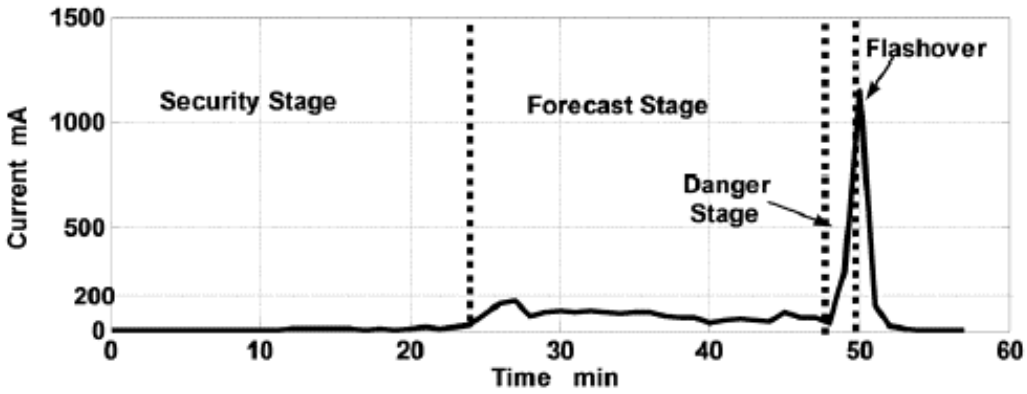

Figure 2.20: Leakage current (RMS values) plot for the entire contamination flashover process (From Li *et al.*, 2009)

Tang *et al*. (2015) focused on the LC evolution on ice covered ac porcelain insulators and found that the LC build-up could be grouped into four stages as shown in Figure 2.21. The input voltage was increased at a rate of ≈ 5 kV/s. From Figure 2.21 it is observed that the LC kept relatively constant in stage 1. With the continuous increase in input voltage, the LC quickly increased due to the formation of arcs on the insulator's bottom surface as shown in Figure 2.22 (a). In stage 2 the LC increased rapidly and visible arcing was occurring. In stage 3, the LC stopped increasing rapidly and was relatively constant. Stage 3 was similar to stage 1, but stage 3's amplitude was higher and the duration of relatively constant LC was much shorter. Near the end of stage 3, as the input voltage continued to increase, white arcs appeared (Figure 2.22 (c)), which grew into an eventual flashover as seen in stage 4 and pictured in Figure 2.22 (d).

Tang *et al*. (2015) also defined four types of LC during their research:

- I_w – characteristic current, which is the average current measured in stage 3;
- I_{FT} – critical current, the peak current measured at the half cycle before flashover occurred (see Figure 2.23);
- I_F – the peak flashover current (see Figure 2.23); and
- I_s – the peak current after flashover occurred (see Figure 2.23).

The I_w and I_{FT} were considered the most important types of LC as they occurred at the critical moment just before flashover.

Similar studies for dc have not been found in literature. Thus, no comparison could be made on the LC stages leading up to flashover. Such experimental results are, however, presented in Chapter 5.

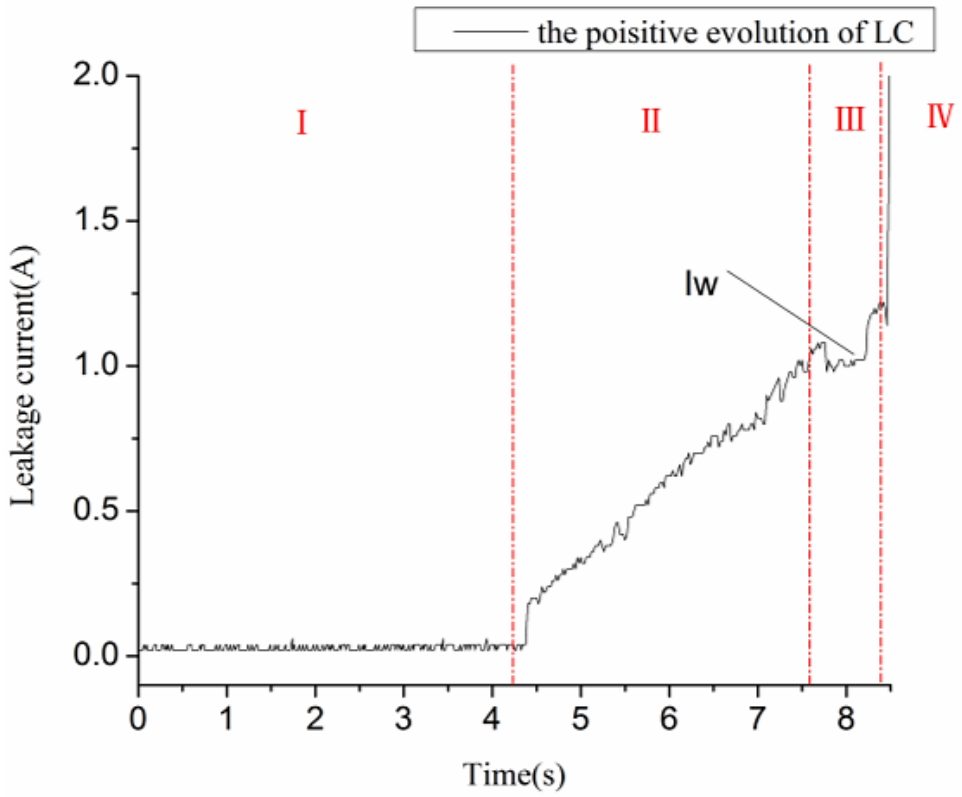

Figure 2.21: Evolution of LC before insulator flashover (From Tang *et al*., 2015)

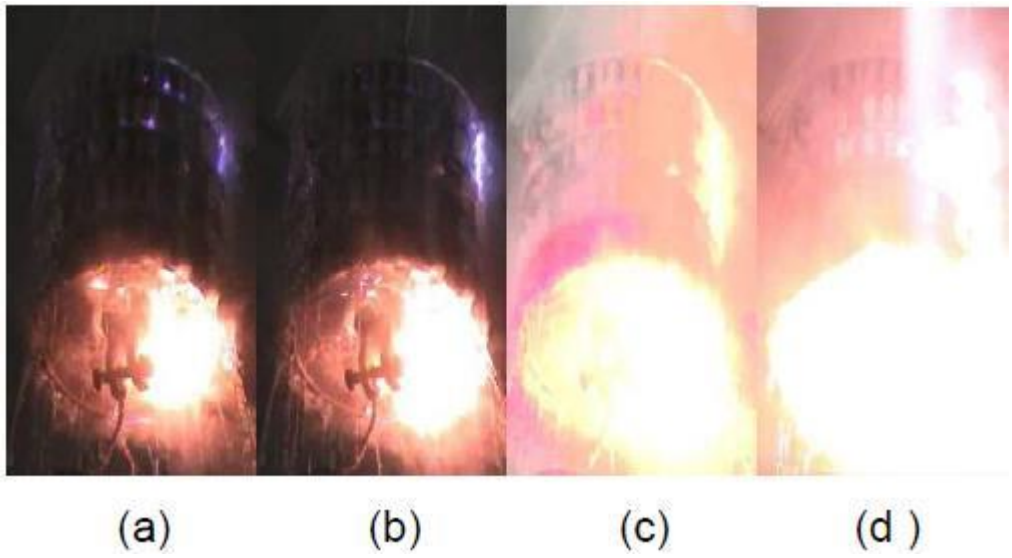

Figure 2.22: Insulator LC, arc development and flashover (From Tang *et al.,* 2015)

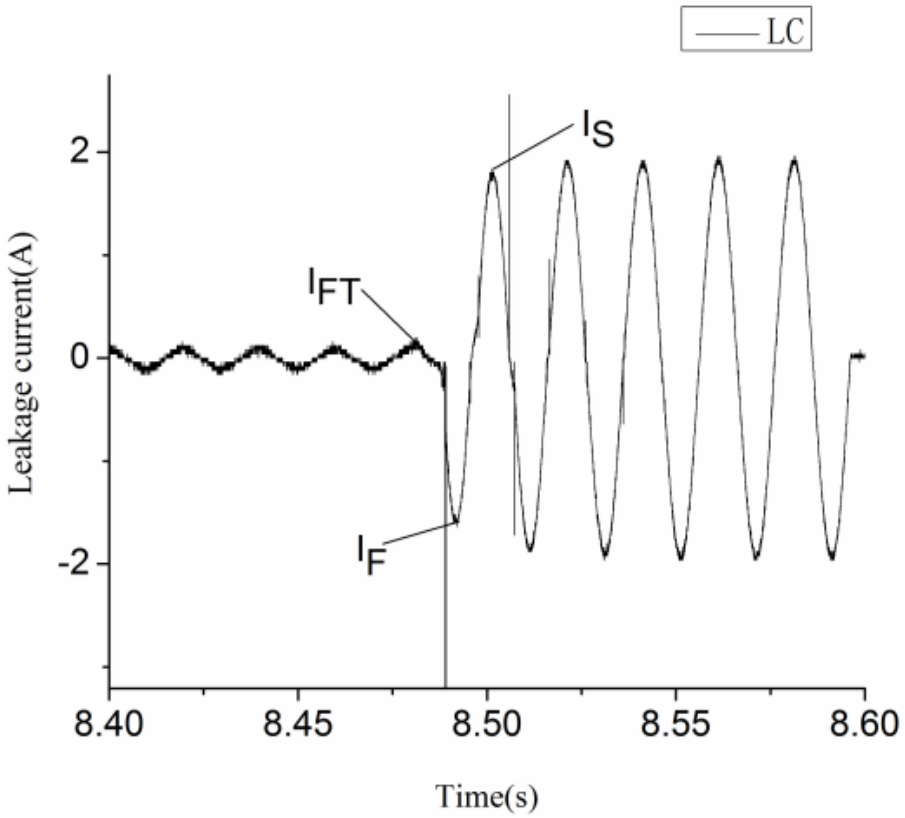

Figure 2.23: LC just before and after flashover (From Tang *et al.*, 2015)

Zhengfa *et al.* (2018) studied LC characteristics and what influences them on a 110 kV ac composite insulator. Figure 2.24 shows the LC waveforms obtained for various ESDDs. It was observed that the LC amplitude increased and the waveform became more distorted as the ESDD increased. Polluted ac insulator tests by studying LC variation have also been performed by Banik *et al*. (2014) and similar results were reported.

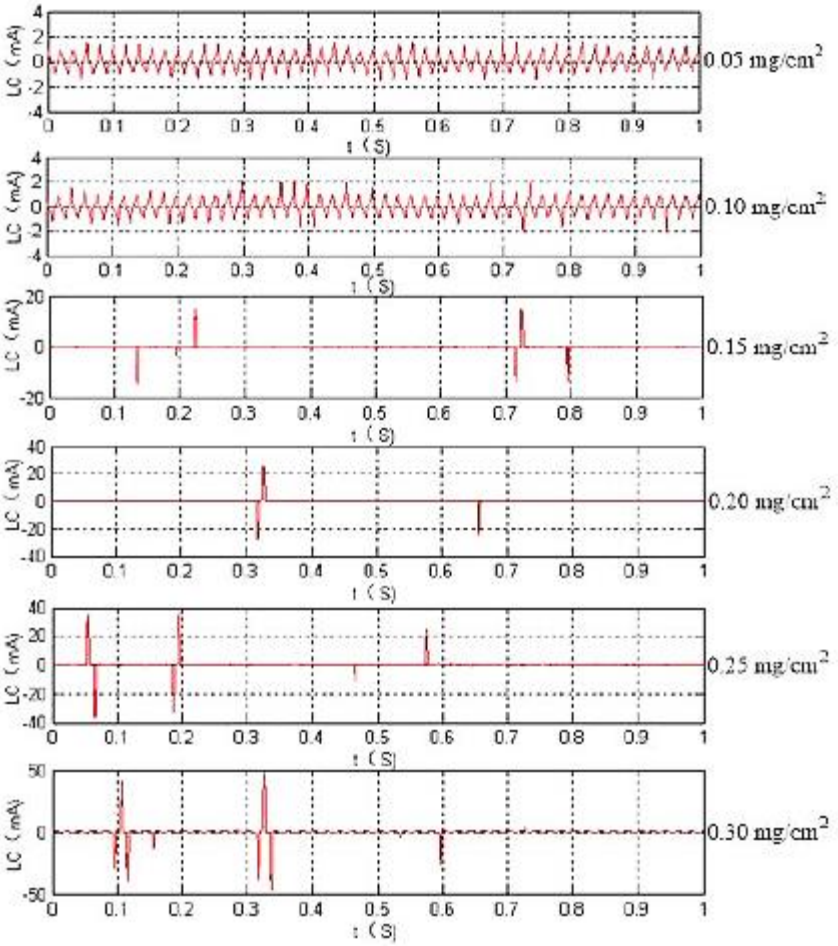

Figure 2.24:Composite insulator LC waveform for different ESDDs (From Zhengfa *et al*., 2018)

2.4.3 Influence of arcs on HVAC and HVDC insulators

The formation of arcs is one of the key characteristics that lead to insulator flashover. Werneck *et al*. (2014) mention the conditions that lead to flashover:

- Pollutants settle on the surface of the insulator;
- These deposits combine with moisture caused by light rain or fog and form a conductive layer on the insulator's surface;
- LC starts to flow;
- Partial discharges start occurring on the insulator's surface;
- Possible flashover.

As stated above, before flashovers occur, arcs are present on insulators. In section 2.4.2 it was also mentioned that arcs have different characteristics under ac and dc conditions. Zhicheng & Renyu (1990) state that under certain conditions, a dc arc will propagate along an insulator's

surface. However, when it reaches a critical insulator leakage distance (≈2/3 of the total leakage distance), insulator flashover suddenly occurs. The insulator flashover process can be represented as a discharge in series with a resistance as shown in Figure 2.25. The discharge represents the arc bridging the dry band gap and the resistance represents insulator resistance.

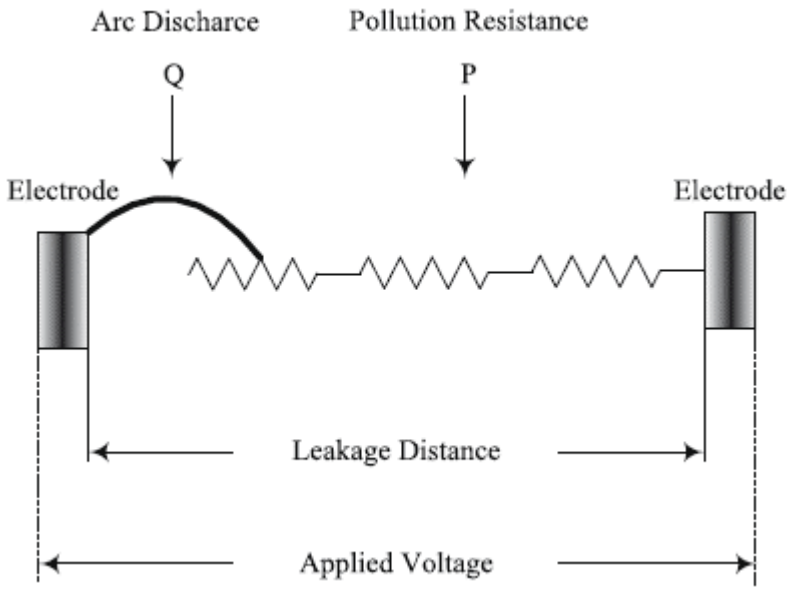

Figure 2.25: Model of a polluted insulator (Obenaus, 1958)

Arcs on ac insulators are more complex since it changes many times per second. The intensity of the arc reaches its peak at maximum ac voltage and at other times it reduces and re-ignites when crossing the zero-voltage line. Zhicheng & Renyu (1990) state two phenomena of ac arcs; first, the arc extinguishes and re-ignites when passing through zero current, and second, the arc does not extinguish but is, however, much weaker when passing through the zero-current level.

The propagation of arcs, such as the bridging of arcs between insulator sheds and ribs, and arcs drifting away from the insulator's surface, is random in nature. The number of arcs in series on an insulator has an effect on the insulator flashover voltage as well. Flashover voltage increases with an increase in the number of arcs in series on an insulator string. Thus, it is more detrimental to the insulator if only one arc appeared before flashover occurred. Hence, a good insulator design should avoid bridging of arcs and increase the number of arcs in series before flashover occurs (Zhicheng & Renyu; 1990). Equation 2.13 can be used to express the dc flashover process of polluted insulators (Zhicheng & Renyu; 1990):

$$U = AXI^{-n} + R(x)I \qquad \textbf{Equation 2.13}$$

where U is insulator's applied voltage, X is the arc length, $R(x)$ is the resistance of the pollution layer, I is the current passing through the surface of the insulator, A and n are constants of the arc characteristics. Equation 2.14 can be used to determine the ac flashover process of polluted insulators (Zhicheng & Renyu; 1990):

$$U_m = AX\ \mathrm{I}_{\mathrm{m}}^{-n} + R(x)I_{\mathrm{m}} \qquad \textbf{Equation 2.14}$$

where U_m and I_m are the peak voltage and current, respectively. Zhicheng & Renyu (1990) also state that two conditions, namely, the arc stability and arc recovery, should be met for an ac flashover to occur. Of the two conditions, the recovery condition of an ac arc is more important. The recovery of an ac arc without it extinguishing can be determined using Equation 2.15 (Zhicheng & Renyu; 1990):

$$U_m = 531\frac{L}{I_{\mathrm{m}}} \qquad \textbf{Equation 2.15}$$

where L is the leakage path along the surface of the insulator. The recovery of an ac arc that extinguishes and re-ignites can be determined using Equation 2.16 (Zhicheng & Renyu; 1990):

$$U_m = 1050\frac{X_c}{I_{\mathrm{m}}} \qquad \textbf{Equation 2.16}$$

where X_c is the critical arc length.

Zhang *et al*. (2013) observed the surface charge (arcs) characteristics on contaminated dc post insulators using a test voltage of 520 kV. The following observations have been made:

- The voltage distribution was non-uniform and partial discharges started from the energised end as seen in Figure 2.26 (b). This phenomenon was also observed on their high-speed camera. The insulator in (a) was superimposed to indicate its position.
- With the growth of the arc, the top section of the insulator was bridged as seen in (c).
- Due to high electric field experience, corona and discharges occur easily and more frequent as seen in (e).
- No significant discharges were seen close to the end fittings.

- Due to the LC that exhibits high current density areas on the insulator surface, dry bands form and are eventually bridged by the arcs due to the high intensity electric field strength of the bands.
- All the arcs did not appear on the same side; thus, it is not uniform.
- Arcs across the dry bands are unstable and they start to move away from the insulator's surface; known as the drifting phenomenon.
- Floating arcs led to the phenomenon of creating arcs between insulator sheds.
- Two types of bridging arcs were observed; the drifting bridge (h) and the semi-bridge (g) as shown in Figure 2.27.
- The drifting bridge means that the arc drifted away from insulator surface and propagated along its edges.
- The semi-bridge means that the arc propagated between the insulator sheds.
- The drifting bridge is significantly more serious as it decreases an insulator's leakage distance more than the semi-bridge.
- The arcs further develop from the energised side of the insulator and eventually connect all the arcs together, leading to flashover.

Figure 2.28 shows the process of the development of an arc into insulator flashover (Zhang *et al*., 2013).

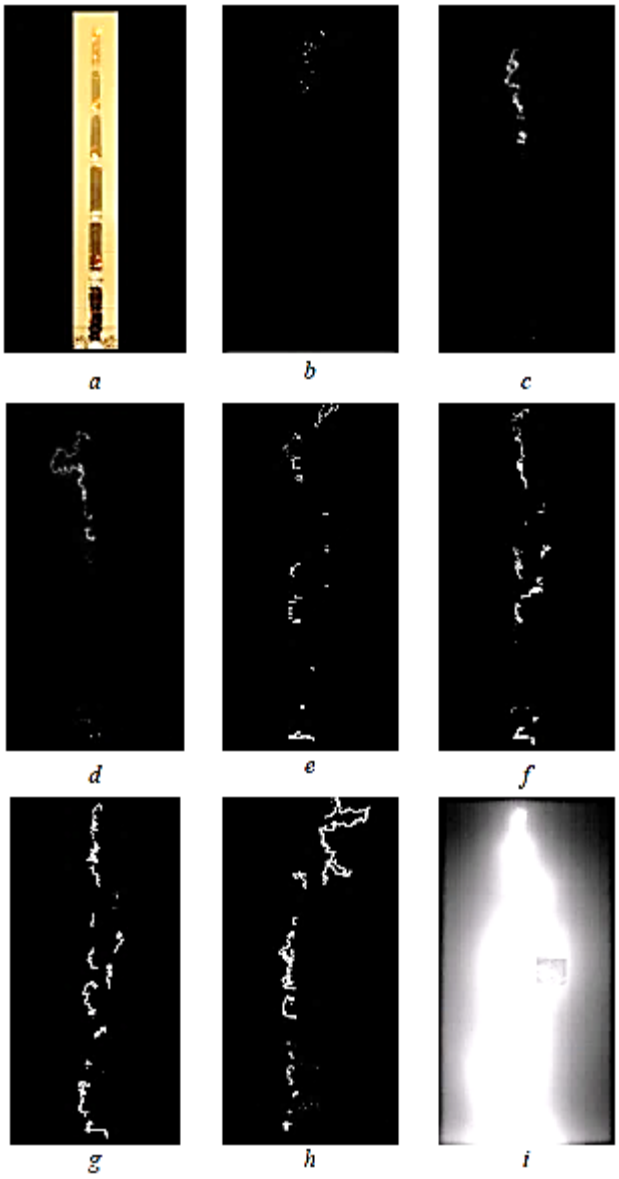

Figure 2.26: Arc propagation during flashover of a dc post insulator (from Zhang *et al*., 2013)

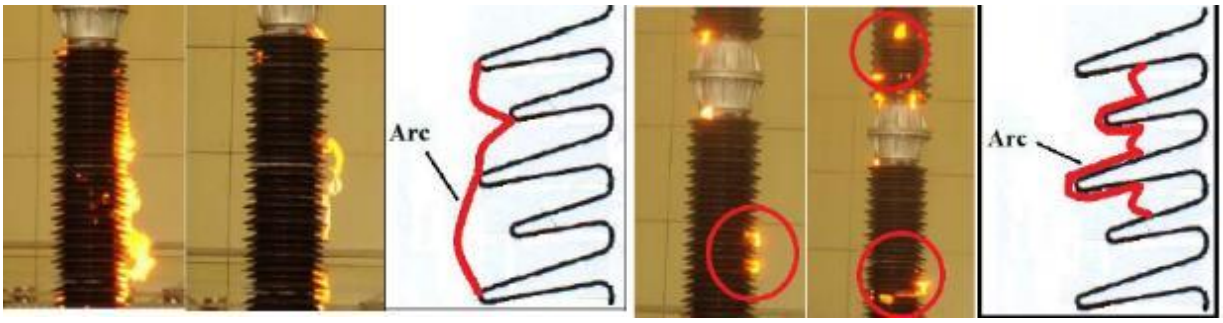

a) **b)**

Figure 2.27: a) Example of a drifting bridge arc and b) Example of a semi-bridge arc (from Zhang *et al*., 2013)

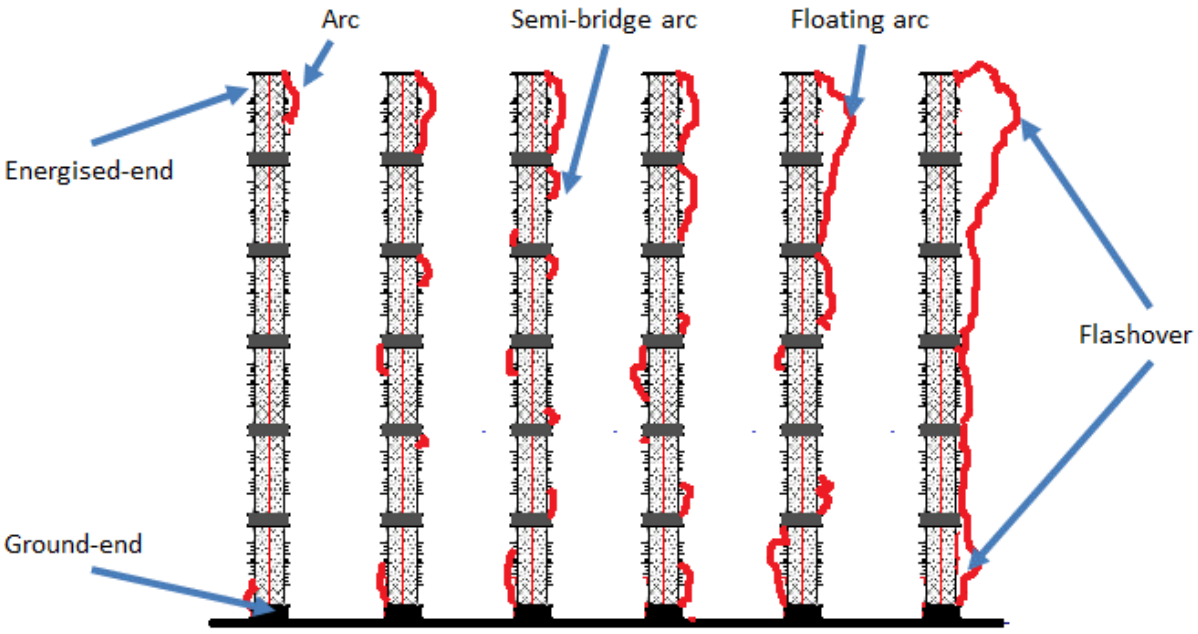

Figure 2.28: **Arc to flashover process on an insulator (Adapted from Zhang *et al*., 2013)**

Zhang *et al.* (2010) performed HVDC flashover pollution tests at high altitudes on a glass insulator string and found that the phenomenon of arcs extinguishing and re-igniting did not exist as for ac arcs as mentioned by Zhicheng & Renyu (1990). They also presented a new model explaining flashover mechanisms at high altitudes. It can be expressed in terms of surface arcs x_1 and air gap arcs x_2 in series with a resistance that represents the pollution layer. They mentioned that the voltage-current characteristics of an arc at sea level and high altitudes can be determined as follows:

$$E = A\left(\frac{P}{P_0}\right)^{m} \cdot I^{-c} \qquad \textbf{Equation 2.17}$$

where E is the voltage gradient along the arc in V/cm, I is the current through the arc in Ampere, P is the air pressure at high altitude in kPa, P_0 is the air pressure at sea level and A, m, c are constants of the arc characteristics. An expression for determining the surface arc characteristics at high altitudes is given in Equation 2.18 and Equation 2.19:

Positive arc

$$E = 103.4\left(\frac{P}{P_0}\right)^{0.51} \cdot I^{-0.52} \qquad \textbf{Equation 2.18}$$

Negative arc

$$E = 129.0\left(\frac{P}{P_0}\right)^{0.51} \bullet I^{-0.52}$$ **Equation 2.19**

For a dc air-gap arc, the equation is as follows:

$$E = 89.4\left(\frac{P}{P_0}\right)^{0.92} \bullet I^{-0.28}$$ **Equation 2.20**

Zhang & Farzaneh (2000) performed ac and dc arc propagation tests and discovered that the arc root (beginning of the arc) increases non-linearly as the LC increased.

From the above it can be seen that extensive research has been conducted on insulator flashover studies, as well on arc development and propagation. It was observed that the following parameters influence insulator flashover:

- Type of applied voltage;
- Type of insulator and insulator profiles;
- Contamination of insulators;
- Insulator length;
- Climatic conditions; and
- Altitude/pressure.

Since the formation of LC on insulators is a pre-requisite for the development of arcs and eventual flashovers (Phillips *et al*., 2009), one can infer that these topics influence LC as well. Moreover, arcs and flashovers can be visually observed. LC, however, cannot be seen with the naked eye and has to be modelled and measured to fully understand its nature. This is the topic of Chapters 4, 5 and 6. Research has also shown that altitude has an impact on arcs and insulator flashover voltage, but little to no information has been found on how it fundamentally influences LC behaviour on an insulator. This will be studied in Chapter 3.

Chapter 3 discusses the development of an LC sensor for dc glass insulators as they are the insulators of interest, and a LC sensor for it did not exist commercially at the commencement of the thesis.

2.5 Current sensing techniques

There are various ways of measuring current, be it directly or measuring its associated magnetic field. Ways of measuring current include intrusive and non-intrusive measurements. For laboratory tests, intrusive measurements are normally used. In the case of active transmission lines, a non-intrusive method is preferred as de-energising of transmission lines is costly. An example of an intrusive technique is the *resistive shunt method*. Non-intrusive measurements can be made with transformers and magnetic field sensors. Measurement of the magnetic field associated with a current source provides a non-invasive mechanism to measure the current (Elmatboly & Homaifar, 2008). The magnetic fields of HVDC lines are static, since their voltage and current sources do not alternate over time. Thus, sensors capable of also measuring static fields are investigated in this work.

In an HV scheme, when deploying magnetic techniques to measure currents indirectly, care should be taken to shield the magnetic fields of the transmission line currents that can be of the order kilo-Ampère, from that of the LC that are of the order micro- to milli-Ampère.

Table 2.1 shows examples of static magnetic levels in close proximity to common electromagnetic sources. The ±500 kV dc transmission line has magnetic field levels of the order 300 - 600 mG (30 - 60 µT) at ground level. The Cahora Bassa is rated nominally as a ± 533 kV, 1800 A HVDC line (ABB, n.d), which is close to the example in Table 2.1.

Table 2.1: Static magnetic fields near common sources (Adapted from Clean line energy partners fact sheet, 2011:1)

Magnetic fields	
Source	**Magnetic field level**
MRI machines	15 000 000 – 40 000 000 mG
Refrigerator magnets	10 000 – 50 000 mG
Battery-operated appliances	3000 – 10 000 mG
Electrified railways	< 10 000 mG
The Earth	300 – 700 mG
± 500 kV dc transmission line (standing beneath the conductors)	300 – 600 mG

As stated earlier, methods of measuring current include the use of a resistive shunt, current transformers or magnetic sensors. Static and time-varying currents produce magnetic fields, which

can be measured to determine the current value. In the case of alternating currents, Faraday's Law is used, while for dc currents, Ampère's Law (Haus *et al*., 1989) can be applied.

Ampère's Law states that the line integral of the induced magnetic field intensity ($\boldsymbol{H}$) around a closed path is equal to the current enclosed within that path, which is mathematically written as (Haus *et al*., 1989):

$$\oint_c \boldsymbol{H} \bullet d\mathbf{L} = I \qquad \textbf{Equation 2.21}$$

where $\boldsymbol{H}$ is the magnetic field intensity, I is the current and $d\mathbf{L}$ is an infinitely small section along the closed integral path.

2.5.1 Current sensing methods for ac

2.5.1.1 Fibre optic sensing

The LC modulates an ultra-bright light-emitting diode (LED) that produces a modulated light signal (Werneck *et al*., 2014). This signal is transmitted along a fibre optic line to a remote unit. This sensor has advantages, such as immunity to electromagnetic interference, low cost, light weight and does not need a power source close to the high voltage transmission line. The sensors are installed on a transmission line and the data logged.

An LED fibre optic sensor for LC monitoring on insulators was designed by Wang *et al.* (2012). Good linearity was reported and sensitivity of 40 mV/mA obtained. This sensor cannot measure dc since its frequency range was 1 Hz to 10 kHz.

2.5.1.2 Current transformers and Rogowski coil

A ferrous current transformer can be used with a straight conductor as the primary winding. Current transformers are only suitable for ac current measurements (Phillips *et al.,* 2009). A non-intrusive sensor that can measure ac LCs over a wide frequency band of several Hertz to tens of MegaHertz was developed by Chen *et al*. (2008). It is based on the Rogowski coil principle. Amin *et al.* (2009) also used a CT for their research. CTs are available as clamp-on devices, but for insulator implementation it becomes quite difficult due to the size of insulators. For HVDC, however, CTs cannot be used as there are no alternating fields to couple into the CT device.

2.5.2 Current sensing methods for dc and ac

Techniques for measuring both ac and dc LCs include the resistive shunt method (Jia *et al*., 2014) and measurement with an online LC analyser (OLCA) (OCLA product description, n.d; Pieterse *et al*., 2011; Elombo *et al*., 2013). The OLCA employs various sensors, such as Hall Effect sensors. A glass stand-off insulator is typically installed in series with the insulator under test – usually at the ground end. This is not practical for actual transmission lines as the insulator string will have to be removed in order to install the stand-off. OLCA and resistive shunt measurements are more applicable to laboratory test configurations.

The next section focuses on magnetic field sensors for the indirect measurement of ac and dc currents, as this is the technology used in this work for the development of an in-situ insulator LC sensor.

Magnetic sensors offer isolation and non-intrusive measurement capabilities. A current sensing magnetic field sensor can be used with cores and can be designed to work in a closed-loop mode, which is discussed in the following sections.

2.5.2.1 Magnetic sensing using cores

Ferromagnetic cores can be used as flux concentrators as they concentrate the magnetic flux density of a current carrying wire/conductor passing through it (El Bacha *et al*.,2014; Aparnathai & Dwivedi, 2015). The concentration of magnetic flux is used in current sensing as shown in Figure 2.29. A magnetic sensor is placed in the gap of the lamination or core and a current carrying wire is passed through the hole of the core or lamination. The magnetic field of the current in the wire is trapped in the core or lamination and passes through the magnetic sensor at the gap (Honeywell, n.d.:3).

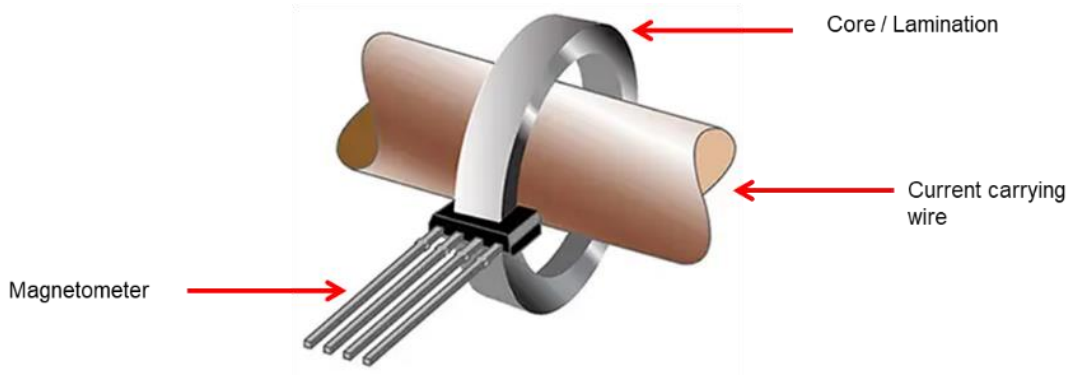

Figure 2.29: Magnetic sensor in a core (From Digikey, 2015)

If a core is not used, the magnetic field sensor may be susceptible to stray magnetic fields, leading to erroneous current measurements (Latham, 2019). Without a core, LC would be very small and difficult to measure accurately. With the addition of the core, magnetic fields can be amplified 20 times or more, depending on the permeability of the core or lamination. Therefore, they are very effective in improving sensor accuracy and resolution (El Bacha *et al*., 2014). If an air gap is cut into the core, it will lower the initial permeability of the core. The resultant permeability is called the core's effective permeability. Permeability is defined by Equation 2.22 below (TDK, 2017):

$$\mu = \frac{\beta}{H} \qquad \textbf{Equation 2.22}$$

where β is the magnetic flux density and H is the magnetic field strength. The effective permeability (μ_e) of a single gap core is calculated using Equation 2.23 below (TDK, 2017):

$$\mu_e = \frac{\mu_i}{1 + \frac{(l_g)(\mu_i)}{l_m}} \qquad \textbf{Equation 2.23}$$

where μ_i is the permeability of the material, l_g is the length of the gap and l_m is the mean magnetic path length.

In addition to concentrating the magnetic flux sensed by the sensors, the core or lamination also offers magnetic shielding, since external fields choose to remain in the lamination by going around the back of the lamination (Honeywell, n.d.:5). This is because the gap has a high magnetic reluctance, as shown in Figure 2.30. However, this magnetic shielding property also increases the size and complexity of the device.

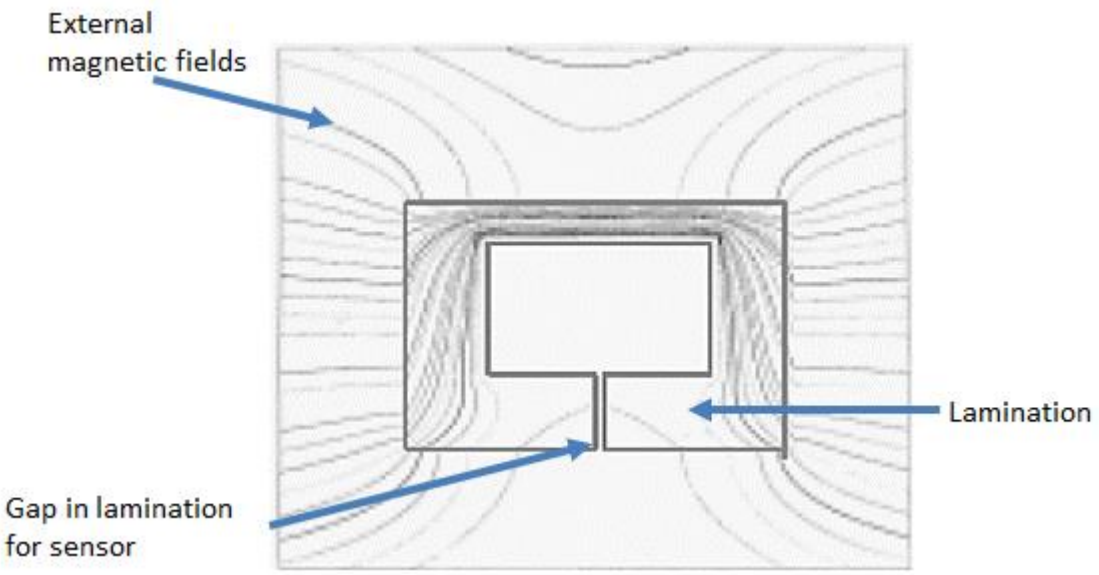

Figure 2.30: Stray magnetic fields around a lamination (From Honeywell, n.d.:5)

The disadvantages of using cores or laminations are (Honeywell, n.d.:5):

- materials may display hysteresis;
- the material may still be magnetised in one direction even with no magnetic field present; and
- saturation of the material can occur if the magnetic field within the core is excessively high.

2.5.2.2 Magnetic sensing in a closed-loop design

Current sensors can be operated in a closed-loop mode whereby the sensor is placed in a compensating field, which forces the field across the sensor to be zero. The compensating field is generated by a coil with *n* turns; thus, the current in the feedback coil is proportional to the current in the primary coil through the turn ratio of the coil. Typically, a resistor is placed in series with the coil to measure the voltage proportional to the input current as shown in Figure 2.31 (Honeywell, n.d.:5).

The advantages of the closed loop current sensing technique include:

- sensing of larger currents is possible without saturating the sensor;
- higher sensor accuracy is obtained with a very linear output;
- the dynamic range of the sensing device increases; and
- a higher measurement bandwidth is obtained.

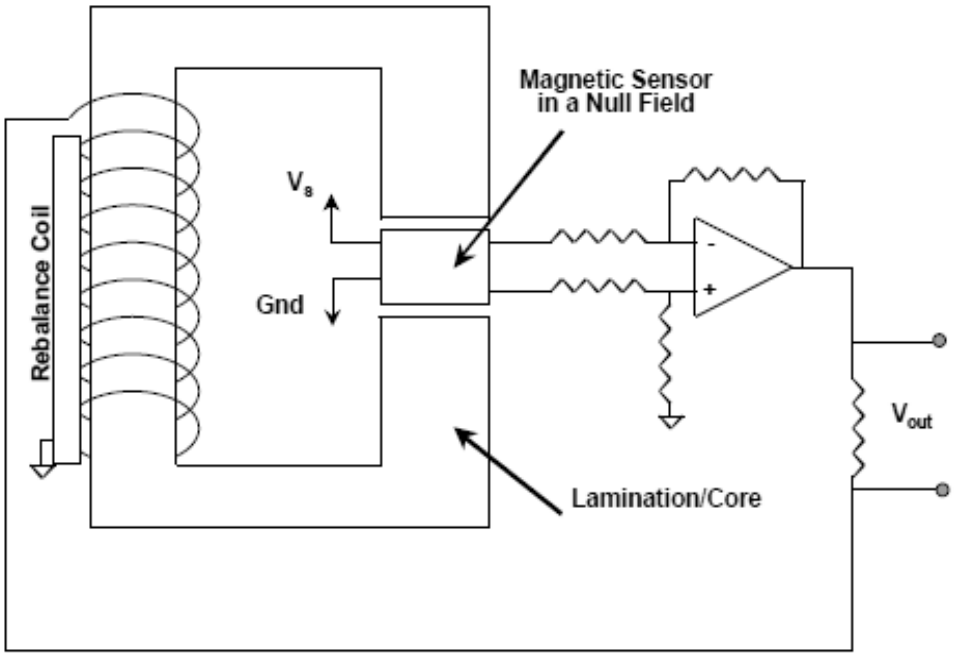

Figure 2.31: Closed-loop current sensing (From Honeywell, n.d.:5)

2.5.3 Mitigation of stray fields

Stray fields can severely affect the performance of magnetic field sensors. One way to remove these unwanted fields is through filtering. Ac coupling can be used to remove nearby unwanted dc fields and also the Earth's magnetic field. Low-pass filters will remove high frequency signals and 50 Hz signals emanating from HV transmission lines. High frequency fields can also be removed by the use of an RF choke (series inductor) or using a shading ring around laminations (Honeywell, n.d.:6). The filtering approach is not very useful when the stray frequencies lie in the same bandwidth where measurements need to be conducted.

Another method of shielding devices from stray magnetic fields is with the use of magnetic shielding material. The shielding material has a very high permeability (μ_r= 55000 – 75000 H/m) relative to air ($\mu_0 = 1.257 \times 10^{-6}$ H/m) and encloses the device under test (Advance Magnetics, 2014). Care must be taken not to shield the sensor from the fields to be measured with this approach as the magnetic field from the current carrying wire might end up in the shielding material, rather than close to the sensor.

Differential measurement techniques are effective in mitigating the effect of ac and dc stray fields. Such an approach is demonstrated in Figure 2.32. In one sensor, the stray field and sensed field are summed, and in the other sensor, they are subtracted. The stray fields must be uniform and

symmetrical over the volume of the two sensors and the summed field must not exceed the sensor's linear range to prevent saturation (Honeywell, n.d.:6). Any miss-alignment of the two sensors can result in a change of the differential output. Thus, the sensors should be aligned as best as practically possible (Latham, 2019).

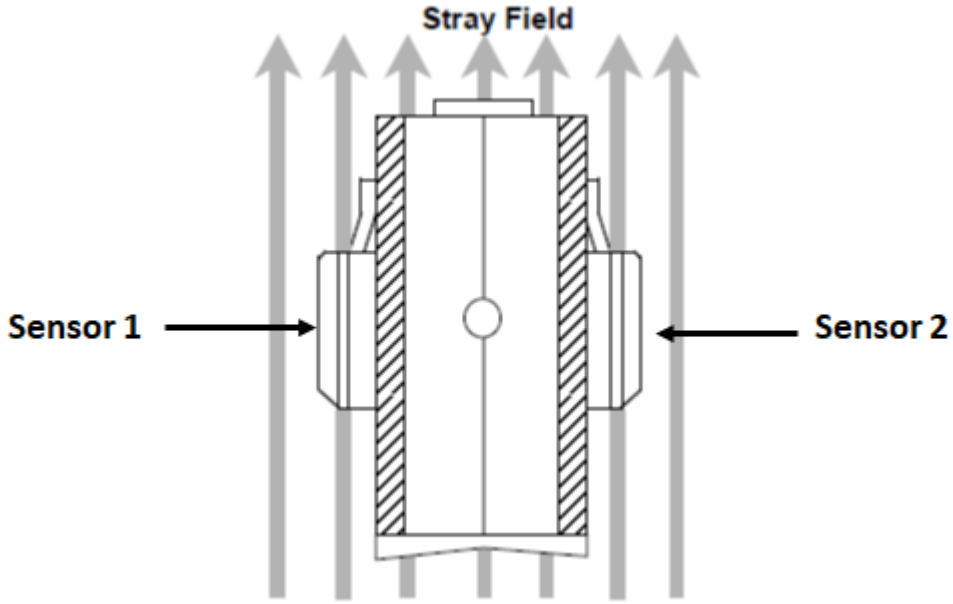

Figure 2.32: Differential sensing using two magnetic field sensors to remove the effect of a stray field (From Honeywell, n.d.:6)

2.6 Conclusion

This chapter covered the effects of LC on HVAC and HVDC insulators. The effects of LC under ac conditions are well understood and documented; however, this is not the case for dc conditions. Contamination and ambient weather conditions play an important role in the LC levels found on insulators. The monitoring of LC can be used as an early warning detection system. This will allow power utilities to act on excessive LC levels before flashover occurs. Various methods of measuring LC on HVAC and HVDC insulators have been described. Chapter 4 will further investigate sensors that can be used for in-situ LC monitoring on HVDC insulators.

3 SIMULATION OF THE VOLTAGE, ELECTRIC FIELD AND CURRENT DISTRIBUTIONS FOR HIGH VOLTAGE AC AND DC GLASS INSULATORS

3.1 Introduction

The aim of the thesis is to characterise the insulator LC found of HVDC transmission lines, with the Cahora Bassa transmission line as a case study. The methodology followed is to first perform initial simulations to gain insight into what may occur during laboratory measurements and when in-situ insulator LC measurements are eventually performed on the Cahora Bassa HVDC insulators. The simulation results are compared to previous studies (mostly for the ac case) to gain confidence in the simulations reported.

Knowledge of the voltage and electric field distributions are vital to the design and development of insulators (Kontargyri *et al*., 2004). Insulator performance under contaminated conditions is one of the key aspects in designing improved insulators. Banik *et al*. (2017) mentions that small amounts of capacitive current (in the ac case) flows on an insulator's surface when it is dry. However, under wet and polluted conditions, resistive currents that are higher in magnitude than capacitive currents, start to flow. This phenomena is supported by the simulations presented here. Also, the pollution of insulators normally occurs in a non-uniform manner, which can lead to the formation of dry bands on the insulator's surface. Continuous appearances of dry bands can eventually lead to insulator flashover. Literature states that dc insulator flashovers occur at lower voltage levels when compared to the ac case (Jiang *et al*., 2008). Thus, the electric field found on and near insulators are also investigated in this chapter for these cases.

This chapter covers the simulation and comparison of voltage, electric field and current density distributions that can be found on and near glass insulators under ac and dc excitation using COMSOL Multiphysics (COMSOL Multiphysics, 2019). COMSOL Multiphysics is a finite element method (FEM) simulation package for modelling designs and processes in all fields of engineering.

The simulations give insight into the relationship between electric field intensity and the current density distributions found on insulators, especially for dc, as this research has not been reported in the literature yet for a complete glass insulator that considers the ambient conductivity as well. These simulations will also show where the peak currents can be expected for glass insulators as only ac composite insulators current densities have been reported in the literature thus far (Netravati *et al*., 2016).

Simulations for ac energised insulators have been performed in this thesis as well to study the differences in the voltage distribution, electric field and current density distributions between the ac and dc energised insulators as no literature was found comparing these parameters, except for a brief study on the electric field reported by Arshad *et al*. (2015).

3.2 Literature survey of electric field distribution studies of polymeric and ceramic ac insulators using finite element methods

Computation of voltage and electric field distributions of insulators (ac and dc) are very important for improved insulator design (Ali *et al*., 2018). Also, simulations are preferred over laboratory measurements, since physical measurements can be costly and time consuming (Banik *et al*., 2017). The following two sections discuss notable simulations of ac insulators that have been performed in the literature.

3.2.1 Polymeric insulators

As discussed in Chapter 2, polymeric insulators consist of composite and resin insulators. In the literature, only the composite type has been studied as the resin insulators are not used for transmission lines.

Murugan *et al*. (2013) studied the electric field distribution of an 11 kV ac composite insulator where they, respectively, fixed 17.5 mm and 25.5 mm radius end-fittings to it. The simulations were done in COMSOL Multiphysics. They found that the 17.5 mm and 25.5 mm radius end-fittings had localised maximum electric fields of 1.81 kV/cm and 1.65 kV/cm, respectively. Thus, having a larger end-fitting resulted in a lower electric field distribution along the length of the insulator.

Netravati *et al*. (2016) studied the effects of different pollution levels and different thicknesses of pollution layers when a uniform pollution layer was applied to a 66 kV ac composite insulator using ANSYS (ANSYS, 2019). They reported that the electric field strength is highest at the metal end-fittings of the insulator and minimal along its surface. Also, the electric field and current density increase with an increase in pollution levels. For a clean insulator, the maximum electric field reported was 2.71 kV/cm. For a uniformly polluted insulator with layer thickness of 1.5 mm and conductivities of 0.028 S/m, 0.056 S/m and 0.083 S/m, the highest electric fields obtained were 1.65 kV/cm, 3.99 kV/cm and 4.02 kV/cm, respectively. They also determined the current density for different conductivities and different thickness layers as listed in Table 3.1. Their conclusion was that increasing the conductivity and the thickness of the pollution layers leads to increased electric field strengths and current density.

Table 3.1: Simulated leakage current for different conductivities and different thickness layers of a 66 kV ac composite insulator (From Netravati *et al*., 2016)

	Leakage current [A]		
Layer thickness	**1 mm**	**1.5 mm**	**2 mm**
Conductivity [S/m]			
0.028	0.49	0.97	1.44
0.056	1	1.32	1.94
0.083	1.00	1.97	2.91

Arshad *et al.* (2015) studied a 33 kV composite insulator using COMSOL Multiphysics and showed that increasing both the conductivity and thickness of the contamination layer increase the maximum electric field, and hence, increased contamination (the combination of conductivity and thickness) will exacerbate conditions for elevated LC and flashover (seen in Figure 3.1). With the layer thickness kept constant at 1 mm, the maximum electric fields obtained for a 1 x 10^{-6} S/m and 1 x 10^{-3} S/m conductivity layer were (a) 0.50 kV/cm and (b) 0.64 kV/cm, respectively. When pollution was kept constant at 0.05 S/m, the maximum electric fields changed from (c) 0.8 kV/cm for a 0.5 mm layer to (d) 1.45 kV/cm for a 2 mm layer.

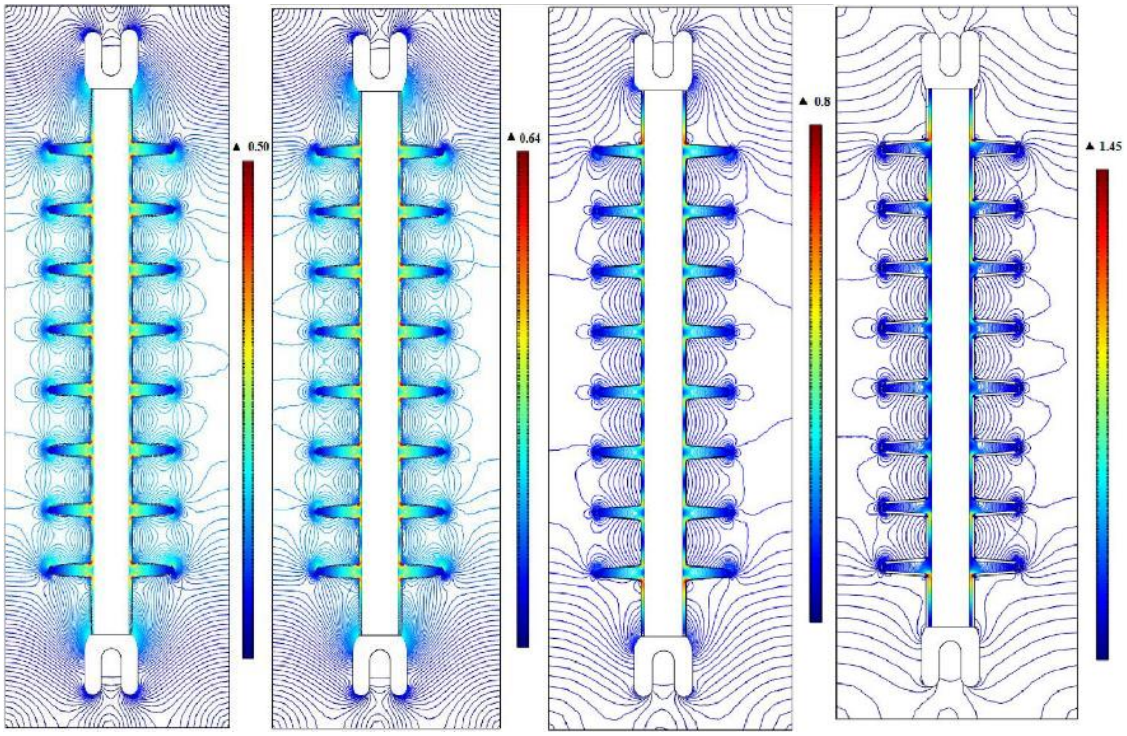

a) b) c) d)

Figure 3.1: Electric field distribution of a uniformly polluted polymeric insulator with layer conductivities (a) 10^{-6} S/m (b) 10^{-3} S/m and with pollution layer thickness of 1mm, and for layer thicknesses of (c) 0.5 mm (d) 2 mm with a conductivity of 0.05 S/m (From Arshad *et al*., 2015)

Krzma *et al*. (2018) computed the electric field and voltage distributions of a polluted silicone-rubber ac insulator, as well as the power dissipation along its surface, in COMSOL Multiphysics. They indicated that the triple junction area (where the insulator material, edge of pollution layer and surrounding air meet) is where the highest electric field is found. The highest power dissipation and electric field were reported close to the end-terminals of the insulator as well.

Arshad *et al.* (2015) and Batalovic *et al*. (2018) studied the effect of dry bands on the electric field distributions of polluted ac polymer insulators in COMSOL Multiphysics. Arshad *et al.* (2015) found that the highest electric field was observed when a dry band was located at the junction of the insulator's core and shed area. Batalovic *et al*. (2018) states that a higher electric field will be found when dry bands exist, compared to a uniform pollution layer on the insulator's surface.

Research has been performed on optimising an ac composite insulator's profile under different pollution levels. El-Sayed *et al.* (2016) used COMSOL Multiphysics to study four different ac composite insulator profiles under clean and uniformly polluted conditions by optimising the 11 kV insulator's shed diameter, shed spacing and its metallic end fittings' diameter. By optimising these three parameters for the insulators, reductions in electric field strength of between 9% and 22%, and between 8% and 13% have been observed for clean and polluted insulators, respectively.

Arshad *et al.* (2015) further investigated the influence of voltage polarity and type (ac and dc voltage) on the electric field distribution of a 33 kV insulator under polluted conditions using COMSOL Multiphysics. They noted that positive and negative polarity voltage yielded similar electric field strengths (1.05 kV/cm and 1.03 kV/cm for dc+ and dc-, respectively). When an ac voltage was applied, the electric field strength was 0.72 kV/cm, which is lower compared to the dc case. This can be attributed to the static charge accumulation on the insulator's surface under dc excitation. Incidentally, the investigation by Arshad *et al.* (2015) was the only literature found that performed electric field simulations on dc insulators.

3.2.2 Ceramic insulators

In the literature, porcelain and glass insulators have been simulated to investigate the voltage and electric field distributions of energised insulators to observe how they perform in a polluted environment.

Krzma & Khamaira (2018) conducted a comparison of the voltage and electric field distributions found on an ac U100BL glass insulator (GIG, 2020) and a 81022 porcelain insulator (PPC

insulator, 2020) energised at 11 kV under clean and polluted conditions. The simulation results showed that the maximum electric field occurs near the end regions of the insulators. The maximum electric fields reported for the glass insulator were 2.8 kV/cm and 3.2 kV/cm, respectively, under clean and uniformly polluted conditions. The maximum electric field reported for the porcelain insulator was 2 kV/cm and 2.25 kV/cm, respectively, under clean and polluted conditions (see Figure 3.2). A uniformly polluted layer with conductivity of 6 x 10^{-4} S/m and layer thickness of 1.5 mm have been applied for these simulations. As with composite insulators, it was observed that the electric field strength of ceramic insulators increases under polluted conditions (Kontargyri, *et al*., 2004; Othman *et al*., 2013; Krzma, 2018; Benguesmia *et al*., 2019). Reddy *et al.* (2010), Banik *et al.* (2017) and Krzma (2018) identified that the high field regions are near the end-fittings of a porcelain insulator. Power dissipation was also shown to be at its highest near the end-fittings (Krzma, 2018).

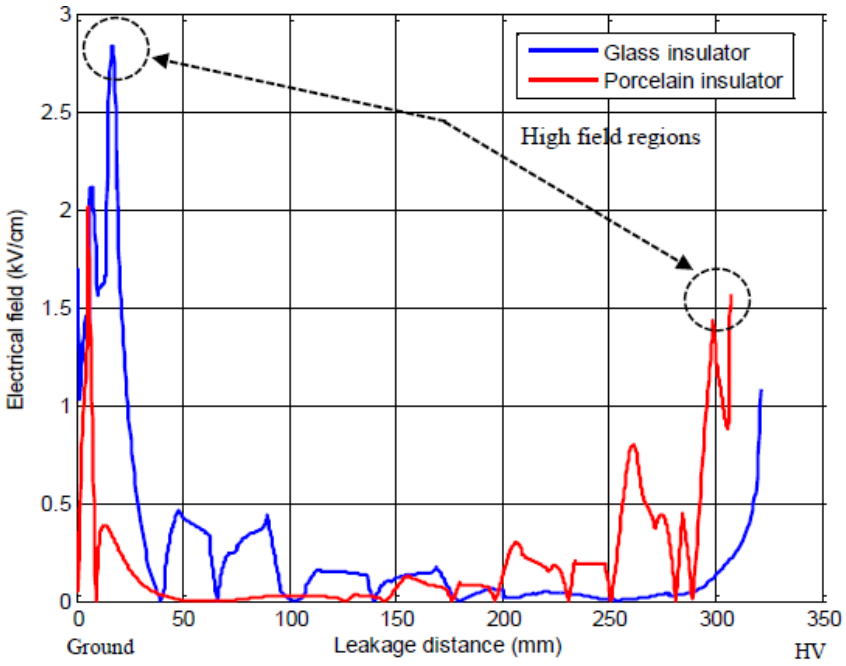

a)

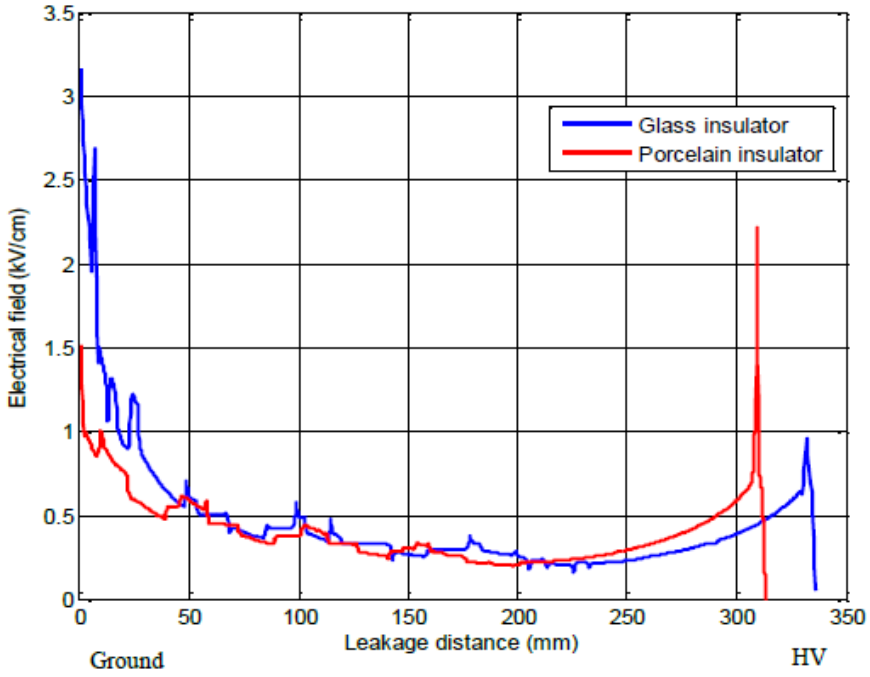

b)

Figure 3.2: Electric field distribution along the surface of the glass (U100BL) and porcelain (81022) insulator, a) under clean condition, b) under uniformly polluted condition

3.2.3 Summary of literature survey

Extensive simulations had been performed by various researchers on the voltage and electric field distributions of polymeric and ceramic ac insulators using finite element methods. Current density simulations on composite ac insulators have only been reported by Netravati *et al*. (2016). For the dc case, one paper made a comparison between ac and dc electric fields (Arshad *et al*., 2015). No literature was found for current density distributions for dc insulators or ac ceramic insulators. From the literature, it was difficult to make a fair comparison between composite and ceramic insulators to determine if one has a better performance than the other if the simulation parameters are not exactly the same. What was observed is that the highest electric fields found on composite and ceramic insulators appears at the same place, i.e. near the end-fittings at the high voltage end. Table 3.2 summarises the literature found for simulations of ac insulators that takes into account the conductivity of the background (air) as well.

Table 3.2: Summary of how the electric field, current density distribution and pollution behave on different types of insulators as well as different excitations

	Insulators under ac excitation		Insulators under dc excitation	
Parameters studied	**Composite**	**Ceramic**	**Composite**	**Ceramic**
Electric field	Electric field increases when a dry insulator becomes wet and polluted. The highest electric field appears near the end-fittings at the high voltage end.	Same as composite case.	Electric field increases when a dry insulator becomes wet and polluted. However, a higher electric field was observed compared to the ac case.	No literature available
Current density distribution	Current density increases when a dry insulator becomes wet and polluted.	No literature available	No literature available	No literature available
Pollution	Electric field and current density increase with an increase in pollution.	Electric field increases with an increase in pollution.	Electric field increases with an increase in pollution.	No literature available

3.3 Simulated electric field and current distributions of a single glass insulator (ac and dc cases)

From the literature reviewed, it can be seen that one brief study was conducted on the electric field distributions of dc insulators under contaminated conditions when the conductivity of the background (air) was taken into account as well (Arshad *et al.*, 2015). The research performed was on composite insulators and not glass insulators, which is the insulator focused on in this thesis. Also, only Netravati *et al.* (2016) attempted to study the current density distribution of composite ac insulators.

This thesis attempts to augment the limited scope of research in the field of dc glass insulators. Simulations under ac conditions have also been performed and compared to those in the literature to gain confidence in the model.

The electric field and current distributions are simulated in three dimensions (3D) using the electric currents solver under the AC/DC module in COMSOL Multiphysics to evaluate the glass insulator's performance under clean and polluted conditions (COMSOL, 2019). For the ac and dc studies, the frequency domain and stationary studies are used, respectively. COMSOL solves Maxwell's equations (Griffiths, 2008) to determine the voltage (V), electric field (E) and current density distributions (J):

$$\nabla \bullet J = Q_{j,v} \qquad \textbf{Equation 3.1}$$

$$J = \sigma E + j\omega D + J_e$$ **Equation 3.2**

$$E = -\nabla V$$ **Equation 3.3**

Where σ is the electric conductivity in S/m, J_e is the externally applied current density in A/m^2, $Q_{j,v}$ is the volume charge density in C/m^3, D is the electric displacement field in C/m^2 and ω is the radial frequency in rad/s. The current density J comprises a conduction current, a displacement current (ac case only) and an externally applied current component. COMSOL uses the same formulas for the dc case, but with the frequency set to zero.

3.3.1 Simulation setup

The insulator modelled is a standard cap and pin glass insulator energised at 33.33 kV for ac (peak value) and dc simulations. This voltage is chosen to obtain the same USCD of 9.6 mm/kV as for the measurements presented in Chapter 5. The geometry and dimensions of the insulator are given in Figure 3.3 and Table 3.3, respectively. The insulator is energised at the pin and grounded at the cap. Figure 3.4 shows the COMSOL insulator model in 3D.

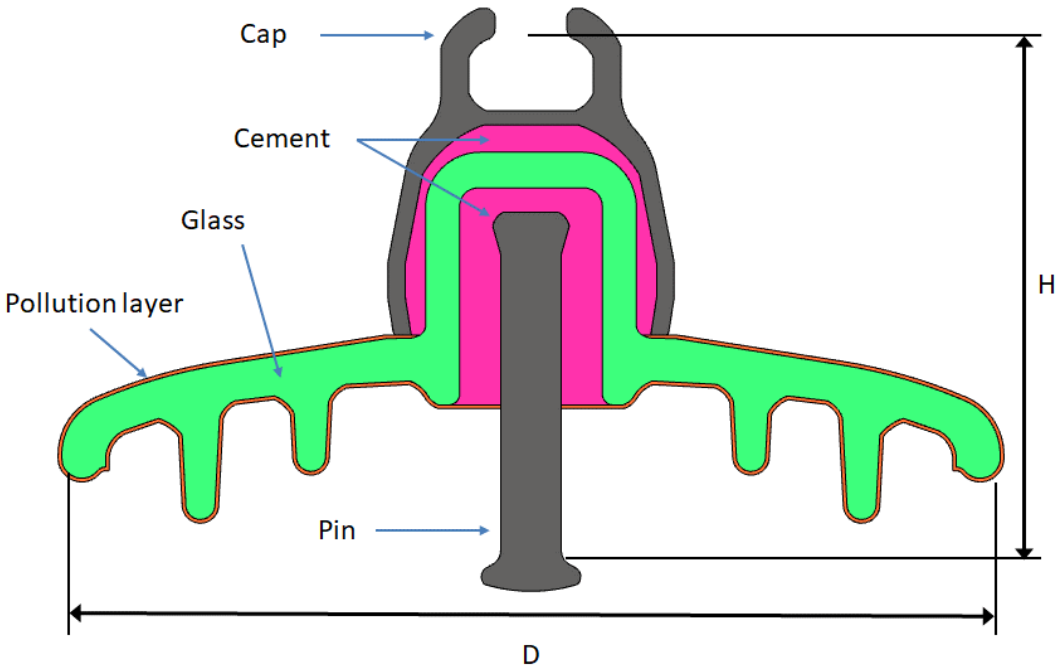

Figure 3.3: Cross-section of the cap and pin glass insulator

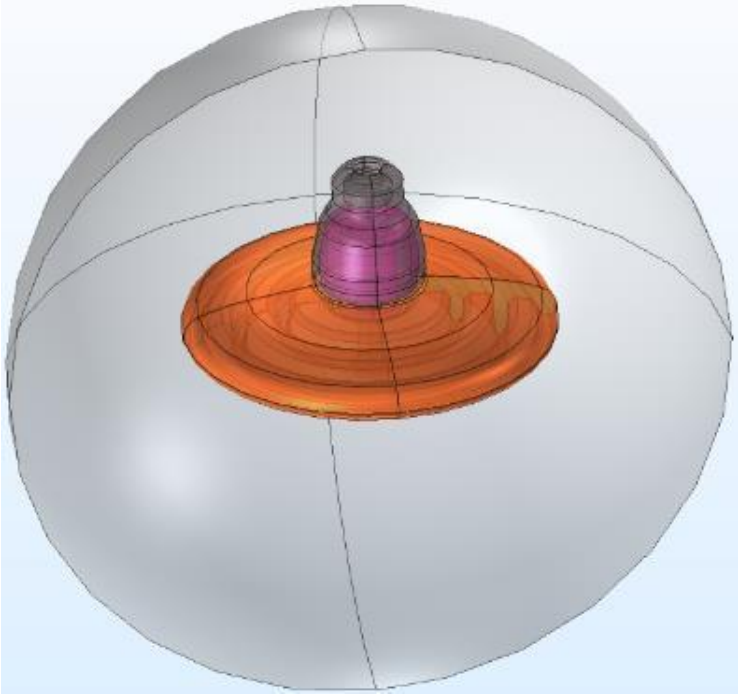

Figure 3.4: 3D representation of glass insulator in COMSOL

Table 3.3 Dimensions of the glass insulator

Height, H (mm)	Diameter, D (mm)	Leakage distance (mm) (see Figure 3.7)
127	255	320

The material properties used are given in Table 3.4. A uniform thin film pollution layer of 0.02 mm is added onto the glass insulator's surface. Gouda *et al.* (2014) used a similar thin film (0.07 mm) when they performed flashover prediction and dry band location simulations on ac energised polluted ceramic insulators. The conductivity of 0.07 S/m for the pollution layer is used to mimic the ESDD of 0.03 mg/cm^3 that is found in the Cahora Bassa transmission line as described in Chapter 6. The insulator is simulated within an air background and the boundary of the air assumes a zero external current boundary condition.

Table 3.4: Material parameters of the simulated insulator

Material	Relative permittivity (ε_r)	Conductivity (S/m)
Glass	4.2	1×10^{-14}
Air	1	1×10^{-14}
Steel	1	1.45×10^{6}
Cement	2	1×10^{-14}
Distilled water	81	5×10^{-6}
Pollution layer	81	0.07

3.3.2 Voltage, electric field and current distributions of a clean and uniformly polluted glass insulator under ac conditions

The voltage, electric field and current distributions are simulated at 50 Hz using the frequency domain study option in COMSOL Multiphysics.

3.3.2.1 Voltage distribution simulations

Figure 3.5 shows a slice plot of the voltage distribution for a clean and uniformly polluted (0.02 mm layer with a 0.07 S/m conductivity applied) ac insulator. It is observed that the voltage distribution is concentrated near the pin of the clean insulator. However, on the polluted insulator, the voltage distribution is spread out more across the insulator's surface due to the presence of the pollution layer.

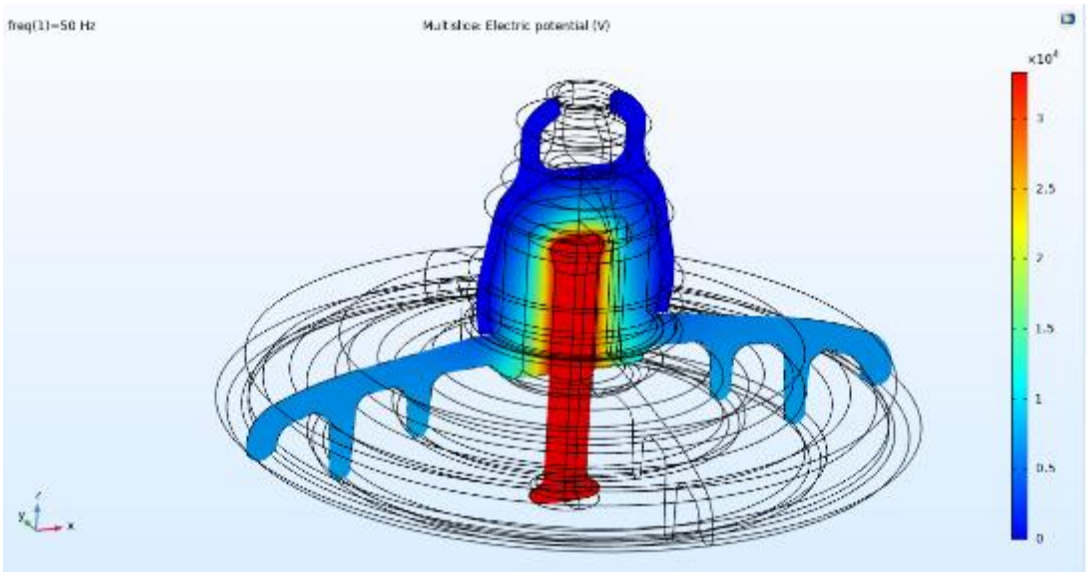

a)

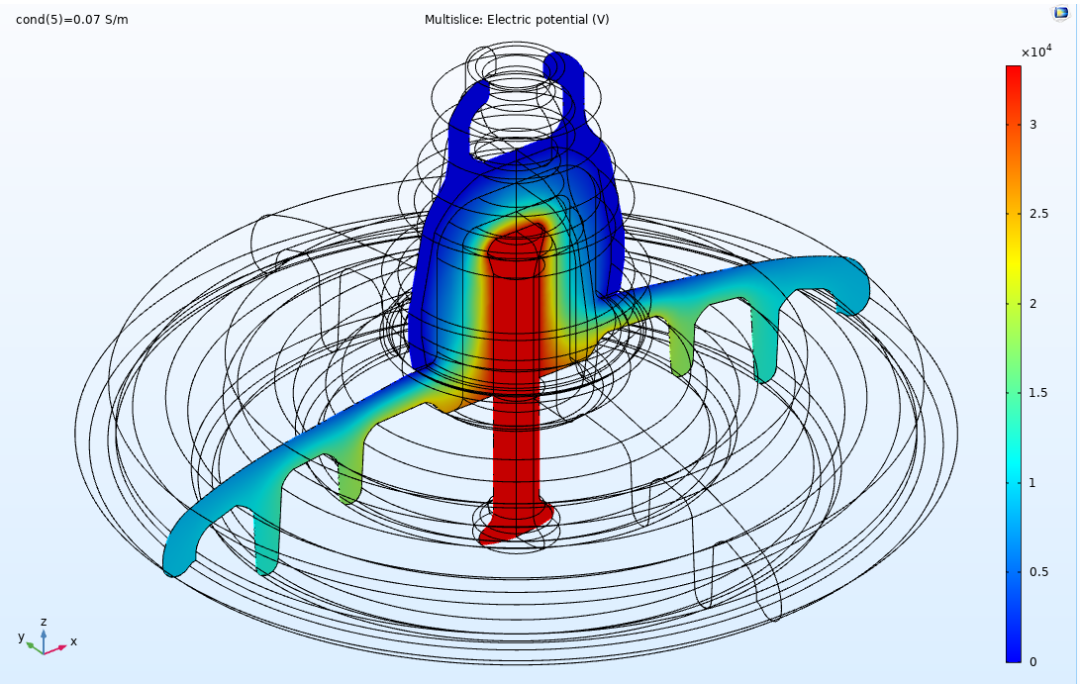

b)

Figure 3.5: Simulated voltage distribution for a) a clean ac insulator, b) a uniformly polluted ac insulator with a 0.07 S/m pollution layer

The voltage profile along a clean and uniformly polluted insulator surface under ac excitation is shown in Figure 3.6. The voltage distribution is calculated along the insulator's surface using the boundary points shown in Figure 3.7. From Figure 3.6 (a), it can be observed that the voltage distribution drops sharply away from the pin of the insulator, indicating the aforementioned concentration around the pin (the energised part of the insulator). However, on the polluted insulator, the voltage drop occurs linearly due to the presence of the uniform pollution layer (for the 0.07 S/m conductivity case). This linear drop-off in voltage can lead to unexpected high voltage areas on the insulator surface.

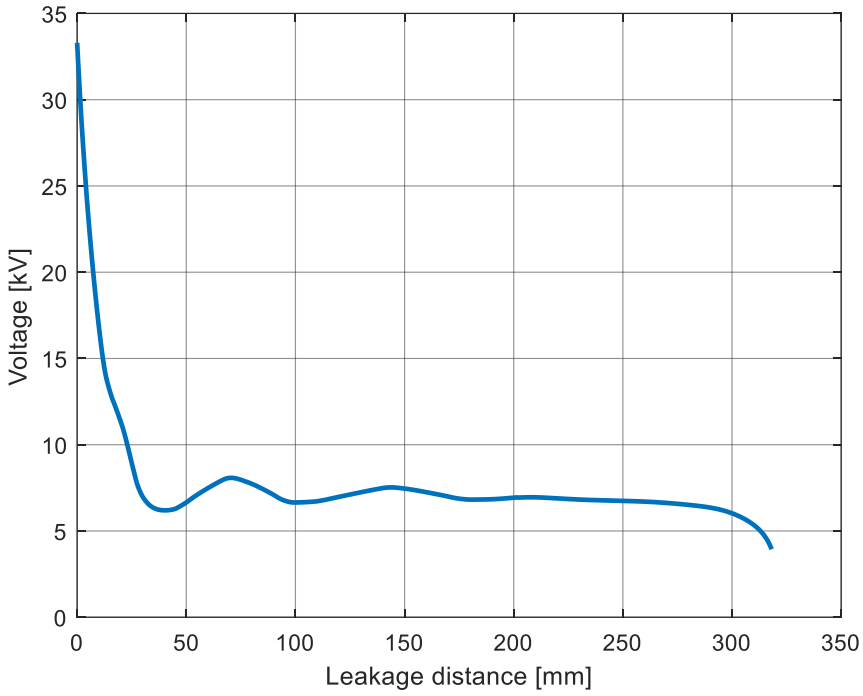

a)

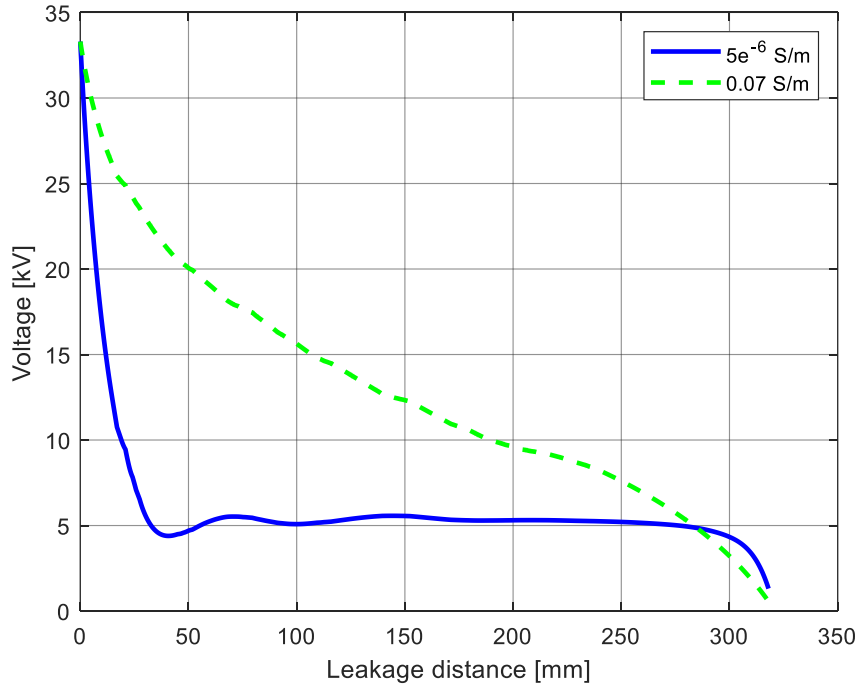

b)

Figure 3.6: Voltage distribution along a) clean ac insulator surface, b) uniform polluted ac insulator surface with two pollution levels as indicated

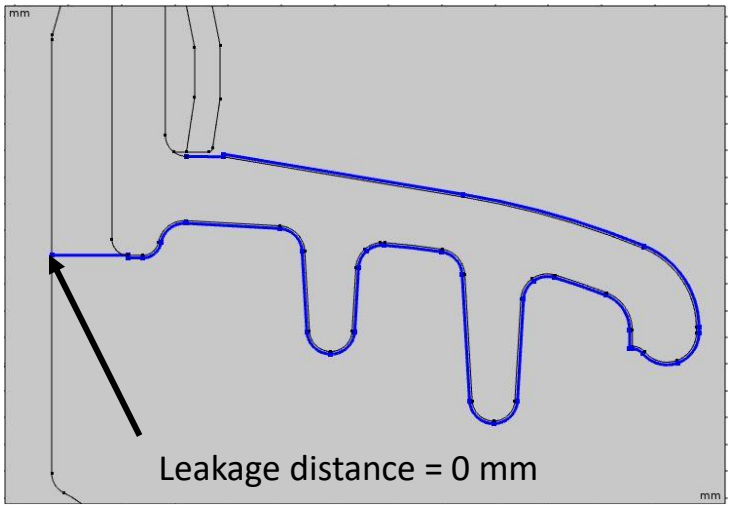

Figure 3.7: Boundary points used to generate the 1D plots

3.3.2.2 Electric field distribution simulations

Figure 3.8 shows the contour plot of the electric field distribution for a clean and uniformly polluted (0.02 mm layer with a 0.07 S/m conductivity applied) ac energised insulator. As expected from the previous section, the maximum electric field is found near the end-fittings of the clean glass insulator, which agrees well with Reddy *et al.* (2010), Banik *et al.* (2017) and Krzma (2018). Away from the cap and pin regions, the electric field is near zero on the clean insulator. However, on the polluted insulator, a notable electric field still exists on the insulator's surface. Localised maxima appear at the bends of the polluted insulator's surface, which can lead to the occurrences of dry bands and arcs.

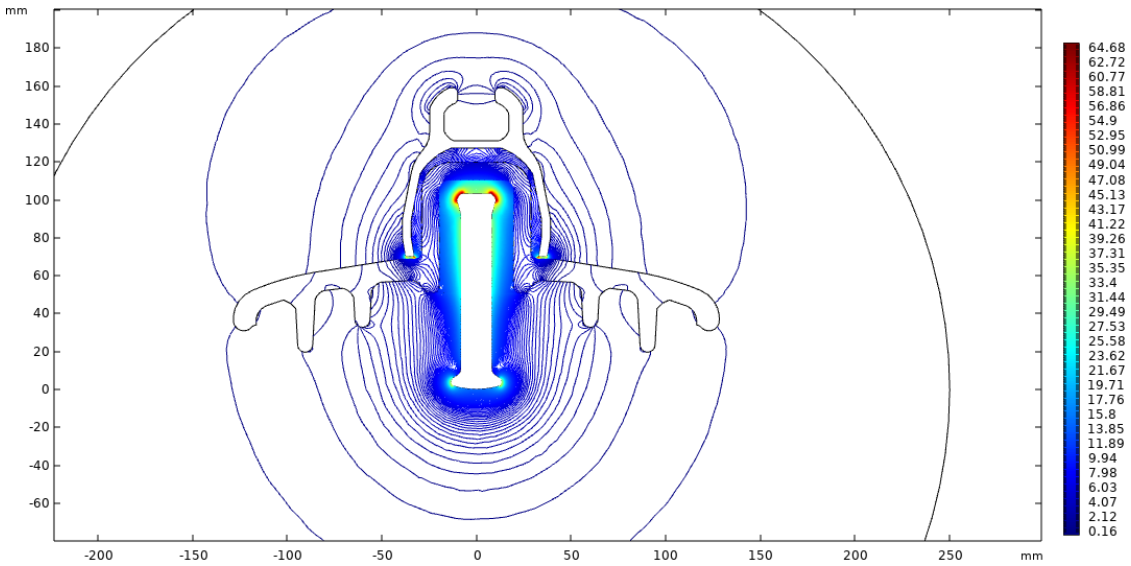

a)

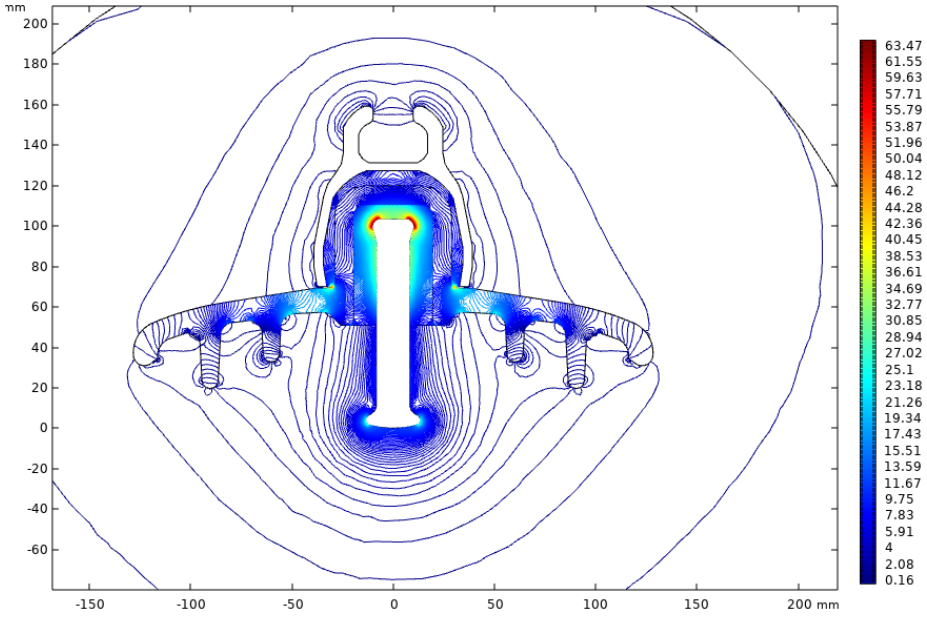

b)

Figure 3.8: Simulated contour plot of the electric field distribution for a) a clean ac insulator, b) a uniformly polluted ac insulator with a 0.07 S/m pollution layer

The tangential electric field distributions of the clean and polluted insulators are presented in Figure 3.9. It is the tangential component of the electric field that drives the LC on the surface of the insulator (refer to Figure 3.2). The tangential electrical field is calculated along the insulator's surface defined by the boundary points shown in Figure 3.7. It is observed that the highest tangential electric field found on the clean and polluted insulator is located at the pin. From the pin of the insulator, it drops to nearly zero on the surface of the clean insulator. On the surface of the polluted insulator, the tangential electric field is just below 1 kV/cm. The average tangential electric field on the clean insulator is 1.50 kV/cm. The polluted insulator experiences an average tangential electric field of 1.37 kV/cm and 2.25 kV/cm when a 5 x 10^{-6} S/m and 0.07 S/m layer conductivity, respectively, is applied. Also, the more polluted an insulator becomes, the higher the intensity of the tangential electric field found on the polluted insulator. This is one of the drivers that increase LC under polluted conditions.

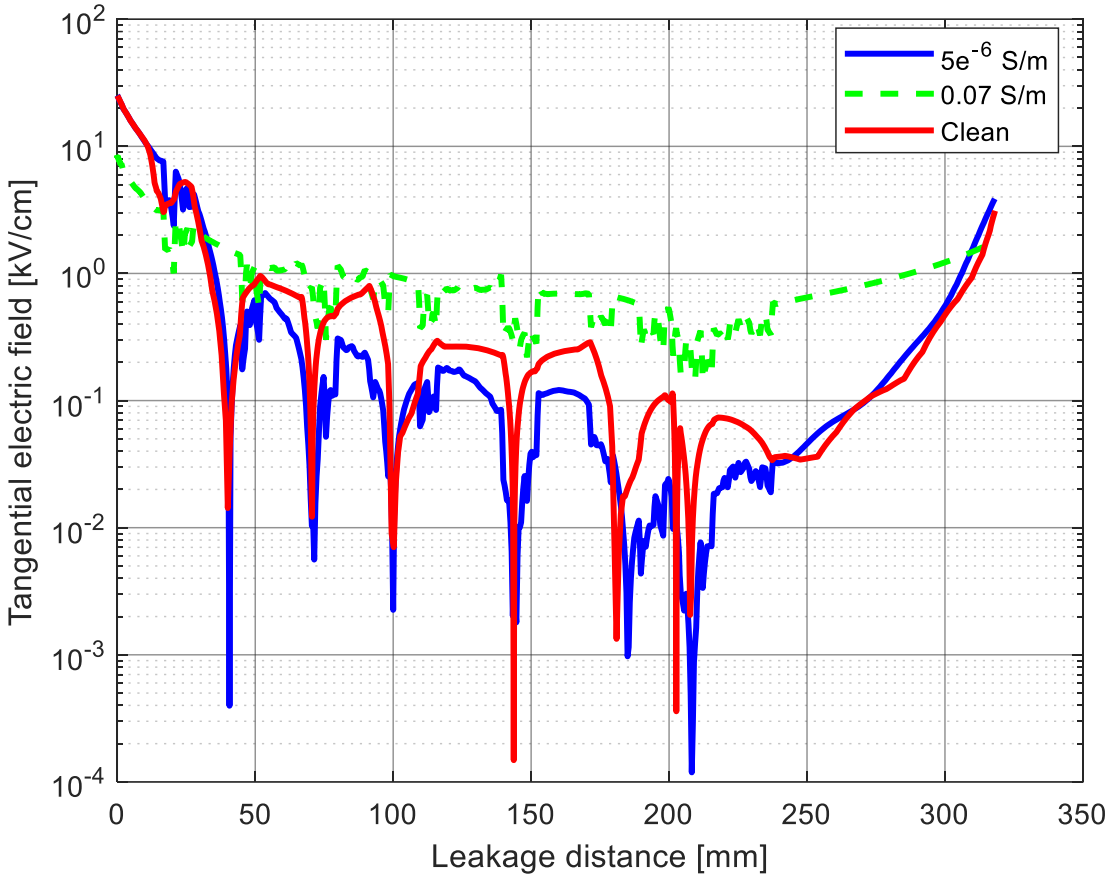

Figure 3.9: Tangential electric field along a clean and uniformly polluted ac insulator surface

3.3.2.3 Current density distribution simulations

Figure 3.10 shows the current density along a clean and polluted insulator's surface defined by the boundary points displayed in Figure 3.7. Figure 3.10 (b) shows the current densities for, respectively, a 5 x 10^{-6} S/m and 0.07 S/m conductivity layer.

The clean insulator has an average current density of 9.65 x 10^{-4} A/m^2. The polluted insulator has an average current density of 0.58 x 10^3 A/m^2 and 4.81 x 10^3 A/m^2 when a conductive layer with conductivity of 5 x 10^{-6} S/m and 0.07 S/m, respectively, is applied. It is observed that there is a marked increased surface current density on the polluted insulators compared to the clean insulator. Also, as can be expected, the current density increases when there is an increase in conductivity. The highest current density is observed near the pin regions for a clean and polluted insulator.

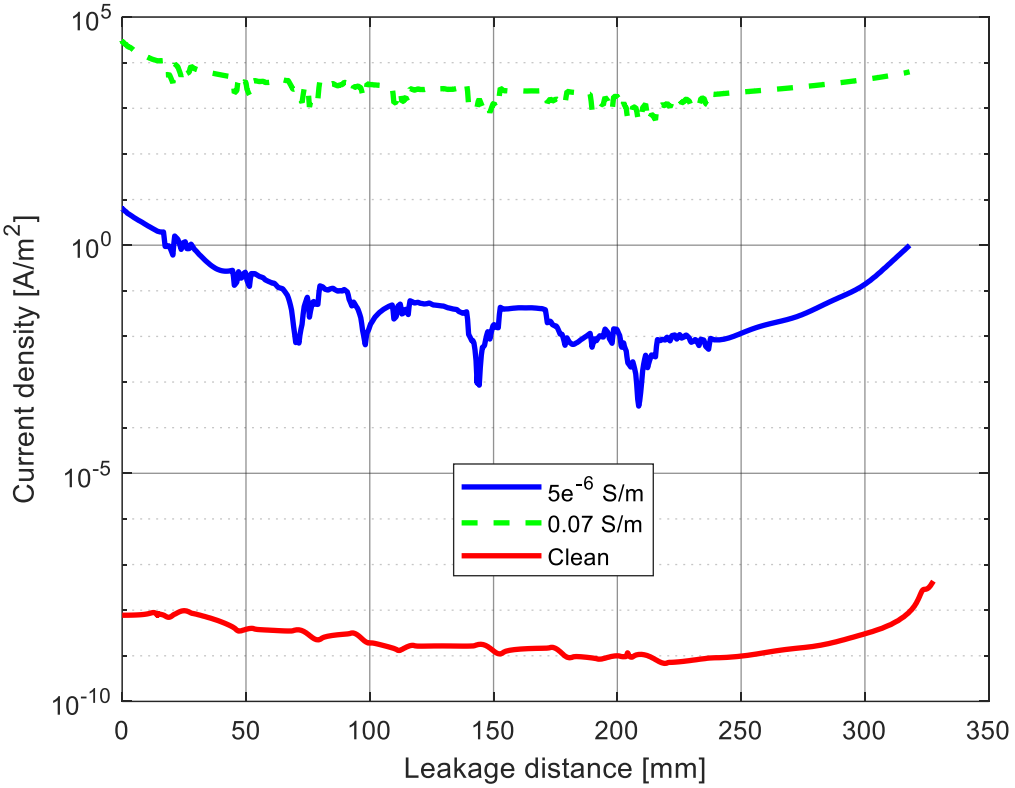

Figure 3.10: Surface current density along a) a clean ac insulator surface, b) a uniformly polluted ac insulator surface

3.3.3 Voltage, electric field and current distributions of a clean and uniformly polluted glass insulator under dc conditions

The voltage, electric field and surface current distributions are simulated at dc using the stationary domain study option in COMSOL Multiphysics.

3.3.3.1 Voltage distribution simulations

Figure 3.11 shows a slice plot of the voltage distribution for a clean and uniformly polluted (0.02 mm layer with a 0.07 S/m conductivity applied) dc insulator. It is observed that the voltage is concentrated near the pin of the clean insulator. However, on the polluted insulator, high voltages can still be observed on the insulator's surface due to the presence of the pollution layer.

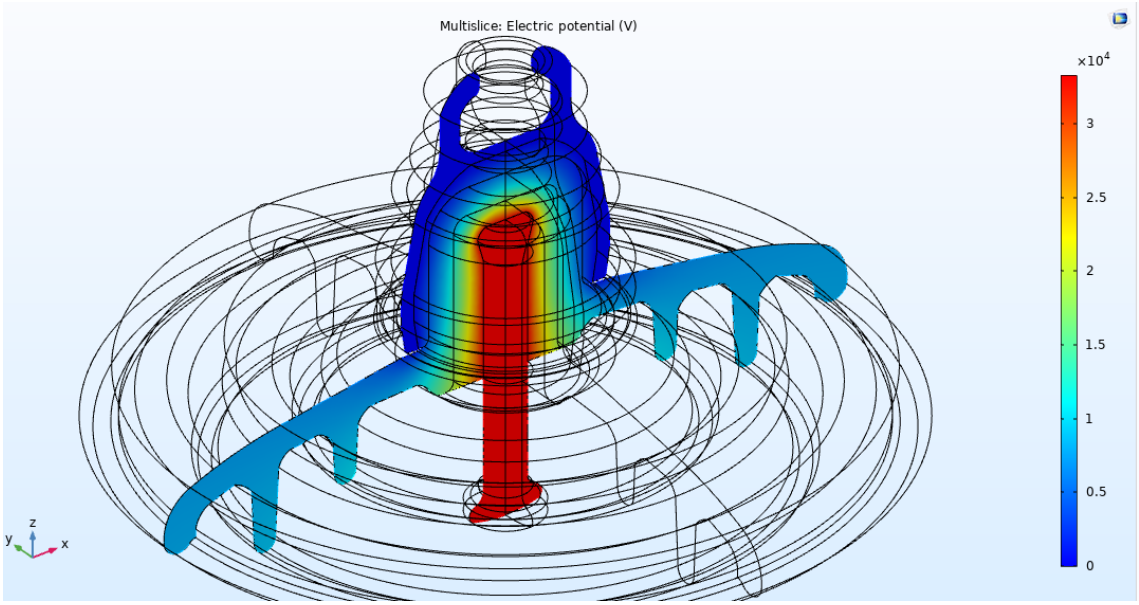

a)

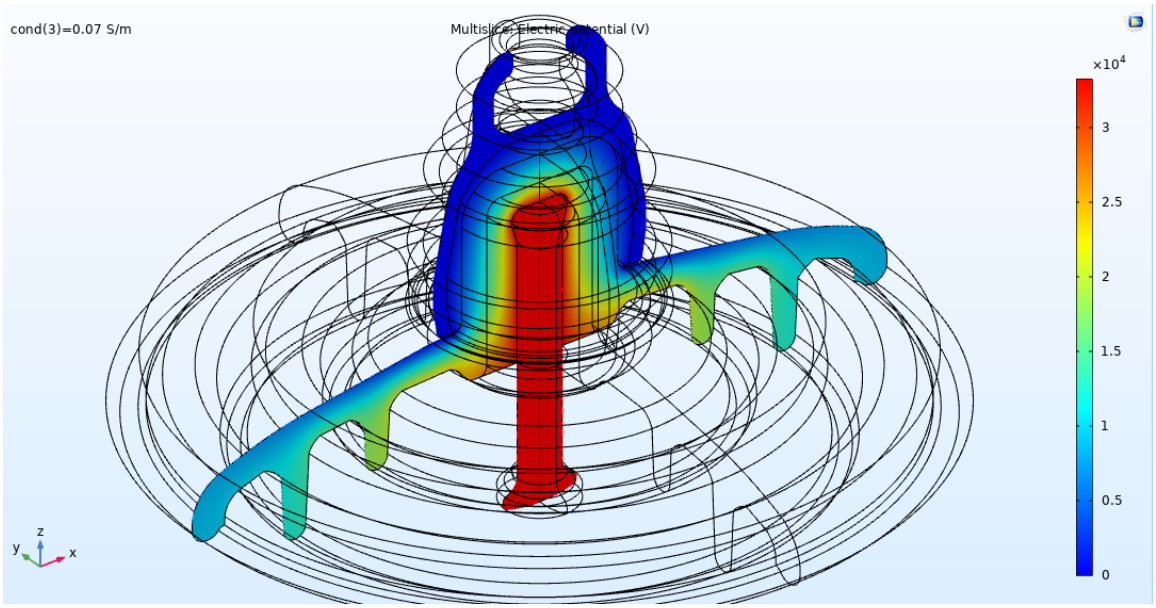

b)

Figure 3.11: Simulated voltage distribution for a) a clean dc insulator, b) a uniformly polluted dc insulator with a 0.07 S/m pollution layer

The voltage profile along a clean and uniformly polluted insulator under dc excitation is shown in Figure 3.12. The voltage distribution is calculated along the insulator's surface defined by the boundary points shown in Figure 3.7.

From Figure 3.12 (a), it can be observed that the voltage distribution drops by approximately 66% away from the pin of the insulator, indicating that the voltage is concentrated around the pin (the energised part of the insulator). However, on the polluted insulator, the voltage drop occurs almost linearly due to the presence of the uniform pollution layer. It is also observed that the conductivity of 5 x 10^{-6} S/m and 0.07 S/m yielded the same response, which did not occur on the polluted ac energised insulator. Thus, it can be inferred that the dc energised insulators are more susceptible to pollution than the ac energised insulators.

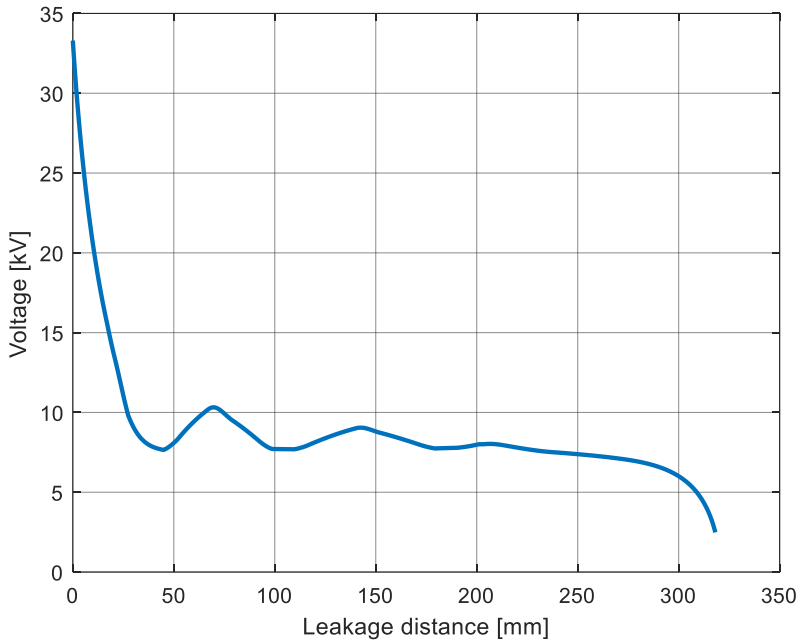

a)

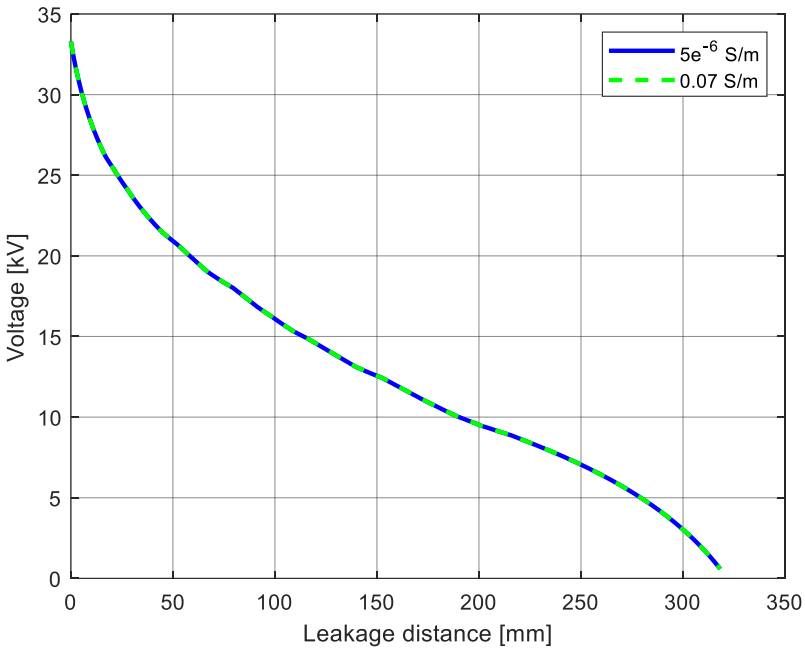

b)

Figure 3.12: Voltage distribution along a) clean dc insulator surface, b) uniform polluted dc insulator surface

3.3.3.2 Electric field distribution simulations

Figure 3.13 shows the contour plot of the electric field distribution of a clean and uniformly polluted (0.02 mm layer with a 0.07 S/m conductivity applied) dc insulator. It is observed that the electric field strength increases when a layer of pollution is added to the surface of the glass insulator, similar to the ac case in Figure 3.8. For the polluted case, the location of the maximum electric field is near the pin of the insulator. The clean insulator has a maximum electric field strength of 55.47 kV/cm and the polluted insulator has a maximum electric field of 64.19 kV/cm (internal). As with the ac energised insulator case, localised maxima appear at the bends of the polluted insulator's surface, which can lead to the occurrences of dry bands and arcs.

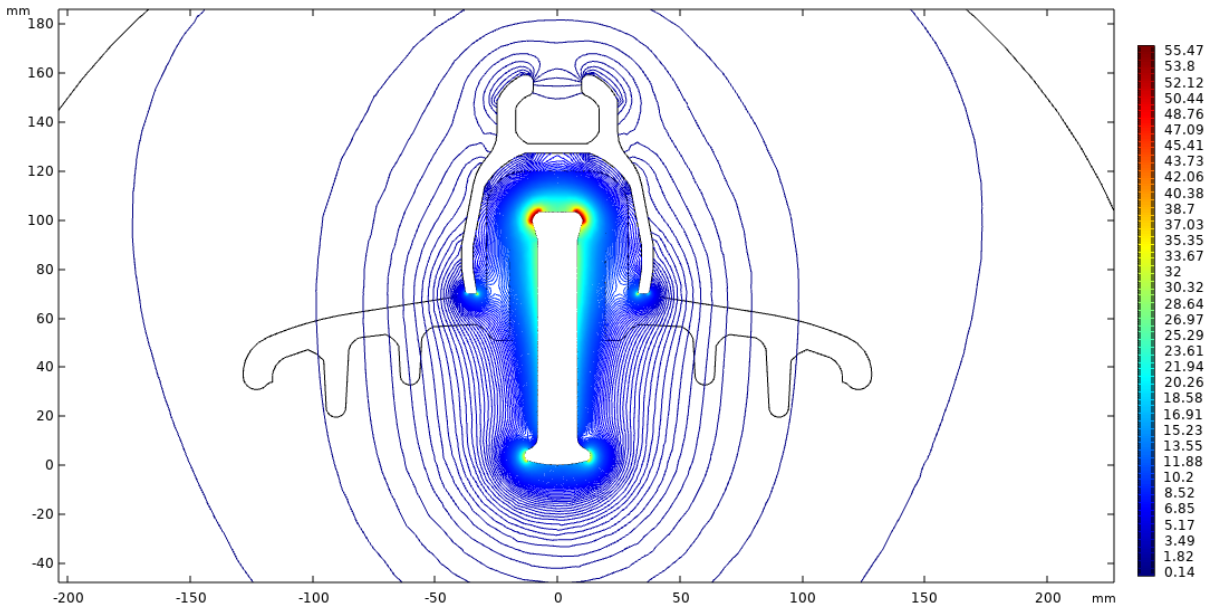

a)

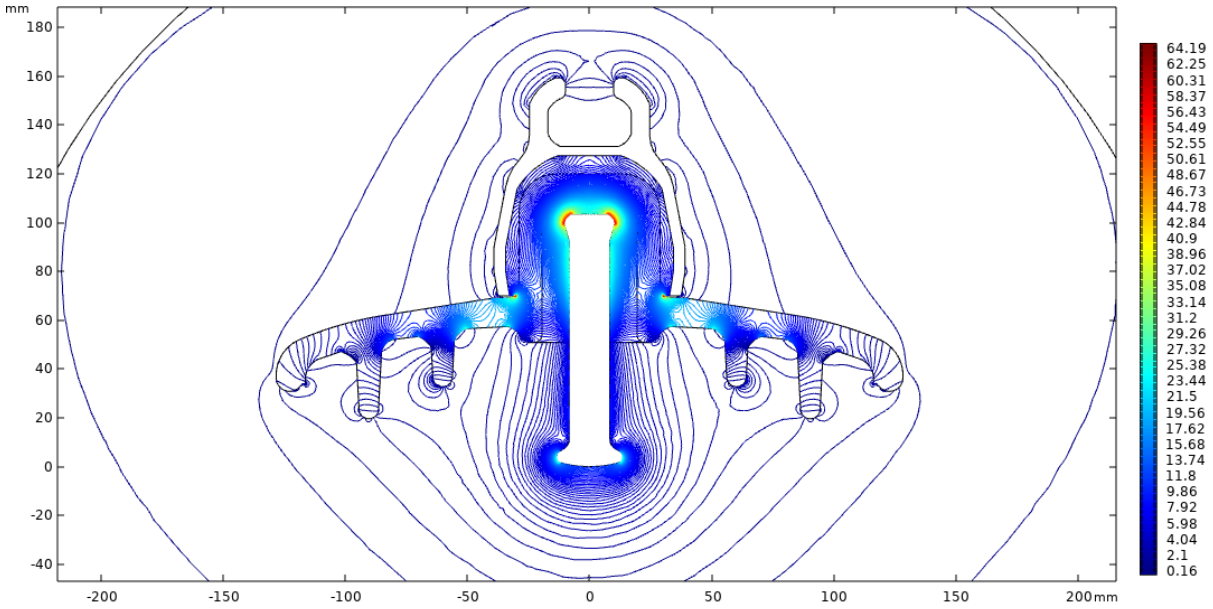

b)

Figure 3.13: a) Contour plot of the electric field distribution of a) a clean dc insulator, and b) a uniformly polluted dc insulator

Figure 3.14shows the tangential electric field along a clean and polluted insulator's surface defined by the boundary points displayed in Figure 3.7. Figure 3.14(a) shows that the location of the maximum tangential electric field along the clean insulator is near the cap and pin regions of the insulator. Figure 3.14 (b) shows the tangential electric field for a 0.02 mm thick, 5 x 10^{-6} S/m and 0.07 S/m conductivity layer, respectively. The average tangential electric field on the clean

insulator is 1.68 kV/cm. The polluted insulator experiences an average tangential electric field of 1.14 kV/cm for both layer conductivities. The clean insulator has a higher average tangential electric field due to the more intense electric field experienced at the pin of the insulator. However, it is observed that the tangential electric field elsewhere on the surface of the polluted insulator is higher when compared to the clean insulator's surface.

It is also observed that the dc energised insulator is more susceptible to pollution when comparing Figure 3.9(b) and Figure 3.14(b). On the ac energised insulator, the response obtained for a conductivity of 5 x 10^{-6} S/m is similar to the tangential electric field obtained for a clean ac insulator. On the dc energised insulator, the response obtained for a conductivity of 5 x 10^{-6} S/m is similar to the tangential electric field obtained for the polluted insulator with a 0.07 S/m conductivity layer.

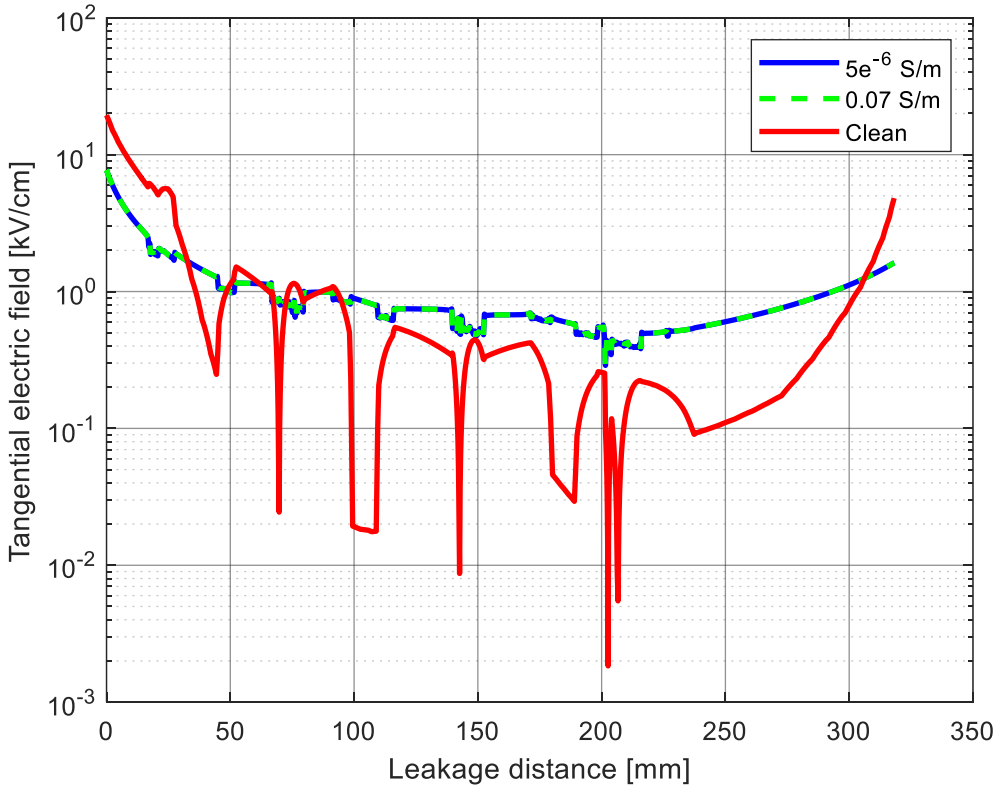

Figure 3.14: Tangential electric field along a clean and uniformly polluted dc insulator surface

3.3.3.3 Current density distribution simulations

Figure 3.15 shows the current density along a clean and polluted insulator's surface defined by the boundary points displayed in Figure 3.7. Figure 3.15 (b) shows the current densities for, respectively, a 5 x 10^{-6} S/m and 0.07 S/m conductivity layer. The clean insulator has an average

current density of 2.05 x 10^{-9} A/m^2. The polluted insulator has an average current density of, respectively, 0.38 x 10^3 A/m^2 and 5.34 x 10^3 A/m^2 when a 5 x 10^{-6} S/m and 0.07 S/m layer conductivity are applied. It is observed that there is an increased surface current density on the polluted insulators compared to the clean insulator. Also, as can be expected, the current density increases when there is an increase in conductivity. The highest current density is located near the pin and cap regions for a clean and polluted insulator; the same as with the tangential electric field distribution. When current starts flowing on the surface of the insulator, it leads to surface heating, which in turn leads to the formation of dry bands. From the simulation results it can be inferred that these dry bands will first form at the energised end of the insulator. These dry bands will continue to form on the surface of the insulator, starting from the energised end. The formation of dry bands due to the presence of LC will result in arcing. These arcs will start bridging each other until a complete flashover occurs.

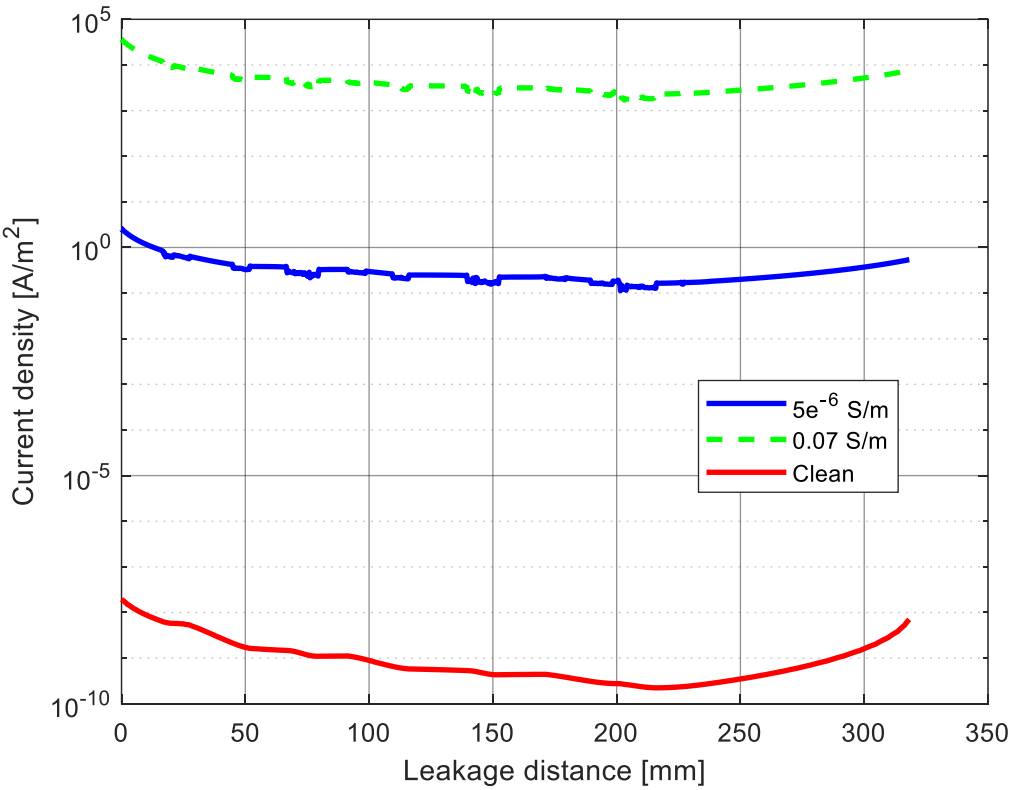

Figure 3.15: Current density along a clean and uniformly polluted dc insulator surface

3.4 Comparison of ac and dc insulator results

A comparison between the electric field current density and power density distributions for ac energised and dc energised glass insulators are presented in this section.

3.4.1 Electric field distribution

Figure 3.16 shows the tangential electric field along a clean ac and dc glass insulator's surface. It is observed that the clean dc insulator exhibits a marginally higher electric field strength on its surface when compared to the clean ac insulator. The average electric field observed on the clean ac and dc insulator is 1.50 kV/cm and 1.68 kV/cm, respectively.

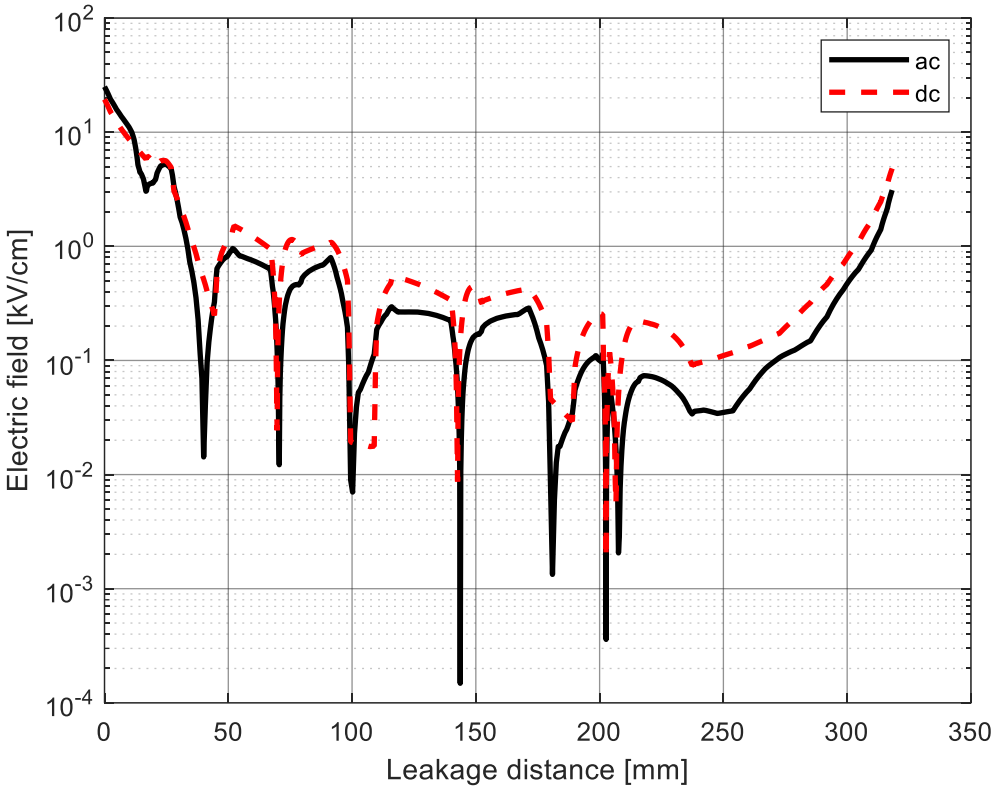

Figure 3.16: Tangential electric field along the surface of a clean ac and dc glass insulator

Figure 3.17 shows the tangential electric field along a polluted ac and dc glass insulator's surface with a 0.07 S/m conductivity. The average electric field observed on the polluted ac and dc insulator is 1.37 kV/cm and 1.14 kV/cm, respectively. The ac energised insulator has a marginally higher electric field concentration at the cap and pin of the insulator compared to the dc energised insulator. However, the dc energised insulator experiences a generally higher electric field strength along its surface, and less of the local minima that the ac case exhibits. Thus, since the

dc energised insulator experiences a generally higher electric field on its surface away from the end-points than the ac energised insulator, it can indicate that the dc case is more susceptible to flashover under the same polluted conditions, which agrees well with Zhang *et al.* (2010) and Zhang *et al.* (2013) who states that the dc flashover voltage is approximately 20% lower than the ac energised insulator case under the same climatic conditions. Zhang *et al.* (2010) also states that the accumulated pollution on the surface under dc excitation can be 20% - 50% more than the ac excitation case under the same climatic conditions, further exacerbating the occurrence of flashover.

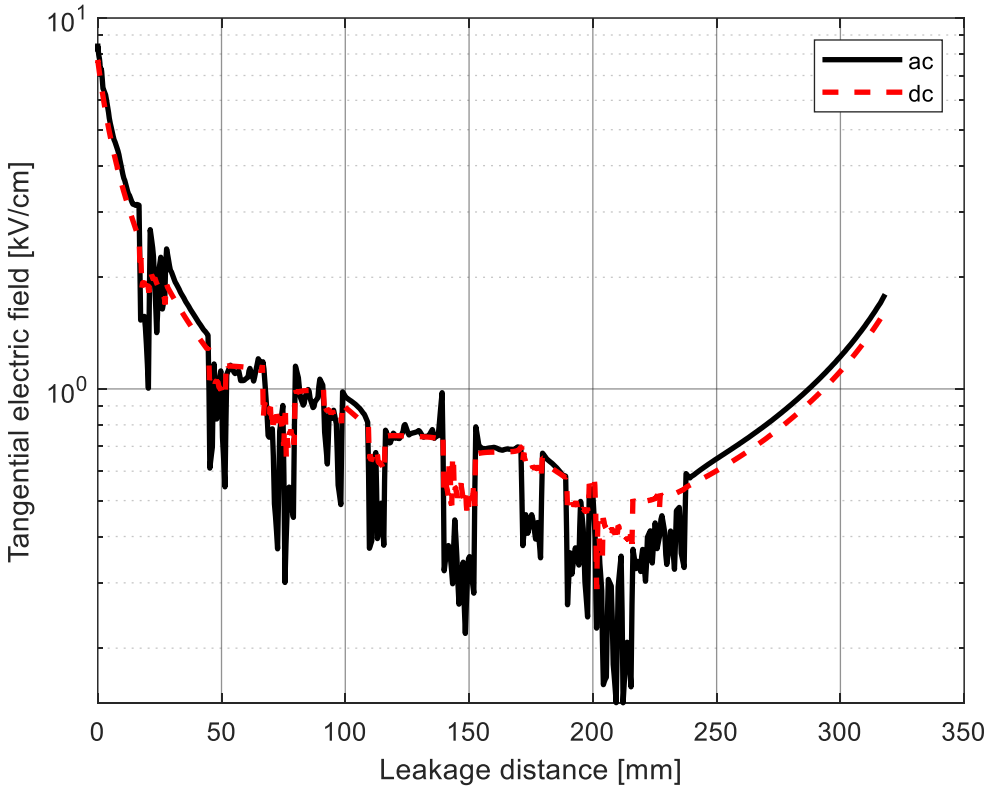

Figure 3.17: Tangential electric field along the surface of a 0.02 mm polluted ac and dc glass insulator

3.4.2 Current density distribution

Figure 3.18 shows the current density distribution along a clean ac and dc glass insulator's surface. It is evident that the clean ac insulator exhibits a higher current density when compared to the clean dc insulator. The average current density observed on a clean ac and dc insulator is 4.59×10^{-9} A/m^2 and 2.05×10^{-9} A/m^2, respectively.

Figure 3.19 shows the current density distribution along a polluted ac and dc glass insulator's surface with a conductivity of 0.07 S/m applied. From Figure 3.19, it is evident that the dc energised insulator experiences a higher current density along its surface. The average current density observed on a polluted ac and dc insulator is of similar magnitude, namely 4.81 x 10^3 A/m^2 and 5.34 x 10^3 A/m^2, respectively.

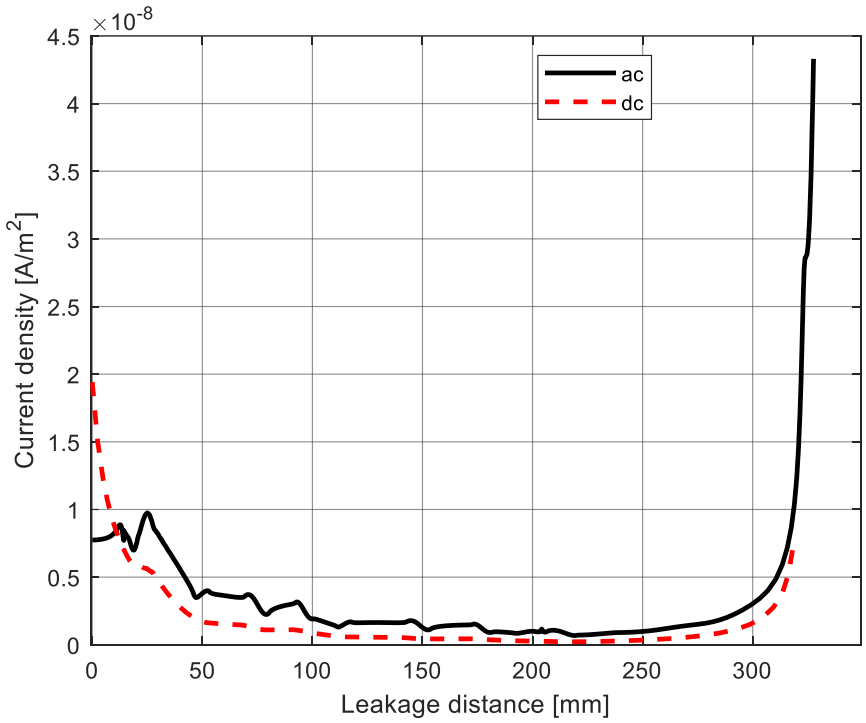

Figure 3.18: Current density along the surface of a clean ac and dc glass insulator

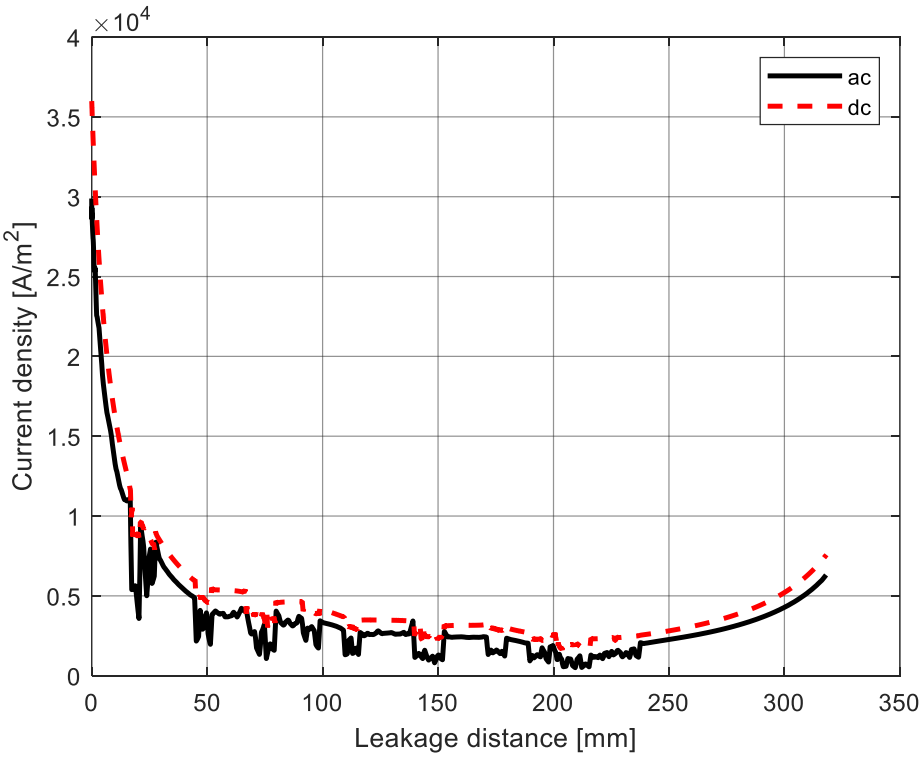

Figure 3.19: Current density along the surface of a 0.02 mm polluted ac and dc glass insulator

3.4.3 Conduction and displacement currents

In this chapter, the absolute current density has been shown for an insulator under ac and dc excitation. From Equation 3.2, it is observed that the current density consists of a conduction current and a displacement current. For the dc case, only a conduction current exists, hence, the absolute current density is equal to the conduction current. However, for the ac case, the absolute current density consists of a conduction (resistive) current and a displacement (capacitive) current.

Thus, the conduction current and the capacitive current have been plotted for the ac case to investigate each current's contribution to the absolute current density. Figure 3.20 displays the conduction current density and the capacitive current density along the surface of a uniformly polluted insulator under ac excitation. From Figure 3.20 it is evident that the capacitive current density's contribution towards the absolute current density is negligible. Thus, it can be inferred that the current found on ac energised insulators are purely resistive currents.

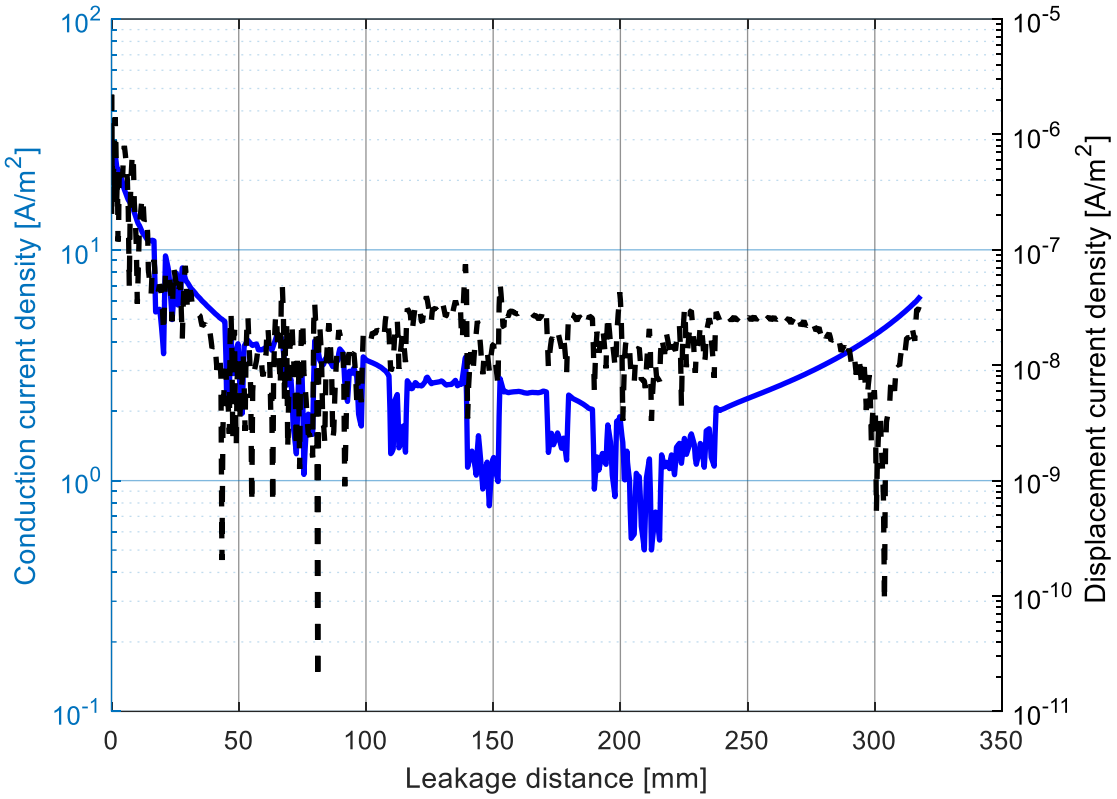

Figure 3.20: Conduction current density and displacement current density along a uniformly polluted (0.07 S/m) insulator surface under ac excitation

3.4.4 Power dissipation on a uniformly polluted insulator's surface

Studying the power dissipation along the surface of the uniformly polluted insulator can indicate where hotspots on the insulator may exist. These hotspots will likely be the place where dry bands first occur due to enhanced evaporation, and the presence of localised increased LCs on the insulator's surface that contribute to power dissipation. Figure 3.21 shows the power density along the surface of a polluted (0.07 S/m) insulator under ac and dc excitation. It is evident that the maximum power dissipation along the insulator occurs at the pin (energised end) of the ac and dc energised insulator. Thus, it can be inferred that dry bands are most likely to first occur at the energised end of the insulator where the highest tangential electric field and current density are experienced as well. It is also observed that the dc energised insulator dissipates more power along its surface than the ac energised insulator, or at least does not exhibit the localised minima in power density as for the ac case, which can be associated with less localised heating. This can lead to the dc energised insulators experiencing more dry bands (which leads to arcing and then flashover) along its surface than the ac energised insulator.

Higher electric fields on the surface of the insulator (as seen in Figure 3.17) lead to the occurrence of dry bands and this leads to eventual flashover that may occur first on the dc insulator. In the field, pollution will be non-uniform on an insulator's surface; this leads to even more occurrences of increased electric field intensity (that leads to increased heating and more dry bands forming) as mentioned by Arshad *et al*. (2015). This agrees well with Mouton (2012) who stated that the high voltage concentration may cause a partial discharge on the insulator surface and, depending on the conductivity of the pollution layers, may lead to a complete flashover event.

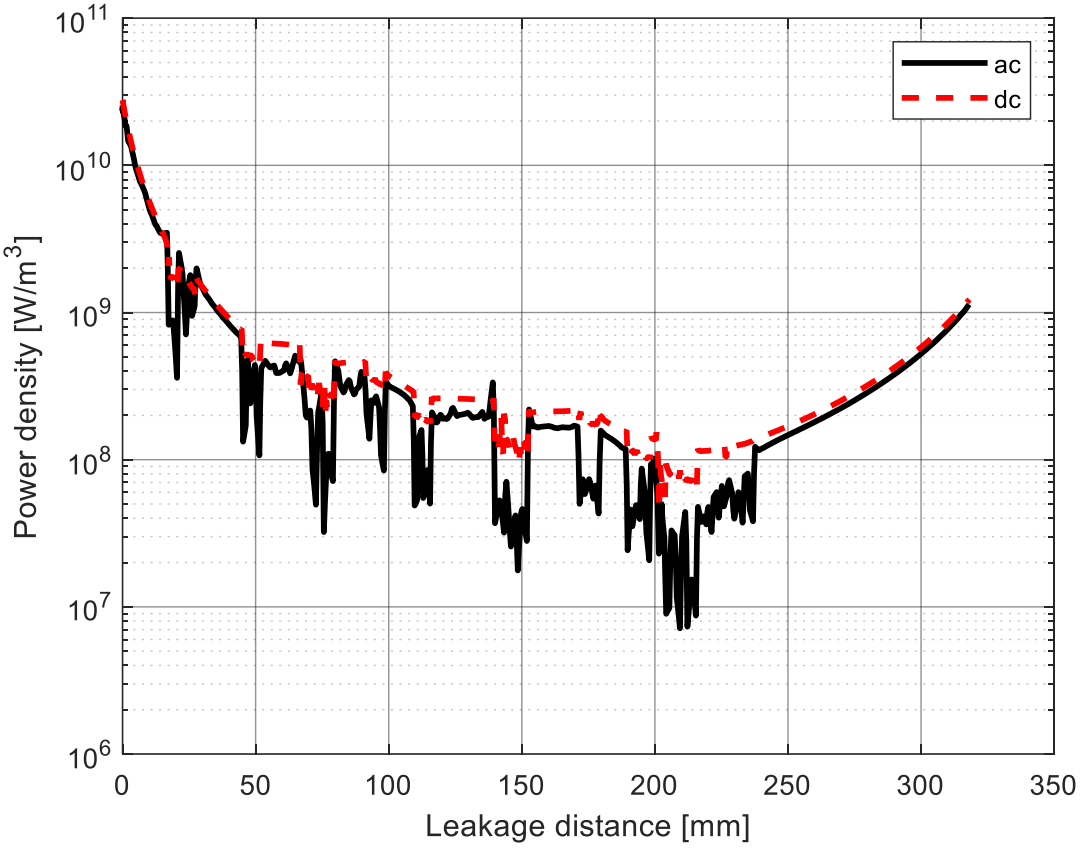

Figure 3.21: Power density along the surface of a 0.02 mm polluted ac and dc glass insulator

The power dissipation on the insulator is calculated as well by performing a volume integration across the entire insulator. The total power dissipated on a clean ac and dc insulator is 1.97 x 10^{-7} W and 1.12 x 10^{-6} W, respectively. The total power dissipated on a polluted ac insulator and dc insulator is 103 W and 188 W, respectively. Thus, it is evident that:

- heat dissipation is almost double for dc under the same conditions;
- heating will be more with dc and dry bands will form quicker;

- this will be exacerbated by the fact that dc has even more contamination as ac (Jiang *et al*., 2010), so this will further increase the heat dissipation due to larger LC;
- hence, the dc case is more prone to flashover.

3.4.5 Simulated leakage current

In conclusion, the simulated leakage current is presented and compared with actual measurements presented in Chapter 5.

During HVDC insulator LC studies performed at the corona cage, a current of 5 mA was obtained for polluted insulators with a conductivity of a 0.07 S/m applied to its surface (refer to Section 5.3.1). The 0.07 S/m conductive layer is simulated with various layer thicknesses to determine what thickness corresponds best with the insulator LC measurements presented in Chapter 5. COMSOL's *global evaluatio*n feature has been used to determine the actual current flowing through the insulator under test. Table 3.5 shows the LC obtained for the dc energised insulator when various pollution layer thicknesses are applied to the insulator. It can be seen that the LC decreases proportionally with a decrease in the thickness of the pollution layer. A LC of 56 mA is obtained for a 0.02 mm film of conductivity. A thickness of 0.02 mm is the thinnest layer that can be simulated with the available hardware due to FEM meshing constraints. However, studying the results, it is evident that a thin film of 0.002 mm will produce a LC of ~ 5.6 mA, similar to what has been measured in Chapter 5. It can therefore be assumed that the thickness of the pollution layer applied during the experiments presented in Chapter 5 is of the order 0.002 mm.

Table 3.5 Leakage current on the dc energised insulator when varying the 0.07 S/m pollution layer thickness

Thickness of pollution layer [mm]	Leakage current [mA]
1.00	2710
0.50	1357
0.25	683
0.10	283
0.05	143
0.02	56

The fact that the COMSOL LC simulations correspond so well with what were measured in the field, gives confidence in the model itself, and the application of FEM-based simulations in future research and development work concerning insulator design.

3.5 Influence of background air conductivity on the electric field and current distributions of insulators under ac and dc excitation

It is known that the onset of rain causes the layer of pollution on the insulator to become more conductive (Zhang *et al.,* 2010; Wang *et al*., 2015; Benguesmia *et al*., 2019; Wang & Wu, 2019). The increase in conductivity of the pollution layer leads to LC activity and a decreased flashover withstand voltage on the insulator. When rainy conditions are present, the humidity is high and it influences the conductive properties of the air significantly. Seran *et al.* (2017) mentions that the electric conductivity of air also increases with altitude. Rakov & Uman (2003) clearly indicates in Figure 3.22 how much the electric conductivity of air increases with altitude. Many transmission lines, including the Cahora Bassa, is situated at high altitude (~ 1600 m above sea level). From Figure 3.22 it can be seen that the electric conductivity at sea level and at 1600 m above sea level is approximately 1 x 10^{-14} S/m and 1 x 10^{-13} S/m, respectively; an order of 10 difference.

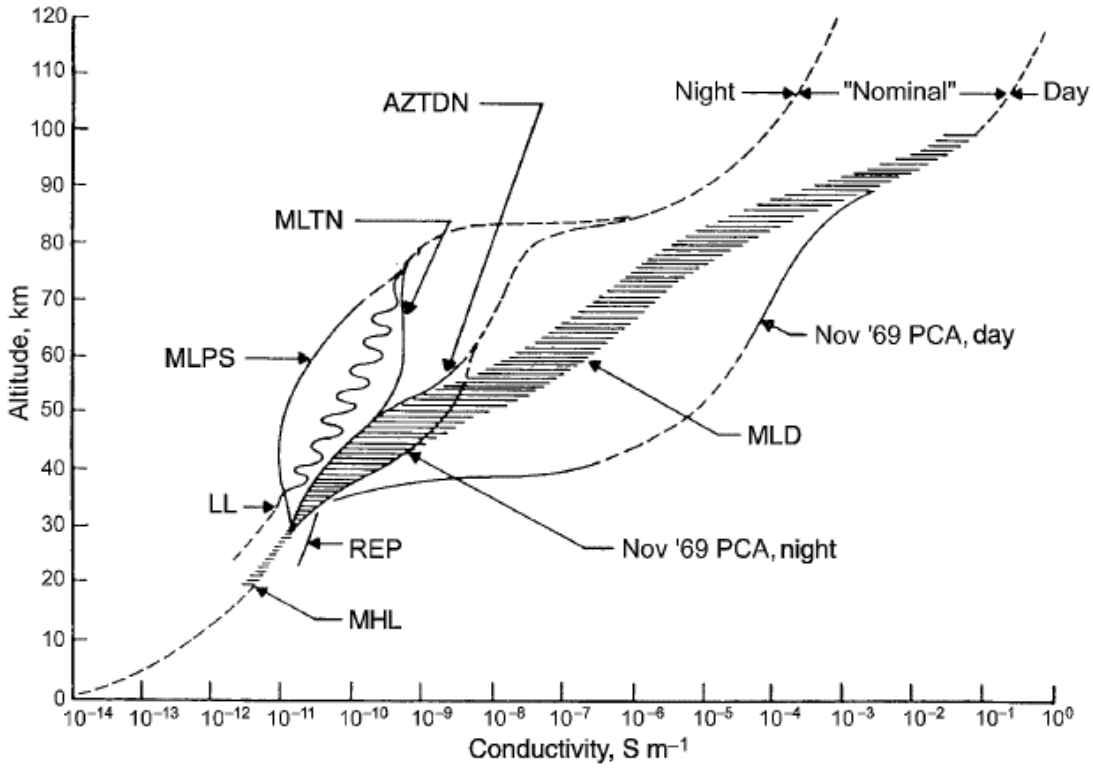

Figure 3.22: Electric conductivity versus altitude under a variety of geophysical conditions. LL, low latitude, "wavy"; MLPS, mid-latitude pre-sunrise (unusual); MLTN, mid-latitude typical night (high-latitude, quiet); AZTDN, auroral zone, typical disturbed night; MLD, mid-latitude day, quiet; MHL, mid-high-latitude, typical of ~ 100 measurements; REP, relativistic electron (energy from a few MeV to 10 MeV) precipitation event (unusual); PCA, polar cap absorption event (an unusually large flux of energetic, ~ 100 MeV solar protons within the polar cap). (Adapted from Rakov & Uman, 2003)

During the literature conducted in Section 3.2, it was observed that the background air conductivity assumed by various authors varies, ranging from 1 x 10^{-15} to 1 x 10^{-12} S/m, without an explanation of why a certain air conductivity level was chosen for their simulations on ac energised insulators (Murugan *et al*., 2013; Hussain *et al*., 2015; Rosli *et al*., 2017; Krzma & Khamaira, 2018).

The lowest conductivity used by an author (Netravati *et al*., 2016) was 1 x 10^{-15} S/m. Incidentally, Netravati *et al.* (2016) is the only author who studied the current density distribution on ac energised insulators, taking into account the background conductivity of air as well.

Arshad *et al.* (2015) performed electric field simulations on composite insulators under dc excitation but no simulation parameters are given in the paper to compare results. Thus, an ideal air conductivity for dc energised insulators are unknown as simulation parameters for the background air was not stated. Abimouloud *et al.* (2018) and Banik *et al*. (2018) used COMSOL to create a flashover prediction model for dc insulators; however, the background air conductivity was not taken into account since they only simulated the insulator's ceramic material and its pollution layer.

The respective distributions (voltage, electric field, current) of sections 3.3.2 and 3.3.3 have been re-simulated but with different background air conductivity levels; these levels have been chosen to correspond with the expected values from sea-level to 10 km altitude in the extreme, i.e. in the ranging of 1 x 10^{-14} S/m to 1 x 10^{-12} S/m. From these simulations, no clear change in the voltage, electric field or current density responses has been observed for the ac and dc energised insulator cases.

Thus, it can be concluded that a change in the conductivity of air as a function of altitude alone does not affect an insulator's performance. However, as stated earlier, it is known that humidity can affect the electric conductivity of air significantly.

Instead of studying the electric conductivity or resistance of air versus humidity, researchers study the electrical breakdown of a material in air versus humidity. Krile *et al.* (2004) performed such dc flashover tests by energising an electrode in air and on a dielectric surface in atmospheric conditions. Figure 3.23 shows the results for breakdown voltage versus relative humidity for an alumina surface. The results show that the electrical breakdown voltage of air on a surface decreases with humidity. From Rakov & Uman (2003), it is observed that electric conductivity increases with altitude. Thus, a combination of increased altitude (which increases the electric

conductivity of air) and humidity conditions can lead to lower flashover with voltages on insulators. Hence, it can be inferred that a combination of high humidity conditions and an increase in altitude, which leads to an increased ambient conductivity, further exacerbates insulator flashovers. This is especially relevant to dc energised insulators, since Yang *et al.* (2014) reported that dc insulators accumulate more pollution and have a lower flashover voltage than the ac energised insulators under the same climatic conditions. The dc insulators accumulate more pollution on its surfaces due to the electrostatic force acting on the contaminants (Zhang *et al.,* 2013). Flashover voltages also decreases with an increase in altitude (Yang *et al*., 2014).

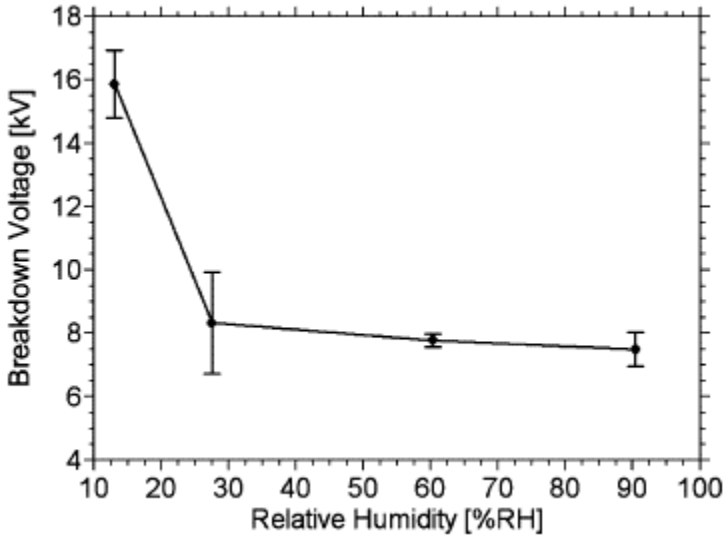

Figure 3.23: Breakdown voltage of air versus relative humidity with an alumina surface. Electrode geometry with a 12 mm gap spacing is used (From Krile *et al*., 2004)

3.6 Conclusion

This chapter presented the simulation results for clean and polluted ac and dc glass insulators.

The highest electric fields are found closest to the cap and pin regions of a clean insulator. The clean ac insulator exhibits a higher current density compared to the clean dc insulator. However, the clean dc insulator exhibits a higher average electric field intensity than the clean ac insulator.

Under polluted conditions, both ac and dc insulators exhibit a dramatic increase in electric field intensity and current density. The electric field on the surface of a polluted insulator is higher on an energised dc insulator than for the ac case. This, together with increased current densities lead to higher power dissipation in the dc case with the effect of causing dry bands; this may lead to a

dc insulator having a higher flashover probability than the ac insulator under the same excitation voltage. It is also observed that there is still a considerable electric field present on the surface of the ac and dc polluted insulators, which is not present on the clean insulator case. These high electric fields along the insulator surface can be an indicator of where dry bands are mostly likely to occur.

From the voltage distribution results it is observed that the voltage is concentrated near the energised end of a clean ac and dc insulator. When the insulator is polluted, the voltage drop across the insulator surface occurs more linearly due to the presence of the pollution layer. When a pollution layer of 5×10^{-6} S/m is applied to an ac excited insulator, the response is similar to that of the clean insulator. However, for the dc excited insulator, when a pollution layer of 5×10^{-6} S/m is applied, it yielded the same response as when the 0.07 S/m pollution layer is applied. Thus, it can be inferred that the insulators under dc excitation are more susceptible to pollution than insulators under ac excitation under the same contamination conditions.

The current density found on polluted dc insulators are also higher compared to the current density found on ac insulators. It is evident that the electric field and current density distributions increase with an increase in pollution layer conductivity for the ac and dc insulators.

The simulated LC found on the polluted insulator have also been compared against the LC measured in the work presented in Chapter 5 where LC measurements have been performed at the corona cage. The simulated LC results agree well with the measurement results reported in Chapter 5 with an adjusted contamination layer thickness.

It is known that only conduction currents exist on dc energised insulators. However, for the ac case, both conduction and capacitive currents are present. Simulations presented here show that the contribution of the capacitive current is negligible under ac excitation and that the currents found on ac energised insulators are predominantly resistive for contaminated insulators.

The power dissipation across an ac and dc energised insulator have been calculated as well. It is observed that power loss in terms of heat dissipation is almost double for dc energised insulators under the same pollution conditions. Thus, more heating will occur on dc energised insulators and dry bands will also form quicker on dc insulators. This will be exacerbated by the fact that dc has even more contamination as ac; this will further increase the heat dissipation due to larger LC. Hence, insulators under dc excitation are more prone to flashover.

The effect of various electric conductivities for air has been studied since it increases with altitude. However, it is concluded that an increase in the air's conductivity as a function of the altitude for typical existing HVDC transmission lines does not affect an insulators performance. However, it is also known that the humidity can affect the ambient air's conductivity significantly. Thus, it can be inferred that a combination of high humidity conditions and an increase in altitude (which leads to an increased ambient conductivity) can exacerbate insulator flashovers, especially on dc energised insulators.

4: DEVELOPMENT OF SENSOR FOR HVDC INSULATOR LC MEASUREMENTS

4.1 Introduction

A sensor capable of detecting LCs flowing on insulators of HVDC transmission lines, such as the Cahora Bassa transmission network, is required for in-situ insulator LC measurements, typically in the range of 1 – 100 mA. A shunt resistor in parallel with an insulator (see Figure 5.1) to measure the LC is quite a common method used (Zhang *et al*., 2013) and it is also used to validate the developed LC sensor's results (as discussed in Section 4.2). This method is, however, impractical and cannot be used in the field because it entails shutting down the power lines. It requires the insertion of a stand-off insulator at the dead-end of the string, which is costly. Magnetic field sensors can detect LC non-intrusively. Various magnetic field sensors and a COTS dc current sensor have been evaluated in this work for the measurement of LC. The COTS LC sensor does not meet all the set requirements; thus, an LC sensor prototype has been developed. The sensor prototype is clamped around the insulator and is based on magnetic field sensors.

Figure 4.1 depicts the typical positions of the line current, current sensor and insulator of the Cahora Bassa HVDC transmission line.

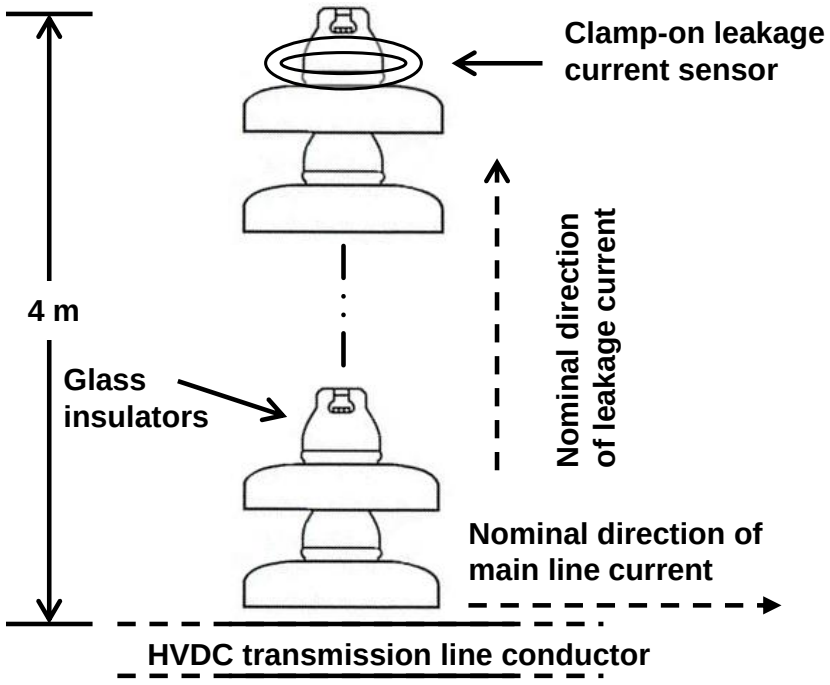

Figure 4.1: Measurement setup showing typical positions of the line current, current sensor and insulator of the Cahora Bassa HVDC transmission line

4.2 COTS dc LC sensor

The commercially-off-the-shelf (COTS) dc LC sensor (Chenyang Technologies, n.d) is similar to that discussed in Cheng *et al.* (2013). The design comprises a soft magnetic core, primary and secondary windings, a square wave generator and a 3rd order low pass filter (the primary components). The COTS sensor fitted around a glass insulator and wire, respectively, is presented in Figure 4.2.

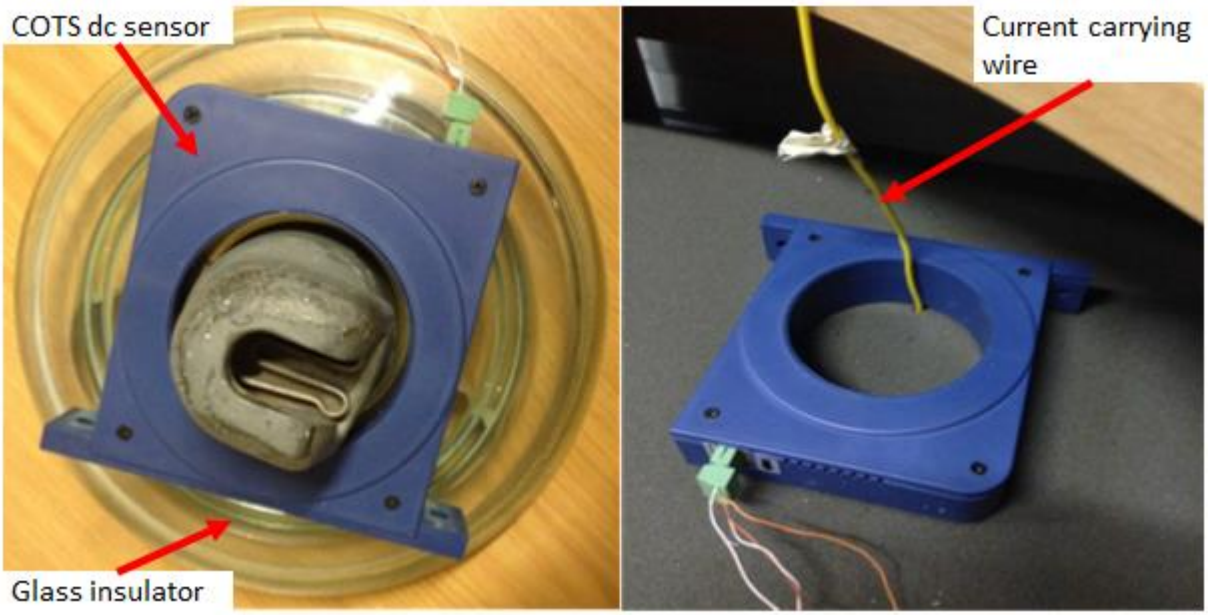

Figure 4.2: COTS dc LC sensor fitted around a glass insulator (left) and a current-carrying wire (right)

4.2.1 Calibration and measurements

The sensor's electronics, contained in an aluminium box, include a current to voltage converter, an amplifier and a 3rd order 1 Hz low-pass filter. The sensor is first calibrated before measurements are performed on the glass insulator. This is done by wrapping aluminium foil around a cylinder and injecting current through the foil. The cylinder fills the sensor's entire measurement window as this allows for the most accurate measurements. The calibration process is repeated ten times to reduce statistical error. Afterwards, the sensor is wrapped in a high permeability shield and the calibration process repeated (as shown in Figure 4.3). It has been observed that the shielding decreases the mean error in repeated measurement sets. The measured sensitivity scale is 8.5 mV/mA for the shielded and non-shielded sensors.

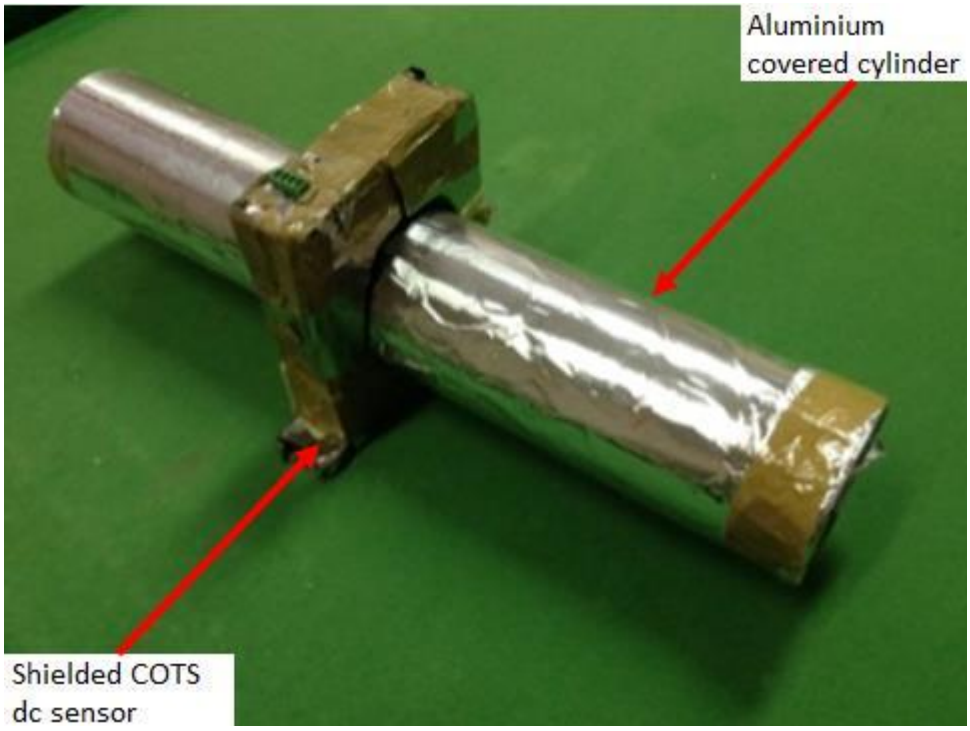

Figure 4.3: Shielded COTS dc sensor fitted around cylinder covered in aluminium foil for calibration

Insulator LC measurements have been performed twice, whereas measurements with the current-carrying wire have been repeated once for each of the following relative positions of the wire; 0° (top), 90° (left), 180° (bottom), and 270° (right). This is to test whether the placement of the current carrying wire has an effect on the measured current.

Figure 4.4 and Figure 4.5 show the measured current up to 100 mA for the non-shielded and shielded sensors, respectively.

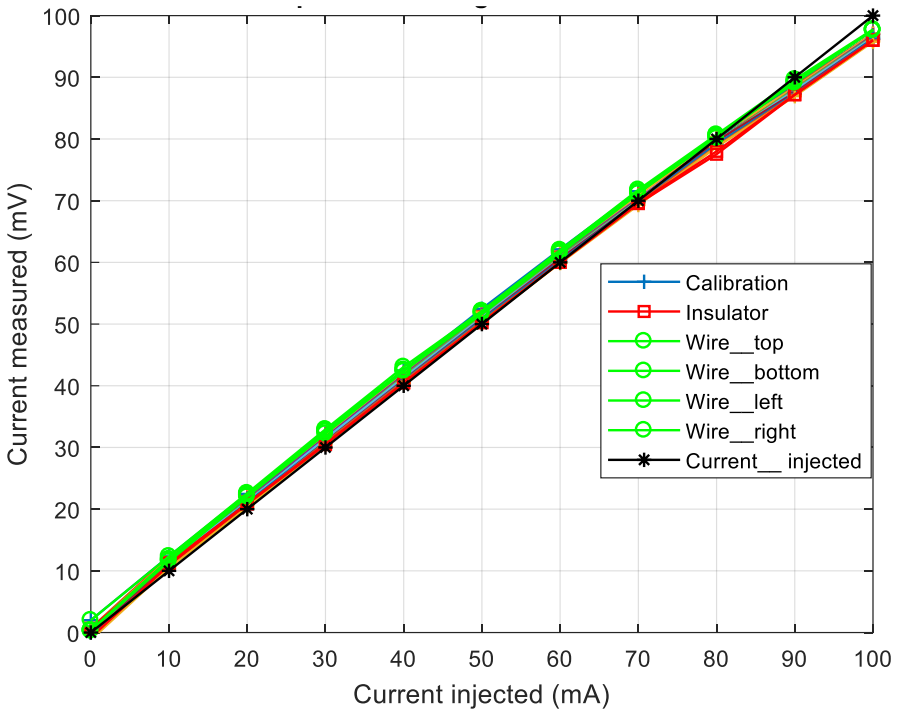

Figure 4.4: Comparison of current up to 100 mA injected versus the measured current obtained with a wire, an insulator and the cylinder used during the calibration process for a non-shielded dc LC sensor

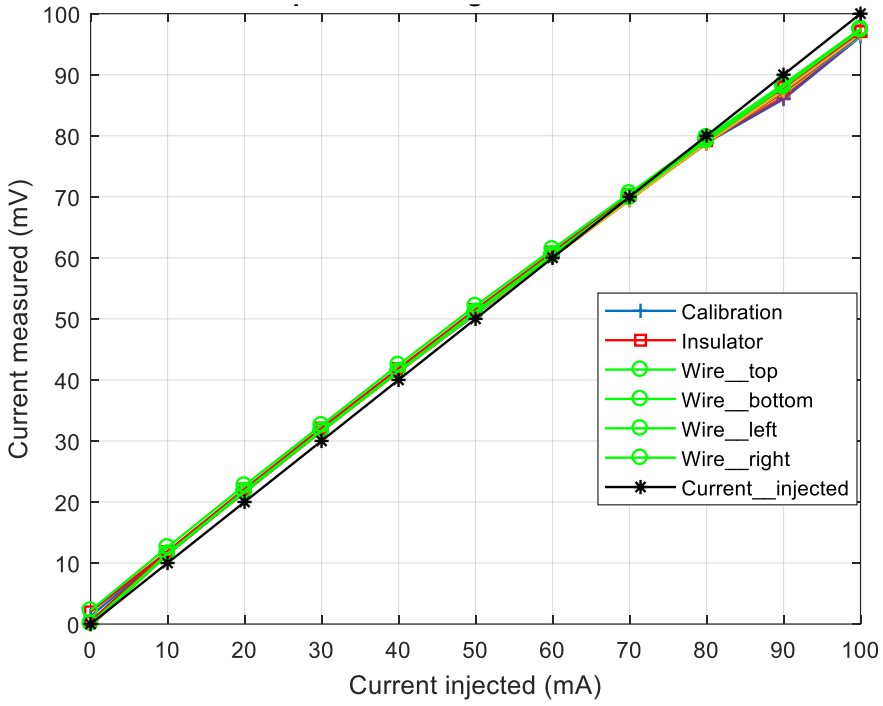

Figure 4.5: Comparison of current up to 100 mA injected versus the measured current obtained with a wire, an insulator and the cylinder used during the calibration process for a shielded sensor dc LC sensor

4.2.2 Discussion of results

The results presented in Figure 4.4 and Figure 4.5 show repeatability of the measurements. The measurements where the current-carrying wire is moved around within the sensor present the worst-case scenario. The average error observed between the current injected over the full range of 1 - 100 mA for the non-shielded and shielded dc LC sensors was calculated using Equation 4.1:

$$Error = \frac{100\%}{n} \sum \frac{|x_1 - x_2|}{x_2} \qquad \textbf{Equation 4.1}$$

where n is the number of data points, x_1 is the actual output value and x_2 is the expected value.

The average error between the current injected and the different cases investigated in Figure 4.4 and Figure 4.5 are listed below:

- Aluminium covered cylinder (used for calibration): 2.75% (non-shielded) and 2.59% (shielded);
- Insulator: 3.77% (non-shielded) and 1.04% (shielded);
- Wire positioned at the top: 6.23% (non-shielded) and 5.72% (shielded);
- Wire positioned at the bottom: 5.25% (non-shielded) and 2.91% (shielded);
- Wire positioned to the left: 4.88% (non-shielded) and 3.08% (shielded);
- Wire positioned to the right: 4.33% (non-shielded) and 2.91% (shielded);

Table 4.1 shows the average error between the current injected and the insulator, aluminium covered cylinder (used for calibration) and the current wire in different positions.

The insulator LC measurement is in agreement with the injected current within approximately 6% for all cases. It is also evident that the shielding of the sensors, generally, decreases the mean error in measurements since it provides shielding from stray magnetic fields. The average error observed between the current carrying wire and the current injected for the shielded dc LC sensor is 3.7%. The average error observed between the insulator and the current injected for the shielded dc LC sensor is 1%. These results confirm what is expected as the dc LC sensor is most accurate when its window is completely filled and the current distributed evenly within the gap.

Table 4.1: Average error in percentage between the current injected and the insulator, aluminium covered cylinder and the current carrying wire in different positions

	Calibration	Insulator	Wire_top	Wire_bottom	Wire_left	Wire_right
Non-shielded	2.75	3.77	6.23	5.25	4.88	4.33
Shielded	2.59	1.04	5.72	2.91	3.08	2.91

4.3 Fluxgate magnetometer current sensor

Fluxgate sensors are typically ring cores of high permeability material that are wrapped with two windings; viz. the driving and sensing windings. A fluxgate magnetometer generates an electrical signal that is proportional in magnitude to the intensity of the magnetic field sensed externally along its axis. It is used for the measurement of dc and low-frequency ac magnetic fields (Siziba, 2011).

Experiments have been conducted in the laboratories at the Cape Peninsula University of Technology (CPUT) to determine whether a fluxgate magnetometer is sensitive enough to measure the expected LC. The specific fluxgate magnetometer used is the LEMI-011B (Applied research, n.d) as displayed in Figure 4.6. The LEMI-011 is an analog, 3-axis fluxgate magnetometer that generates an output voltage. It measures the magnetic field associated with the current that is flowing in the wire. Figure 4.7 illustrates the laboratory measurement setup.

Figure 4.6: LEMI magnetometer with the cover removed

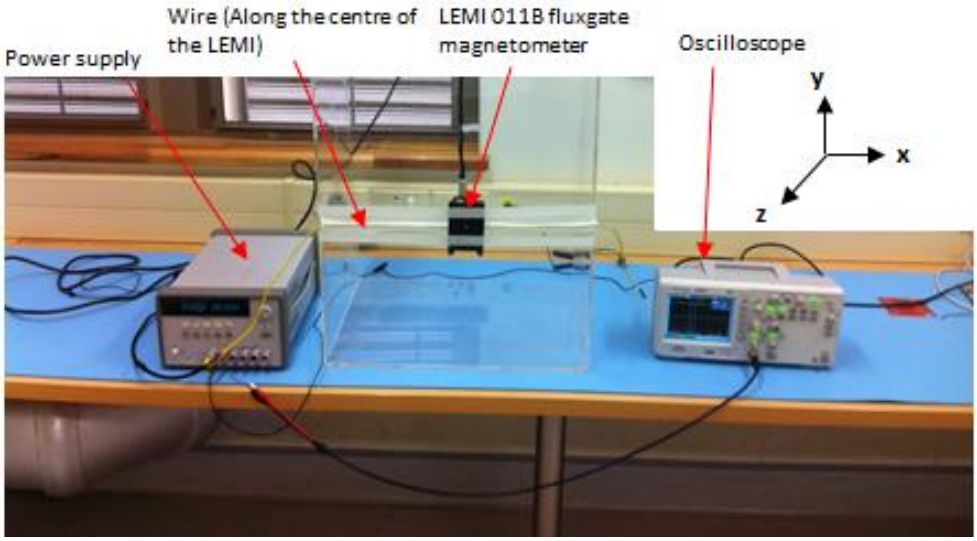

Figure 4.7: LEMI fluxgate magnetometer LC measurement setup

4.3.1 Calibration and measurements

A set of measurements of a current injected in a single, straight wire has been taken, including a reference measurement where no current is flowing through the wire. This is done because the LEMI has an internal offset voltage due to the ambient magnetic field. The results obtained from the measurements are subtracted from the reference measurement in order to obtain the actual measurement at the specified supplied current. To obtain the measured magnetic field, an output sensitivity of 45 μV/nT is applied (Applied research, n.d). Figure 4.8 shows the comparison of the actual current injected into the wire and the current measured indirectly through this method with the LEMI. An average error of 5% has been observed over the measurement range by applying Equation 4.1. This is within the acceptable limit.

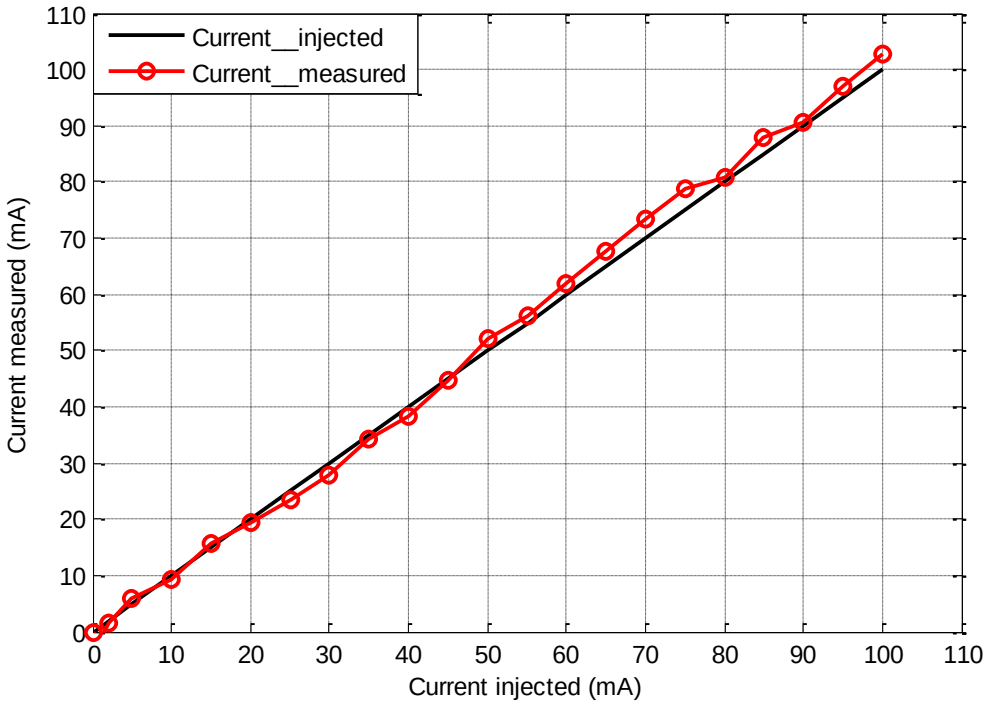

Figure 4.8: Comparison of current injected through the wire versus the current measured with the LEMI

4.3.2 Measurement of LC on glass insulators

LC measurements have been conducted at the fog chamber located at the University of Witwatersrand (Wits) to determine whether the fluxgate magnetometer can measure LC on an energised glass-type insulator (the device under test). The fog chamber can be used to replicate humid conditions that an insulator may experience in its intended environment. Figure 4.9 and Figure 4.10 present the measurement setup. The shunt resistor is used as a control measurement.

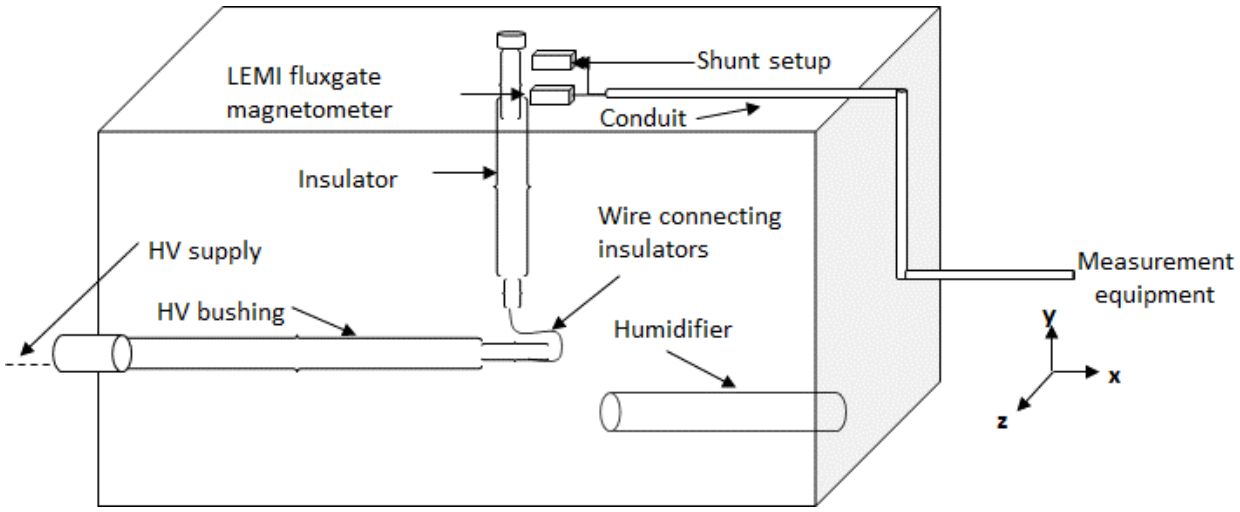

Figure 4.9: Test setup configuration for insulator LC measurement in the fog chamber at Wits

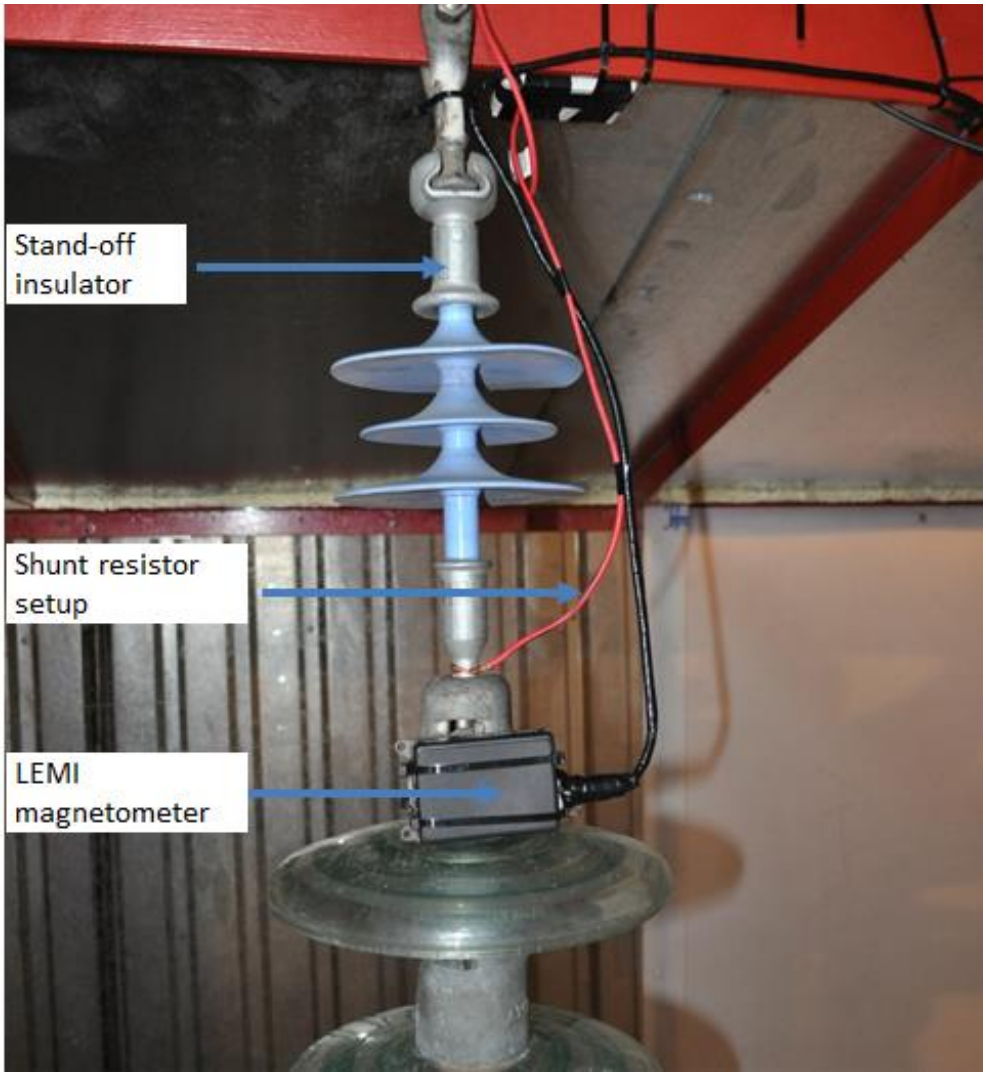

Figure 4.10: Position of the LEMI magnetometer and the shunt measurement setup at Wits

Cold fog is injected into the chamber using an ultrasonic humidifier. The insulator is sprayed with a saltwater solution and constantly wetted with fog inside the chamber in order for LC to flow. The LEMI's measurements are compared to the shunt method's control measurement data. The shunt method entails placing a 50 Ω resistor between the dead-end of the insulator and ground. The magnetometer measures the magnetic field at the dead-end of the insulator.

An HV power supply is used to drive LC in 10 mA steps from 0 to 100 mA. The X- and Z- channels (axes) of the LEMI are logged simultaneously with the shunt resistor measurements.

The current associated with the X- and Z- directed magnetic fields are calculated individually. Thereafter, the absolute values of the X- and Z- current vectors are calculated for the LC magnitude. The LC measurements, together with that obtained from the shunt resistor, are presented in Figure 4.11. The Y- channel's data is not logged as this channel will not measure the magnetic field due to its Y- sensor being in the same direction as the current to be measured. Figure 4.11 shows that the magnetometer accurately detects the current that was measured by the shunt resistor as well, including the flashover event that occurred. The results are discussed in the following section.

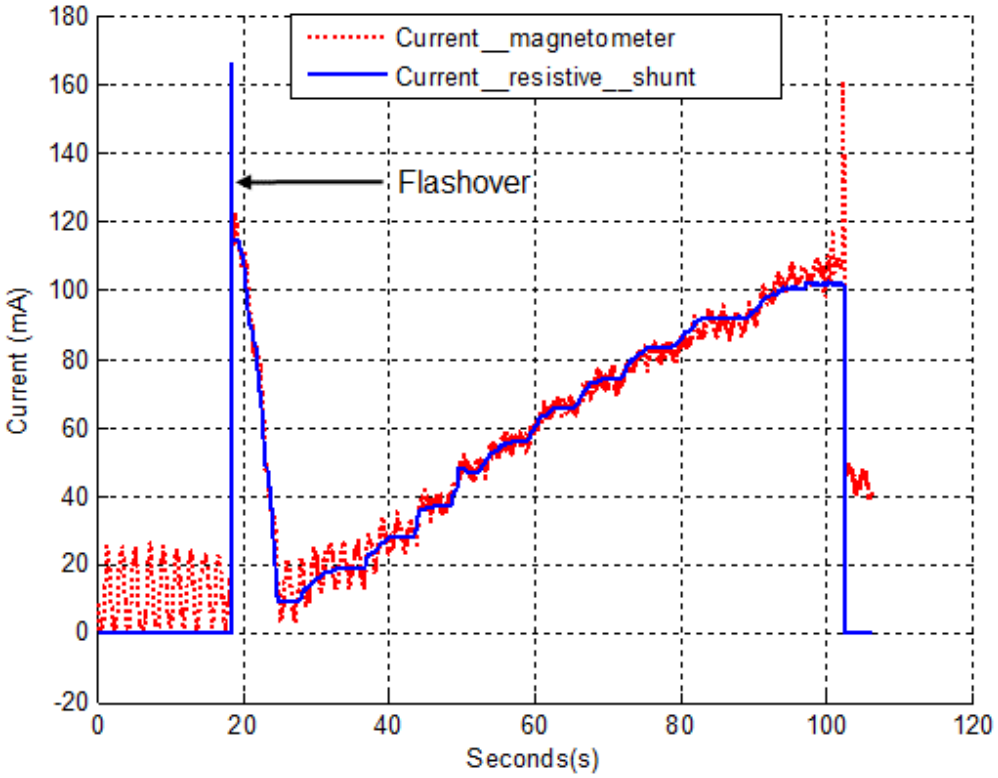

Figure 4.11: Comparison of LC on an energised insulator as measured with the LEMI-011B magnetometer (red line) and the shunt resistor (blue line)

4.3.3 Discussion of LEMI fluxgate magnetometer LC results

LC measurements have been performed with the LEMI-011B fluxgate magnetometer for a current-carrying wire and a glass insulator. The results show that this particular magnetometer is sufficiently sensitive and linear to detect LCs in both the control experiment and when applied to an energised glass insulator, in the range of 0 - 100 mA. From Figure 4.11 it is noted that the LEMI also detects a quasi-dc field before the measurement process started (0 - 18 s). This may be attributed to ambient noise as the LEMI's bandwidth spans dc to 20 Hz (Applied research, n.d). This implies that screening of the LEMI from external magnetic fields may be necessary if deployed in practice. At 18.2 s, a flashover suddenly appears. However, no LC build-up is observed prior to the flashover event. This may be due to how fast the voltage has been applied to the test setup by the technician or that the measuring equipment is not capable of detecting such fast transitions in LC since Krile *et al*. (2014) mentions that flashovers can occur within a few nanoseconds. Following the flashover event, increased LC is observed with the LEMI and shunt resistor as is evident between 20 - 100 s. Upon de-energising the insulator string (at 100s), a spike in the LEMI's current reading has been observed, which is not evident on the resistive shunt measurement. The spike observed can be due to the power supply switching abruptly to zero, causing electromagnetic transients that are sensed by the LEMI magnetometer. Another purpose of these LC measurements at the Wits lab was to observe the LEMI's response to electromagnetic interference. During the tests, the LEMI withstood direct flashover events as observed in Figure 4.12 whilst producing reliable results.

Figure 4.12: Flashover during LEMI LC measurements

4.4 Summary on the dc LC sensor and LEMI fluxgate magnetometer

Both the LEMI fluxgate magnetometer and COTS dc LC sensor exhibit good linearity, sensitivity and accuracy across the range of 0 - 100 mA. The magnetometer can, however, be used for non-intrusive measurements, which is not possible with the COTS current sensor. The LEMI's enclosure, furthermore, provides adequate protection against flashovers. However, it is sensitive to ambient magnetic fields, which will have to be screened when deployed. This may be impractical as their fundamental mode of operation depends on measuring magnetic fields. Moreover, LEMI magnetometers are relatively expensive (~R 6000 without any additional signal conditioning circuitry) and not readily available off-the-shelf. These constraints pose a challenge especially when deployed in magnetically harsh conditions, and in large numbers along HVDC transmission lines. Hence, they are unsuitable for wide development on HVDC lines, and especially for the Cahora Bassa line case study presented later, to monitor insulator LC.

4.5 Design and development of an LC sensor prototype

The COTS LC sensors that were investigated in Sections 4.2 and 4.3 do not meet all the set requirements; thus, an LC sensor prototype has been developed. The LC sensor prototype was designed and developed with the following requirements:

- a hand-held, clamp-on type device for online HVDC insulator measurements;
- performing in-situ measurements on energised insulators and in the vicinity of an HVDC transmission line (1800 A Cahora Bassa HVDC transmission line);
- measuring LC from 1 mA to 100 mA; and
- withstanding flashovers that might occur during measurements.

These requirements stem from the current rating of the Cahora Bassa HVDC transmission, the fact that continuous LC build-up will eventually lead to flashover, and that measurements have to be performed on already energised insulators in the field.

As discussed in the previous sections, magnetic field sensors can be deployed to accurately detect LC non-intrusively if sufficient screening from stray ambient fields is implemented. The following section discusses the development of a clamp-on type sensor prototype to measure LC non-intrusively on HVDC insulators.

4.5.1 Construction of single core dc LC sensor prototype

The first version of the dc LC sensor prototype consists of the following components:

- HMC 1021Z MR 1-axis magnetic field sensor (Honeywell, n.d);

- single high permeability soft magnetic core; and
- signal conditioning circuitry.

For ease of reference, this single core sensor prototype is named LCPR1 (leakage current prototype 1). Each component is described below.

4.5.1.1 HMC 1021Z MR 1-axis magnetic field sensor

The magneto-resistive (MR) sensor is a surface-mount magnetometer as shown in Figure 4.13. The HMC 1021Z magnetometer utilises Honeywell's anisotropic magnetoresistance (AMR) technology (Honeywell, n.d). It employs a simple resistive Wheatstone bridge that only requires a bias voltage to operate. This sensor is compatible with battery powered applications, has stray magnetic field compensation and can be used in strong magnetic field environments. The HMC 1021Z has an operating bandwidth of 0 to 5 MHz. This MR sensor is also the smallest, most sensitive and cost-effective in the Honeywell MR sensor range; small enough to be slotted inside a soft magnetic core, which will be explained in the upcoming sections.

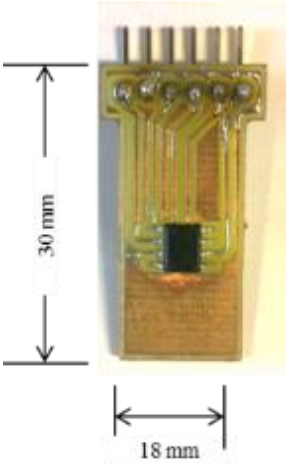

Figure 4.13: HMC 1021Z magneto-resistive magnetometer

4.5.1.2 High permeability soft magnetic core

The prototype uses a high permeability (μr > 2000) toroidal core in conjunction with the MR sensor. A slot is cut into the soft magnetic core using waterjet cutting and the sensor placed within it. The toroidal core "traps" the magnetic field generated by the LC inside the core opening. This causes the magnetic field in the air gap to be of similar magnitude, irrespective of the position of the LC inside the core opening. It also provides a level of screening from external and ambient magnetic fields. These effects will be discussed further in Section 4.5.2

4.5.1.3 Signal conditioning circuitry

The signal conditioning circuitry essentially amplifies the two output voltages of the LC sensor differentially. Figure 4.14 shows the dc LC sensor with its electronics fitted around a glass insulator.

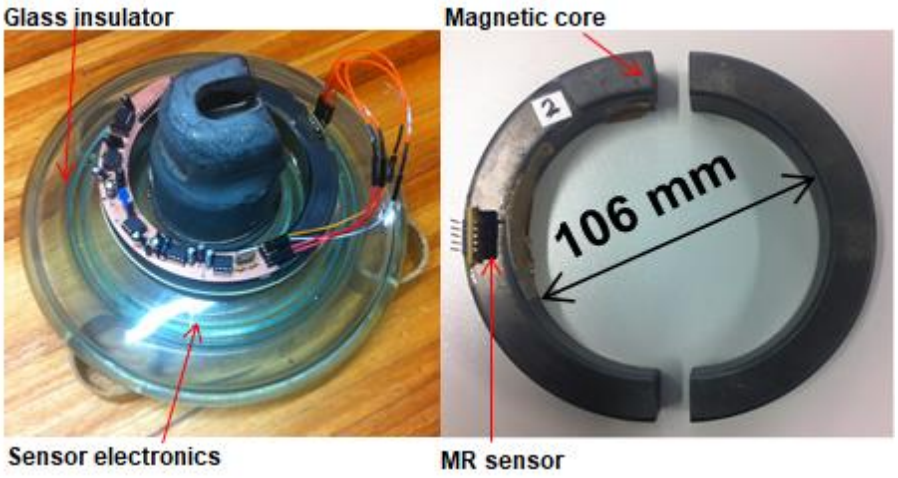

Figure 4.14: LCPR1 sensor fitted around glass insulator

4.5.2 Magnetic field simulations for the LCPR1 sensor

The purpose of the magnetic field simulations is to validate the benefits of embedding the MR sensor within the soft magnetic core.

4.5.2.1 Capturing of the LC magnetic field within the core

The MR sensor, like the LEMI magnetometer, is a magnetic field sensor that can measure the magnetic field associated with an electric current. However, during initial LC measurements without a magnetic core, it has been observed that the magnetic field measured by the LEMI magnetometer or MR sensor changes with respect to the position of the line current source, even though the magnitude of the current is unchanged. These simulations will demonstrate that the current inside the core opening (the LC) will indeed generate a field that is "captured" in the core, irrespective of the position of the LC, and concentrate the magnetic field, enabling more sensitive measurements. The core also provides screening of external fields, which are always present.

Magnetic field simulations are performed using the *Finite Element Method Magnetics* (FEMM) software to observe the effect of the core on the LC measurements (Finite Element Method Magnetics, 2014). A core with an inner diameter of 100 mm and with a slot size of 20 mm is

simulated and a line current of 10 mA is placed at different positions within the core. This mimics the LC that can flow anywhere on the surface of the insulator. The MR sensor will be situated in the slot, which is where the magnetic field is sampled. The FEMM output box in the screen presents the simulated field vectors at the sampling location.

Figure 4.15 through Figure 4.18 show the simulated magnetic field distributions for the line current positioned to the left, top, right and centre of the core opening, respectively. The simulations show that the core “traps” the magnetic fields and that the sensor will experience similar magnitudes of magnetic field in the centre of the slot for all positions of LC within the core opening. The magnitude of the magnetic flux density |B| at the sampling location in the slot varies between 43.318 nT and 45.447 nT for the respective LC positions; a relative difference of the order 5%. These results are also in agreement with the COTS dc LC sensor that uses a solid core, as described in Section 4.2 where it has been observed that a similar magnetic field will be measured, irrespective of where the current source is within the core opening. These results prove that the magnetic field measured within the slot will be similar in magnitude, irrespective of the position of the LC within the core, and hence, will yield more reliable LC measurements in practical scenarios where the LC is distributed unevenly on the insulator’s surface.

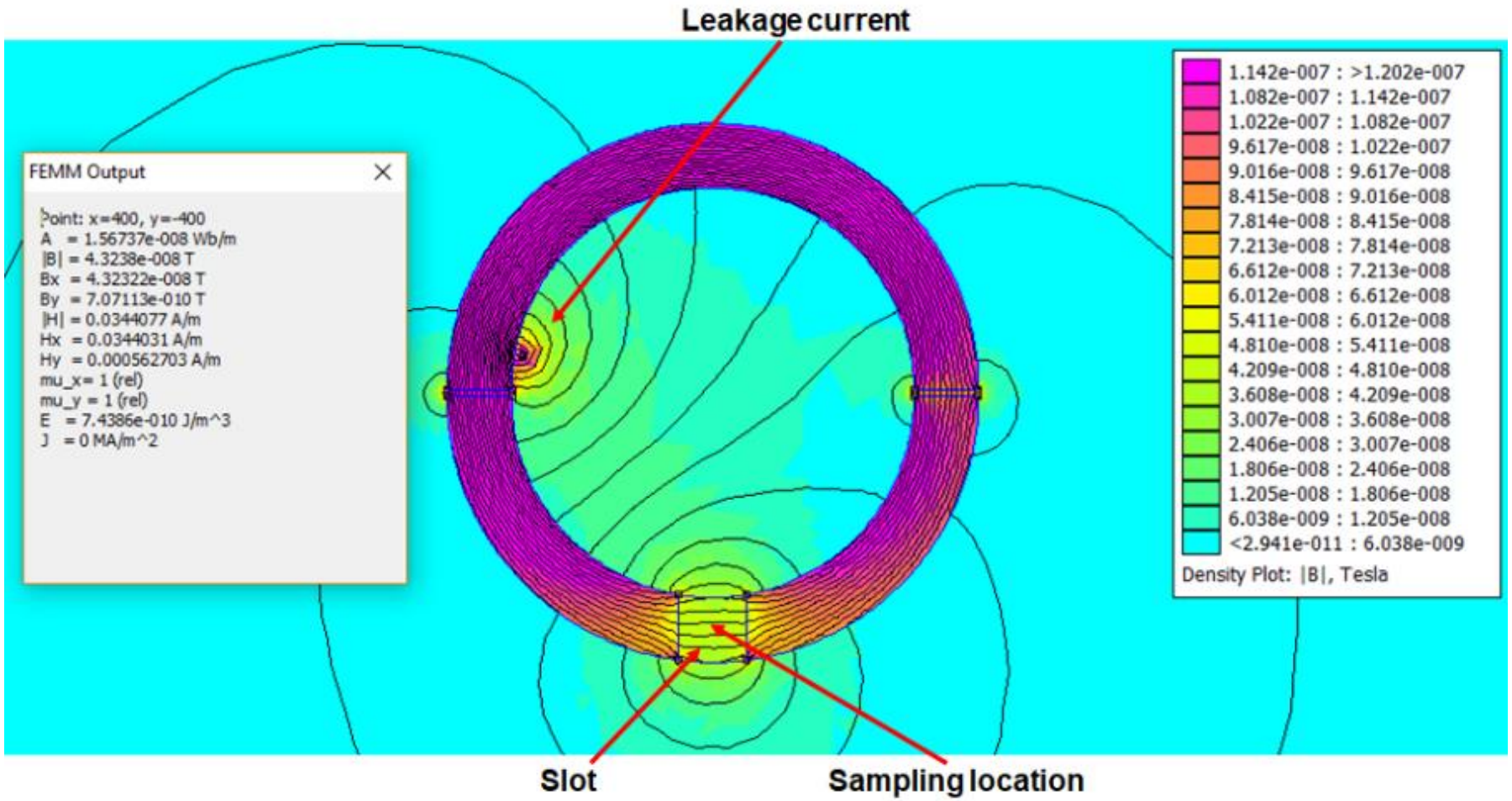

Figure 4.15: Simulated magnetic field distribution for a 10 mA line current positioned to the left of the core opening

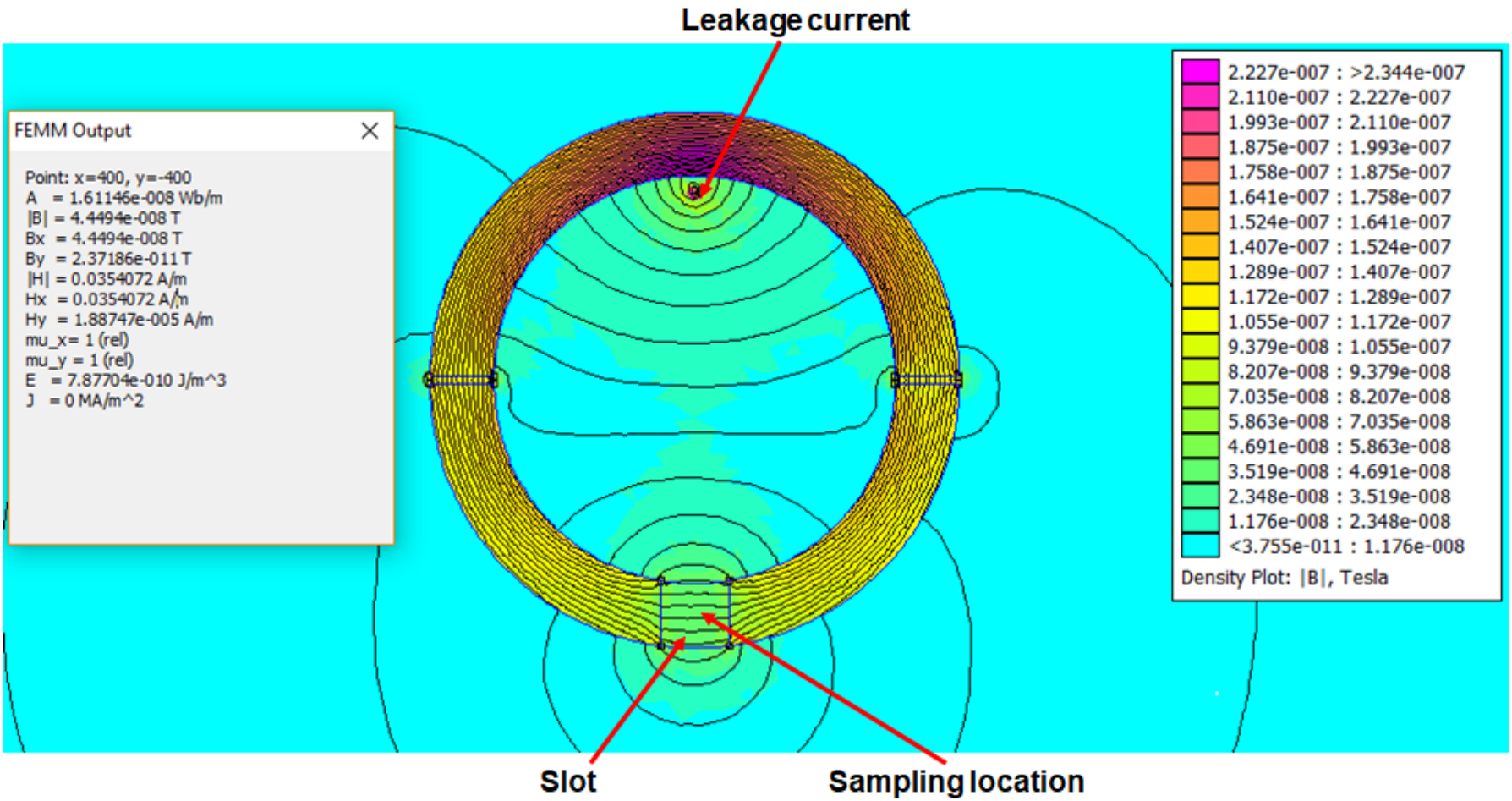

Figure 4.16: Simulated magnetic field distribution for a 10 mA line current positioned to the top of the core opening

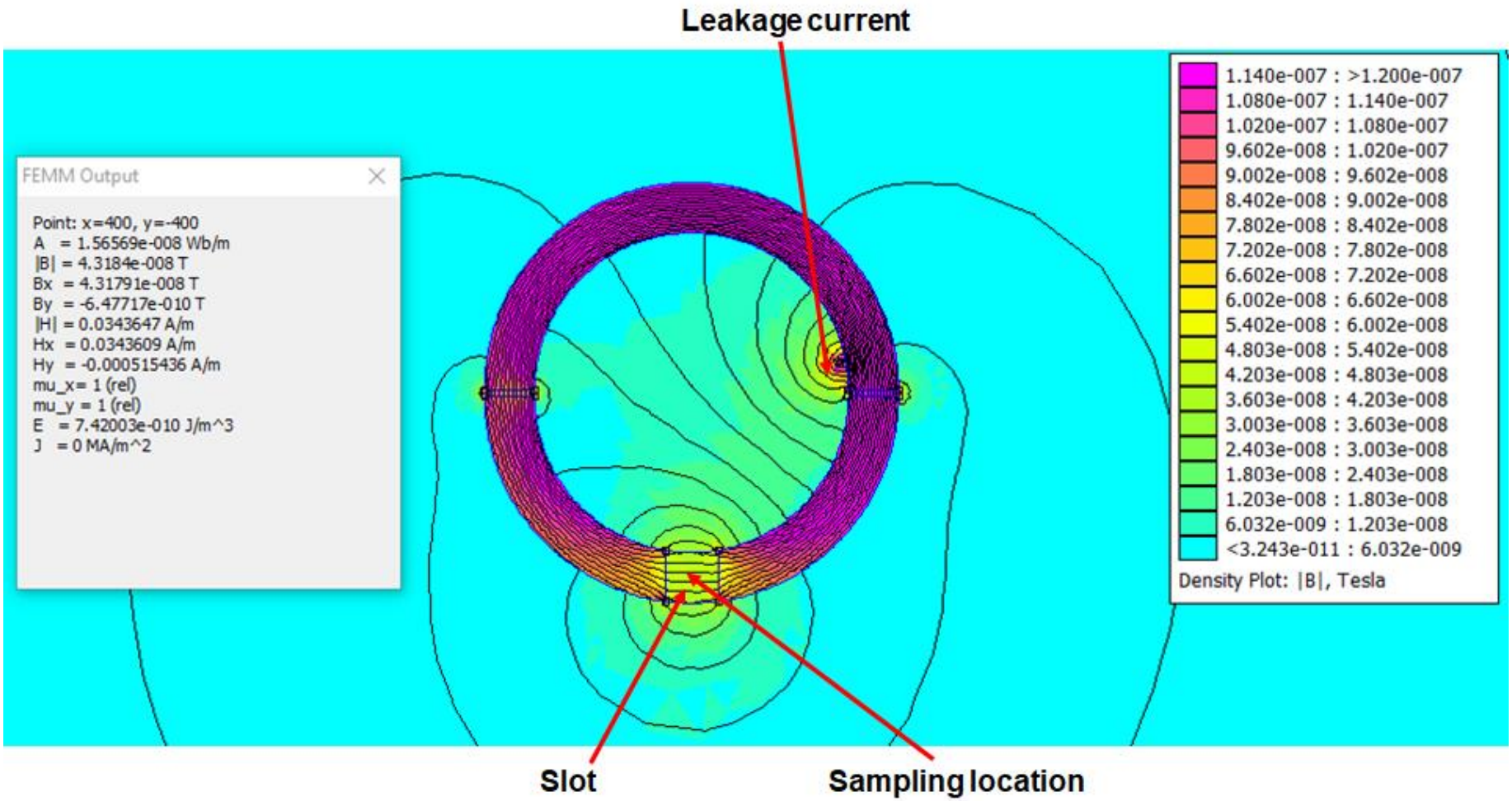

Figure 4.17: Simulated magnetic field distribution for a 10 mA line current positioned to the right of the core opening

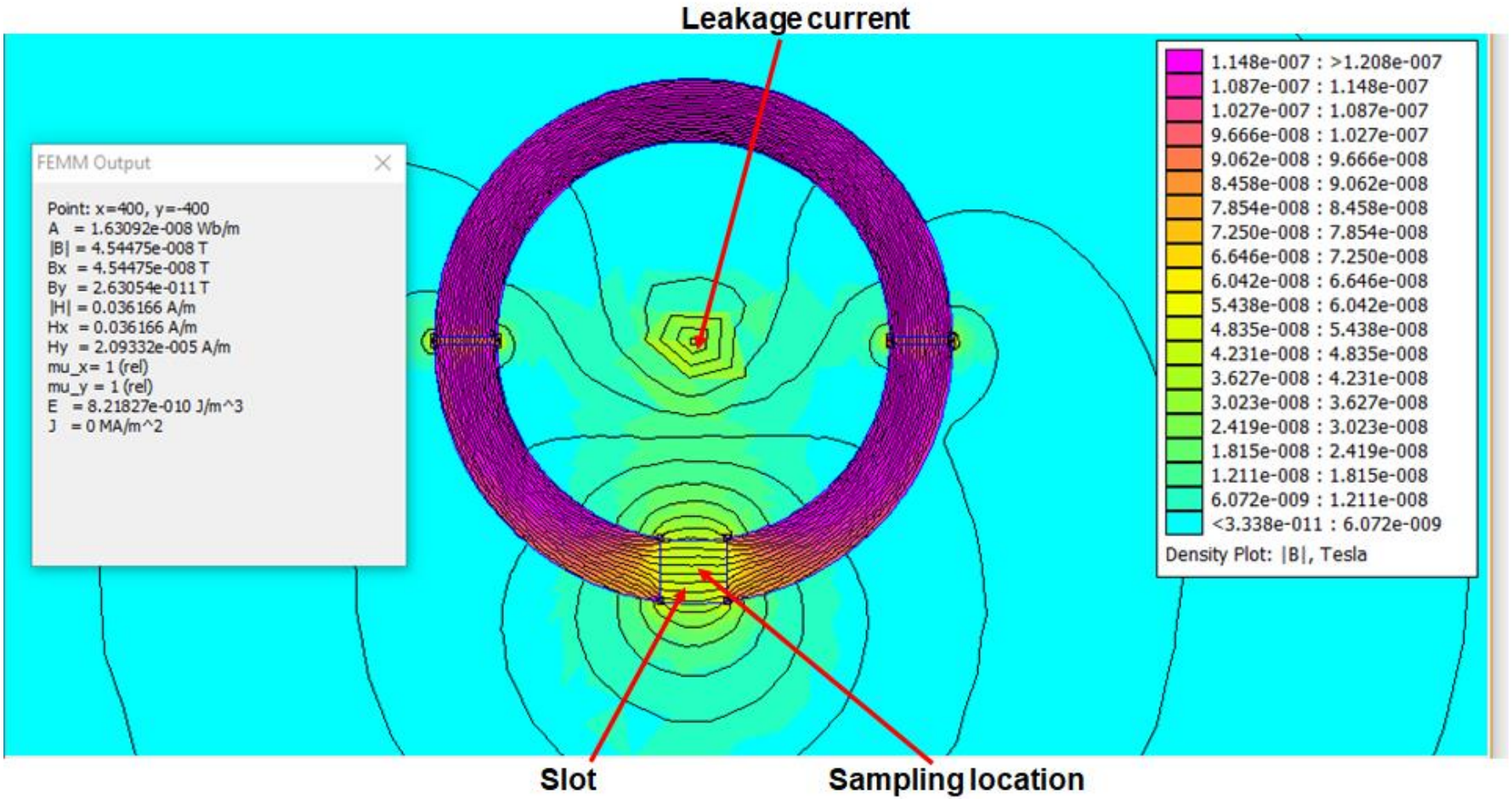

Figure 4.18: Simulated magnetic field distribution for a 10 mA line current positioned at the centre of the core opening

4.5.2.2 Increased measurement sensitivity

Simulations have also been performed to observe what the magnetic field reading would be without the core if a line current (representing LC) was still applied close to the sensor. The magnetic field is sampled at the same position where the slot in the core would have been.

Figure 4.19 shows the simulated magnetic field distribution. It is observed from Figure 4.18 and Figure 4.19 that the magnetic flux density is an order of magnitude lower than for the case of LC within the opening of a core (3.46 nT without the core as opposed to 45.45 nT with the core).

The core, therefore, has the added advantage of increasing the sensitivity of LC measurements.

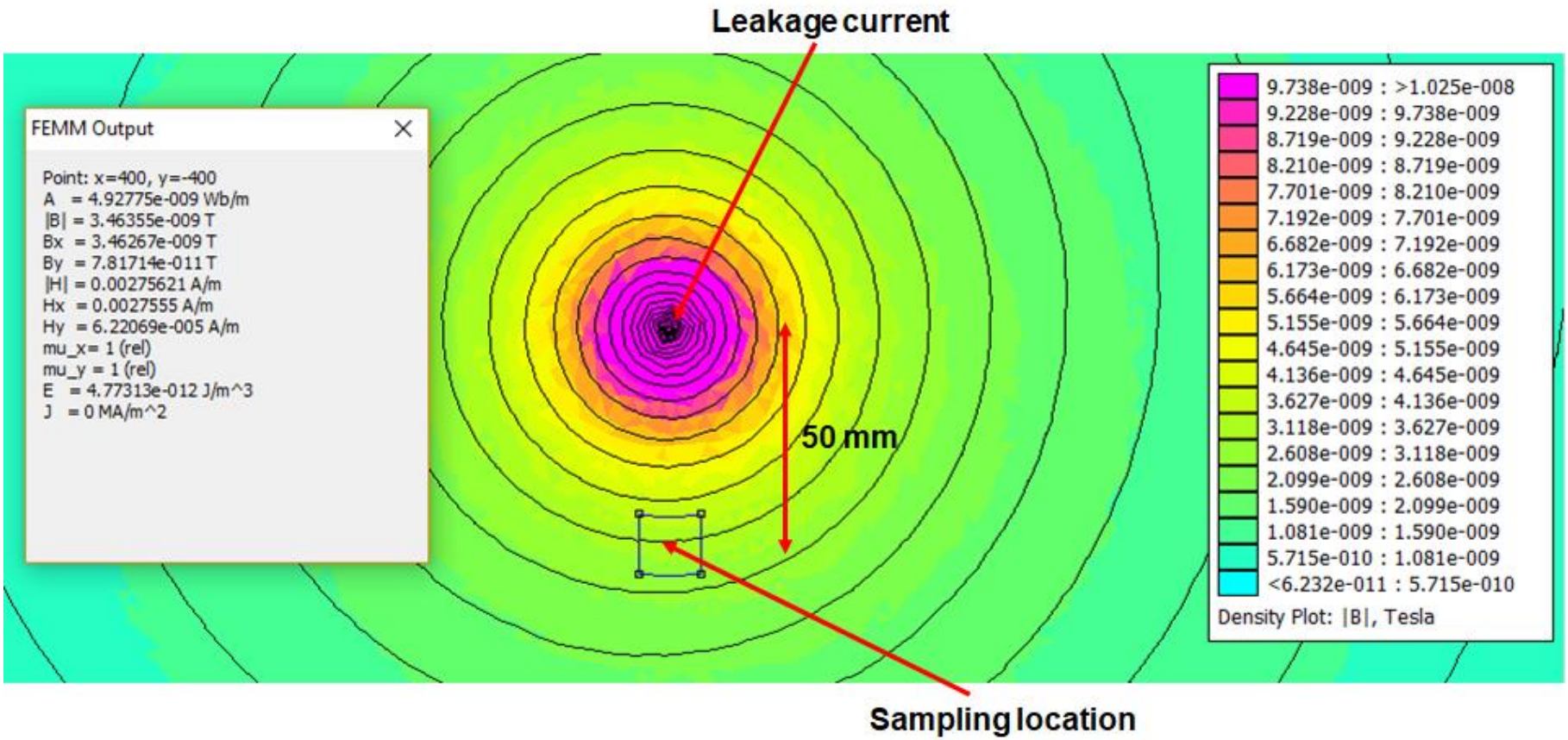

Figure 4.19: Simulated magnetic field distribution in the absence of a core for a 10 mA LC positioned at the centre of where the core would have been (50 mm from the sensor)

4.5.2.3 Shielding of external magnetic fields

Another advantage of the core is that it also provides shielding from external and ambient magnetic fields to a certain extent. Magnetic field simulations of the Cahora Bassa line current and insulator LC have been performed to determine the magnetic field strength that the sensor will experience when placed in the slot of the core.

The core fitted around the insulator can be assumed to be in the plane of the magnetic field lines of the line current (as seen in Figure 4.20). The magnetic field across the 25 mm height of the core can be approximated as being uniform. Therefore, for simulation purposes, the core can be placed in a uniform magnetic field with the same value as that created by the line current in the vicinity of the core. Applying Ampère's Law, the magnetic flux density is approximately 90 µT at a distance of 4 m away from the line current, which is approximately the separation between the line current and LC sensor in practice. Using the FEMM simulation software, the uniform field was created through placing the core in the centre of a solenoid, as shown in Figure 4.21 (solenoid not shown). In this case, the position of the slot is assumed to be perpendicular to the direction of the main line current. The magnetic flux density in the slot is approximately 17.01 µT.

Another simulation was also carried out with the position of the slot *aligned* with the direction of the line current. Figure 4.22 shows that in this case the magnetic flux density in the slot is approximately 1.32 µT. These simulation results show that the core provides some magnetic field screening of the sensor, reducing the measured field at the position of the sensor from 90 µT without the core to 17.01 µT and 1.32 µT, respectively for the cases presented in Figure 4.21and Figure 4.22. The best screening is evidently with the slot positioned in the same direction of the main line current.

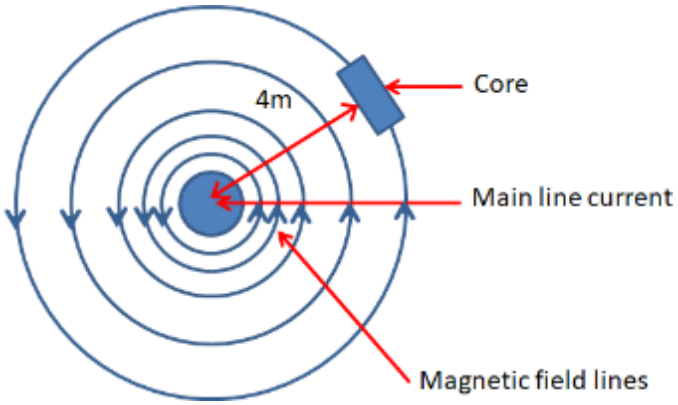

Figure 4.20: Magnetic field distribution of a 1800 A line current at a distance of 4 m away from the core

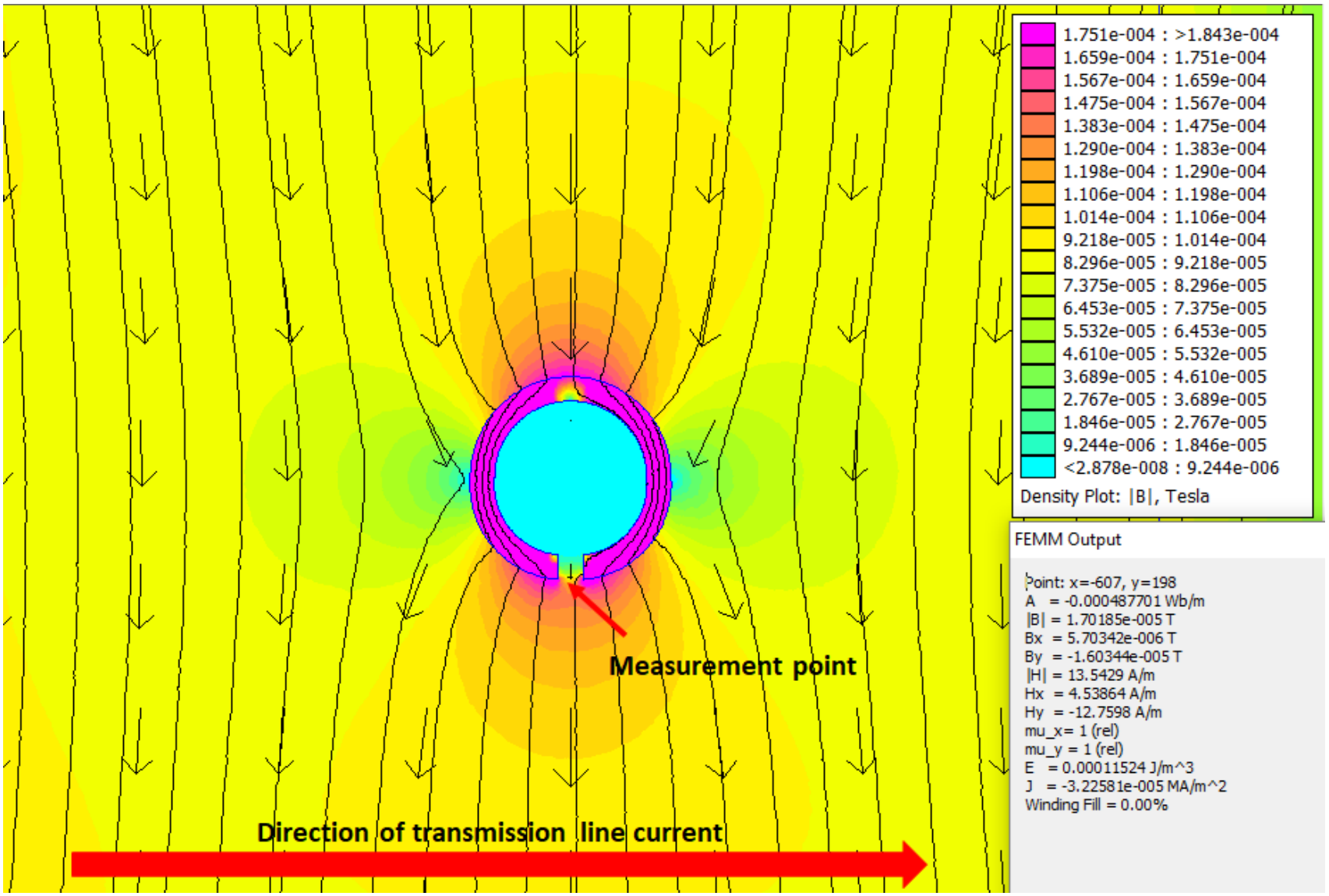

Figure 4.21: Simulated magnetic field distribution in the centre of the slot in the presence of an infinitely long 1800 A line current that is approximately 4 m away from the sampling location and with the slot positioned perpendicular to the direction of the line current

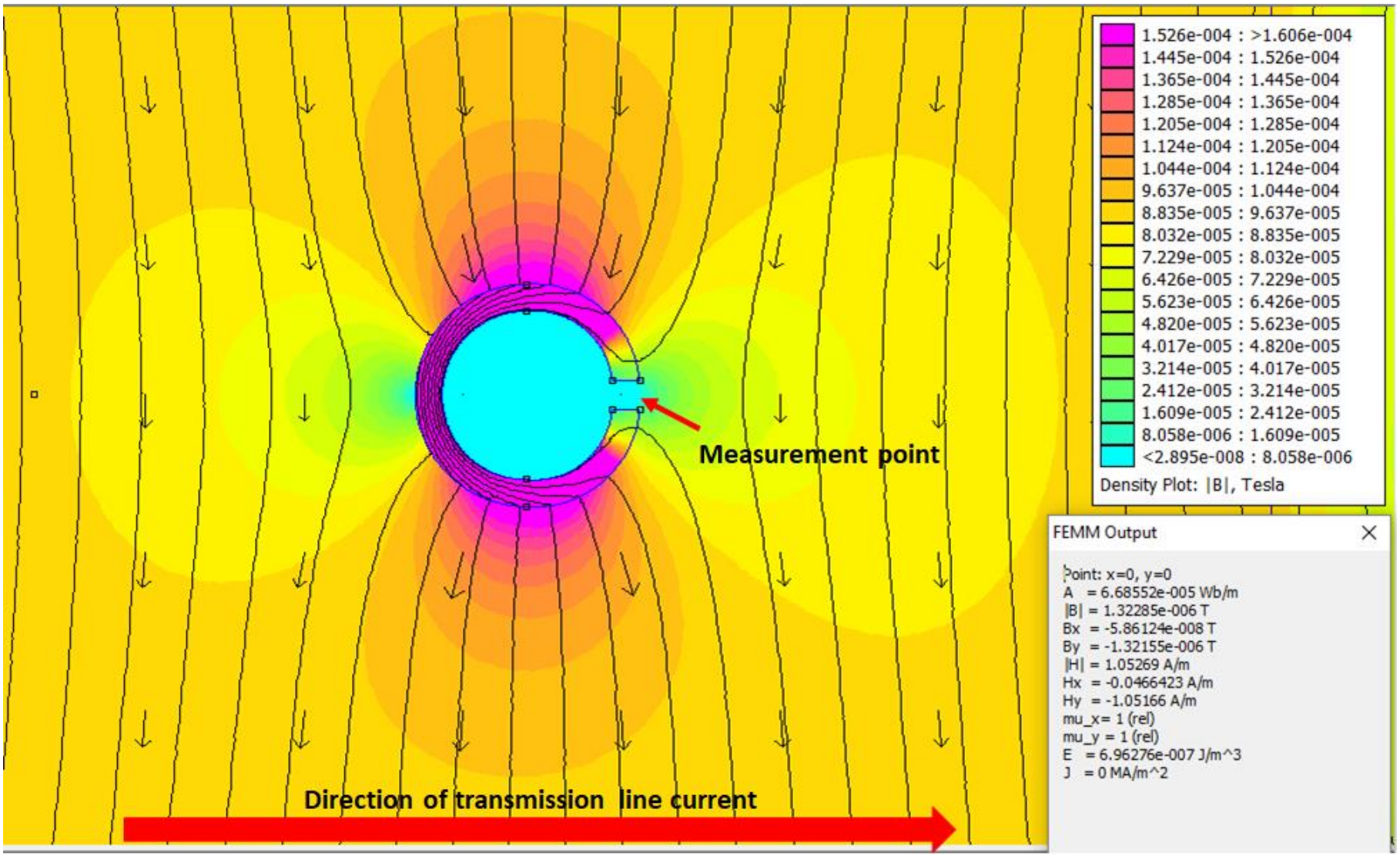

Figure 4.22: Simulated magnetic field distribution in the centre of the slot in the presence of an infinitely long 1800 A line current that is approximately 4 m away from the sampling location and with the slot positioned along the direction of the line current

4.5.3 Dual core sensor prototype

LC measurements have been performed with the LCPR1 sensor and the results are discussed in detail in Chapter 5. Studying those LC measurements, it is evident that the prototype sensor can indeed measure LC to the prescribed levels. However, since it is based on a magnetometer, it is influenced by the presence of ambient magnetic fields. It is also evident from the simulations presented in Section 4.5.2.3 that the single core does not provide sufficient screening of the sensor from the ambient magnetic fields. Thus, the single core configuration of the prototype is not suitable for in-situ measurements on energised insulators.

A *differential magnetometer method* (DMM) has been implemented to mitigate the effect of external fields (Matandirotya *et al*., 2014). This method requires two dc LC sensors, both measuring the ambient magnetic field. However, one sensor will be clamped around the insulator or current carrying wire, and it will measure the fields of both the LC and the external ambient fields. The two sensors' outputs will be subtracted to remove the effect of the ambient magnetic field, leaving only the contribution of the actual LC from the insulator. The initial singe core LC prototype (LCPR1) sensor configuration and the new dual core configuration (LCPR2) using the DMM are shown in Figure 4.23 and Figure 4.24, respectively. The signal conditioning circuitry has been adapted and shown in Figure 4.25. Pin "Out3" is the differential output with the ambient field cancelled.

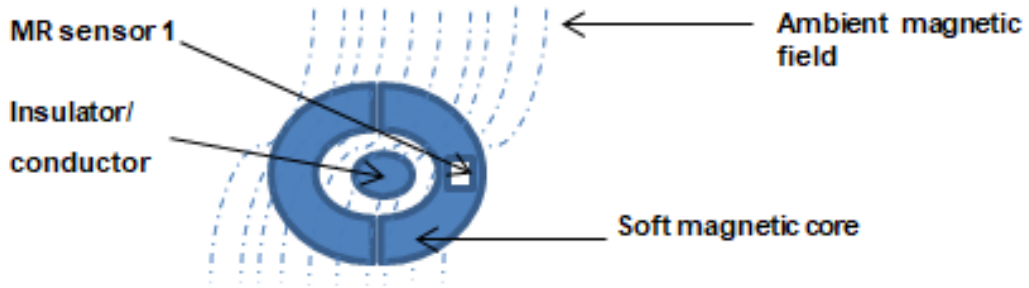

Figure 4.23: Single magnetometer configuration to detect LC (LCPR1)

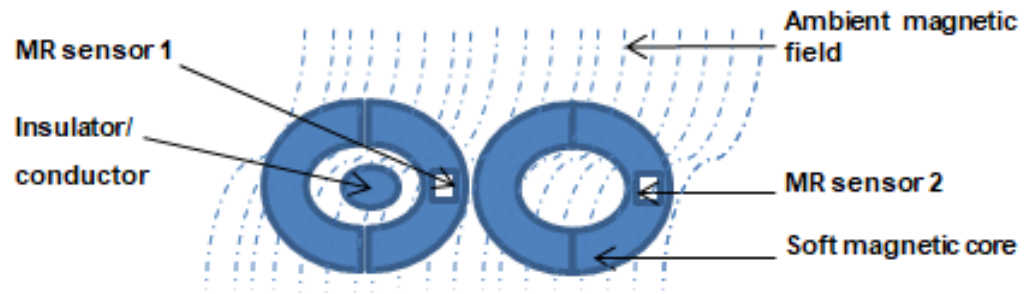

Figure 4.24: Differential magnetometer configuration to detect LC (LCPR2)

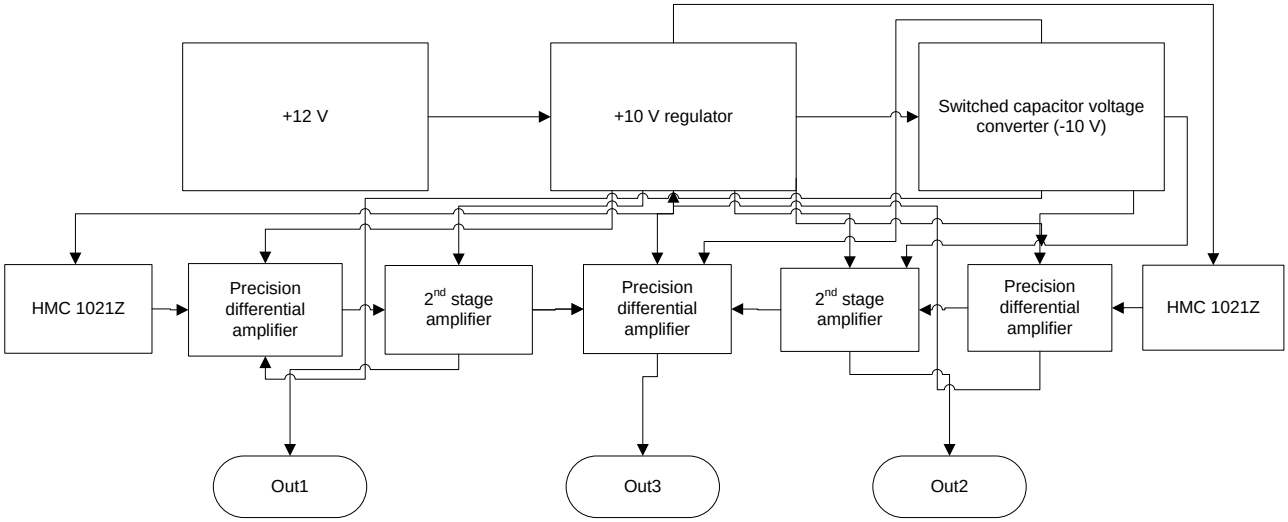

Figure 4.25: Block diagram of LCPR2 signal conditioning circuitry

Since the prototype needs to perform in-situ LC measurements on energised insulators, a clamp has been designed for it. Figure 4.26 and Figure 4.27 show the CAD model and the physical LCPR2, respectively. The circuitry has been designed to fit on the circumference of the core that measures only the ambient field (the core that remains closed).

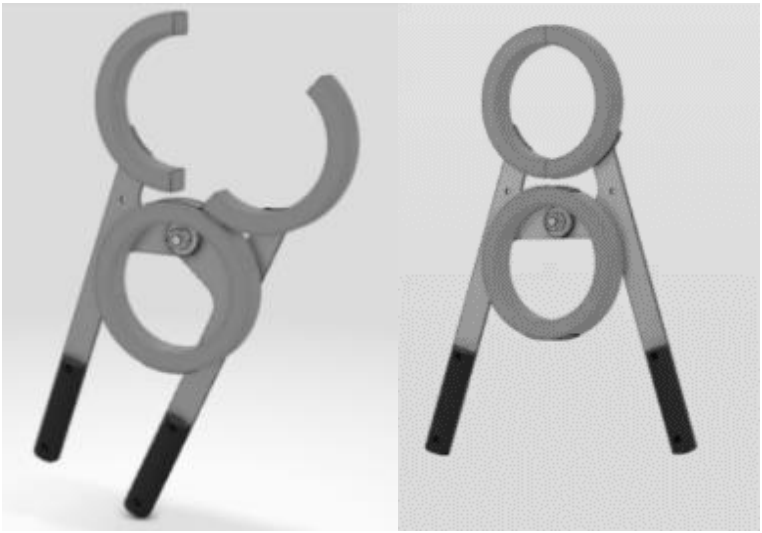

Figure 4.26: CAD model of LCPR2 sensor

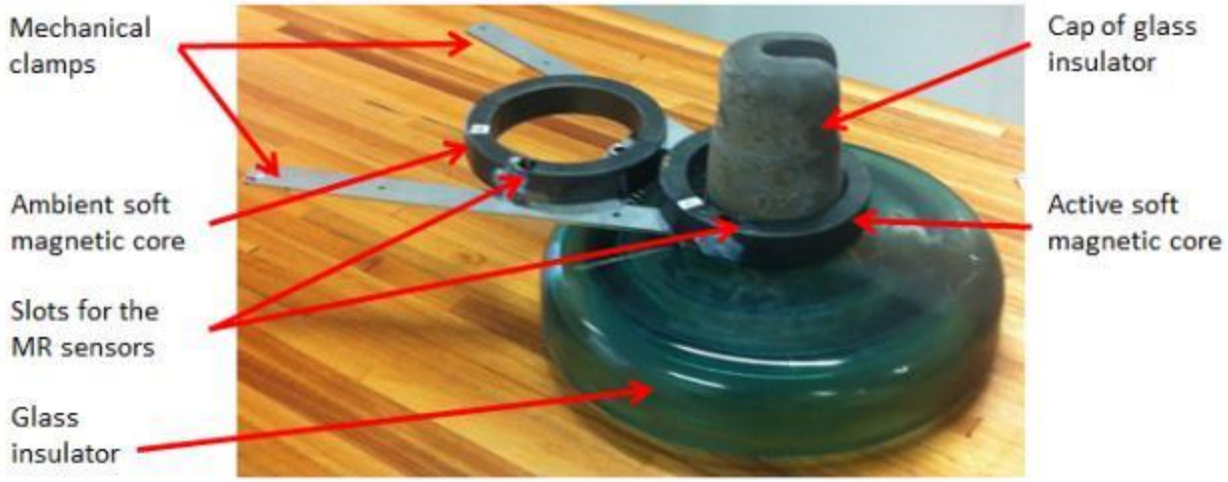

Figure 4.27: LCPR2 sensor with its mechanical clamps around a glass insulator

4.5.4 Calibration of the dual core sensor prototype

The LCPR2 sensor requires calibration in the presence of external magnetic fields that are equivalent to those that will be experienced in the Cahora Bassa scheme before in-situ measurements can be performed on the energised insulators. The magnetic field environment around the Cahora Bassa transmission has been simulated in Section 4.5.2. It has been calculated that the magnetic field from the 1800 A line current is approximately 90 µT at 4 m distance from the line where the sensor will be placed, which is similar in order to that of the magnetic field of the Earth (around 60 µT). The magnetic field from the LC is, however, orders of magnitude smaller than the main line and the Earth's magnetic field as observed in Section 4.5.2. Thus, the sensor needs to be calibrated in these magnitudes of magnetic fields to prove that it will still provide reliable measurements in such an environment.

For laboratory tests and measurements, a Helmholtz coil (Griffiths, 2008) is used to mimic the ambient magnetic field that will be experienced by the sensor. A Helmholtz coil produces a near uniform and controlled magnetic field in the centre of its working volume and it will be used to mimic the environmental magnetic field that the LCPR2 sensor will be exposed to. The Helmholtz coil's axes have different lengths so that it can fit into each other. Thus, it requires different current inputs to generate the same magnetic field. A magnetic field can be generated by applying a known current through the Helmholtz coils.

4.5.4.1 Calibration of LCPR2 sensor at CPUT

A 3-axis Helmholtz coil with a 1 m^3 working volume located at CPUT has been used as a calibration instrument. A 3-axis LEMI-011B fluxgate magnetometer was used to calibrate the

Helmholtz coil system. A B-I curve was created by applying a known current through the Helmholtz coil and then measuring the associated magnetic field with the LEMI-011B fluxgate magnetometer.

The schematic representation of the Helmholtz coil calibration system using the LEMI-011B fluxgate magnetometer is shown in Figure 4.28. Figure 4.29 shows the actual LEMI-011B fluxgate magnetometer in the centre of the Helmholtz coil.

The measured B-I curve of the coil systems is presented in Figure 4.30. This B-I curve has been used to calibrate the LCPR2 in the Helmholtz coil.

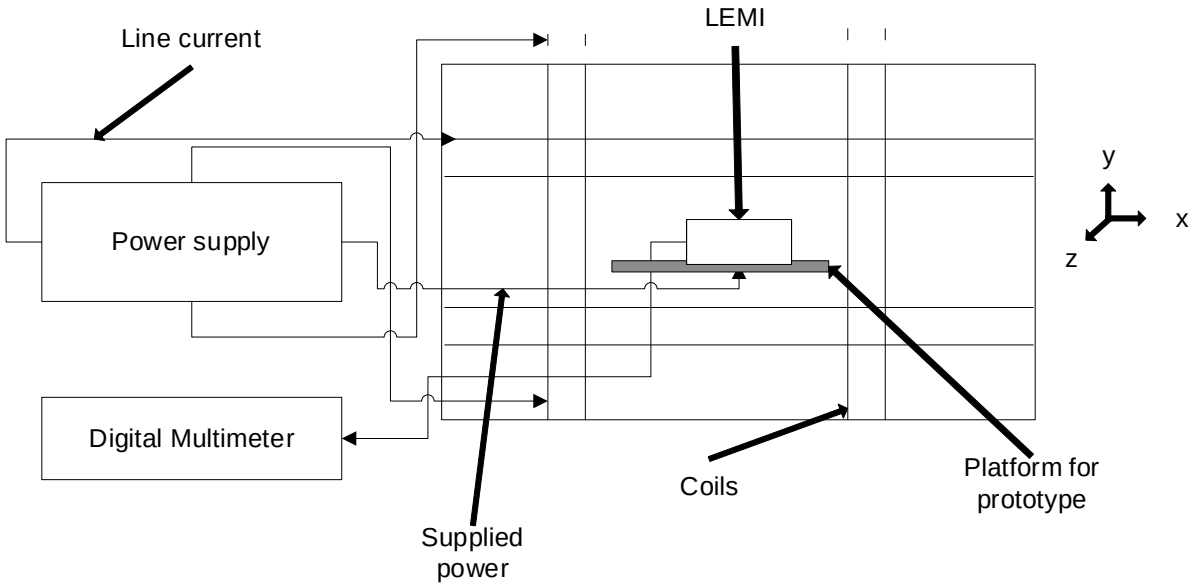

Figure 4.28: Diagram of a Helmholtz coil system using a LEMI fluxgate magnetometer as a calibration mechanism

Figure 4.29: LEMI-011B fluxgate magnetometer inside Helmholtz coil at CPUT

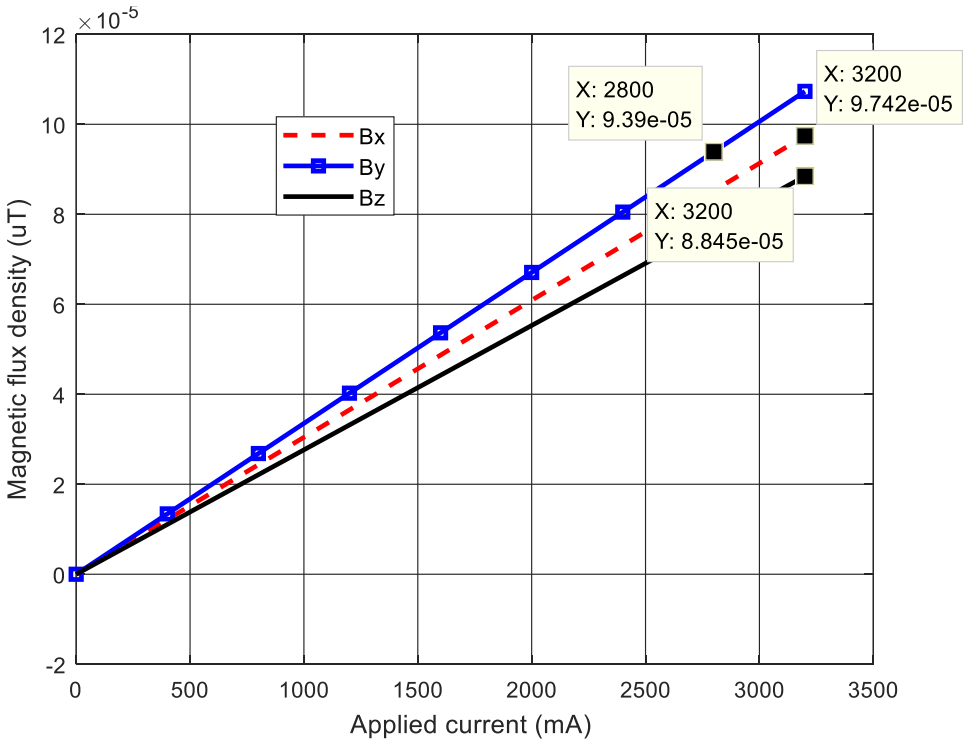

Figure 4.30: Generated B-I curve of CPUT Helmholtz coil using LEMI-011B fluxgate magnetometer

A field of 90 µT is required to be generated as this is the magnitude of the magnetic field that the LCPR2 sensor will be exposed to during LC measurements in the field at the Cahora Bassa HVDC transmission line, as determined with the simulations in Section 4.5.2. Using the generated B-I curves for the Helmholtz coil, the LCPR2 sensor is now calibrated. The sensor is placed inside the working volume as shown in Figure 4.31. Figure 4.32 through Figure 4.34 show the calibration curves of the prototype sensor for the X-, Y- and Z- axes, respectively. In these figures, S_a is the sensor that measures only the ambient magnetic field, while S_m measures the ambient magnetic field and the magnetic field associated with an insulator's LC as previously shown in Figure 4.24.

These measurements show that the prototype's two sensor outputs are very similar when it is exposed to the same 3-dimensional magnetic field. The average error obtained, using Equation 4.1, between the two sensor outputs for the X-, Y- and Z-axis was 0.15%, 3.59% and 38.8%, respectively. This will allow for a zero-offset reading in the presence of an ambient field when these two outputs are fed through the final differential amplifier stage. The offset in the Z-axis calibration can be attributed to a slight offset in height between the two soft magnetic cores. However, when performing insulator LC measurements, a magnetic field in the Z-axis will not exist (and thus, inconsequential) because it will be in the same direction as the current to be measured.

Figure 4.31: LCPR2 sensor placed around an insulator inside the Helmholtz coil at CPUT

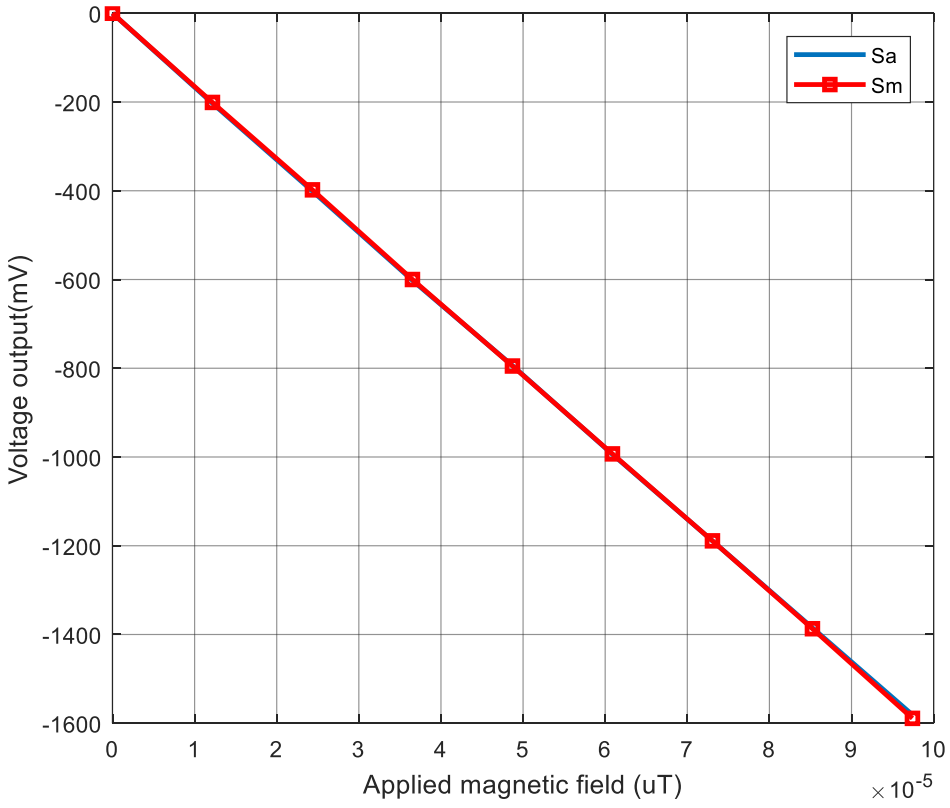

Figure 4.32: Calibration curve of LCPR2 in the X-axis

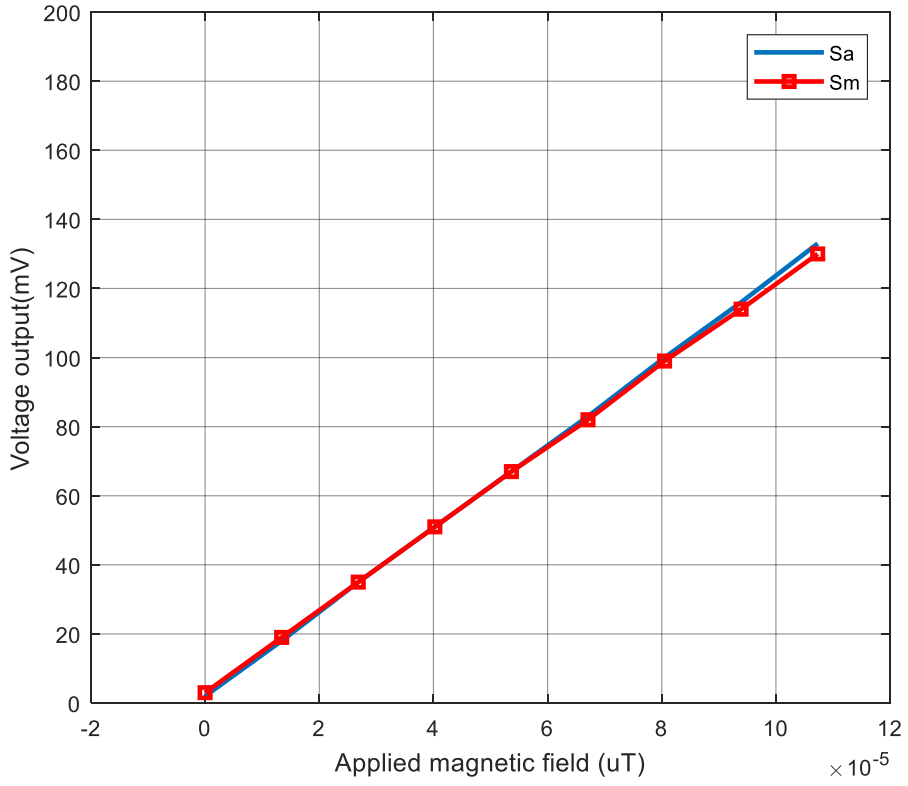

Figure 4.33: Calibration curve of LCPR2 in the Y-axis

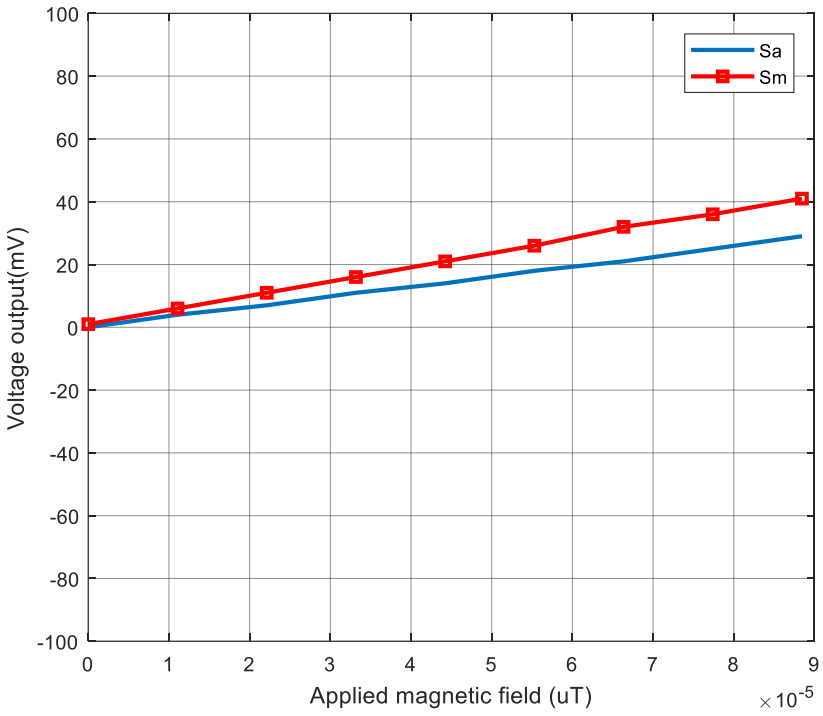

Figure 4.34: Calibration curve of LCPR2 in the Z-axis

4.5.4.2 Calibration of LCPR2 sensor at SANSA

The LCPR2 sensor has subsequently been validated at the South African National Space Agency's (SANSA's) Helmholtz coil facility, which is certified. The same procedure followed at CPUT has been applied in SANSA's Helmholtz coil. Figure 4.35 shows the user software interface to control the magnetic field within the SANSA Helmholtz coil (in this case it shows how much current is required in each coil to generate a 10 µT field in the X-axis). Figure 4.36 shows the LCPR2 within the Helmholtz coil.

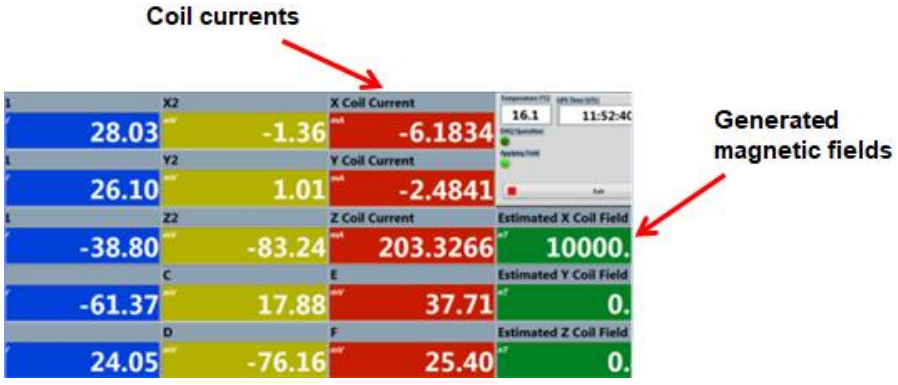

Figure 4.35: SANSA's software interface controlling the magnetic field inside the Helmholtz coil (showing a 10 µT field in the X-axis)

Figure 4.36: LCPR2 sensor placed within the working volume of the SANSA's Helmholtz coil

4.5.4.3 Linearity measurements at SANSA

A linearity test has been performed to generate the prototype's V-I curve whilst in the presence of 70 µT magnetic field (the highest magnetic field that could be generated by this Helmholtz coil) that is generated by the SANSA Helmholtz coil in the X, Y and Z directions simultaneously. A current carrying wire is passed through the LCPR2 sensor as shown in Figure 4.37 and the current stepped in increments of 10 mA from 0 - 200 mA. The measurement results are presented in Figure 4.38 when measuring a current through a current carrying wire and insulator in the presence of a 70 µT magnetic field. Applying Equation 4.1, the calculated average error when measuring the current through the insulator and current carrying wire using the LCPR2 is 0.77% and 2.38%, respectively. The measured sensitivity of the LCPR2 sensor is ~ 4.5 mV/mA, which can be adjusted.

Figure 4.37: Current carrying wire passed through the LCPR2 for linearity tests

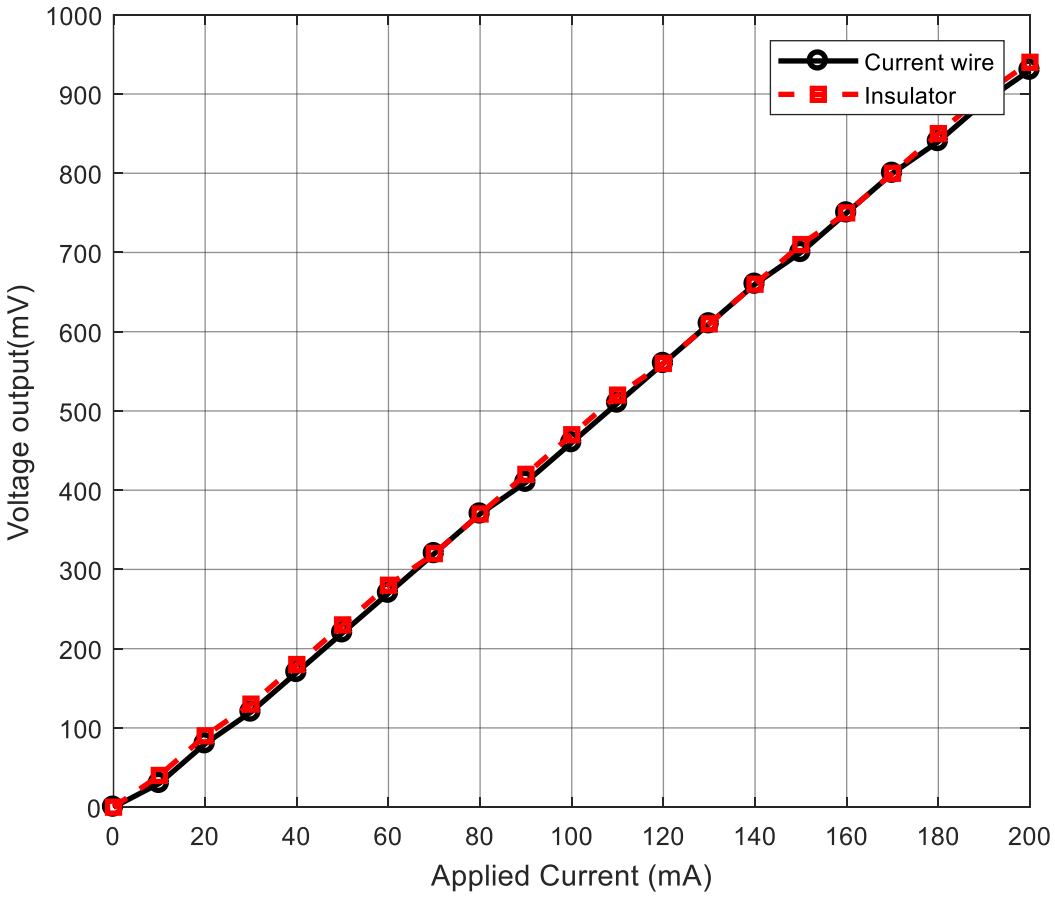

Figure 4.38: dc LC measurement results for the LCPR2 sensor

4.6 Conclusion

This chapter investigated different sensors for the in-situ, non-intrusive monitoring of LCs on insulators of HVDC transmission lines. All the sensors exhibited good linearity, sensitivity and accuracy across the range of 0 - 100 mA. However, the LEMI fluxgate magnetometer and the COTS dc sensor are not appropriate for in-situ insulator LC monitoring. Thus, a new LC prototype sensor has been developed, which makes use of magnetic cores and MR sensors. This prototype is based on magnetic field sensing and has been calibrated within a Helmholtz coil at CPUT and validated at SANSA. The calibration results at CPUT and SANSA are in agreement. Simulations have also been performed, which show that the core traps magnetic fields emanating from an insulator under test and mitigates external magnetic fields to a certain extent. If a core is not used, the measured insulator LC may be erroneous. The developed prototype has good linearity and a sensitivity of ~4.5 mV/mA, which can be adjusted. The measurement results also showed that the ambient magnetic fields that the prototype will be exposed to are sufficiently supressed while LC measurements were being performed through a current carrying wire and insulator.

5: HVDC INSULATOR LC STUDIES PERFORMED AT A CORONA CAGE

5.1 Introduction

Various sensor prototypes have been reported in Chapter 4 as possible LC sensors for HVDC insulators. This chapter covers the HVDC insulator LC measurements performed with the single core LCPR1 sensor at the Eskom corona cage high voltage testing facility to verify if it can detect LC on an energised insulator. LC measurements have only been performed on glass insulators in this chapter since most faults reported on the Cahora Bassa transmission line have been linked to them. Two case studies are reported, namely to determine the relationship between current and increased pollution layer conductivity, and to determine the probability of flashover occurring as a function of LC at a constant ESDD level of 0.03 mg/cm^3. These case studies have been performed to obtain a better understanding of how contamination influences the LC levels on HVDC insulators, especially glass insulators, as these LC tests are the precursors to the field tests on the Cahora Bassa HVDC line described in Chapter 6.

5.2 Initial LC measurements with the LCPR1 sensor

5.2.1 Determining the V-I curve of the LCPR1 and shunt resistor setup

Calibration of the LCPR1 sensor is performed against a 10 Ω, 5 W shunt resistor reference measurement. The schematic diagram of the setup is shown in Figure 5.1. To ensure the proper functioning of this setup, the relative resistive values of the clean and polluted insulators, and that of the shunt resistor need to be such that the shunt resistor is orders of magnitude *smaller* than both the insulators. This will ensure that (1) any LC flowing through the polluted insulator will be flowing through the shunt resistor, bypassing the clean insulator, and (2) the shunt resistor voltage will be negligible compared to the applied voltage and will have no material influence on the voltage applied to the polluted insulator (which will effectively be the same as the applied high voltage supply). The shunt resistor is indeed orders of magnitude smaller than that of both insulators. In Section 3.4.5, it was shown that the LC flowing in a similar insulator energised with a 33 kV source, and polluted with a 0,07 S/m layer, is of the order 5.6 mA for a layer thickness of 0,002 mm. This translates into an effective resistance of 5.8 MΩ. The resistance of the clean insulator is of course orders of magnitude larger than this due to the absence of a conduction layer. It can be noted that in this setup, the clean insulator may even conduct LC due to residual contamination during the experiments, but that this will not influence the results due to the much smaller shunt resistor that will effectively bypass all LC from that insulator.

Calibration entails adjusting the sensor's voltage offset to zero and its output voltage to be the same as the shunt resistor when injecting a current on the insulator under test.

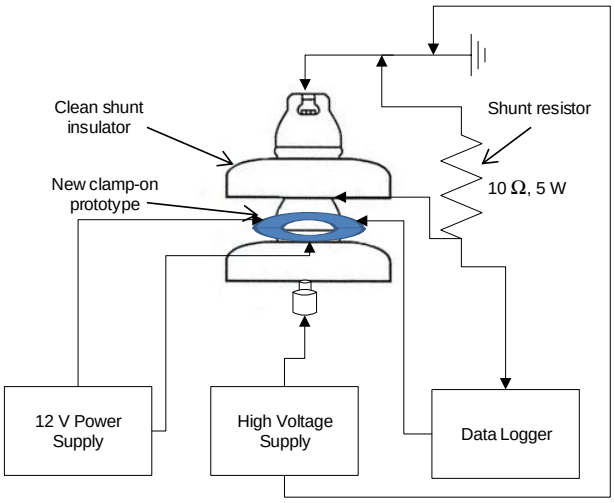

Figure 5.1: Schematic diagram of leakage current measurement setup at Eskom's corona cage high voltage test facility

Figure 5.2 shows the physical test setup at the corona cage test facility. Figure 5.3 shows the LCPR1 sensor clamped around a test glass insulator. A known current (low voltage) is injected through the insulator setup to determine the V-I curves of the LCPR1 sensor and shunt resistor. This is performed by connecting a wire from the cap to the pin of the insulator (creating a short circuit of the glass area of the insulator disc). The shunt resistor is used with a clean (unpolluted) stand-off glass insulator to ensure that most of the LC will be 'directed' into the shunt resistor. A stand-off insulator typically supports a conductor at a distance from the surface, or substrate, to which it is attached. In this case, it actually provides support for the polluted insulator in the test setup. The LCPR1 sensor is covered with aluminium and non-conductive (insulation tape) material to, respectively, protect its electronics from the salt water that will be sprayed and to isolate its enclosure from the insulator's cap (which is conductive).

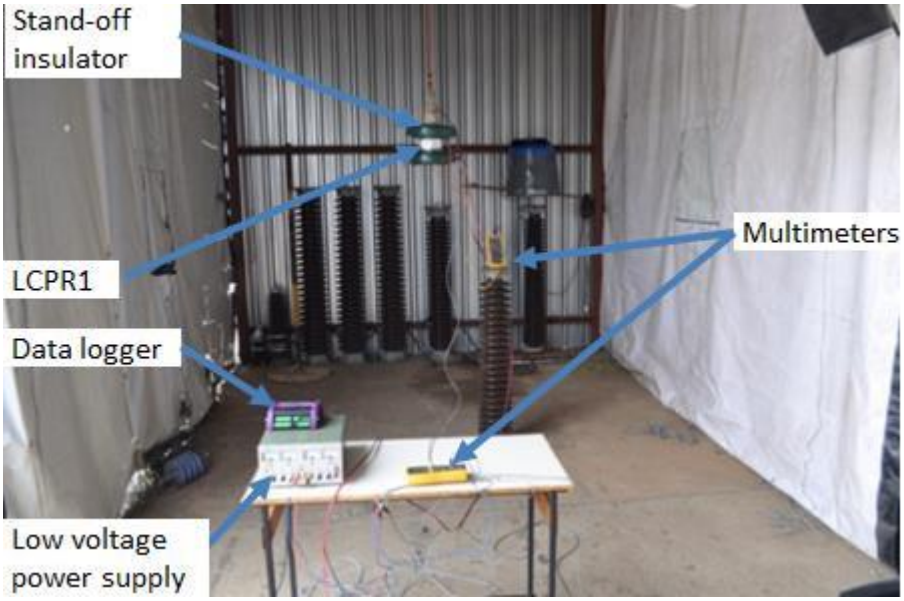

Figure 5.2: Calibration test setup for the LCPR1 sensor and the shunt resistor at the Eskom corona cage high voltage test facility

Figure 5.3: Position of the LCPR1 sensor and shunt resistor in the calibration setup of Figure 5.2

Figure 5.4 shows the measured V-I curves of the LCPR1 sensor and shunt resistor. The measurements show that the LCPR1 sensor is linear over the current range of interest and does not saturate. Applying Equation 4.1, the calculated average error between the LCPR1 sensor and shunt resistor measurements across the full range of measurements is 2.6%. The V-I curves will

be used to determine the actual current that is flowing on the insulator during subsequent HVDC LC tests. The resolution can be adjusted with the electronic conditioning circuitry.

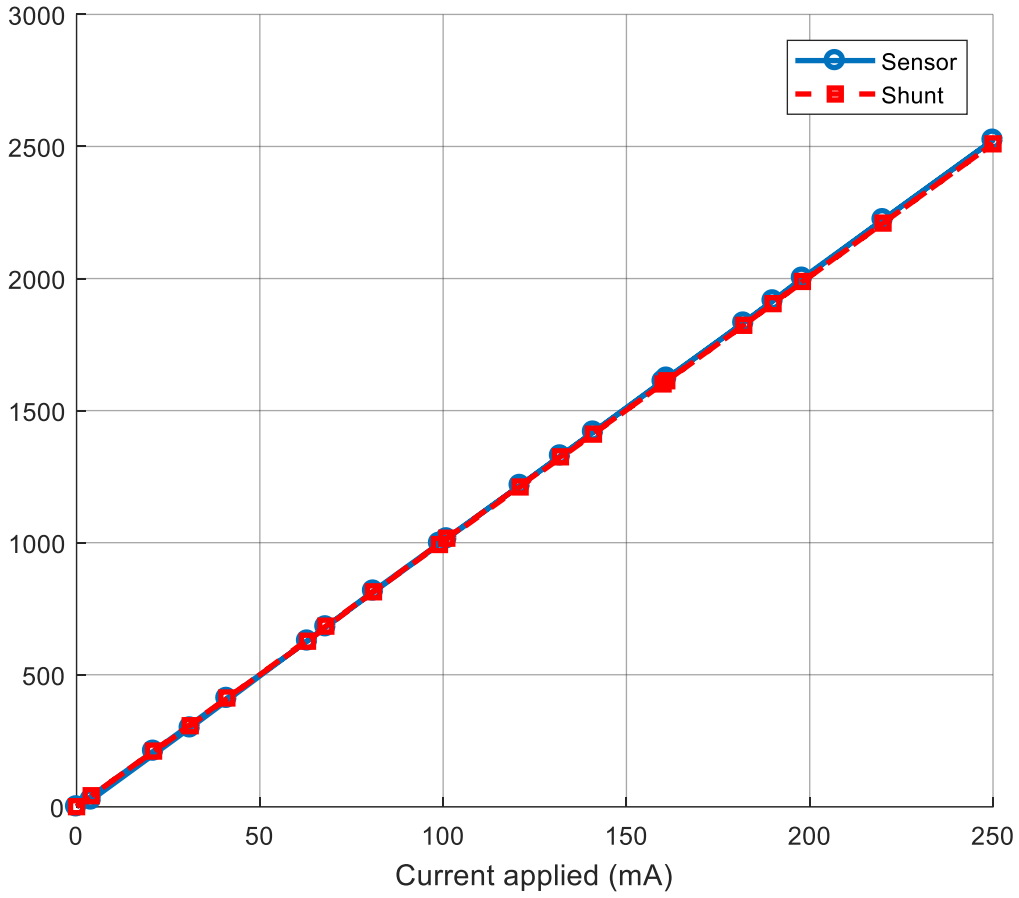

Figure 5.4: V-I curves of LCPR1 sensor and shunt resistor

5.2.2 LC measurements using a high voltage supply

5.2.2.1 Test setup

The test setup schematic is presented in Figure 5.1, and the actual setup illustrated in Figure 5.2 and Figure 5.3. An HVDC power supply with a 12 mA maximum rating (the highest rated current power supply available during tests) is used to generate LC on a polluted insulator after calibrating the LCPR1 sensor. The insulator is sprayed with salt water to aid the flow of LC on the insulator's surface. The unprocessed measurement data is presented in Figure 5.5.

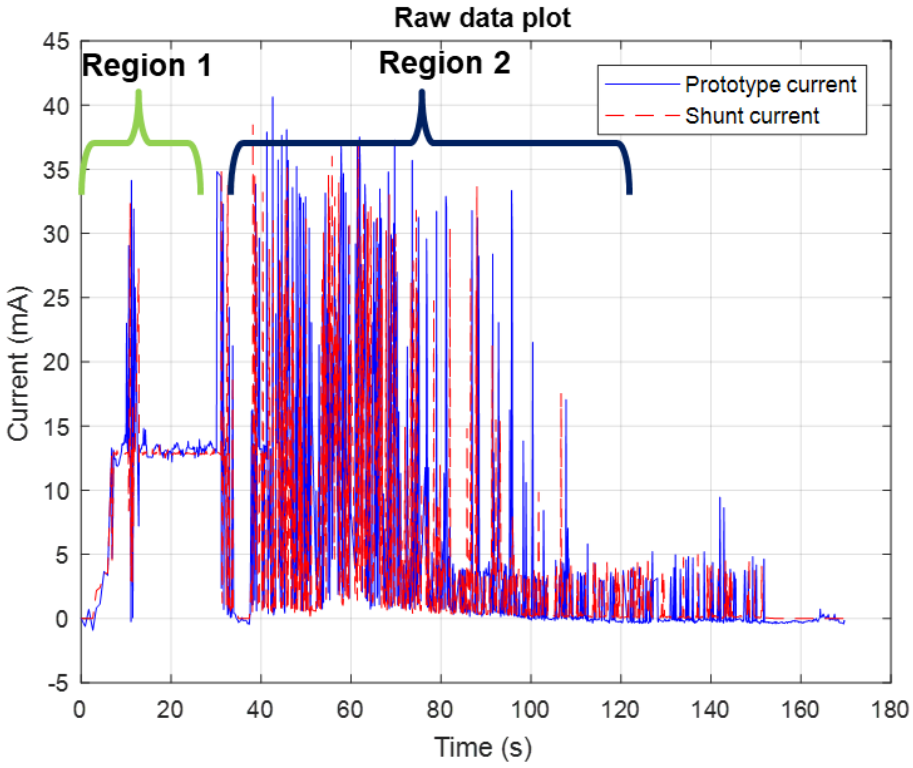

Figure 5.5: Leakage current measurements of the shunt resistor and LCPR1 sensor (100 ms sampling rate)

5.2.2.2 Discussion of results

Due to the nature of the response in Figure 5.5, it can be split into separate regions, namely Region 1 and Region 2.

- **Region 1**

By observing Figure 5.5, Region 1 essentially has a steady linear response, where the LC of the LCPR1 sensor and shunt resistor is similar. Surface arcs develops at 10 s. This data is, however, not included in the linear region plot in Figure 5.6. Figure 5.6 compares the LC measurement of the LCPR1 sensor and the shunt resistor for Region 1. It also shows the scatter plot of these measurements. The first few seconds (~ 7s) in Figure 5.6 can be seen as the charging phase of the insulator as the HV supply is manually increased to the test voltage.

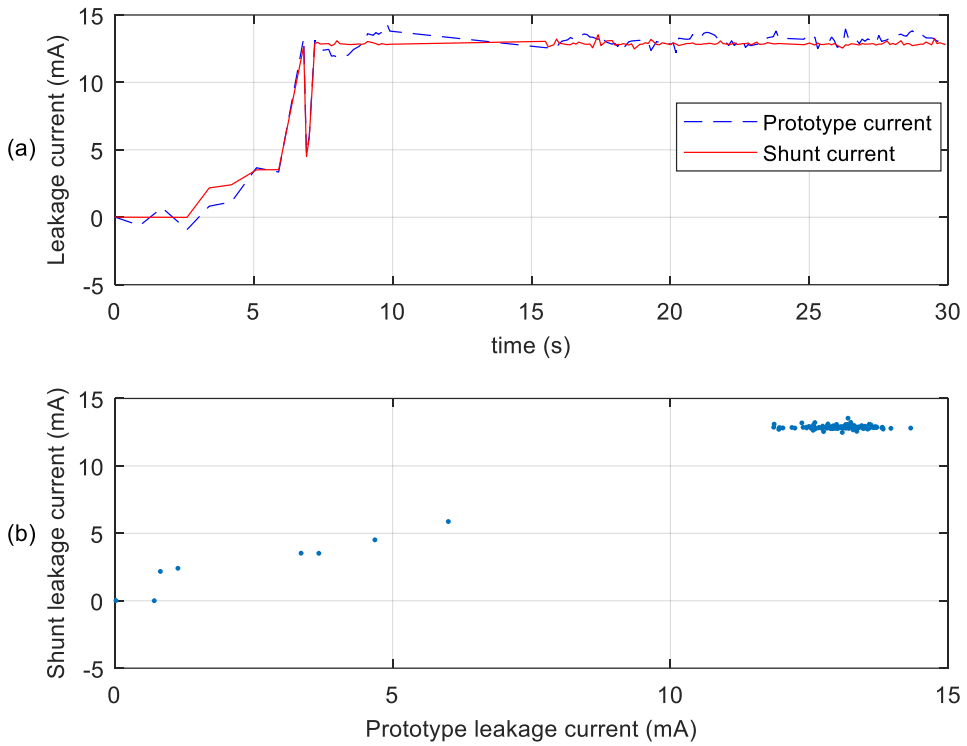

Figure 5.6: (a) Leakage current measurements of the shunt resistor and LCPR1 sensor in Region 1, (b) Scatter plot of measurements presented in (a)

From Figure 5.6 it is evident that the measurements of both sensors are correlated; the calculated correlation coefficient for the two sets, excluding the discharge, is 0.98. The equation for the correlation coefficient of two random variables A (LC in shunt resistor) and B (LC measured by prototype sensor) is shown below:

$$\rho(A,B) = \frac{1}{N-1}\sum_{i=1}^{N}\left(\frac{\overline{A_i - \mu_A}}{\sigma_A}\right)\left(\frac{B_i - \mu_B}{\sigma_B}\right) \qquad \textbf{Equation 5.1}$$

where N is the number of iterations, μ_A and σ_A are the mean value and standard deviation of A, respectively, and μ_B and σ_B are the mean value and standard deviation of B.

In Figure 5.6 (b), a wider spread of LC between 10 mA and 15 mA is observed with the LCPR1 sensor when compared to the shunt resistor's results. Further investigation is required into this aspect. Figure 5.7 shows the histogram of the calculated error differences between the two measurement sets. The error (difference) distribution has an average value and a standard

deviation σ of 0.19 mA and 0.5 mA, respectively. The formula below has been applied to calculate the standard deviation between the two sets of measurements:

$$\sigma = \left(\frac{1}{n-1} \sum_{i=1}^{n} \left(x_i - \bar{x} \right)^2 \right)^{\frac{1}{2}}$$

Equation 5.2

where x is the difference between the LCPR1 sensor and shunt measurement sets.

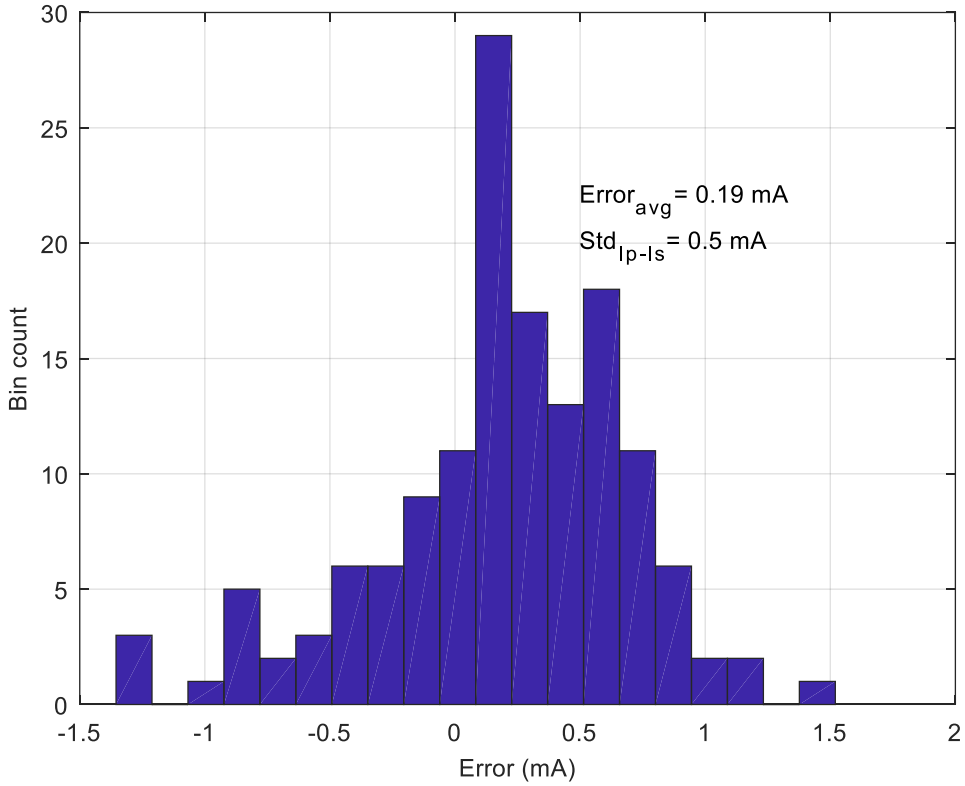

Figure 5.7: Error distribution of leakage current measurements for Region 1

Figure 5.8 displays the arcs that developed during the current measurements on an HVDC glass insulator. It is observed that these arcs are random in nature as stated by Zhicheng & Renyu (1990). Smoke could be seen as well from the energised end, which is caused by the high current density heating of the insulator's surface.

Figure 5.8: Development of surface arcs on glass insulator's surface

- **Region 2**

The measurements in Region 2 of both the shunt and LCPR1 sensor appear to be random, as depicted by the scatter plot in Figure 5.9. The apparent randomness depicted in Figure 5.9 can be ascribed to under-sampling of the data. The observed discharges are current pulses that occur in the millisecond to nanosecond range (Sarkar & Patil, 2014). Consequently, the sampling frequency should conform to Shannon's Theorem. Due to the data logger's limitations, the sampling rate was set at 100 ms, resulting in under-sampling. The relationship between the two sets of measurement therefore also appears random as is evident from the scatter plot. (A straight line with unity gradient would have indicated exact correlation between the two sets.)

In future work, wideband time- and frequency-domain techniques will be investigated to study the partial discharges in more detail as described in Otto & Reader (2010).

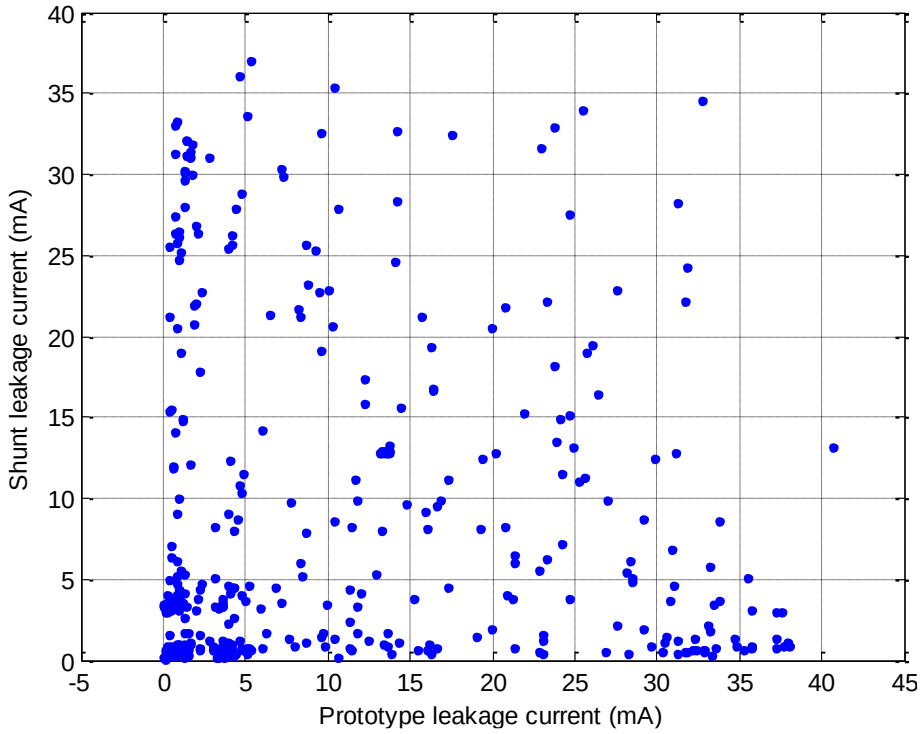

Figure 5.9: Scatter plot of shunt resistor and LCPR1 sensor LC measurements in Region 2

Figure 5.10 shows that the insulation tape, which forms part of the LCPR1 sensor's enclosure, was covered with salt pollution after the tests. This induced salt pollution is a phenomenon that was not anticipated, and that may have affected the results as LC could have flowed on the outside of the LCPR1 sensor. This may have attributed to the LCPR1 sensor having a wider spread in current values compared to that of the shunt as observed in the scatter plot of Figure 5.6 (b).

The contamination of the clean stand-off insulator is also noted. However, as explained in Section 5.2.1, this will not influence the measurements.

Figure 5.10: Leakage current test setup showing the pollution on the outside of the LCPR1 sensor and insulators (with two stand-off insulators) after testing

- **Summary of initial HVDC LC measurements using the LCPR1 sensor**

The initial HVDC LC tests show that the LCPR1 sensor can accurately detect and measure dc LC that is flowing on an insulator's surface even in the presence of discharges. However, for the HV pollution tests (Figure 5.5), differences in the magnitude of the current pulses are noted. These differences can also be attributed to under-sampling of the LC data as discharges can occur in the microsecond range.

5.3 Case studies performed at Eskom's corona cage high voltage test facility

After the successful measurements with the LCPR1 sensor, two case studies have been performed at the corona cage. These studies were conducted concurrently with the design of the LCPR2 sensor. The LCPR1 sensor forms part of the LCPR2 sensor; thus, in the absence of the LCPR1 sensor, *only the shunt resistor method has been used for the following round of tests*.

The case studies presented here are to determine:

- the relationship between current and increased pollution layer conductivity; and
- the probability of a flashover occurring as a function of LC at a constant ESDD level of 0.03 mg/cm^3.

5.3.1 Case study 1: Relationship between current and increased pollution layer conductivity

5.3.1.1 Test setup

The first study entails spraying a salt solution of known conductivity on the insulator string. The conductivity of each 100 ml solution is measured with a conductivity meter. The LC is measured with the shunt resistor method. The multimeter measuring the voltage across the resistor is set to the maximum hold mode to log the highest current measured for each test. The schematic of the setup is shown in Figure 5.11. The shunt is connected to a clean (unpolluted) stand-off glass insulator (from the cap to the pin of the insulator to create a low impedance path for the LC to bypass the glass area of the insulator disc). The insulator string consists of 3 glass insulators, each with a creepage distance of 320 mm, and the extra stand-off insulator as seen in Figure 5.11. The unified specific creepage distance (USCD) for the setup is, therefore, 9.6 mm/kV as a 100 kV applied voltage source was used as the test voltage. The limiting factor for the USCD is the clearance distance to ground. The HVDC power supply has a maximum current rating of 12 mA.

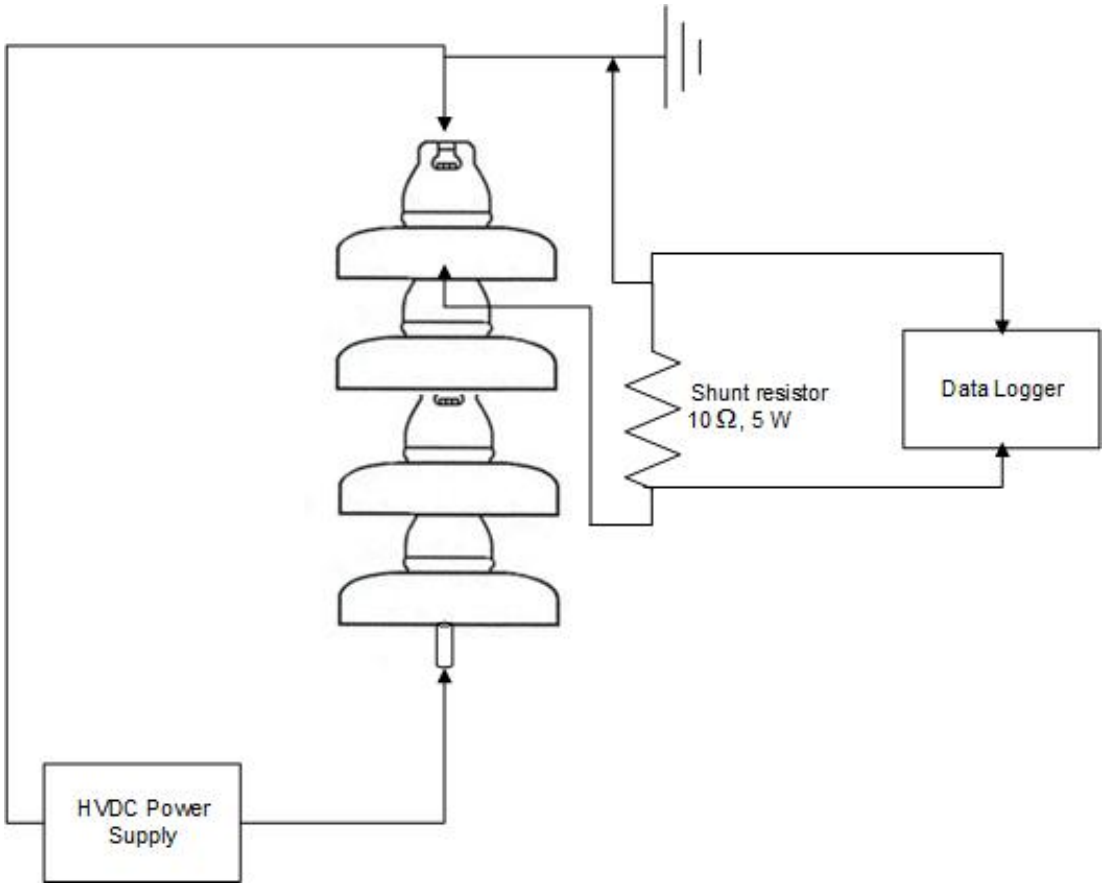

Figure 5.11: Schematic of the test setup for both case studies

After spraying the insulator string, it is energised to 100 kV and LC measurements taken. The string is then de-energised. After a period of between 30-60 seconds, the string is re-energised and a second set of measurements taken. For the purpose of these tests, this sequence is defined as a single *iteration*. Five iterations have been done for each level of salt conductivity. The conductivity of the salt solution for each set is increased in 0.01 S/m increments. After each contamination level, the string is cleaned and re-sprayed with the next solution at the higher conductivity level.

5.3.1.2 Results and observations

Figure 5.12 shows the maximum current observed as a function of increased surface conductivity. Table 5.1 shows the tabulated results of Figure 5.12. LC tests are terminated once the insulator string under test flashes at each of the 5 iterations. During the measurements, the voltage is energised to 100 kV. However, at higher conductivities, the insulator string flashes over at lower voltage levels as well.

For the setup investigated, flashover occurs at LC levels of 1.4 mA and higher. No flashovers occur below 1.4 mA. If the current exceeds the 1.4 mA threshold, flashover occurs, irrespective of the surface conductivity level.

At low surface conductivity levels, flashovers mostly occur during the first iteration only. At high surface conductivities, flashovers occur during almost all of the iterations. After a flashover at low conductivity levels, the water evaporates and leaves behind a low density salt deposit; thus, leading to lower current levels during subsequent iterations. After a flashover at high conductivity levels, the water still evaporates, but there is enough contamination left for the insulator string to reach the flashover threshold level of 1.4 mA.

The current levels increase with an increase in conductivity. This is in agreement with Seifert *et al.* (2007); Phillips *et al.* (2009); Jiang *et al*. (2010); Yang *et al*. (2012) and Sivaraman and Sivadasan (2014) (in Section 2.4), which state that the insulator's flashover voltage decreases with an increase in ESDD (surface conductivity in the case of the thesis). Zhang *et al*. (2010) also state that the ESDD affects the insulator flashover voltages more at high altitudes than at sea level.

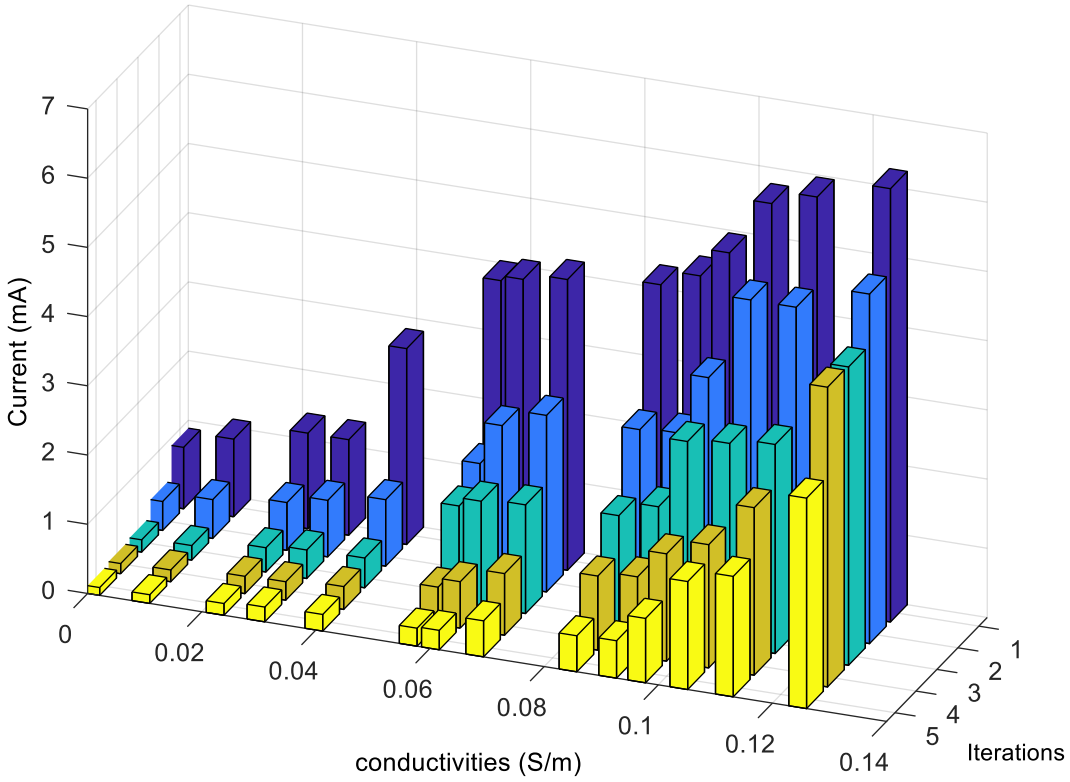

Figure 5.12: Insulator current versus surface conductivity energised up to a 100 kV

Table 5.1: Tabulated results of insulator current versus surface conductivity energised up to 100 kV

Conductivity [S/m]	Iterations				
	#1 [mA]	#2 [mA]	#3 [mA]	#4 [mA]	#5 [mA]
5.56×10^{-4}	0.89	0.42	0.18	0.15	0.11
0.009	1.12	0.56	0.21	0.17	0.13
0.022	1.38	0.69	0.35	0.25	0.17
0.029	1.38	0.82	0.41	0.27	0.21
0.040	2.83	0.96	0.43	0.33	0.24
0.056	4.03	1.70	1.40	0.54	0.26
0.060	4.10	2.30	1.52	0.67	0.28
0.068	4.20	2.55	1.57	0.89	0.52
0.084	4.34	2.56	1.63	1.07	0.52
0.091	4.56	2.60	1.85	1.15	0.54
0.096	4.96	3.47	2.86	1.55	0.93
0.104	5.77	4.69	2.93	1.78	1.56
0.112	5.97	4.69	3.02	2.42	1.74
0.124	6.26	5.05	4.31	4.33	3.04

Figure 5.13 shows the average decay in measured current after each iteration for all conductivities. At each surface conductivity level, the measured current is normalised to the first iteration's current measurement. Thereafter, the mean decay is calculated of the data sets (#1 to #5) for all surface conductivities. On average, there is a 40% decrease in the current level observed between the 1st

and 2nd iteration for all the conductivity levels. During the 5th iteration, the accumulative decrease in current compared to the current measured in the first iteration exceeds 80%. During this time lapse, the insulator dried (either due to the heat from the dry-band arcs or through natural evaporation), which causes an increase in the insulator's resistance, leading to a decrease in measured current thereafter. This decay is observed even without the occurrence of flashover.

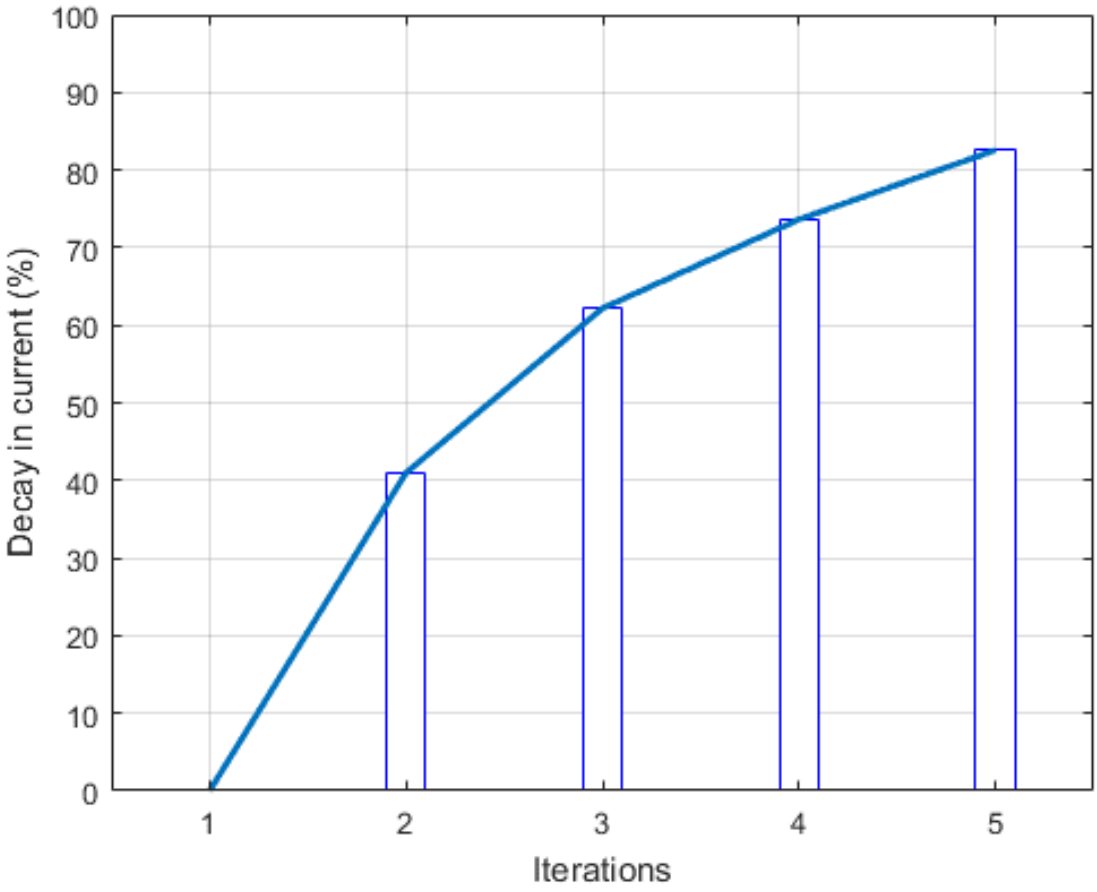

Figure 5.13: Average decay in current after each iteration for case study 1

5.3.2 Case study 2: Probability of flashover occurring as a function of LC at a constant ESDD level of 0.03 mg/cm^2

The second study involves determining the probability of a flashover occurring with an increase in LC at a constant equivalent salt deposit density (ESDD) level of 0.03 mg/cm^2. This level of ESDD is consistent with that found on the Cahora Bassa HVDC transmission line (Narain *et al*., 2012). The insulators under test are sprayed with a 0.07 S/m conductivity solution. The ESDD is determined from the conductivity as follows (Suzuki & Vosloo, 2011):

$$ESDD = \frac{(5.7\sigma_{20})^{1.03} \cdot V}{A}$$ **Equation 5.3**

with

$$\sigma_{20} = \sigma_{\theta}[1 - b(\theta - 20)]$$ **Equation 5.4**

where θ: is the solution's temperature in °C

σ_{20}: conductivity [S/m] at 20°C,

σ_{θ}: solution conductivity at a temperature θ [°C],

b: factor depending on the temperature θ,

V: volume [cm^3] of the saline solution,

A: insulator surface area [cm^2].

Using the above formulas, it is determined that a conductivity of 0.07 S/m is equivalent to an ESDD of 0.03 mg/cm^2.

5.3.2.1 Test setup

The setup for the second case study is the same as for the first. For this study, the HV is increased until a predetermined current is obtained, whilst the setup was only polluted with a 0.07 S/m solution. At the lower current levels, a minimum of 50 excitations are performed. The insulator string is sprayed after 10 excitations in order to ensure that it does not dry out during the test. Whist conducting the 1st case study, 6 consecutive (6 iterations as explained in Section 5.3.1.1) flashover events on the insulator string rarely occurred. This may be that the insulator's surface had dried out. Thus, if 5 consecutive flashovers occurred, the insulator string is re-sprayed with the salt solution to avoid completely drying out of the insulator. A similar setup was followed by Guo *et al.* (2015) for performing insulator flashover measurements.

5.3.2.2 Results and observations

Figure 5.14 shows the probability of a flashover occurring as a function of LC. It shows that at 0.6 mA, there is a possibility of a flashover occurring at a contamination level of 0.07 S/m. At 0.2 mA and 0.4 mA, no flashovers occur. During the tests, it was also seen that if, for example, a current of 1.6 mA needs to be tested, the insulator string sometimes flashed at a lower current level. The value is recorded for that specific current level. Thus, at certain current levels, there are

more than 50 excitations recorded but still normalised to a total percentage, for example, 11/62 excitations flashed over at a certain current level. When tests are performed at 2 mA, the insulator string, on most occasions, flashed over at a lower current level; thus, the 2 mA level is the 100% mark for this setup. The response seen in Figure 5.14 agrees well with that of Phillips *et al*. (2009) for the ac case (seen in Figure 2.18) where the probability of flashover also increases with an increase in current. Such a probability graph as shown in Figure 5.14 has huge significance. First, it informs the power utilities of the condition of the insulators and the probability of flashover, and second, can also be of significance to live line workers. When they are performing maintenance on in-service insulators this graph serves as an indication of what the present LC level and corresponding probability of a flashover are. If the LC level is below 0.6 mA, maintenance can be performed if a power utility requires a zero probability of a flashover occurring.

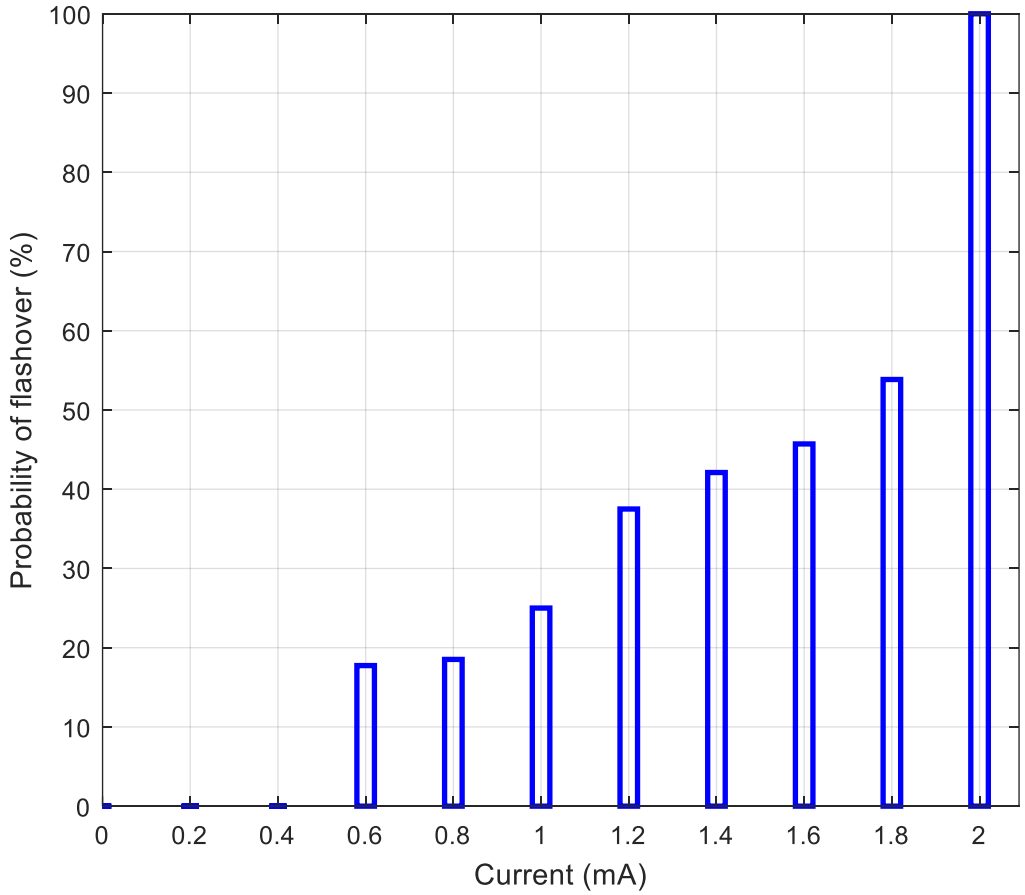

Figure 5.14: Probability of flashover versus current at a conductivity level of 0.07 S/m

Another case study has been conducted where the number of insulators is increased after each set of tests.

At each number of insulators, the setup is energised 5 times and the average current calculated. The first test is conducted with 3 glass insulators, with 1 glass insulator added after every test. Figure 5.15 shows a string of 6 glass insulators. Figure 5.16 shows the result for LC versus number of insulators. It is observed that the current decreases each time another insulator is added to the string. This observation agrees well with the findings of Jiang *et al*. (2008), Zhang *et al*. (2010) and Tang *et al.* (2015), which states that the flashover withstand voltage increases with an increase in insulator string length and current decreases with an increase in insulator string length. This response is also observed in Figure 2.12 by Pigini & Cortina (2011) where the risk of flashover decreases with an increase in insulator length.

Figure 5.15: Six glass insulators in a string (including the stand-off insulator)

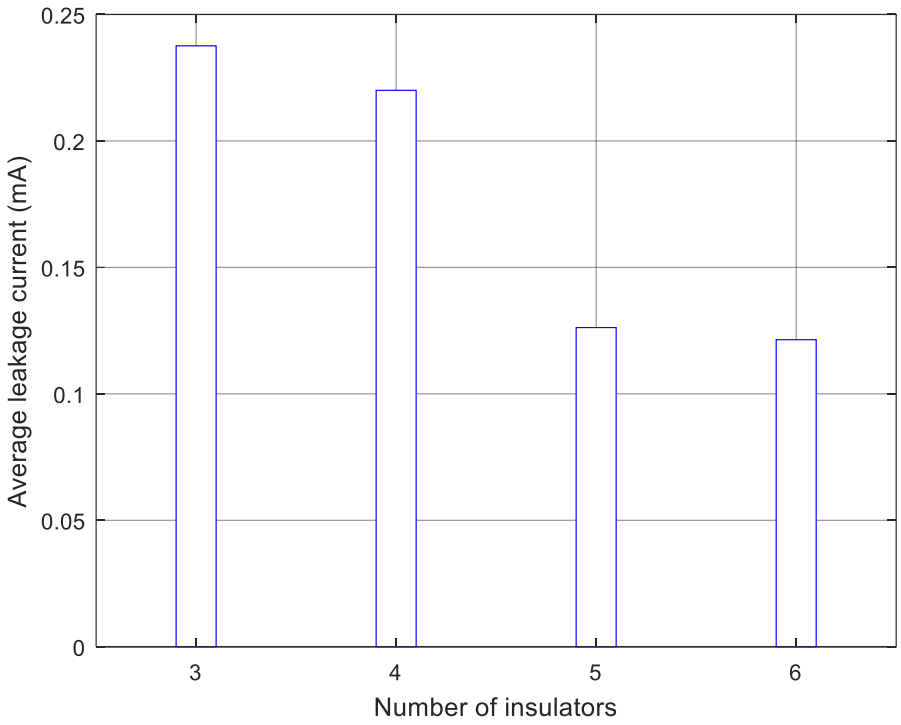

Figure 5.16: Leakage current versus number of insulators energised up to a 100 kV

The results of Figure 5.16 are also intuitively anticipated, as the addition of insulators in series effectively increases the resistance of the insulator string.

5.3.3 Summary of case studies performed at the corona cage

During measurements at Eskom's corona cage high voltage test facility, two case studies have been performed regarding leakage current, level of pollution and the probability of flashover.

The first case study involved increasing the contamination level but keeping the voltage constant at 100 kV. The current increases with an increase in contamination level. Thus, the probability of insulator flashover also increases with an increase in contamination severity. This observation agrees well with the findings of Jiang *et al.* (2010) and Abbasi *et al.* (2014) for dc insulators, which state that the flashover withstand voltage decreases with increased contamination. Figure 5.17 shows the results reported by Jiang *et al.* (2010) for the relationship between the 50% pollution flashover voltages, U_{50}, and salt deposit density (SDD), or SDD_B (SSD on an insulator's bottom surface), at various T/B (ratio of pollution on insulator's top surface to that on the bottom surface) for a porcelain insulator.

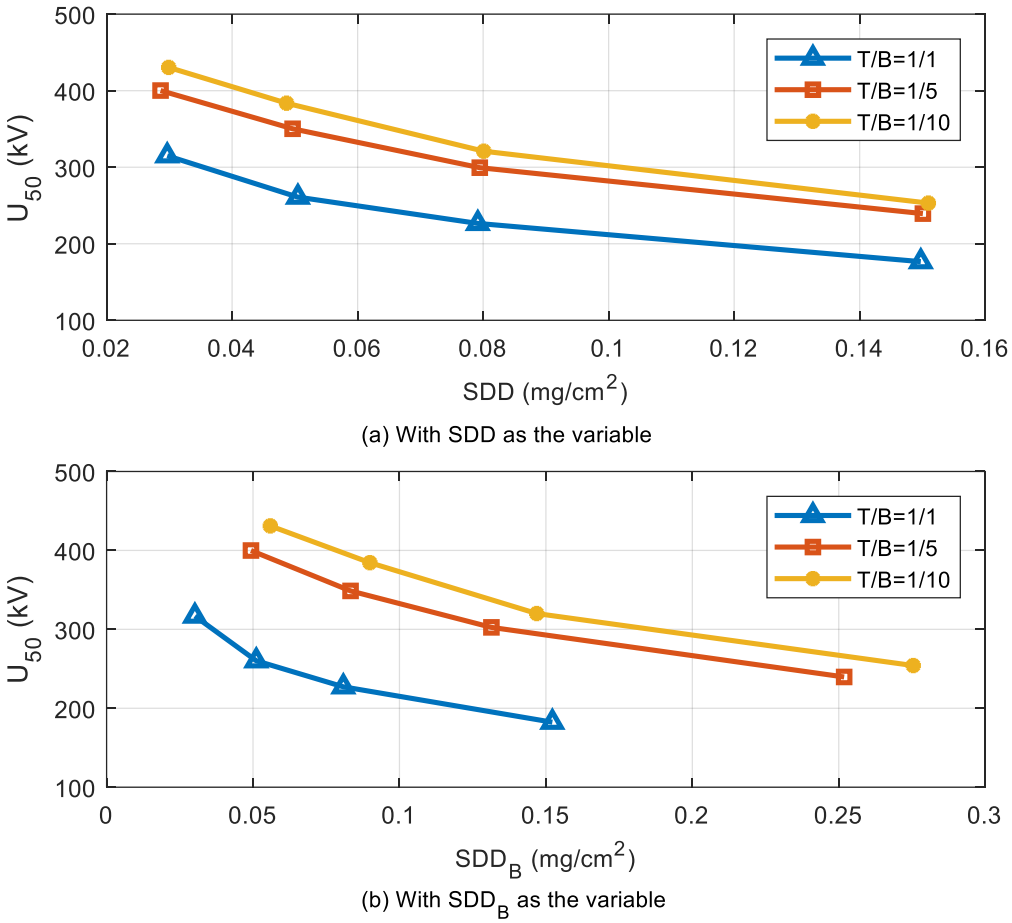

Figure 5.17: Relationship between U_{50} and SDD or SSD_B at various T/B for an XZP-210 porcelain insulator (Adapted from Jiang *et al*., 2010)

The second case study, where the contamination level was kept constant, showed that at a current of 0.6 mA there existed a possibility of a flashover occurring. According to Equation 2.4, the highest LC measured before flashover for an ac insulator string with USCD of 9.6 mm/kV should have been approximately 400 mA, or 100 mA according to Equation 2.5 where a more conservative approach is followed. However, these tests show that the insulator string for the dc case already flashed over at 0.6 mA, which is considerably lower. It should be noted that Equation 2.4 was applied for HVAC conditions and may not hold for its dc counterpart. For example, Equation 2.4 and Equation 2.5 ignore the dependency of LC on contamination levels completely, which from the results presented in Section 5.3.1 seems to be an over-simplification. More work will have to be done in future to explore this phenomenon for HVDC schemes further and a possible adaption and augmentation of Equation 2.4 and Equation 2.5 for the HVDC case.

It is also noted that the minimum flashover current between the two case studies differed. This can be attributed to the wetting process used during the case studies. The first study's insulators have been wetted after 5 excitations leading to less insulator resistance and, hence, a higher current. The second study, where the contamination has been kept constant, insulators' have been wetted after 10 excitations, which lead to the insulator string having a higher resistance and, hence, a lower overall current.

5.4 Conclusion

The first part of the chapter covered the initial HVDC insulator LC measurements performed with the developed prototype at the corona cage high voltage testing facility. It has been observed that the prototype can accurately detect LC on an insulator when the insulator is energised by an HVDC power supply. The second part of the chapter covered the two case studies conducted at the corona cage.

The first case study was to observe the relationship between current and increased pollution layer conductivity. It showed that the current increases with an increase in contamination level. It also showed that if the current exceeds the 1.4 mA threshold, flashover occurs, irrespective of the surface conductivity level.

The second case study was to observe the probability of flashover occurring as a function of LC at a constant ESDD level of 0.03 mg/cm^2. It was shown that at an LC exceeding 0.6 mA, a flashover can occur for an insulator string with an USCD of 9.6 mm/kV

To the knowledge of the author, this is the first time that such a relationship has been determined for the HVDC case.

6: IN-SITU LC MEASUREMENTS OF INSULATORS OF THE CAHORA BASSA HVDC TRANSMISSION LINE

6.1 Introduction

Little has been published (at least publicly) relating to operational data of typical leakage current (LC) magnitudes, waveforms and consequential effects thereof for HVDC transmission lines. Thus, an effort has been made to perform in-situ insulator LC measurements on an energised transmission HVDC transmission line over an extended period of almost a year, and on more than one type of insulator (glass and composite). This has not been attempted before. LC measurements were performed over a period of 11 months on Tower 1 of Line 1 of the Cahora Bassa HVDC transmission line at Apollo in Johannesburg, South Africa, as a case study of an operational HVDC line. This deepens our understanding of LC behaviour on in-service insulators under HVDC conditions, at least at high altitudes. The LC measurements have been correlated with the ambient temperature, humidity, rain, and dew point, as well as the HVDC transmission line's voltage and current.

6.2 In-situ tests on the Cahora Bassa HVDC transmission line insulators

Live line workers installed the prototype LC sensor on the glass insulator and a shunt resistor on both the composite and glass insulator strings in August 2016. Figure 6.1 shows the inverted-V insulator string and the live line workers installing the prototype and shunt resistor. The inverted-V insulator string has a glass and composite insulator string. This setup presents a controlled environment where the composite and glass insulators are on the same inverted-V string and exposed to the same environmental conditions; thus, their LC behaviour can be reliably compared.

The insulator strings' unified specific creepage distance (USCD) at Apollo is approximately 40 mm/kV and the equivalent salt deposit density (ESDD) approximately 0.03 mg/cm^2 (Narain *et al*., 2012).

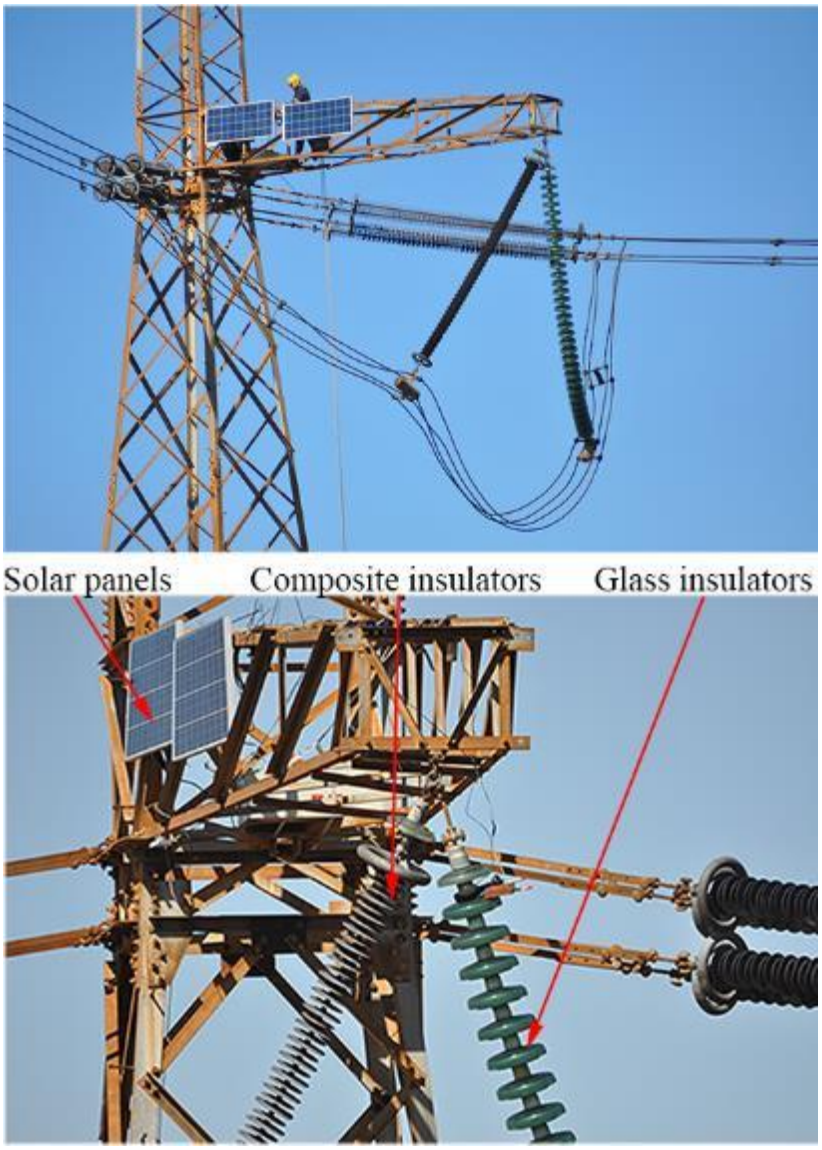

Figure 6.1: Live line workers installing the LCPR2B sensor and shunt resistors on an inverted-V insulator string at Apollo

Upon installation of the LCPR2, it was deemed too bulky and heavy for operational deployment due to its weight and size. It was consequently decided to remove the second core but to still keep the second MR sensor for implementing the differential magnetometer method (DDM). This prototype is named LCPR2B to avoid confusion. The second MR sensor was placed in foam and aligned with the other MR sensor. The prototype was re-calibrated within the HelmHoltz coil at CPUT. The LCPR2B's electronics were placed inside a Perspex enclosure and the cores covered with insulation material to protect it from the rain, as displayed in Figure 6.2.

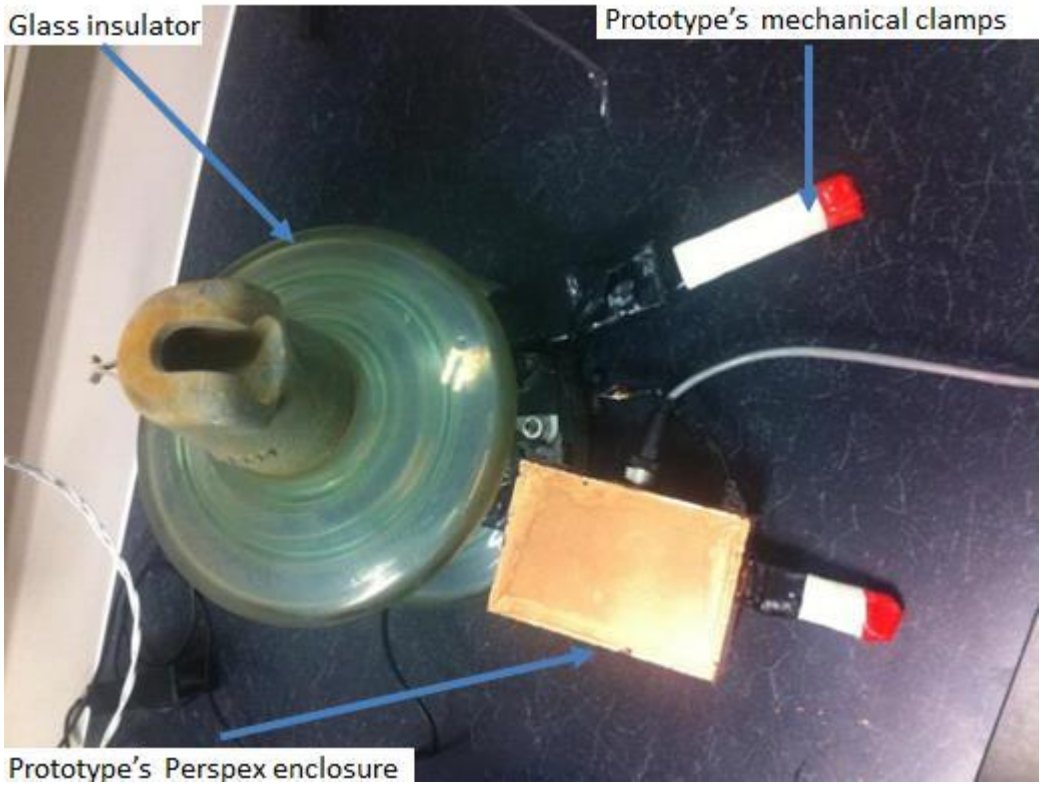

Figure 6.2: LCPR2B sensor with a Perspex enclosure around a glass insulator

The measurement setup comprises a data logger, two 12 V batteries and two solar panels. LC is sampled and logged at 10-second intervals. The ambient climatic data is logged at 6-minute intervals at a station installed less than a kilometre away. The measured LC datasets have been analysed on a weekly basis against ambient temperature, humidity, dew, rain and the HVDC line's voltage and current. For analysis purposes, the maximum measured LC and climatic parameters over successive hourly intervals are considered, since dry-band discharges occur in short durations and might be averaged out if the mean measurement is taken. The LC and weather data were collected between August 2016 and June 2017. Due to the huge amount of data obtained, only the data for those weeks that exhibited increased LC activity are presented. The rest of the weekly insulator LC activity can be found in Appendix A.

The setup was visually inspected on a quarterly basis. During the first inspection after 3 months the ambient field sensor of the LCPR2B appeared damaged, but there were no Eskom resources available to replace the sensor due to cost. Thus, to validate the concept of the prototype sensor, the LC data for the sensor had to be mathematically post-processed. This has been performed by removing the expected offset caused by ambient magnetic fields so that the prototype's LC measurements match that of the shunt resistor on the glass insulator (control measurement).

Important note:
The prototype sensor measurements have not been used during the analyses of the data as this was potentially compromised in view of the damaged ambient field sensor. The post-processed results of the prototype sensor are only given in Figure 6.3 (LC activity from the 3rd to the 9th of August 2016) along with the rest of the data as discussed in the next section to verify that the prototype sensor is capable of in-situ measurement of the insulator LC. The LC measured with the shunt resistor method is used for characterisation of the LC.

6.3 Weekly LC activity

6.3.1 LC measurements using the shunt resistors and LCPR2B: August 3rd - 9th

Figure 6.3 shows the LC activity from the 3rd to the 9th of August 2016. The weather conditions and the Cahora Bassa's line voltage and current are presented in Figure 6.4 and Figure 6.5 for the same period, respectively. It is evident that LC for both the glass and composite insulators behave similarly, except under high humidity conditions. The nominal LC value varies between 20 µA and 60 µA under low humidity conditions, but rises to above 5 mA in high humidity conditions on the glass insulator. No rain was present during this week. Literature states that a good working insulator normally has LC in the micro-Ampère range (Ferreira *et al.*, 2010:1), which agrees with the measurements presented here. Between the 4th and 5th of August, LC was present but no line voltage and current data were available from Apollo. The line current and voltage fluctuations have little influence on the nominal LC levels. This is an observation that applies throughout the 11-month in-situ tests. It can be seen that the prototype's LC measurements track the glass shunt resistor's LC pattern quite accurately.

However, the prototype did not detect the increased LC activity on the 9th of August. Several reasons can be considered for the apparent discrepancy between the shunt and prototype measurements on this date.

First, the discharges may have been occurring too rapidly for the signal conditioning circuitry of the LCPR2B sensor. Second, the datalogger was set to an even slower sampling time (10s) during the field tests as for the corona cage measurements due to the expected slow natural build-up of LC. This may have impacted on how accurately arcs were captured. Third, a similar occurrence was observed in Figure 5.5 where the LC detected by the prototype sometimes led or lagged the LC measured by the shunt by a few milliseconds. A zoomed-in plot of Figure 5.5 is shown in Figure 6.6 that displays this effect. On some occasions the prototype detected a different LC magnitude

than what the shunt reported as well. Fourth, it must be considered that the shunt measurements are corrupt, as this was the only day where such high LC was measured. Finally, it cannot be ignored that the LCPR2B sensor had to be used with one soft core, as explained earlier. The differential measurements might therefore have been compromised during times of high ambient fields, which are associated with arcing conditions.

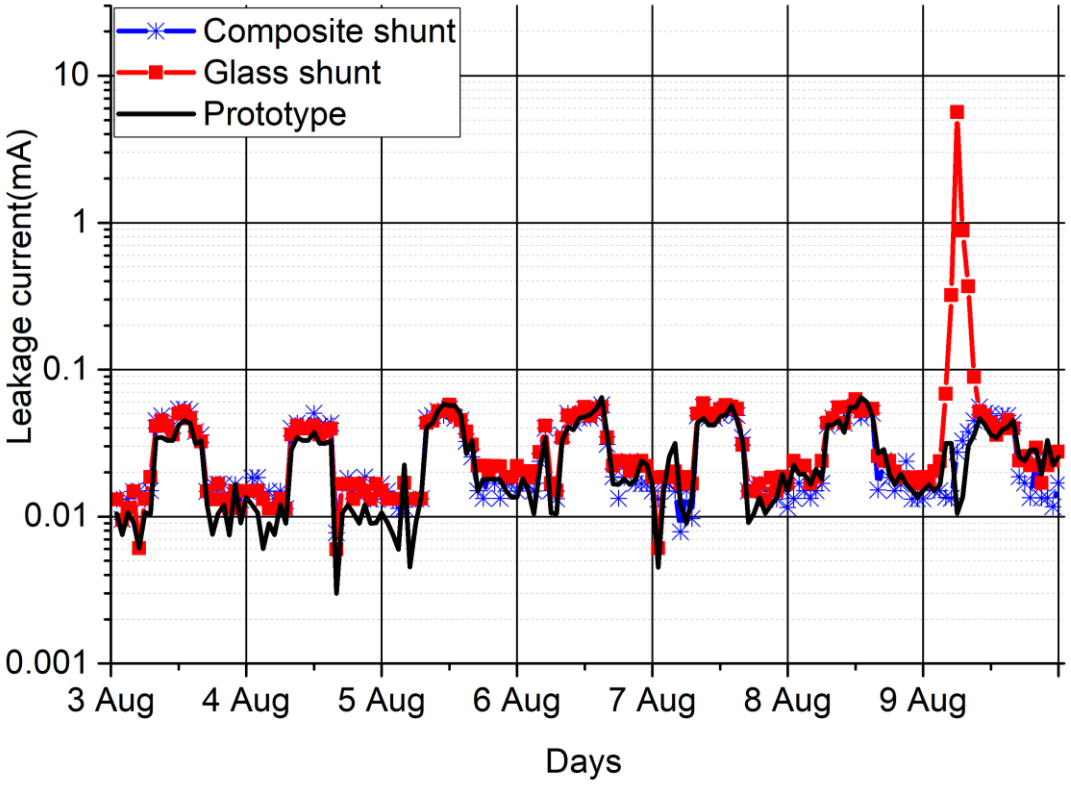

Figure 6.3: Leakage current activity using the shunts and the LCPR2B: 3rd - 9th of August

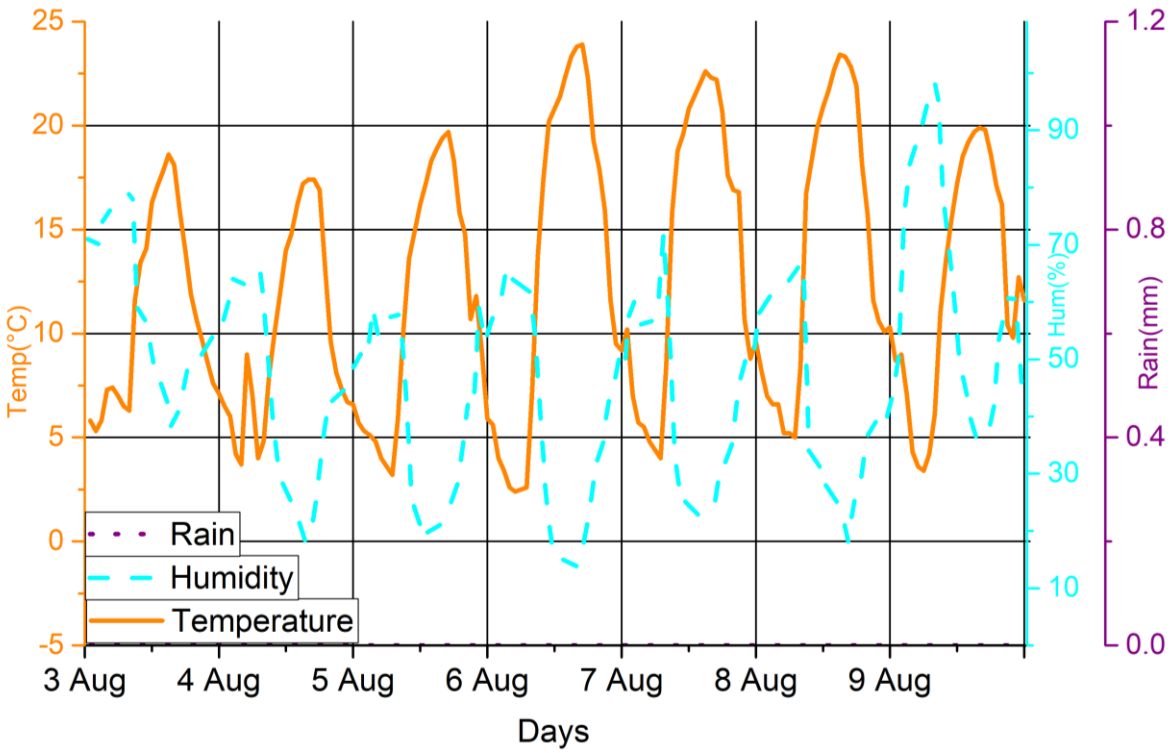

Figure 6.4: Weather conditions: 3rd - 9th of August

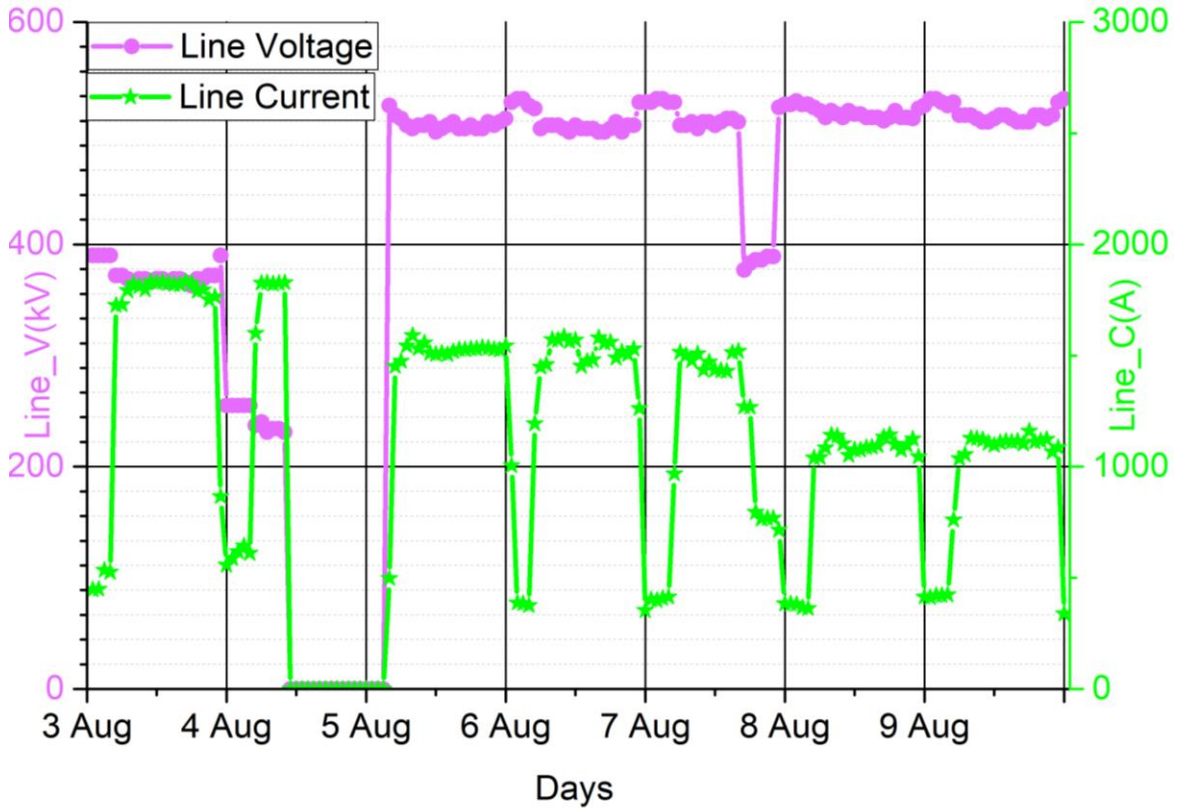

Figure 6.5: Line voltage and current: 3rd - 9th of August

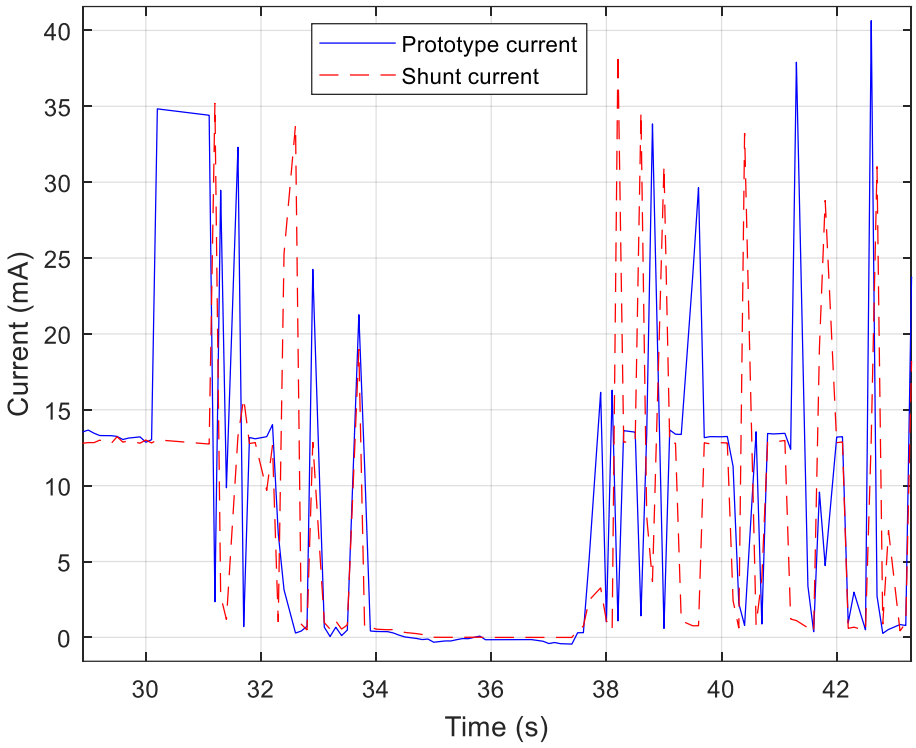

Figure 6.6: Zoomed-in view of leakage current measurements of the shunt resistor and LCPR1 sensor at the corona cage

Correlation between LC and weather conditions: August 3rd - 9th

The correlation matrix for LC versus weather parameters have been calculated for this week as shown in Table 6.1. The daily average of each parameter studied is also given in Table 6.2. An interesting phenomenon is the positive correlation coefficient of 0.48 observed between the composite insulator LC and temperature. This indicates that the composite insulator LC increases as the ambient temperature increases. When humidity increases, the composite and glass insulator LC behave in an opposite manner, as shown in Table 6.1, where a correlation coefficient of -0.19 and 0.22 is observed for the composite and glass insulator cases, respectively. The composite insulator LC decreases when humidity increases, while the glass insulator LC increases with increasing humidity. The composite insulator LC had a positive correlation with the line current whereas the glass insulator LC showed no correlation with the line parameters. The composite insulator's LC remain relatively constant during the week. The glass insulator experienced elevated LC on the 9th of August.

Table 6.1: Correlation matrix between LC and weather conditions for August 3rd - 9th

	Composite shunt	Glass shunt	Temperature	Humidity	Line voltage	Line current
Composite shunt	1.00					
Glass shunt	0.04	1.00				
Temperature	0.48	-0.12	1.00			
Humidity	-0.19	0.22	-0.78	1.00		
Line voltage	0.11	0.07	0.13	0.09	1.00	
Line current	0.33	0.00	0.28	-0.05	0.46	1.00

Table 6.2: Daily averages of each parameter studied for August 3rd - 9th

Days	Composite shunt [mA]	Glass shunt [mA]	Temperature [°C]	Humidity [%]	Line voltage [kV]	Line current [A]
03-Aug	0.03	0.02	11.00	59.04	368.38	1490.92
04-Aug	0.02	0.02	10.03	43.52	101.13	549.79
05-Aug	0.02	0.03	11.35	40.29	444.75	1291.42
06-Aug	0.03	0.03	13.46	39.71	511.38	1286.92
07-Aug	0.03	0.03	14.03	42.04	483.58	1065.42
08-Aug	0.03	0.03	14.18	42.83	518.50	943.79
09-Aug	0.03	0.33	12.38	62.13	518.00	944.42
Weekly average	0.03	0.07	12.34	47.08	420.82	1081.81

6.3.2 LC measurements using the shunt resistors only: September 14th - 20th

Figure 6.7 shows the LC activity from the 14th to the 20th of September. The weather conditions and the Cahora Bassa's line voltage and current are presented in Figure 6.8 and Figure 6.9 for the same period, respectively. On the 18th of September, the ambient temperature is at its lowest for the week, humidity is above 90% and rain is present. These conditions have given rise to an increase in LC of just over 0.6 mA on the glass insulator with the commencement of rain. The increase in LC concurs with literature, which states that the probability for increased LC is high if humidity is higher than 90% (Meyer *et al*., 2011; Zchariades *et al*., 2013; Werneck *et al.,* 2014). In Section 2.4.2 it was stated that rain can produce increasingly large LC on insulators (Muniraj & Chandrasekar, 2009). However, during the same timeframe, the composite insulator experienced even lower than usual LC, behaving completely opposite to the glass insulator. This can be ascribed to the composite insulator being washed by the rain and also exhibiting its hydrophobicity properties (Sunitha *et al.,* 2015).

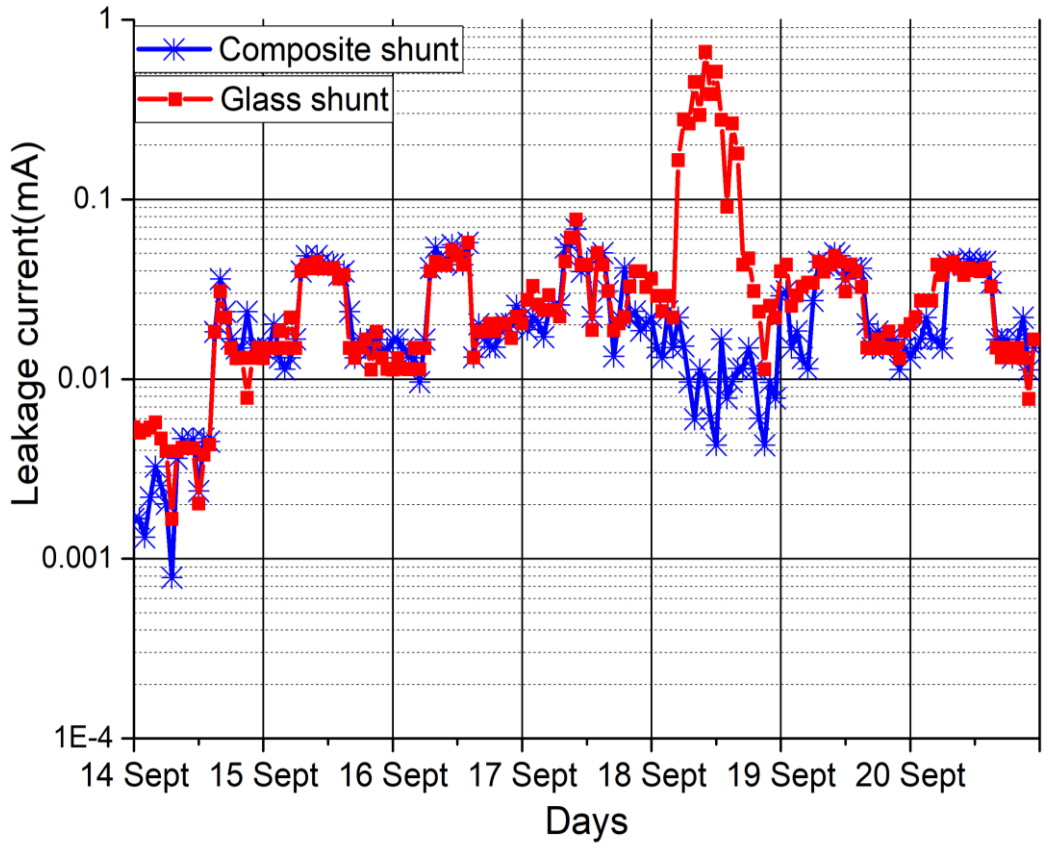

Figure 6.7: Leakage current activity using the shunt resistors only: 14th - 20th of September

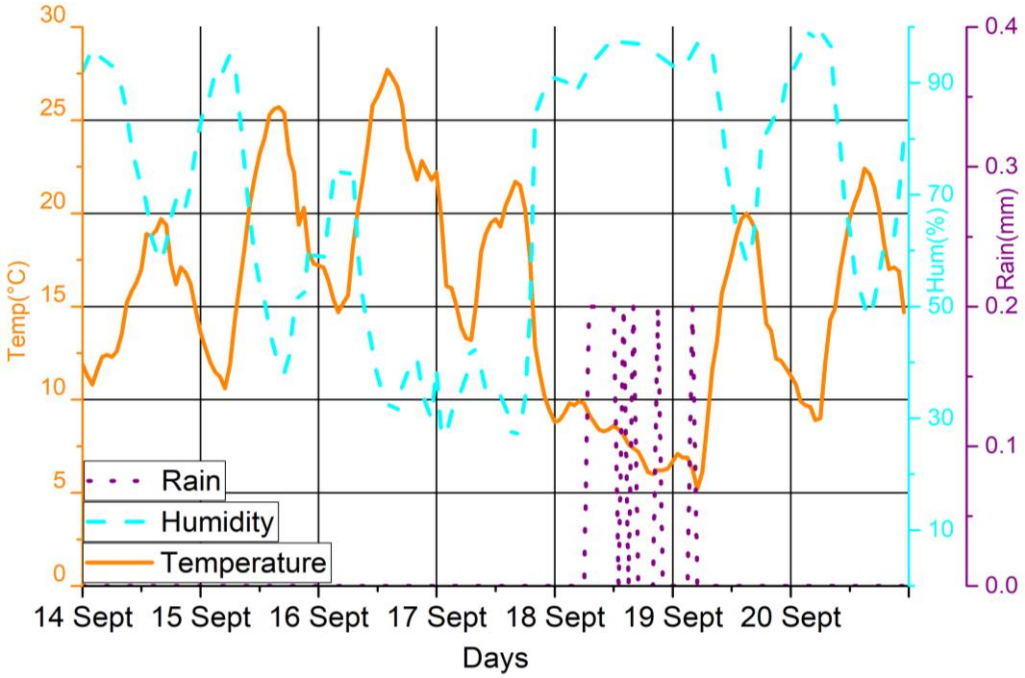

Figure 6.8: Weather conditions: 14th - 20th of September

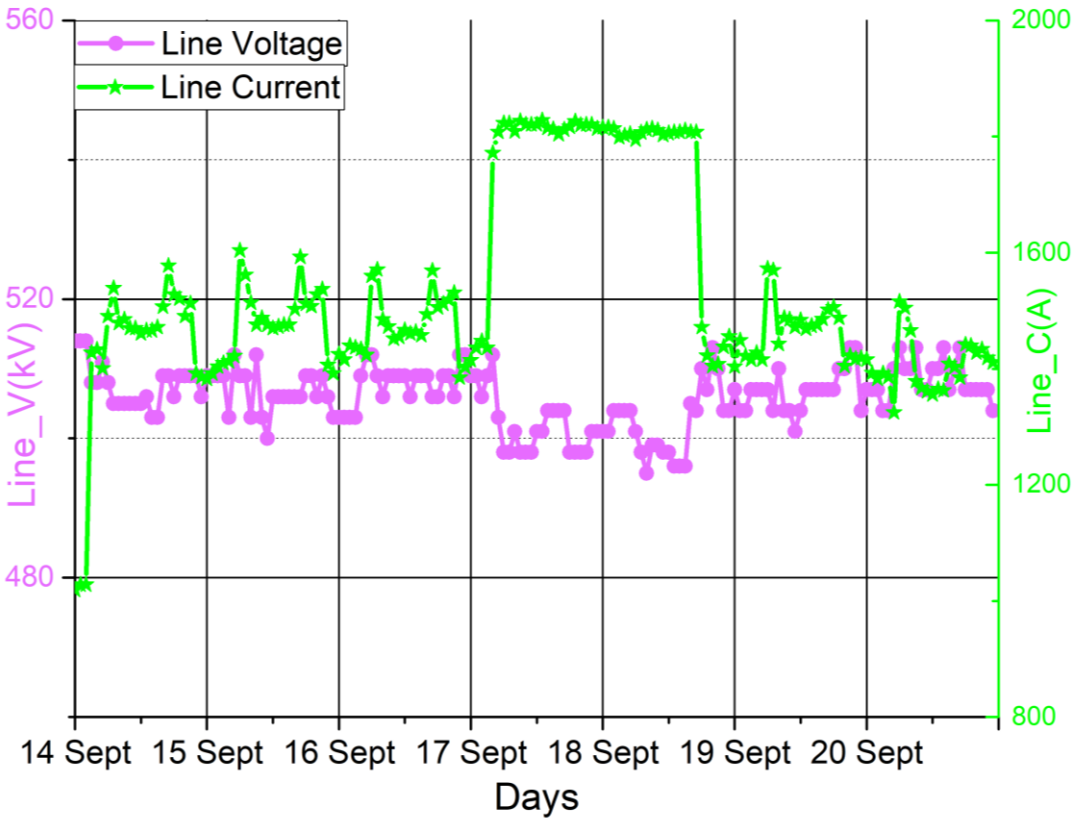

Figure 6.9: Line voltage and current: 14th - 20th of September

Correlation between LC and weather conditions: September 14th - 20th

The correlation matrix for LC versus weather parameters have been calculated for this week as shown in Table 6.3. The daily average of each parameter studied is also given in Table 6.4. A positive correlation between composite insulator LC and temperature is again observed as seen in Table 6.1. A correlation coefficient of 0.44 has been calculated between the composite insulator LC and temperature. During this week, the glass insulator exhibited a negative correlation coefficient of -0.29 with temperature, indicating that the glass insulator LC decreased as temperature increased. When humidity increases, the composite and glass insulator LC again behaved in a completely opposite manner as shown in Table 6.3, where a correlation coefficient of -0.39 and 0.24 have been observed for the composite and glass insulator cases, respectively. The composite insulator LC decreases when humidity increases, while the glass insulator LC increases with increasing humidity.

A strong positive correlation coefficient of 0.7 has been calculated between the glass insulator LC and rain. For the composite insulator case, a negative correlation coefficient of -0.24 has been

calculated for LC versus rain. This can indicate that washing of the composite insulator takes place due to its hydrophobicity properties during rainy conditions, leading to the insulator exhibiting even lower LC. The average LC experienced by the glass insulator was higher than the LC observed on the composite insulator. From Table 6.4 it is also evident that the most elevated LC activity occurred on the 18th of September, which is the day when rain was present and the humidity was the highest for that week.

Table 6.3: Correlation matrix between LC and weather conditions for September 14th - 20th

	Composite shunt	Glass shunt	Temperature	Humidity	Rain	Line voltage	Line current
Composite shunt	1.00						
Glass shunt	-0.08	1.00					
Temperature	0.44	-0.29	1.00				
Humidity	-0.39	0.24	-0.85	1.00			
Rain	-0.24	0.70	-0.34	0.28	1.00		
Line voltage	-0.06	-0.46	0.19	-0.02	-0.32	1.00	
Line current	0.11	0.44	-0.13	-0.11	0.30	-0.72	1.00

Table 6.4: Daily averages of each parameter studied for September 14th - 20th

Days	Composite shunt [mA]	Glass shunt [mA]	Temperature [°C]	Humidity [%]	Rain [mm]	Line voltage [kV]	Line current [A]
14-Sep	0.01	0.01	15.31	78.25	0.00	507.71	1418.83
15-Sep	0.03	0.02	18.51	66.25	0.00	506.88	1475.79
16-Sep	0.03	0.03	21.54	48.75	0.00	507.88	1472.54
17-Sep	0.03	0.03	16.92	43.25	0.00	502.13	1752.13
18-Sep	0.01	0.17	8.09	94.13	0.08	502.13	1714.38
19-Sep	0.03	0.03	12.76	82.67	0.01	506.75	1463.13
20-Sep	0.03	0.03	15.72	75.63	0.00	508.38	1406.00
Weekly average	0.02	0.05	15.55	69.85	0.01	505.98	1528.97

6.3.3 LC measurements using the shunt resistors only: October 13th - 19th

Figure 6.10 shows the LC activity from the 13th to the 19th of October. The weather conditions and the Cahora Bassa's line voltage and current are presented in Figure 6.11 and Figure 6.12 for the same period, respectively. During the evening of the 15th of October, humidity is very high and rain commenced, which continued into the morning hours of the 16th. Elevated LC on the glass insulator is observed. On the 19th of October, elevated LC is observed on the glass insulator again.

During this time rain is present, humidity is high and the temperature is low. During the periods of elevated LC on the glass insulator, the composite insulator suppresses the LC surges.

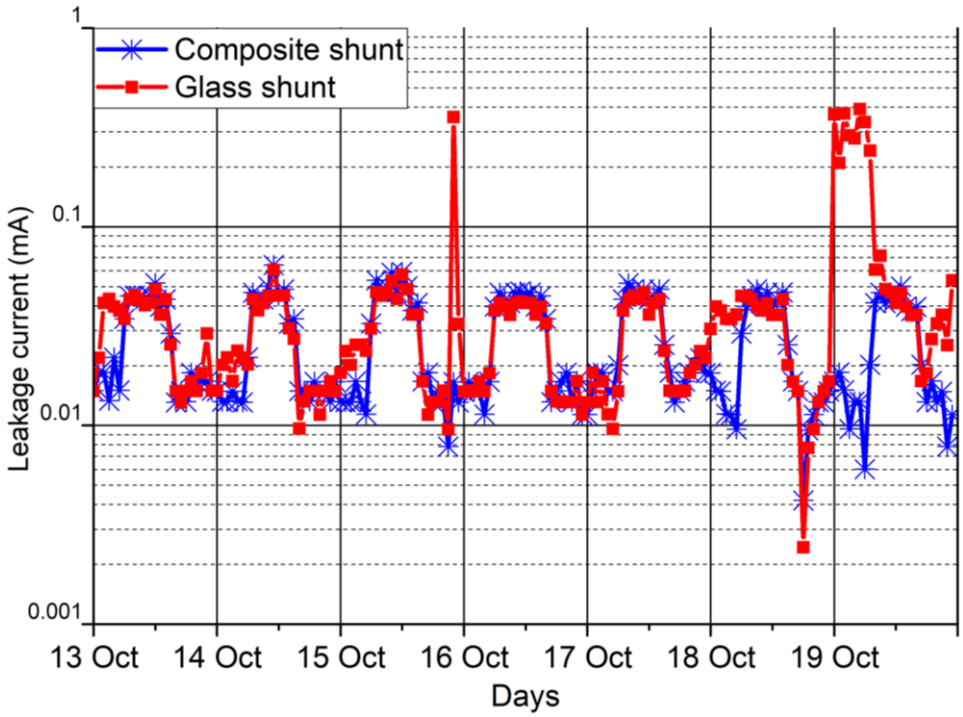

Figure 6.10: Leakage current activity using the shunt resistors only: 13th - 19th of October

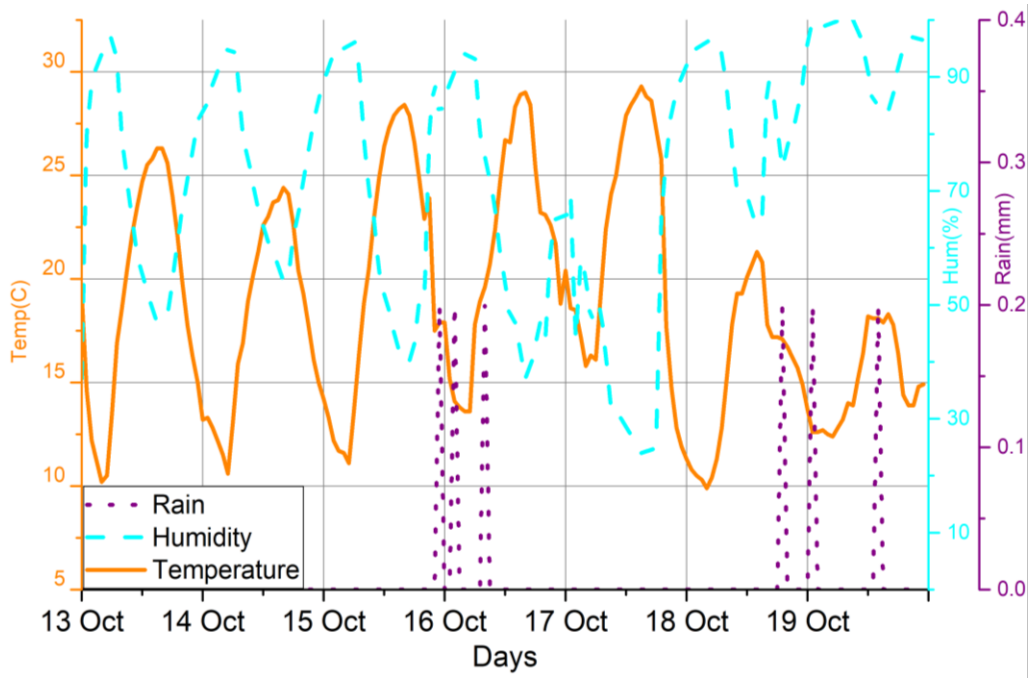

Figure 6.11: Weather conditions: 13th - 19th of October

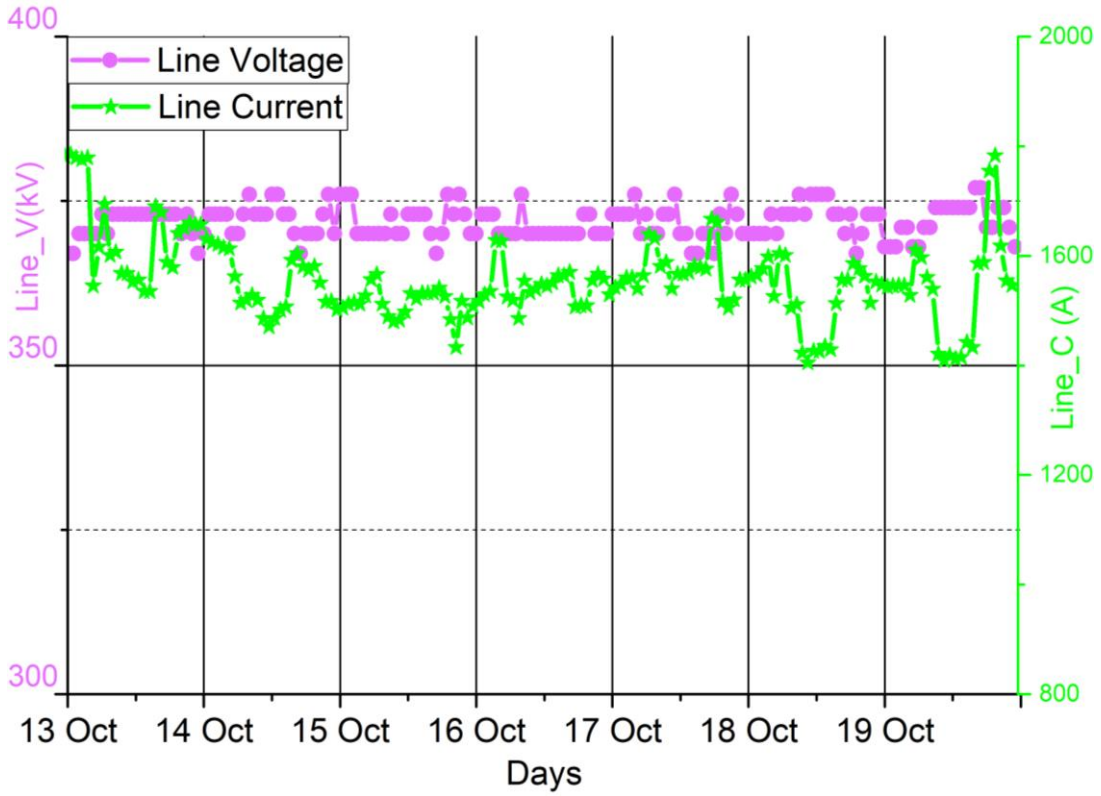

Figure 6.12: Line voltage and current: 13th - 19th of October

Correlation between LC and weather conditions: October 13th - 19th

The correlation matrix for LC versus weather parameters is shown in Table 6.5. The daily average of each parameter studied is also given in Table 6.6. A positive correlation between composite insulator LC and temperature is again observed, as seen in the previous weeks. A positive correlation coefficient of 0.39 has been calculated between the composite insulator LC and temperature for the week. This indicates that the composite insulator LC increases as the ambient temperature increases. During this week, the glass insulator exhibited a negative correlation of -0.22 with temperature, indicating that the glass insulator LC decreased as temperature increased.

When humidity increases, the composite and glass insulator LC again behaved in an opposite manner as observed in previous weeks. A negative correlation coefficient of -0.26 has been calculated for composite insulator LC versus humidity and a positive correlation coefficient for glass insulator LC versus humidity. The composite insulator LC decreases when humidity increases while the glass insulator LC increases with increasing humidity. A low correlation between insulator LC and rain has been observed for this week on both insulators. An explanation for the low correlation can be that *continuous* rainfall occurred during this week, which led to washing of the insulators instead of LC build-up, which normally occurs during drizzly conditions.

Table 6.5: Correlation matrix between LC and weather conditions for October 13th - 19th

	Composite shunt	Glass shunt	Temperature	Humidity	Rain	Line voltage	Line current
Composite shunt	1.00						
Glass shunt	-0.03	1.00					
Temperature	0.39	-0.22	1.00				
Humidity	-0.26	0.29	-0.90	1.00			
Rain	-0.04	0.04	-0.08	0.11	1.00		
Line voltage	0.25	-0.19	0.00	0.07	-0.03	1.00	
Line current	-0.34	-0.05	-0.16	0.00	-0.12	-0.42	1.00

Table 6.6: Daily averages of each parameter studied for October 13th - 19th

Days	Composite shunt [mA]	Glass shunt [mA]	Temperature [°C]	Humidity [%]	Rain [mm]	Line voltage [kV]	Line current [A]
13-Oct	0.03	0.03	19.26	69.38	0.00	371.38	1642.67
14-Oct	0.03	0.03	18.03	75.46	0.00	372.25	1557.00
15-Oct	0.03	0.04	20.45	70.25	0.01	372.00	1512.29
16-Oct	0.03	0.03	21.46	66.08	0.02	370.88	1543.63
17-Oct	0.03	0.03	21.76	48.08	0.00	371.50	1570.42
18-Oct	0.02	0.03	15.61	83.08	0.01	372.50	1523.63
19-Oct	0.02	0.13	14.95	95.00	0.02	371.88	1539.33
Weekly average	0.03	0.04	18.79	72.48	0.01	371.77	1555.57

6.3.4 LC measurements using the shunt resistors only: November 7th - 13th

Figure 6.13 shows the LC activity from the 7th to the 13th of November. The weather conditions and the Cahora Bassa's line voltage and current are presented in Figure 6.14 and Figure 6.15 for the same period, respectively. On the 9th of November, when high rainfall commenced, the LC on the glass insulator increased. Incidentally, during this week and especially on the 9th of November, flash floods occurred in Johannesburg (News24, 2017), which account for the spikes in LC on the glass insulator throughout this week. Low levels of increased LC activity have been observed on the composite insulator throughout the week, especially during the evenings.

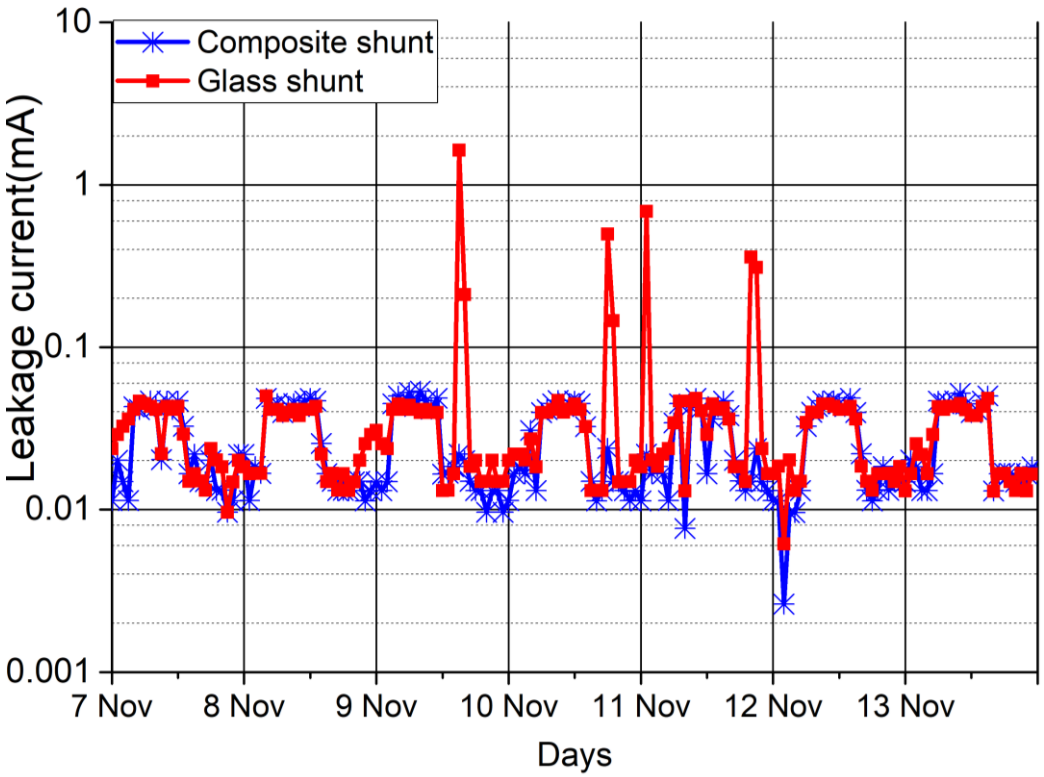

Figure 6.13: Leakage current activity using the shunt resistors only: 7th - 13th of November

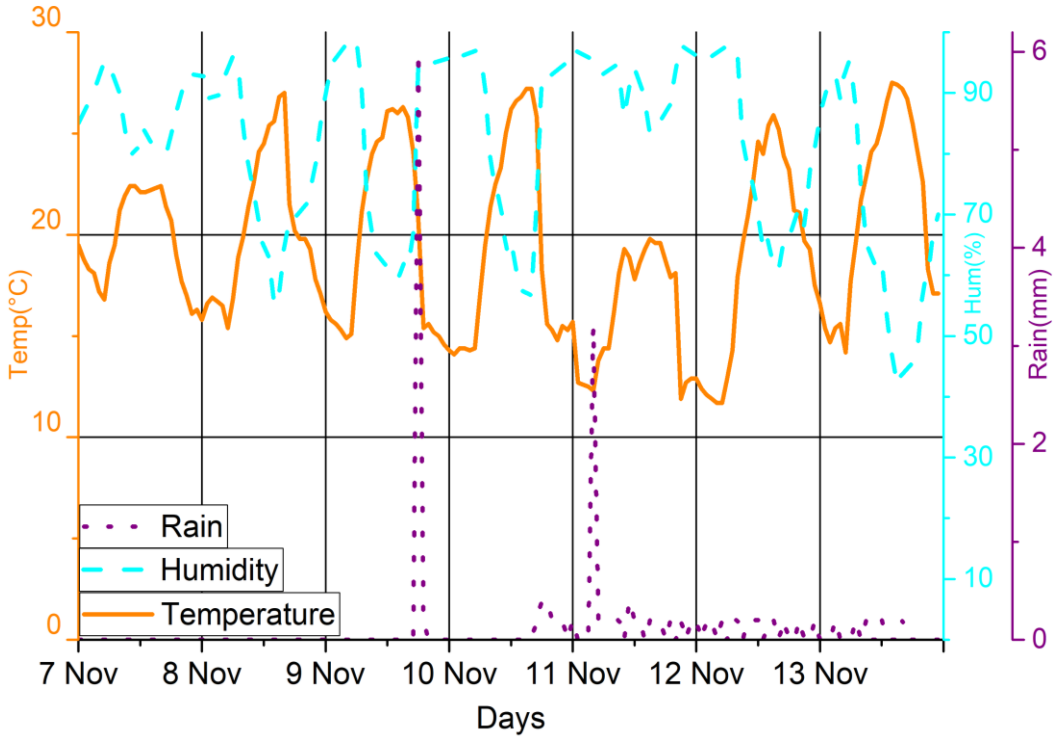

Figure 6.14: Weather conditions: 7th - 13th of November

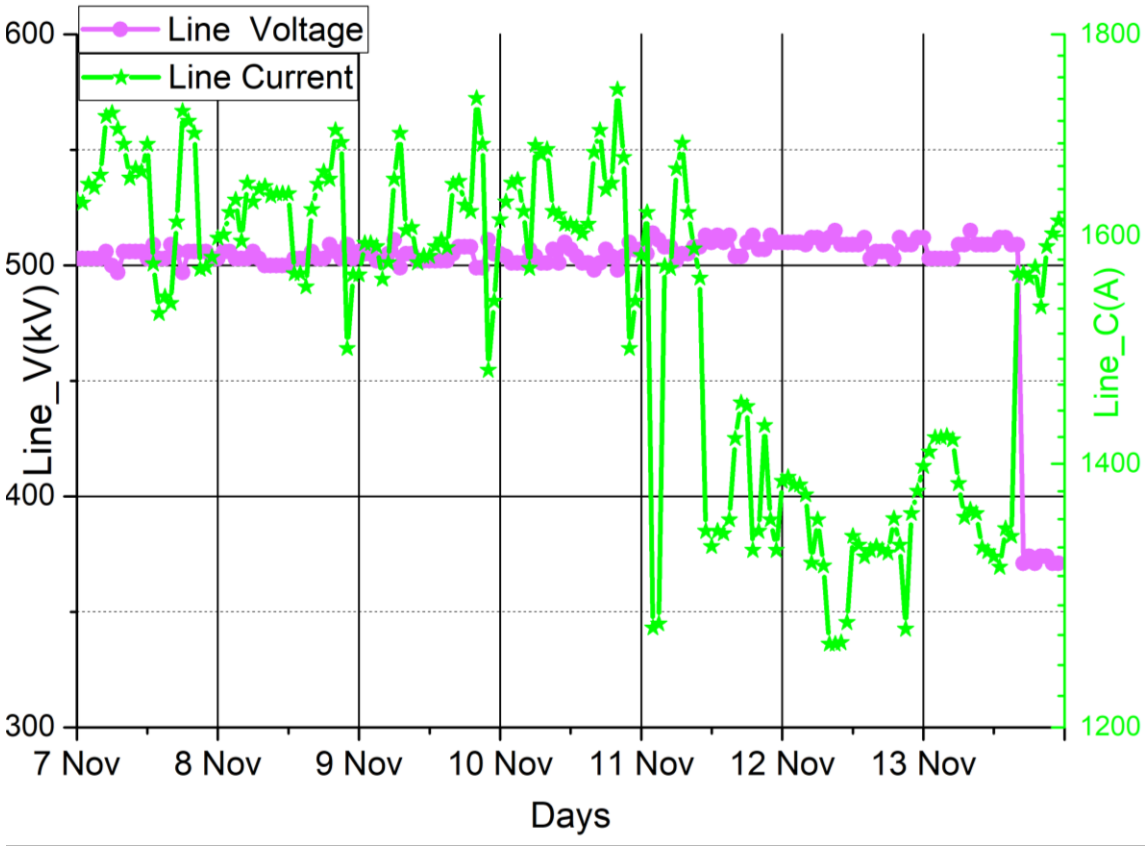

Figure 6.15: Line voltage and current: 7th - 13th of November

Correlation between LC and weather conditions: November 7th -13th

The correlation matrix for LC versus the weather parameters is shown in Table 6.7. The daily average of each parameter studied is also given in Table 6.8. A positive correlation between composite insulator LC and temperature is again observed, as seen in the previous weeks. A positive correlation coefficient of 0.34 has been found between the composite insulator LC and temperature. During this week, the glass insulator exhibited a slightly positive correlation coefficient of 0.06 with temperature, indicating that the glass insulator LC increased marginally with increasing temperature. For humidity, the composite insulator LC again had a negative correlation coefficient (-0.15), but the glass insulator LC was essentially uncorrelated (correlation coefficient of -0.03).

A low correlation between insulator LC and rain has been observed for this week on both insulators. As explained for the previous week, the low correlation found could be due to continuous rainfall taking place, which leads to washing of the insulators instead of LC build-up that normally occurs during drizzly conditions. A low correlation between LC and line parameters were observed during this week.

From Table 6.8 it is evident that the composite insulator LC remains constant throughout the week in spite of the adverse weather conditions, whereas the presence of rain and high humidity led to elevated LC on the glass insulator.

Table 6.7: Correlation matrix between LC and weather conditions for November 7th - 13th

	Composite shunt	Glass shunt	Temperature	Humidity	Rain	Line voltage	Line current
Composite shunt	1.00						
Glass shunt	0.02	1.00					
Temperature	0.34	0.06	1.00				
Humidity	-0.15	-0.03	-0.88	1.00			
Rain	-0.09	-0.01	-0.07	0.13	1.00		
Line voltage	0.14	0.04	-0.12	0.36	0.06	1.00	
Line current	-0.05	0.04	0.04	0.07	0.00	-0.17	1.00

Table 6.8: Daily averages of each parameter studied for November 7th - 13th

Days	Composite shunt [mA]	Glass shunt [mA]	Temperature [°C]	Humidity [%]	Rain [mm]	Line voltage [kV]	Line current [A]
07-Nov	0.03	0.03	19.75	87.00	0.00	504.13	1640.04
08-Nov	0.03	0.03	20.26	77.67	0.00	503.50	1621.13
09-Nov	0.03	0.10	19.98	82.08	0.26	504.17	1606.13
10-Nov	0.03	0.05	19.55	82.83	0.07	503.54	1633.71
11-Nov	0.03	0.08	16.16	92.33	0.27	508.67	1452.38
12-Nov	0.03	0.03	18.83	80.21	0.12	509.29	1333.17
13-Nov	0.03	0.03	21.17	68.00	0.04	468.50	1439.96
Weekly average	0.03	0.05	19.39	81.45	0.11	500.26	1532.36

6.3.5 LC measurements using the shunt resistors only: December 8th - 14th

Figure 6.16 shows the LC activity between the 8th and 14th of December.

No HVDC line voltage and current have been obtainable at Apollo since the beginning of December 2016 and are, therefore, not presented.

Figure 6.17 shows the weather conditions for the same period. On the 10th of December, when high rainfall commenced, an increase in LC is observed on the glass insulator. No elevated LC activity is observed on the composite insulator during the same timeframe. During sustained

periods of rain, the LC levels on the glass insulator revert back to nominal levels, indicating the washing of insulators.

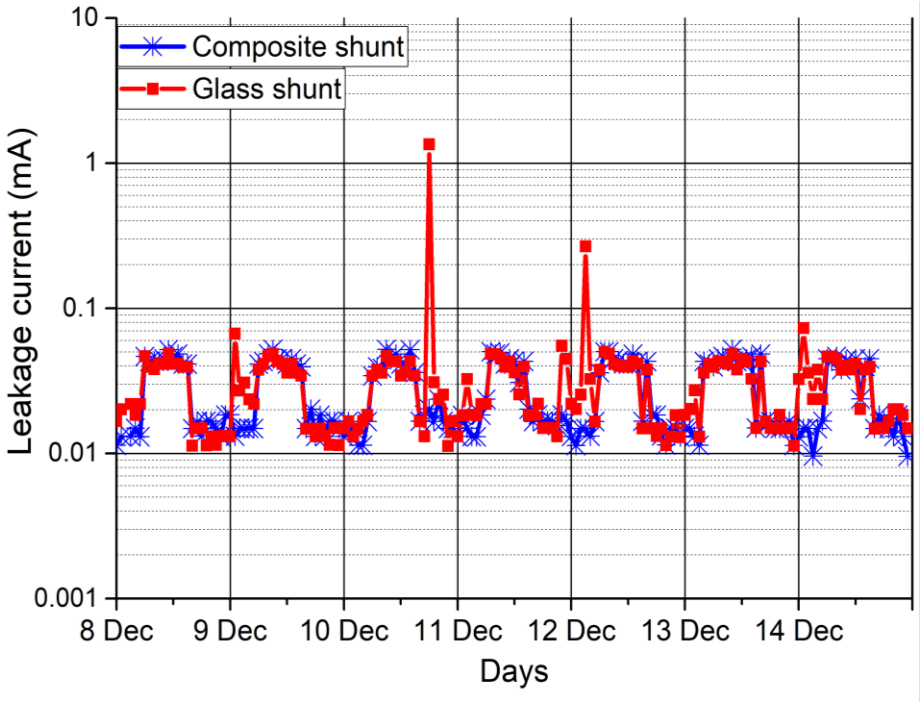

Figure 6.16: Leakage current activity using the shunt resistors only: 8th - 14th of December

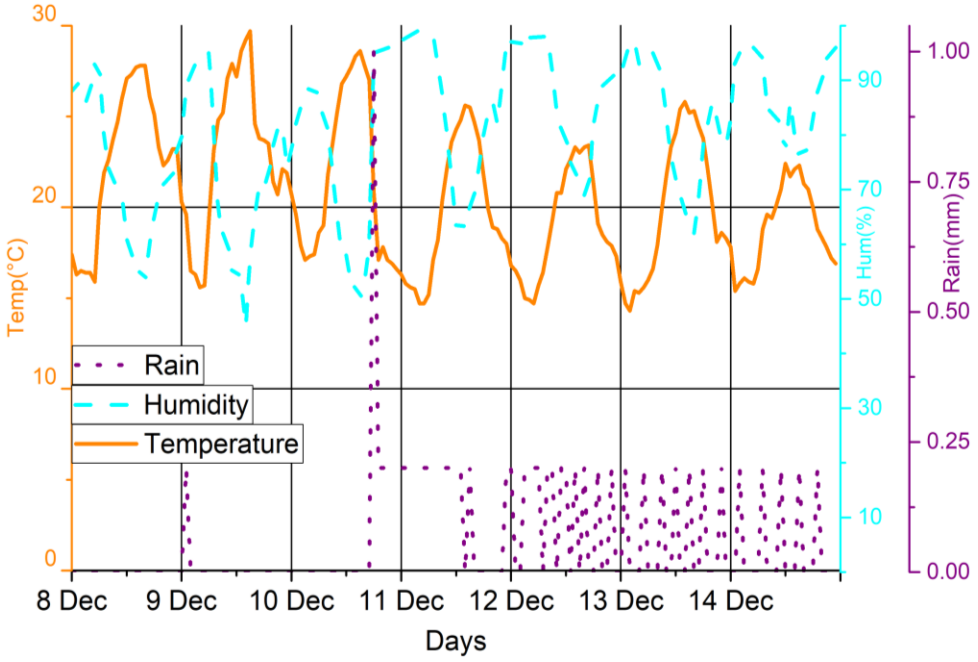

Figure 6.17: Weather conditions: 8th - 14th of December

Correlation between LC and weather conditions: December 8th - 14th

The correlation matrix for LC versus weather parameters have been calculated for this week as shown in Table 6.9. The daily average of each parameter studied is also given in Table 6.10.

A positive correlation between composite insulator LC and temperature is again observed as seen in the previous weeks. A positive correlation coefficient of 0.45 has been calculated between the composite insulator LC and temperature. During this week, the glass insulator exhibited an essentially uncorrelated behaviour with temperature (correlation coefficient of 0.01).

When humidity increases, the composite and glass insulator LC again behaved in an opposite manner. A negative correlation coefficient of -0.35 has been calculated for composite insulator LC versus humidity and a positive correlation coefficient of 0.08 for glass insulator LC versus humidity. The composite insulator LC decreases when humidity increases, while the glass insulator LC slightly increases with increasing humidity.

A strong positive correlation coefficient of 0.64 has been identified between glass insulator LC and rain. This indicated that the glass insulator LC increases when rain is present. The composite insulator case had a correlation coefficient of -0.01 indicating that there was no relationship between composite insulator LC and rain for this week. Studying Table 6.10, the composite insulator LC remained unchanged when high humidity conditions and rain were present. The glass insulator experienced elevated LC during this timeframe.

Table 6.9: Correlation matrix between LC and weather conditions for December 8th - 14th

	Composite shunt	Glass shunt	Temperature	Humidity	Rain
Composite shunt	1.00				
Glass shunt	0.06	1.00			
Temperature	0.45	0.01	1.00		
Humidity	-0.35	0.08	-0.95	1.00	
Rain	-0.01	0.64	-0.21	0.30	1.00

Table 6.10: Daily averages of each parameter studied for December 8th - 14th

Days	Composite shunt [mA]	Glass shunt [mA]	Temperature [°C]	Humidity [%]	Rain [mm]
08-Dec	0.03	0.03	22.55	73.42	0.00
09-Dec	0.03	0.03	22.83	73.58	0.01
10-Dec	0.03	0.08	21.58	77.42	0.08
11-Dec	0.03	0.03	19.73	84.83	0.13
12-Dec	0.03	0.04	18.94	87.58	0.11
13-Dec	0.03	0.03	19.92	82.79	0.06
14-Dec	0.03	0.03	18.84	87.54	0.04
Weekly average	0.03	0.04	20.63	81.02	0.06

6.3.6 LC measurements using the shunt resistors only: December 29th - January 4th

Figure 6.18 shows the LC activity between the 29th of December to the 4th of January. Figure 6.19 shows the weather conditions for the same period. During the evening, on the 3rd of January, increased LC is observed on the glass insulator. This increase coincides again with the commencement of high rainfall and high humidity. No increased LC behaviour is observed on the composite insulator.

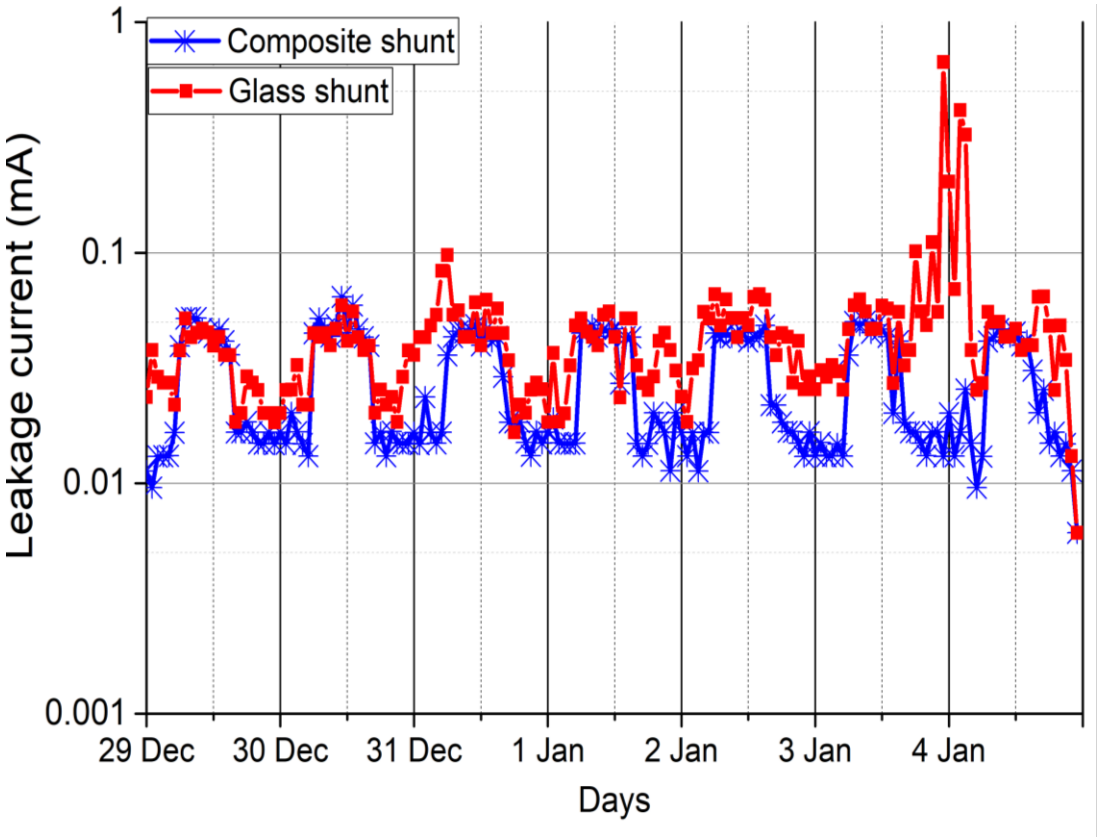

Figure 6.18: Leakage current activity using the shunt resistors only: 29th of December - 4th of January

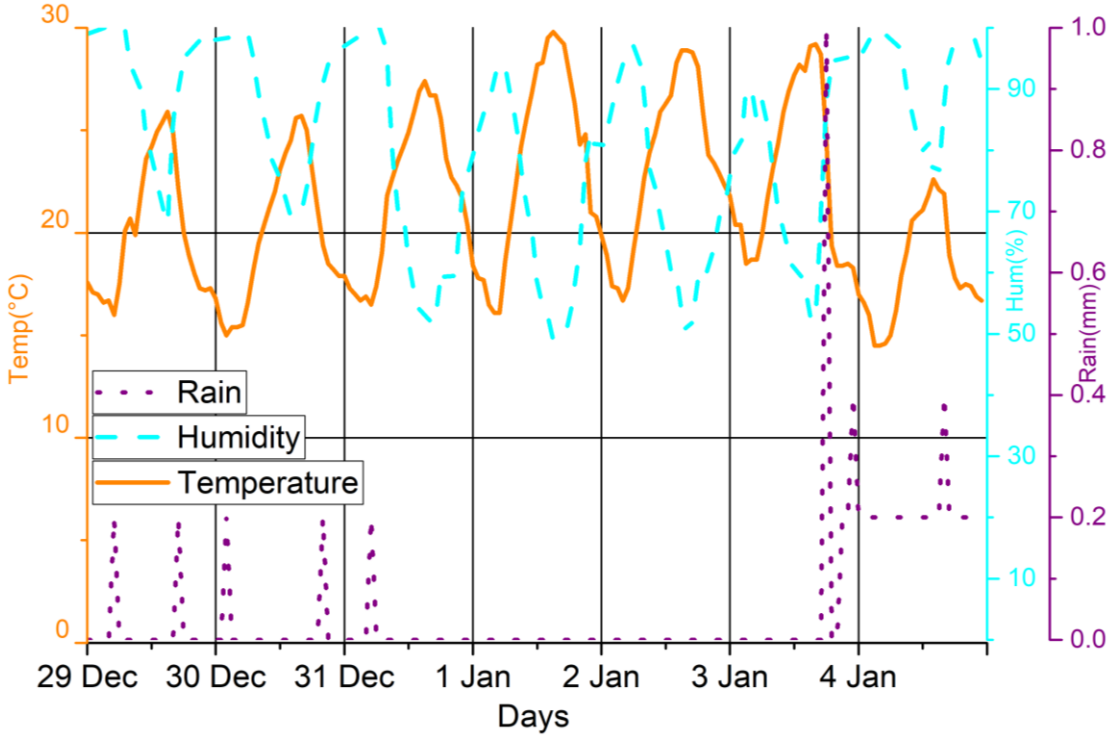

Figure 6.19: Weather conditions: 29th of December - 4th of January

Correlation between LC and weather conditions: December 29th - January 4th

The correlation matrix for LC versus weather parameters is shown in Table 6.11. The daily average of each parameter studied is also given in Table 6.12. A positive correlation between composite insulator LC and temperature is again observed as seen in the previous weeks. A positive correlation coefficient of 0.41 has been calculated between the composite insulator LC and temperature. During this week, the glass insulator exhibited a slightly negative correlation coefficient of -0.1 with temperature. When humidity increases, the composite and glass insulator's LC decreased and increased, respectively. A negative correlation coefficient of -0.26 has been calculated for composite insulator LC versus humidity, and a positive correlation coefficient of 0.13 for the glass insulator LC versus humidity. The composite insulator LC decreases when humidity increases, while the glass insulator LC slightly increases with increasing humidity.

A positive correlation coefficient of 0.36 has been observed between glass insulator LC and rain. This indicates that the glass insulator LC increases when rain is present. The composite insulator case had a negative correlation coefficient of -0.16 indicating that the composite insulator LC decreases slightly when rain is present. The highest LC activity was observed on the glass insulator when high humidity conditions and rain were present. The LC level of the composite insulator remained unchanged throughout the week.

Table 6.11: Correlation matrix between LC and weather conditions for December 29th - January 4th

	Composite shunt	Glass shunt	Temperature	Humidity	Rain
Composite shunt	1.00				
Glass shunt	0.03	1.00			
Temperature	0.41	-0.10	1.00		
Humidity	-0.26	0.13	-0.92	1.00	
Rain	-0.16	0.36	-0.23	0.28	1.00

Table 6.12: Daily averages of each parameter studied for December 29th - January 4th

Days	Composite shunt [mA]	Glass shunt [mA]	Temperature [°C]	Humidity [%]	Rain [mm]
29-Dec	0.03	0.03	20.04	92.00	0.02
30-Dec	0.03	0.03	19.90	87.08	0.02
31-Dec	0.03	0.05	21.90	76.00	0.01
01-Jan	0.03	0.04	23.33	72.21	0.00
02-Jan	0.03	0.04	23.29	73.13	0.00
03-Jan	0.03	0.08	22.86	77.79	0.08
04-Jan	0.03	0.08	18.12	92.42	0.21
Weekly average	0.03	0.05	21.35	81.52	0.05

6.3.7 LC measurements using the shunt resistors only: February 16th - 22nd

Figure 6.20 shows the LC activity between the 16th and 22nd of February. Figure 6.21 shows the weather conditions for the same period. Between the 20th and 22nd of February increased LC is observed on glass insulator. During this timeframe, rain is present, humidity is high and the temperature is low. Figure 6.20 displays that LC on the glass insulator is only elevated when rain commences, and then returns back to nominal levels. The LC on composite insulators again shows no increase above nominal levels.

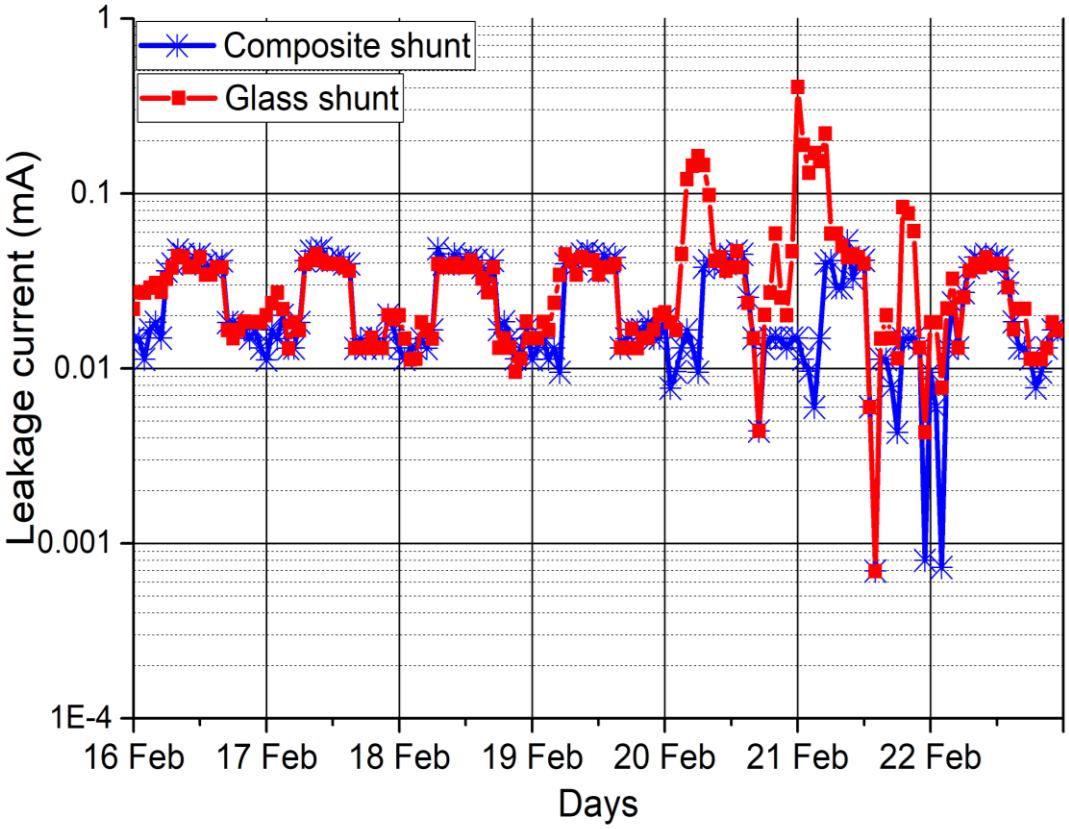

Figure 6.20: Leakage current activity using the shunt resistors only: 16th - 22nd February

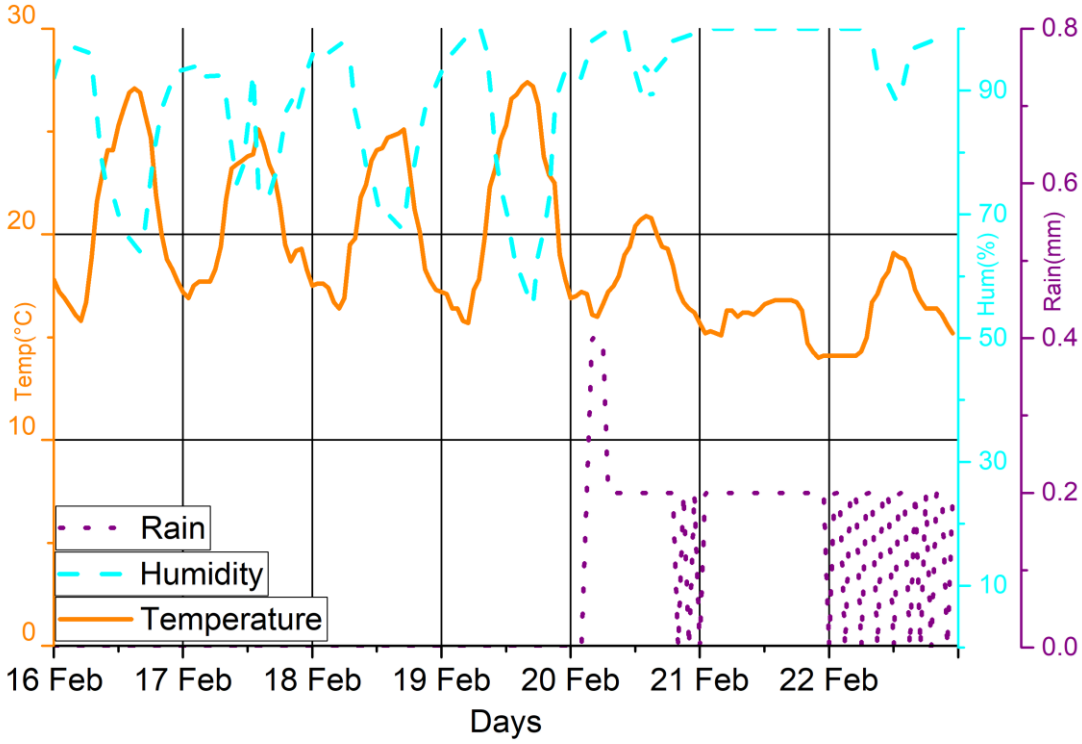

Figure 6.21: Weather conditions: 16th - 22nd February

Correlation between LC and weather conditions: February 16th - 22nd

The correlation matrix for LC versus weather parameters is shown in Table 6.13. The daily average of each parameter studied is also given in Table 6.14. A positive correlation between composite insulator LC and temperature is again observed as seen in the previous weeks. A positive correlation coefficient of 0.5 is calculated between the composite insulator LC and temperature. During this week, the glass insulator exhibited a negative correlation coefficient of -0.15 with temperature. When humidity increases, the composite and glass insulator LC again behaved in an opposite manner. A negative correlation coefficient of -0.36 has been calculated for composite insulator LC versus humidity and a positive correlation coefficient of 0.18 for glass insulator LC versus humidity.

When rain was present, the composite insulator exhibited a slightly negative correlation coefficient of -0.11 and the glass insulator a positive correlation coefficient of 0.31. This indicates that the composite insulator LC decreased when rain is present and the glass insulator increases when rain is present. High humidity and continuous rain were present for the last 3 days of the week (as shown in Table 6.14). However, on the last day of the week, the glass insulator did not exhibit elevated LC. This can again be due to the glass insulator being washed by the rain and that no more contaminants remained on the glass insulator's surface due to the continuous rain.

Table 6.13: Correlation matrix between LC and weather conditions for February 16th - 22nd

	Composite shunt	Glass shunt	Temperature	Humidity	Rain
Composite shunt	1.00				
Glass shunt	0.12	1.00			
Temperature	0.50	-0.15	1.00		
Humidity	-0.36	0.18	-0.94	1.00	
Rain	-0.11	0.31	-0.46	0.50	1.00

Table 6.14: Daily averages of each parameter studied for February 16th - 22nd

Days	Composite shunt [mA]	Glass shunt [mA]	Temperature [°C]	Humidity [%]	Rain [mm]
16-Feb	0.03	0.03	21.17	83.17	0.00
17-Feb	0.03	0.03	20.59	86.00	0.00
18-Feb	0.03	0.02	20.54	83.88	0.00
19-Feb	0.03	0.03	21.52	81.83	0.00
20-Feb	0.02	0.05	18.11	96.21	0.18
21-Feb	0.02	0.08	15.85	99.96	0.19
22-Feb	0.02	0.02	16.21	96.58	0.13
Weekly average	0.02	0.04	19.14	89.66	0.07

6.3.8 LC measurements using the shunt resistors only: April 12th - 18th

Figure 6.22 shows the LC activity between the 12th and 18th April. Figure 6.23 shows the weather conditions for the same period. At the onset of rain on the 12th of April, elevated LC is observed on the glass insulator. On the 15th of April when humidity is above 90%, increased LC on the glass insulator is seen again. The composite insulator remains at its nominal LC level throughout the week.

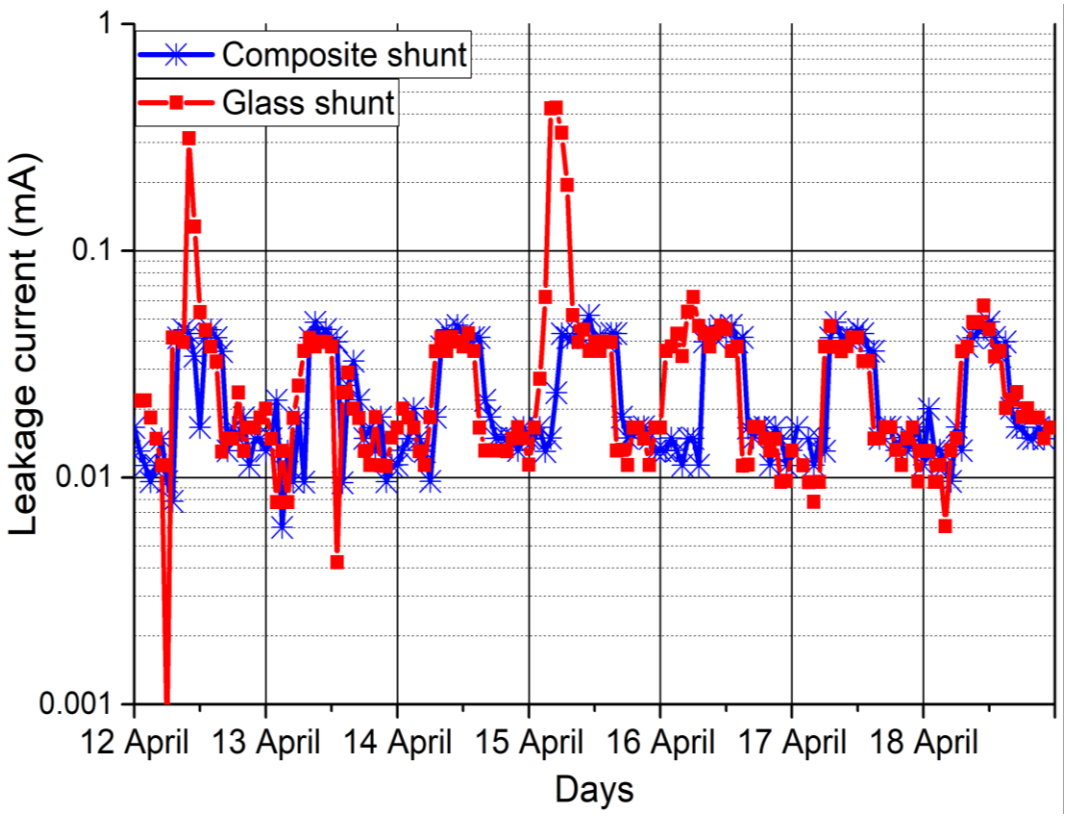

Figure 6.22: Leakage current activity using the shunt resistors only: 12th - 18th April

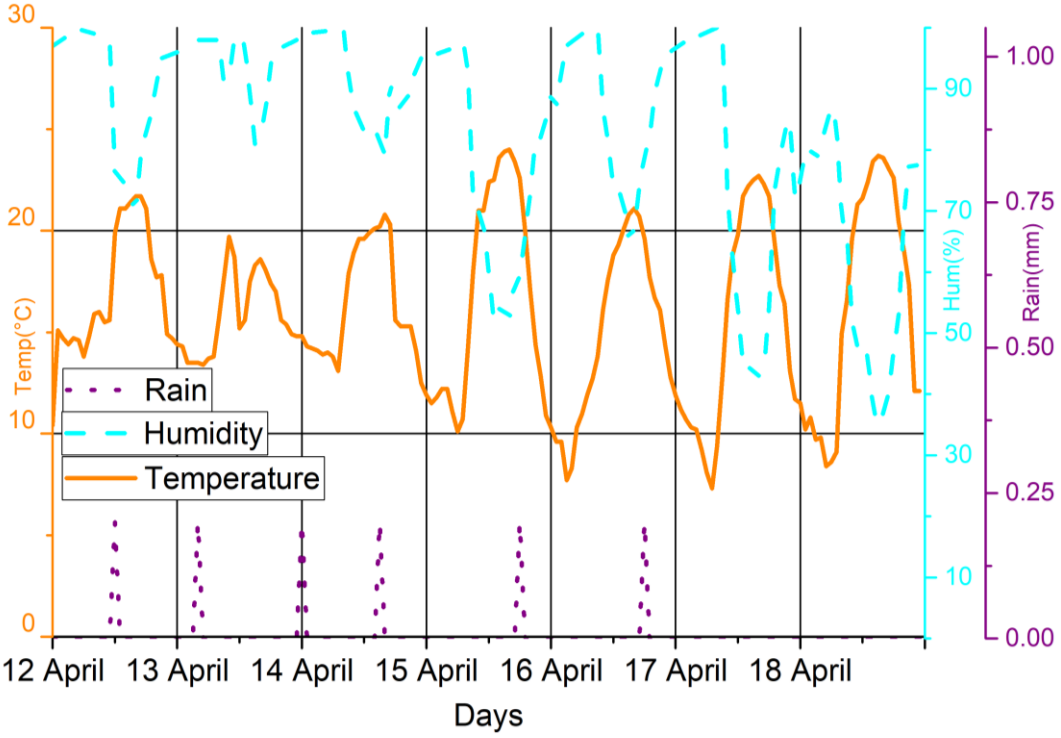

Figure 6.23: Weather conditions: 12th - 18th April

Correlation between LC and weather conditions: April 12th - 18th

The correlation matrix for LC versus the weather parameters is shown in Table 6.15. The daily average of each parameter studied is also given in Table 6.16. A positive correlation between composite insulator LC and temperature is again observed as seen in the previous weeks. A positive correlation coefficient of 0.46 is observed between the composite insulator LC and temperature. The glass insulator exhibited a slightly negative correlation coefficient of -0.1 with temperature.

When humidity increases, the composite and glass insulator LC decreased and increased, respectively. The correlation coefficient between composite and glass insulator LC versus humidity is -0.2 and 0.2, respectively. When rain was present, the composite and glass insulator LC decreased and increased, respectively, as before. The correlation coefficient between composite and glass insulator LC versus rain was -0.13 and 0.2, respectively. No elevated LC were observed on the composite insulator during this week, even in high humidity and rainy conditions. The glass insulator, however, was affected by the adverse conditions.

Table 6.15: Correlation matrix between LC and weather conditions for April 12th - 18th

	Composite shunt [mA]	Glass shunt [mA]	Temperature [°C]	Humidity [%]	Rain [mm]
Composite shunt [mA]	1.00				
Glass shunt [mA]	0.24	1.00			
Temperature [°C]	0.46	-0.10	1.00		
Humidity [%]	-0.20	0.20	-0.71	1.00	
Rain [mm]	-0.13	0.20	0.01	0.10	1.00

Table 6.16: Daily averages of each parameter studied for April 12th - 18th

Days	Composite shunt [mA]	Glass shunt [mA]	Temperature [°C]	Humidity [%]	Rain [mm]
12-Apr	0.02	0.05	18.98	83.25	0.03
13-Apr	0.02	0.05	18.98	83.25	0.03
14-Apr	0.02	0.04	15.86	94.79	0.01
15-Apr	0.02	0.02	16.26	91.63	0.02
16-Apr	0.02	0.02	16.75	77.13	0.01
17-Apr	0.03	0.08	14.94	87.04	0.01
18-Apr	0.02	0.03	15.30	76.71	0.00
Weekly average	0.02	0.04	16.72	84.83	0.02

6.3.9 LC measurements using the shunt resistors only: May 10th - 16th

Figure 6.24 shows the LC activity between the 10th and 16th of May. Figure 6.25 shows the weather conditions for the same period. Elevated LC activity is seen from the 11th to the 13th of May on the glass insulator. Low temperatures, high humidity conditions and the onset of continuous rain are observed in this timeframe. Continuous rainfall is present from the 13th of May but the LC levels remain close to nominal levels on the glass and composite insulator. The effect of the ambient weather conditions on the composite insulator is minimal.

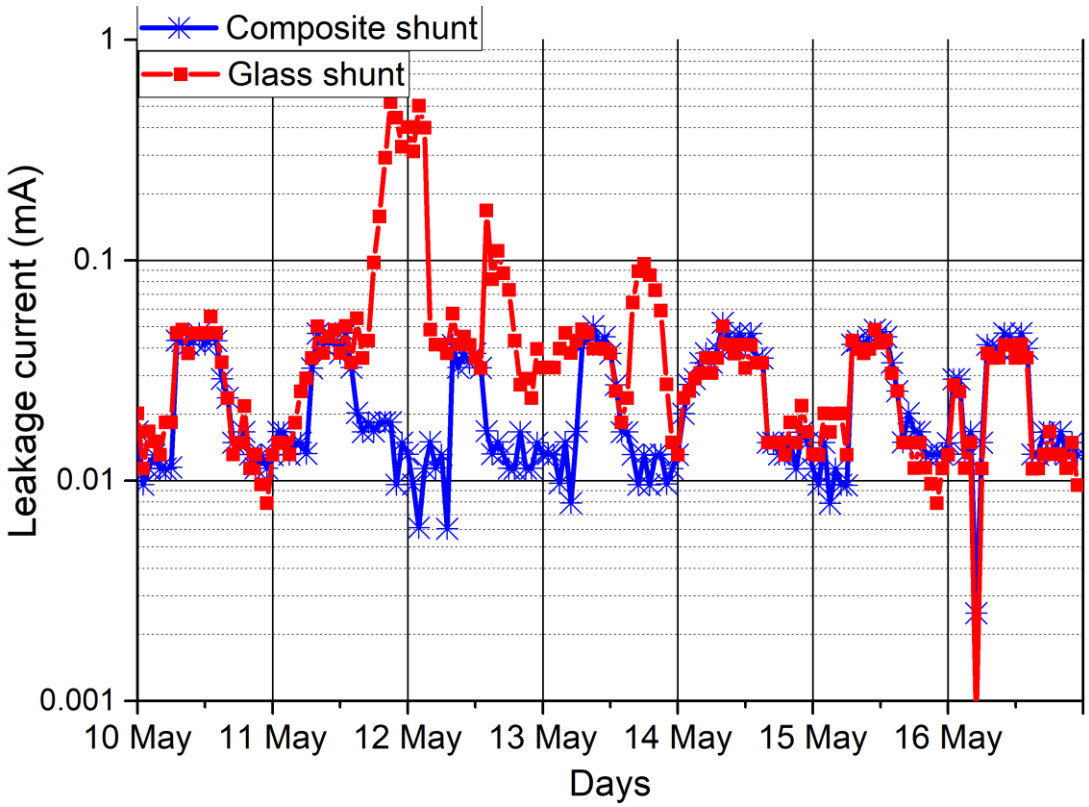

Figure 6.24: Leakage current activity using the shunt resistors only: 10th - 16th May

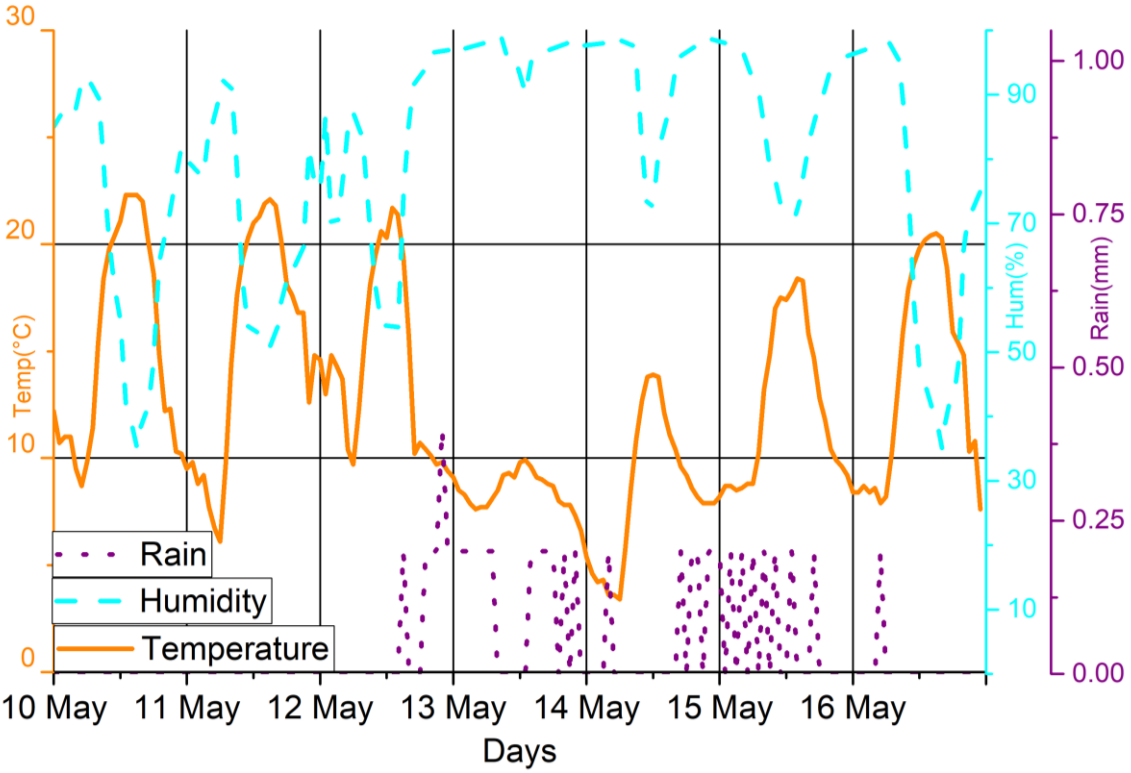

Figure 6.25: Weather conditions: 10th - 16th May

Correlation between LC and weather conditions: May 10th - 16th

The correlation matrix for LC versus the weather parameters is shown in Table 6.17. The daily average of each parameter studied is also given in Table 6.18. A positive correlation (correlation coefficient = 0.54) between composite insulator LC and temperature is again observed as seen in the previous weeks. During this week, the glass insulator exhibited a slightly negative correlation coefficient of -0.16 with temperature. When humidity increases, the composite and glass insulator LC decreased and increased, respectively. The correlation coefficient between composite and glass insulator LC versus humidity is -0.34 and 0.23, respectively. When rain was present, the composite and glass insulator LC decreased and increased, respectively. The correlation coefficient between composite and glass insulator LC versus rain was -0.24 and 0.54, respectively. Studying the correlation of rain and composite insulator LC, it can also be inferred that washing of the composite insulators has taken place this week due to the negative correlation with rain. From Table 6.18 it is observed that the highest glass insulator LC occurred on the 14th of May when the average humidity was the highest for the week and the most rain fell. During the same period, the composite insulator LC remain unchanged at 0.02 mA.

Table 6.17: Correlation matrix between LC and weather conditions for May 10th - 16th

	Composite shunt [mA]	Glass shunt [mA]	Temperature [°C]	Humidity [%]	Rain [mm]
Composite shunt [mA]	1.00				
Glass shunt [mA]	-0.11	1.00			
Temperature [°C]	0.54	-0.16	1.00		
Humidity [%]	-0.34	0.23	-0.88	1.00	
Rain [mm]	-0.24	0.54	-0.31	0.39	1.00

Table 6.18: Daily averages of each parameter studied for May 10th - 16th

Days	Composite shunt [mA]	Glass shunt [mA]	Temperature [°C]	Humidity [%]	Rain [mm]
10-May	0.02	0.03	15.46	68.88	0.00
11-May	0.02	0.03	15.46	68.88	0.00
12-May	0.02	0.03	15.18	70.25	0.00
13-May	0.02	0.10	14.38	78.54	0.06
14-May	0.02	0.11	8.48	96.71	0.13
15-May	0.02	0.05	8.39	93.21	0.05
16-May	0.03	0.03	12.46	87.67	0.07
Weekly average	0.02	0.05	12.83	80.59	0.04

6.3.10 LC behaviour over a year

The insulators' LC has been monitored throughout the year to account for seasonal variations and anomalies. This provides a better understanding of the insulators' LC activity. Figure 6.26 shows the LC activity for the composite and glass insulators from August 2016 to June 2017.

From Figure 6.26, it is evident that elevated LC activity occurs more frequently in the spring-summer period (September to February), which is the rainy season for Johannesburg. In winter (June to August), there have been far fewer occurrences of elevated LC on the insulators. It is also observed that the glass insulator experiences higher levels of LC throughout the measurement period when compared to the composite insulator. This can be attributed to the composite insulator's hydrophobicity properties. The average LC for the 11-month period was calculated as well for the composite and glass insulator. On average, the LC over the 11-month period was 0.026 mA and 0.034 mA for the composite and glass insulator, respectively. Thus, more power is lost (13.89 kW and 18.12 kW for composite and glass insulator strings, respectively, when the LC is multiplied by 533 kV) when the transmission line is equipped with glass insulators. Also, the adverse weather conditions did not affect the performance of the composite insulator but resulted in elevated LCs on the glass insulator.

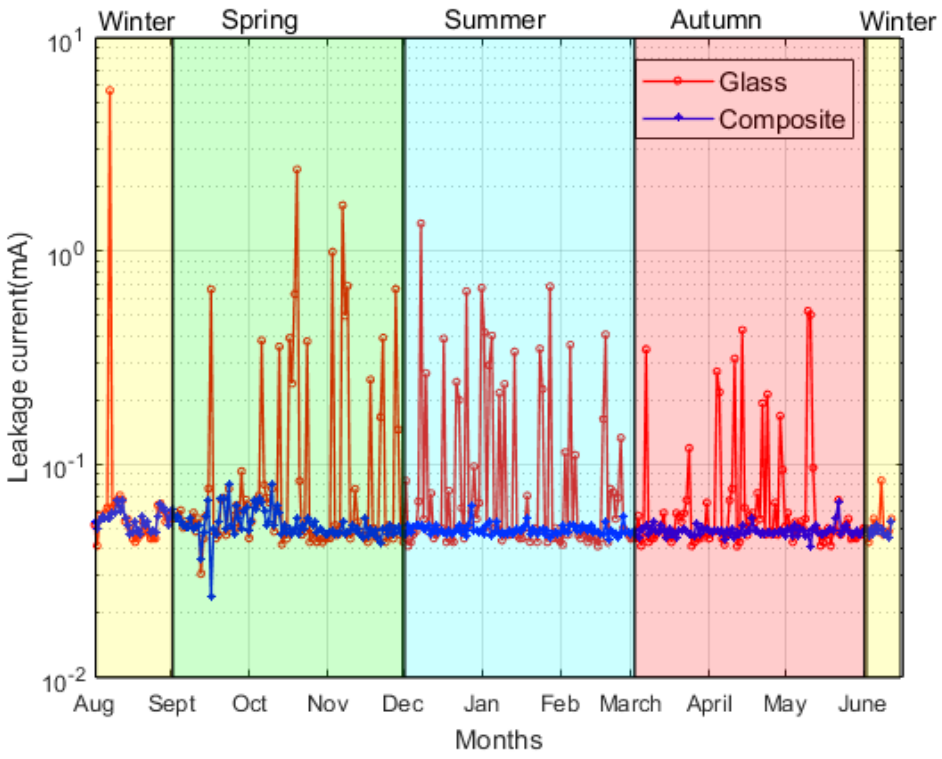

Figure 6.26: Daily leakage current from Aug 2016 - June 2017

Correlation between LC and weather conditions over a year

It is informative to determine the overall correlation of the LC with the weather parameters over the period of a year to draw general conclusions. The correlation matrix as shown in Table 6.19 for LC versus the weather parameters have been calculated over the period of a year.

Temperature

A strong positive correlation between composite insulator LC and temperature was observed over the 11-month period. A positive correlation coefficient of 0.4 is calculated, indicating that as the ambient temperature increases, so does the LC. During the same timeframe, the glass insulator exhibited a slightly negative correlation coefficient of -0.12 with temperature; essentially showing that glass insulators are not much influenced by temperature.

Humidity

When humidity increased, the composite and glass insulator LC decreased and increased, respectively. The correlation between composite and glass insulator LC versus humidity is calculated to be -0.28 and 0.13, respectively.

Rain

When rain was present, no correlation between the composite insulator LC and rain was observed. This indicates that rain had minimal impact on the composite insulator's performance. However, for the glass insulator LC, a positive correlation coefficient of 0.43 was observed. This indicates that the glass insulators performance is far more susceptible to adverse weather conditions (rain) as compared to composite insulators.

Table 6.19: Correlation matrix between LC and weather conditions from August 2016 to June 2017

	Composite shunt [mA]	Glass shunt [mA]	Temperature [°C]	Humidity [%]	Rain [mm]
Composite shunt [mA]	1.00				
Glass shunt [mA]	-0.04	1.00			
Temperature [°C]	0.40	-0.12	1.00		
Humidity [%]	-0.28	0.13	-0.73	1.00	
Rain [mm]	-0.03	0.43	0.00	0.06	1.00

Correlation between LC and line conditions

Although line voltage and current measurements were only available from August to November 2016 of the in-situ tests, it is still informative to determine the average correlation between the LC and these parameters for the time that the combined data was available.

Line voltage

For the composite and glass insulator LC, correlation coefficients of, respectively, 0.06 and -0.17 are calculated. This implies that the composite insulator LC is essentially not influenced by the line voltage. For the glass insulator, the LC exhibits a slightly negative correlation, which is counter-intuitive as higher line voltages would ostensibly led to increased LC. Nevertheless, the analysis might be prone to statistical noise due to the limited number of data points, as well as the noisy nature of the data. For example, the correlation coefficients of one week considered was -0.46, which was an outlier in terms the other weeks considered (coefficients of 0.04, -0.19, 0.07, respectively). Ignoring the apparent outlier, an average correlation coefficient of -0.07 would have been calculated, which implies effective independence of the LC to the line voltage. Further studies of this phenomenon can be done in future.

Line current

For the composite and glass insulator LC, correlation coefficients of, respectively, 0.01 and 0.11 are calculated. This implies that the composite insulator LC is essentially independent of the line current, but that the line current on the glass insulator has a marginally positive correlation.

6.4 Additional observations from in-situ measurements

6.4.1 Effect of condensation on LC

During the measurement period, it has been observed that increased LC activity on both types of insulators normally takes place late evening to early morning when the temperature is at its lowest and humidity at its highest. This is in agreement with the HVAC insulator LC measurements reported in literature (Suwarno & Parhusip, 2010; Ferreira *et al*., 2010; Meyer *et al*., 2011; Werneck *et al*., 2014). Furthermore, under nominal weather conditions of no rain and low humidity, the LC measurements exhibit an almost square-wave behaviour with LC switching between lower and higher values with relatively short transitions on a daily basis. This behaviour cannot be explained directly in terms of the ambient humidity and temperature, as these parameters display more gradual daily temporal cycles. It can also not be ascribed to fluctuations in the line current or voltages, as these have been found to have little or no correlation with the LC behaviour. This

has led to an investigation of the possible effect of the ambient dew point, and the corresponding occurrence of condensation, on the LC.

Figure 6.27 and Figure 6.28 show the composite and glass insulator LC along with the difference between the ambient temperature (T) and dew point temperature (Td) from the 3rd to the 8th of August and from the 8th to the 14th of June, respectively. The data for the 9th of August has been omitted, as very high humidity conditions are present on the day.

Figure 6.29 shows the composite and glass insulator LC along with the difference temperature (T – Td) for the 9th and 10th of June to clearly show the quick transition in LC when the difference between the T and Td is at its lowest and highest.

It is evident that as soon as the ambient temperature approaches the dew point temperature (where the likelihood of condensation on the insulators is high), a sharp rise in the nominal LC is triggered. This is observed for both types of insulators. On the other hand, when the difference between the ambient temperature and the dew point temperature is at its highest (where the likelihood of condensation on the insulators is low), the LC falls quickly. Hence, it can be deduced that condensation triggers the sharp daily rise and fall of LC between its nominally low and high values of 20 µA and 60 µA, respectively. A similar trend has been observed throughout the measurement period, although not presented here.

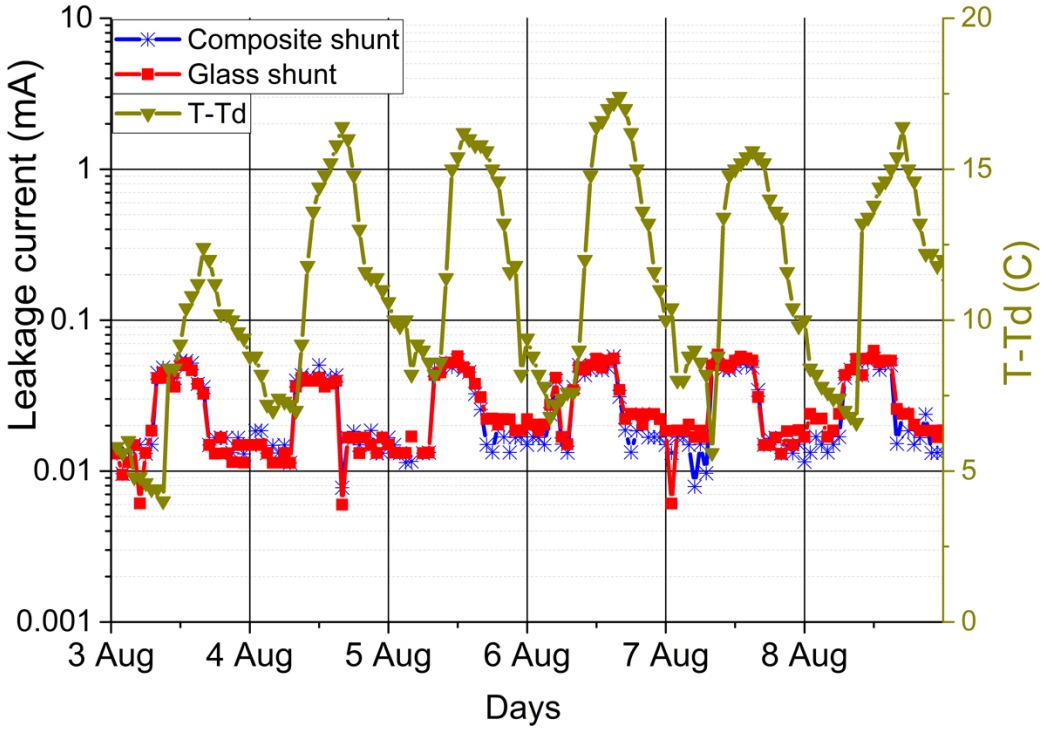

Figure 6.27: Leakage current activity with the difference between ambient temperature and dewpoint (T-Td): 3rd - 8th of August

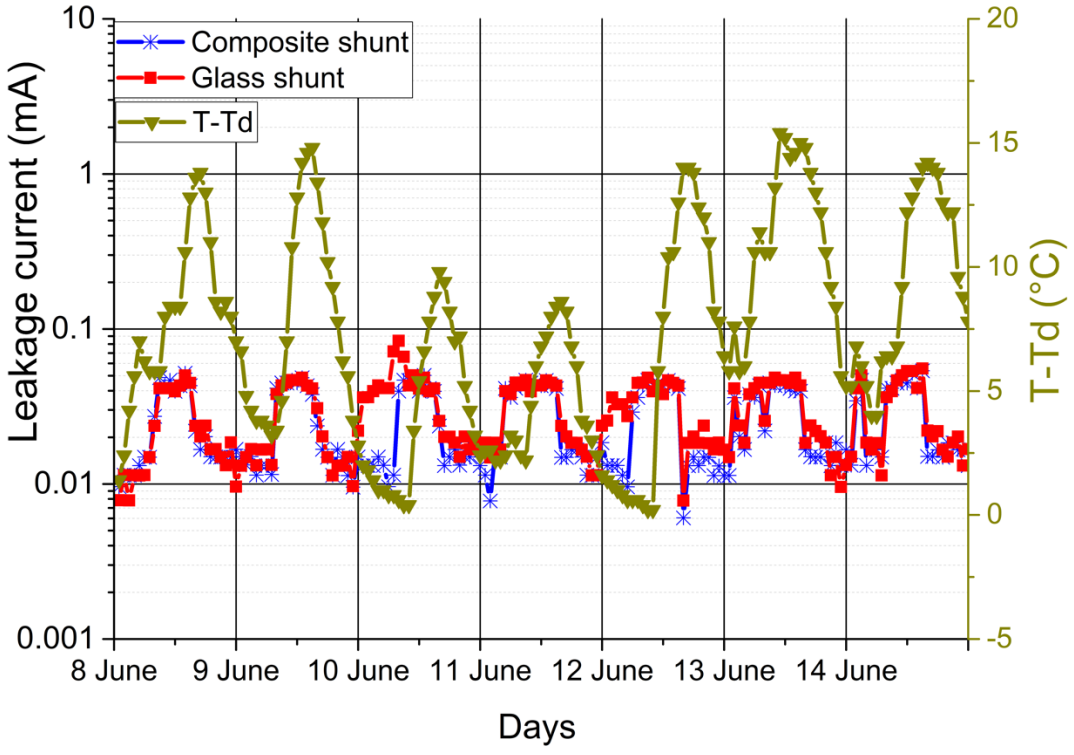

Figure 6.28: Leakage current activity with the difference between ambient temperature and dewpoint (T-Td): 8th - 14th of June

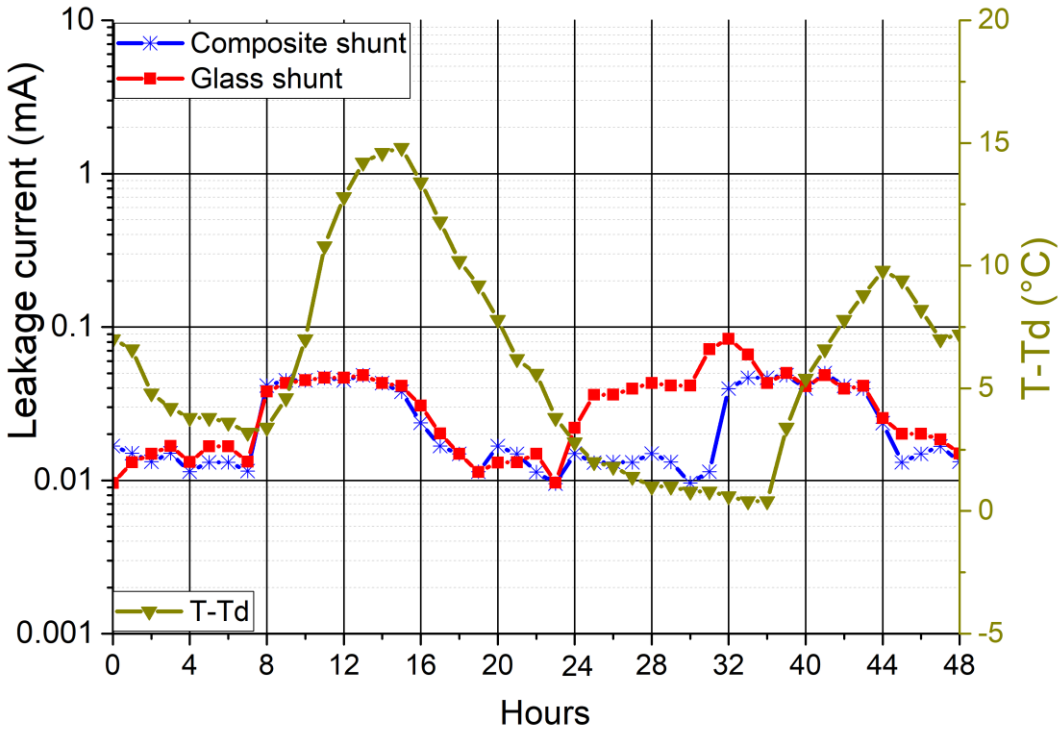

Figure 6.29: Leakage current activity with the difference between ambient temperature and dewpoint for the 9th and 10th of June

6.4.2 Cahora Bassa LC compared to LC of other operational ac transmission lines

The Cahora Bassa LC measurements were also compared to other LC measurements performed on operational ac transmission lines (no LC data for other operational dc transmission lines were found in literature) with similar voltage ratings. These are discussed here.

Oliveira *et al.* (2009) performed online glass insulator LC measurements on a 500 kV ac transmission line, specifically a tower located on top of the Maranguape Mountain (approximately 800 m above sea level) in the State of Ceará, Brazil. This transmission line resides in a tropical-humid climate that only has 1 to 3 dry months per year. The measured LC for this transmission line is presented in Figure 6.30.

Oliveira *et al.* (2009) defined 3 LC levels during their studies. All LC magnitudes less than 5 mA, 10 mA or 20 mA were classified as level 1, level 2 or level 3, respectively. The results showed that most LC magnitudes were under 20 mA. It is mentioned that wind, pollution and humidity were the major contributors to the increased LC.

This transmission line had higher LC magnitudes than those observed on the Cahora Bassa transmission line in this thesis. This area can be considered a medium to high pollution severity site due to its climatic conditions whereas the Cahora Bassa is a low pollution severity site with an ESDD of 0.03 mg/cm^2; thus, increased LC magnitudes were observed.

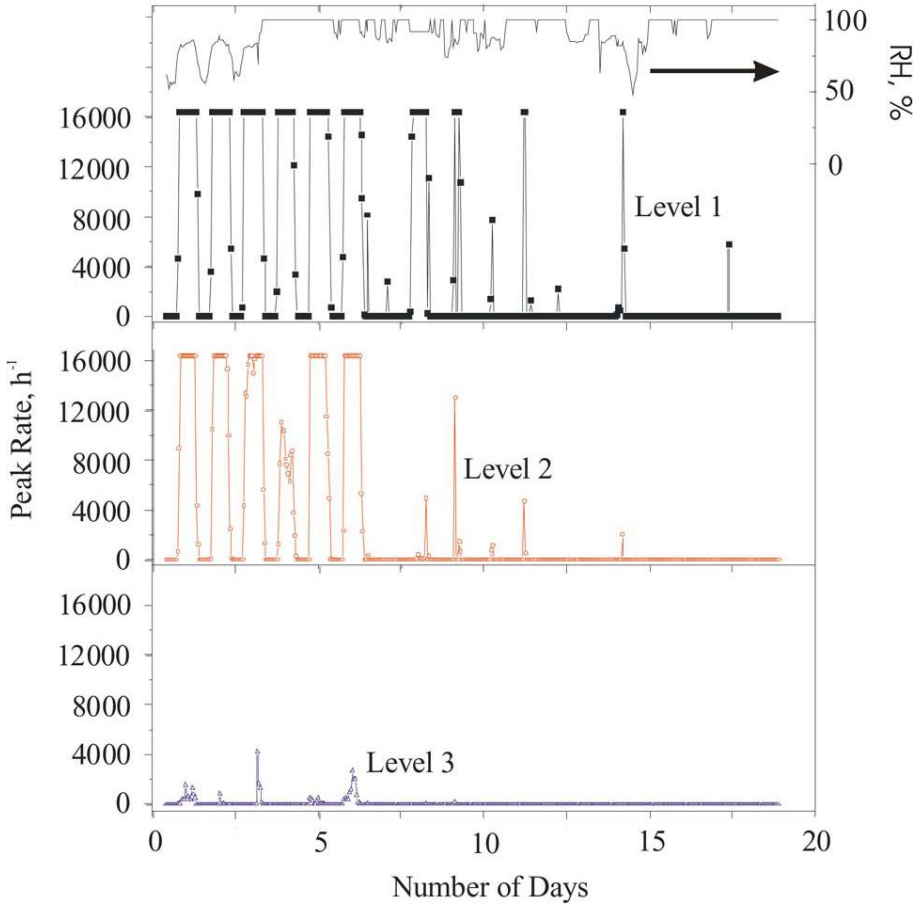

Figure 6.30: LC activity on the transmission line located on top of the Maranguape Mountain (From Oliveira *et al.*, 2009)

Werneck *et al*. (2014) performed real-time glass insulator LC monitoring on an 500 kV ac transmission line, located in São Luis, Brazil, where strong winds blow pollutants on the insulators. The LC results compared to climatic conditions can be seen in Figure 6.31. Higher LC activity is observed for these glass insulators compared to those of the Cahora Bassa. This area can also be considered to be a medium to high severity site based on the strong wind blowing pollutants from the sea. A similar LC pattern (although higher in magnitude) to those seen on the Cahora Bassa transmission line is observed.

From these 2 ac transmission line comparisons, it can be concluded that environmental conditions affect ac and dc insulators in a similar manner.

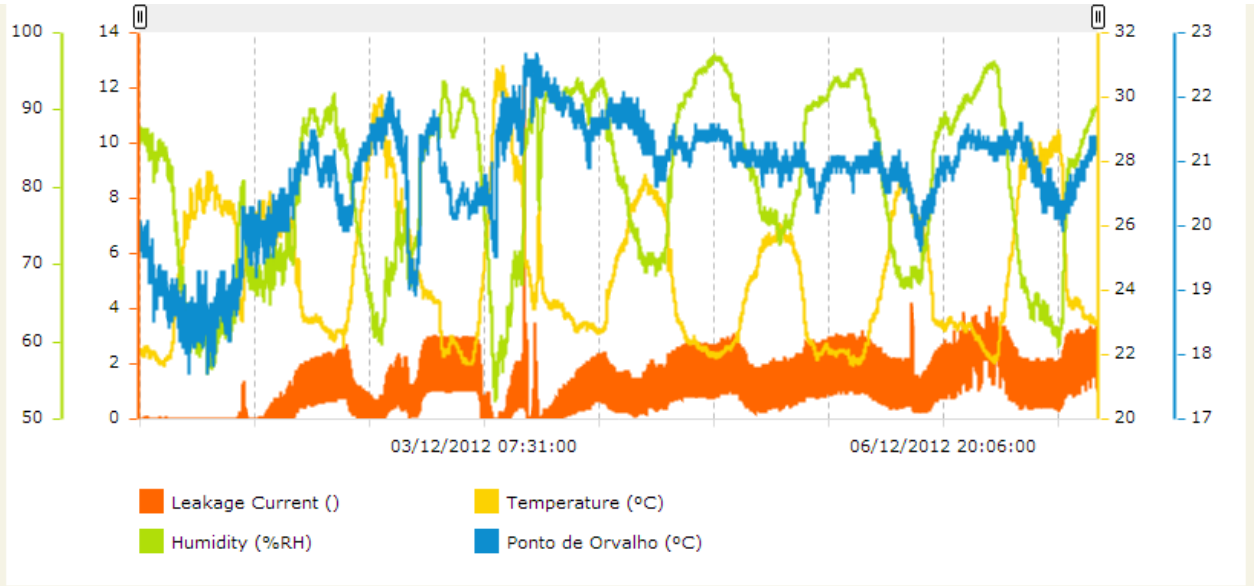

Figure 6.31: Insulator LC for a 500 kV ac transmission line located in São Luis, Brazil (From Werneck *et al.*, 2014)

6.4.3 Linear approximation of expected LC under HVDC conditions

For glass insulators, the nominal LC at the Cahora Bassa transmission line as measured at Apollo ranges from 20 µA to 60 µA, with an average of 34 µA over 11 months and no flashover reported. Instantaneous LC as high as 6 mA has been measured on the glass insulators, with typical elevated LC of the order 0.4 mA (refer to Figure 6.26).

An attempt is made here to determine if these levels of LC are consistent with the measured LC levels in the corona cage high voltage test facility under the same ESDD levels of 0.03 mg/cm^2 (Section 5.3) and if the measurements under those controlled conditions can be used to estimate the nominal LC levels in the actual transmission line. A first order linear approximation for determining the LC for HVDC insulator strings is described below. Such an approximation for HVDC insulators will be useful in predicting the performance of insulators based on tests done in the corona cage. This is akin to equations Equation 2.5 and Equation 2.11 where the highest LC on HVAC insulators is calculated in terms of ESDD and USCD.

It is assumed that the LC measured at Apollo and the corona cage can be approximated by the following equations, respectively:

$$LC_{Apollo} = V_{DC\_Apollo} \cdot G_{eff\_Apollo}$$ **Equation 6.1**

$$LC_{corona} = V_{DC\_corona} \cdot G_{eff\_corona}$$ **Equation 6.2**

with

$$G_{eff\_Apollo} = \frac{\sigma_{Apollo} \cdot A_{Apollo}}{L_{Apollo}}$$ **Equation 6.3**

$$G_{eff\_corona} = \frac{\sigma_{corona} \cdot A_{corona}}{L_{corona}}$$ **Equation 6.4**

where A_{Apollo} is the cross-sectional area of the insulator contamination layer at Apollo;
A_{corona} is the cross-sectional area of the insulator contamination layer at the corona cage;
σ_{Apollo} is the conductivity of the insulator contamination layer at Apollo;
σ_{corona} is the conductivity of the insulator contamination layer at the corona cage;
L_{Apollo} is the insulator leakage distance at Apollo; and
L_{corona} is the insulator leakage distance at the corona cage.

Further refinement for the cross-sectional areas gives:

$$A_{Apollo} = \phi_{Apollo} \cdot D_{Apollo}$$ **Equation 6.5**

$$A_{corona} = \phi_{corona} \cdot D_{corona}$$ **Equation 6.6**

where ϕ_{Apollo} is the mean diameter of the contamination layer at Apollo;
ϕ_{corona} is the mean diameter of the contamination layer at the corona cage;
D_{Apollo} is the thickness of the insulator contamination layer at Apollo; and
D_{corona} is the thickness of the insulator contamination layer at the corona cage.

Substituting Equations 6.3 through 6.6 into Equations 6.1 and 6.2 gives:

$$\frac{LC_{Apollo}}{LC_{corona}} = \frac{V_{DC\_Apollo}}{V_{DC\_corona}} \cdot \frac{G_{eff\_Apollo}}{G_{eff\_corona}} \qquad \textbf{Equation 6.7}$$

$$\frac{LC_{Apollo}}{LC_{corona}} = \frac{V_{DC\_Apollo}}{V_{DC\_corona}} \cdot \frac{\sigma_{Apollo}}{\sigma_{corona}} \cdot \frac{L_{corona}}{L_{Apollo}} \cdot \frac{A_{Apollo}}{A_{corona}} \qquad \textbf{Equation 6.8}$$

$$\frac{LC_{Apollo}}{LC_{corona}} = \frac{USCD_{corona}}{USCD_{Apollo}} \cdot \frac{\sigma_{Apollo}}{\sigma_{corona}} \cdot \frac{\phi_{Apollo}}{\phi_{corona}} \cdot \frac{D_{Apollo}}{D_{corona}} \qquad \textbf{Equation 6.9}$$

$$\frac{LC_{Apollo}}{LC_{corona}} = \frac{1}{USCD_{ratio}} \cdot \sigma_{ratio} \cdot \phi_{ratio} \cdot D_{ratio} \qquad \textbf{Equation 6.10}$$

With “ratio” referring to the ratio between the respective Apollo and corona cage parameters.

In Equation 6.10, the following ratios can be deemed as reliably known; $USCD_{ratio}$ (at Apollo, the USCD is 34 mm/kV for the glass insulators yielding a ratio of ≈ 3.54) and ϕ_{ratio} (the structure of the insulators at Apollo and at the corona cage is identical yielding a ratio of 1). The ratios of conductivity (assumed the same at 0.07 S/m) and contamination thickness are less reliably estimated. Both these ratios are highly dependent on the state of the insulators. For example, the conductivity of the Apollo glass insulator contamination layer was based on measurements that had been performed on these insulators before they had been replaced. Hence, a lower conductivity can be assumed for the Apollo insulators due to their improved condition. The same is applicable to the ratio of the layer thicknesses.

Considering the above, it is apparent from Equation 6.10 that LC measured at Apollo will at least be of the order 3.54 times smaller than those measured at the corona cage, which was done under conditions of aggressive wetting of the insulators. It can thus be expected that indeed both conductivity and thickness ratios be less than unity. Assuming the ratios of conductivity and layer thickness approximately 1 would then most likely apply to wet conditions at Apollo, where elevated currents of the order 0.4 mA had been measured as mentioned earlier.

Applying Equation 6.10 would thus approximate the currents measured at the corona cage to be of the order 3.54 times the value of 0.4 mA, which is in the region of 1.4 mA. This is indeed in the

range of currents measured at the corona cage before the onset of flashover (refer to section 5.3.1)

The linear approximation, therefore, seems plausible, although further research is required to assess the validity of Equation 6.1 through Equation 6.10. This first order linear approximation can only be applied to glass insulators as no elevated LC has been observed on the composite insulators.

6.5 Conclusion

Shunt resistors and the LCPR2B sensor have been placed on composite and glass HVDC insulator strings and left in the field for 11 months to conduct insulator LC measurements. During this period, when no rain and relatively low humidity conditions are present, the LC for both the glass and composite insulators behave similarly. High humidity of > 90% and the onset of rain raise the nominal LC levels on the glass insulator, whereas rain has had the opposite effect on the composite insulator's LC. Increased LC activity normally takes place late evening to early morning when the temperature is at its lowest and humidity at its highest. Condensation on the insulators has been shown to be a primary determinant of the LC levels on the insulators.

The nominal LC over the 11-month test period varies between 20 µA and 60 µA, which is well within the acceptable range for nominally performing insulators.

For a more formal statistical analysis of the data, the correlation between insulator LC and climatic and line conditions were investigated using the data collected over the 11-month period.

Broadly, it was observed that there is a positive correlation between composite insulator LC and temperature. An increase in humidity leads to a decrease in composite insulator LC, but an increase in glass insulator LC. The negative correlation determined between the composite insulator LC and humidity can indicate that self-cleaning of the insulator takes place due to its hydrophobicity properties. When rain was present, the correlation between rain and composite insulator LC was almost zero (correlation coefficient of -0.03), indicating that rain had minimal impact on the composite insulator's performance. However, for the glass insulator, a positive correlation coefficient of 0.43 was calculated, indicating that rain does affect the performance of the glass insulator.

Regarding the correlation between LC and the line conditions, it is evident that the composite insulator LC is not influenced by the line voltage or current. However, for the glass insulator, the LC showed a marginally positive correlation with the line current, but a negative correlation with line voltage. The latter may be attributed to statistical noise, and can be investigated further.

Pigini & Cortina (2011) performed a statistical evaluation of the polluted performance of composite and glass insulators under dc stress. It has been observed that the risk of flashover for a 40 mm/kV insulator string with an ESDD of 0.05 mg/cm^2 was less than 1%. This agrees well with the low LC levels seen on the Cahora Bassa line. Literature mentions that composite insulators have superior performance over glass insulators under dc excitation, which has been observed as well (Zhang *et al*., 2010; Engelbrecht *et al*., 2012; Abbasi *et al.,* 2014; Yu *et al*., 2016). Chrzan *et al*. (2011) mention that hydrophobic insulators (composite) have higher flashover voltages and lower LC when compared to hydrophilic (glass) insulators.

7: CONCLUSION AND RECOMMENDATIONS

7.1 Introduction

In this thesis a leakage current (LC) sensor prototype has been developed to perform HVDC insulator LC measurements. Also, composite and glass insulator LC have been monitored on energised HVDC insulators of the Cahora Bassa transmission line over an 11-month period. This was the first time that such long-term LC measurements have been conducted on composite and glass insulators using an actual HVDC transmission line where these insulators experienced the same climatic conditions and the same line voltage. This situation gave the author a unique opportunity to reliably compare the two different insulators, since they were situated on the same inverted-V insulator string.

The South African power utility noted that the glass insulators situated on the South African side of the Cahora Bassa have been performing poorly in the sense of flashovers occurring on it, which lead to unexpected downtime. The reason for the poor performance was unknown and no online insulator LC tests have been conducted on the transmission line before. The research questions of the thesis and how they were addressed are discussed in detail below.

7.2 Responses to research questions

Finite element method simulations of a glass insulator

- What is the comparison between the voltage, electric field and current density distributions of clean and polluted HVAC and HVDC glass insulators, respectively?
    - Simulations were conducted of clean and polluted ac and dc glass insulators in COMSOL Multiphysics to study the voltage, electric and current distributions of the insulator. It was observed that the voltage is concentrated around the pin (energised end) of the clean insulator for the ac and dc case. However, on the polluted insulator, the voltage drop occurs almost linearly along the pollution layer due to the presence of the uniform pollution layer. For the dc case, a pollution conductivity of 5 x 10^{-6} S/m and 0.07 S/m yielded the same voltage distribution response, which did not occur on the polluted ac energised insulator. Thus, it can be inferred that the dc energised insulators are more susceptible to pollution than the ac energised insulators. A polluted ac and dc energised insulator exhibited a sharp increase in current density when compared to a clean insulator case. The surface current on the uniformly polluted ac and dc energised insulator was 4.81 x

10^3 A/m^2 and 5.34 x 10^3 A/m^2, respectively. The tangential electric field found on the surface of a polluted dc energised insulator was higher when compared to the ac energised insulator case. The higher tangential electric field found on the dc energised insulator can lead to the dc insulator having a higher flashover probability than the ac insulator under the same excitation voltage. It was also noted that a significant tangential electric field still exists along the surface of the ac and dc polluted insulators, which were not present for the clean insulator case. The presence of these high electric fields on the insulator surface can be an indicator of where dry bands are mostly likely to occur. It was also observed that the highest electric field is located near the energised end of the ac and dc insulators, indicating that arcs, that can lead to flashover, will first emanate from the energised end of an insulator.

- What can be derived from the simulations in terms of LC behaviour?
    - The highest insulator LC density will be located near the energised end of a polluted insulator. The higher concentration of LC can cause excessive heating on the insulators' surface, which can lead to the formation of dry bands and eventual flashover. The simulations showed that the dc insulator exhibited higher LC than ac energised insulators. More heating also occurs on dc insulators under similar excitations, which can further exacerbate the flashover process on dc insulators. From the simulations it was observed that conduction current is the predominant LC on AC glass insulators and that the capacitive current's affect is negligible.

- How reliable is the finite element method models compared to the real-life performance of insulators?
    - The simulated LC obtained in Chapter 3 for a polluted dc insulator was compared with actual insulator LC measurements found in Chapter 5. At the corona cage, a current of the order 5 mA was obtained for dc polluted insulators with a conductivity of 0.07 S/m applied to its surface (see Section 5.3.1). A simulated current of 5.6 mA was obtained when a pollution layer thickness of 0.002 mm was applied to the FEM simulation. Thus, the LC obtained with the simulations are comparable with the actual insulator LC measurements of Chapter 5. This gives confidence that FEM based simulations can aid in future research and development work concerning insulator design, and that the model presented in this work is reliable.

Development of LC measurement technology

Once all literature was reviewed, a set of requirements for the developed prototype sensor was listed:

- hand-held clamped-on type device;
- capable of performing in-situ measurements of 1 mA to 100 mA; and
- perform LC measurements in the vicinity of an HVDC transmission line (1800 A Cahora Bassa HVDC transmission line).

- *Which sensors can measure small currents (mA) or small magnetic fields (nT) in the vicinity of kilo-Ampère (kA) currents and milli-Tesla (mT) magnetic fields?*
    - Research has shown that a commercial-off-the-shelf (COTS) dc current sensor that is discussed in Chapter 4 can measure the prescribed insulator LC. The COTS sensor shows good linearity over the desired range of LC. However, the COTS dc sensor is a solid non-hinged device and, therefore, cannot clamp around an insulator. The insulator string first has to be disconnected in order to place the COTS sensor around it. Therefore, it is not an appropriate device for the given requirements. Another drawback is that the COTS sensor does not rely on differential measurement to cancel ambient magnetic fields, which was implemented on the prototype. This may influence the measurement in harsh magnetic field conditions.
    - Magnetic field sensors can detect LC non-intrusively. CPUT has a partnership with the South African National Space Agency (SANSA) who are experts in the magnetic sensing domain. A fluxgate magnetometer (LEMI) has been obtained from SANSA and tested as a possible LC sensor. The fluxgate magnetometer detects the magnetic field associated with the insulator LC. Laboratory tests on insulator LC with the LEMI have been conducted at CPUT and at the University of Witwatersrand (Wits). During tests, good linearity has been observed over the desired measurement range as observed in Section 4.3. During high voltage tests at Wits, it has also been observed that the LEMI fluxgate magnetometer can withstand flashover events. However, due to it being a magnetic field sensor, it will always detect ambient magnetic fields. For in-situ measurements on energised insulators, this is a problem as the ambient magnetic field will be added to the insulator's magnetic field associated with the LC. The ambient magnetic field is not everywhere the same and it changes depending on the LEMI's position. Furthermore, the LEMI fluxgate magnetometer is a costly device, which limits wide

deployment. It is sensitive to ambient magnetic fields as well, which needs to be screened off if deployed. This may be impractical as their fundamental mode of operation depends on measuring magnetic fields. Thus, this magnetometer is unsuitable for use as an in-situ insulator LC sensor.

- Since none of the available COTS sensors fulfilled all the requirements, one had to be developed. The developed prototype in Section 4.5 is also based on magnetic field sensing. It uses magnetoresistive (MR) sensors that are simple resistive Wheatstone bridges to measure magnetic fields and only require an applied voltage to obtain measurements. With a voltage applied to the bridges, it converts any incident magnetic fields into differential outputs. The use of magnetic cores has proven to increase the sensitivity of the sensor whilst also providing some screening from the ambient magnetic fields. In the field, the differential magnetometer method (DMM) has been implemented using the MR sensors to mitigate the effect ambient magnetic fields on LC measurements. By implementing the DMM, the MR sensors overcome the drawback mentioned of the LEMI.

- *How can the sensor be modified to perform non-intrusive measurements of LC on HVDC insulators?*
  - The developed prototype has been chosen to perform in-situ insulator LC measurements on an HVDC transmission line. It is non-intrusive by design as it uses magnetic field sensors to detect the magnetic field of the associated insulator LC. There is no need to disconnect an insulator string in order to clamp the prototype sensor. The prototype consists of 2 cores, 2 MR sensors, signal conditioning circuitry and a mechanical clamp. The prototype has been calibrated at CPUT and SANSA using a Helmholtz coil.

- How do HVDC transmission lines affect measurements from the LC sensor and how can that be mitigated?
  - The prototype will be clamped on the glass insulators of the Cahora Bassa HVDC transmission line. The line current rating of the Cahora Bassa scheme is 1800 A. The LC that needs to be measured is in the milli-Ampère (mA) range. The HVDC transmission is approximately 4 m away from the insulator under test. Preliminary magnetic field simulations (Section 4.5.2) have shown that the ambient field can be orders of magnitude higher than that of the insulator LC. As with the LEMI, the MR sensors are affected by ambient magnetic fields as well. To overcome this issue, a

technique called the differential magnetometer method (DMM) has been implemented. This method requires two dc LC sensors. Both of these LC sensors will measure the ambient magnetic field. However, one sensor will be clamped around the insulator or current carrying wire and measure its LC and the ambient field. Thus, subtracting the two sensors' outputs removes the effect of the ambient magnetic field. This leaves only the contribution of the actual LC emanating from the insulator. The calibration results in Section 4.5 shows that the dual core prototype sensor is capable of measuring the LC in the presence of the Cahora Bassa's ambient magnetic fields. A clamp on prototype (LCPR2) has been developed (as seen in Section 4.5.3) using the DMM to mitigate the effects of the transmission line on the LCPR2. For the in-situ insulator LC measurements, LCPR2B (which consisted of 2 MR sensors; one in a soft core and the other in a polystyrene foam) was eventually implemented in the field. Thus, the DMM was implemented and insulator LC was measured accurately in the field.

Empirical characterisation of LC on HVDC transmission lines, with Cahora Bassa HVDC transmission lines as case study

- *What is the relationship between contamination and insulator LC?*
    - A case study of the relationship between insulator contamination and insulator LC have been performed at Eskom's corona cage high voltage test facility. This study entailed spraying salt solutions with various salt concentrations on a glass insulator string with a USCD of 9.6 mm/kV. After each known contamination level, the glass insulator string was cleaned and re-sprayed with a different contamination level. The results show that for the setup described in Chapter 5, flashover occurred on the glass insulators from LC levels of 1.4 mA and higher. It has been observed that once the current reaches 1.4 mA, the glass insulator string flashed over, irrespective of the contamination level. The LC levels also increased with an increase in contamination level. The results are in agreement with Seifert *et al.* (2007), Jiang *et al*. (2010), Yang *et al*. (2012), and Sivaraman and Sivadasan (2014), which state that the insulator's flashover voltage decreases with an increase in ESDD (surface conductivity in the case of the thesis).

- *What is the probability of a flashover occurring as a function of LC?*

- A second case study, with regards to the probability of flashover occurring as a function of LC, has also been performed at Eskom's corona cage and had the same setup as the abovementioned case study. In this study, the HV insulator was energised up to a predetermined current with a constant contamination level of 0.07 S/m. This contamination level has been chosen since it is equivalent to an ESDD level of 0.03 mg/cm^2, which is consistent with that found on the Cahora Bassa HVDC transmission line (Narain *et al.,* 2012). The experimental results show that at an LC of 0.6 mA, there is a possibility of a flashover occurring at a contamination level of 0.07 S/m. The experimental results also showed that the insulator string always had a flashover event at 2 mA, indicating that at 2 mA, there is a 100% probability of a flashover occurring for this setup. No flashovers occurred below 0.6 mA. The minimum flashover current between the first case study*, the relationship between contamination and insulator LC,* and the second case study, *the probability of a flashover occurring as a function of LC,* differed. An explanation for this can be that the first case study's insulators have been wetted more frequently, leading to less insulator resistance, and hence, a higher current.
- An analytical expression for the highest LC before the onset of flashover has been derived from the case studies presented in Section 5.3.1 and is captured in Equation 2.6. It shows that the highest LC is much lower for dc insulators than their ac counterparts.

- *What is the behaviour of LC of the Cahora Bassa transmission lines?*
  - During the 11-month insulator LC monitoring period, it was seen that under nominal weather conditions of no rain and low humidity, the LC measurements exhibit an almost square-wave behaviour with LC switching between lower (≈ 20 µA) and higher values (≈ 60 µA) with relatively short transitions on a daily basis. These values are in agreement with nominally functional insulators (Ferreira *et al.*, 2010:1). This current switching phenomenon of relatively quick transitions can be attributed to condensation. It has been observed that as soon as the ambient temperature approaches the dew point temperature (where the likelihood of condensation on the insulators is high), a sharp rise in the nominal LC is triggered. On the other hand, when the difference between the ambient temperature and the dew point temperature is at its highest (where the likelihood of condensation on the insulators is low), the LC falls quickly. The typical elevated LC during the 11-month measurement period was of the order 0.4 mA and the highest instantaneous LC

measured over the 11-month period was approximately 5 mA; no flashover event was seen nor reported during this period on the Cahora Bassa line. Thus, it may suggest that LC activity under 5 mA will not lead to a flashover event on this HVDC scheme.

- Applying the linear approximation of Equation 6.10 yields LC measured at the corona cage to be of the order 3.54 times 0.4 mA, which is in the region of 1.4 mA. This is indeed in the range of currents measured at the corona cage before the onset of flashover (refer to section 5.3.1)

- *What is the impact of temperature, humidity, rain and the Cahora Bassa HVDC line voltage and current on the insulators' LC?*

  Impact of temperature, humidity and rain

  - Increased LC activity normally occurs in the late evening to early morning hours when the temperature is at its lowest and humidity at its highest. This is in agreement with the ac insulator LC measurements reported in the literature (Suwarno & Parhusip, 2010; Ferreira *et al*., 2010; Meyer *et al*., 2011; Werneck *et al*., 2014). In high humidity conditions of > 90% and at the commencement of rain, there is a high probability of elevated LC on the glass insulators. Composite insulators also tend to have elevated LC present in high humidity conditions as reported by Muniraj & Chandrasekar (2009) for ac insulators, although not observed during these insulator LC measurements.

  Cahora Bassa HVDC line voltage and current

  - The line current and voltage fluctuations have little or no influence on the LC levels throughout the monitoring period, especially for the composite insulator. For the glass insulator, the effect of the line current and voltage was more pronounced, although still small.

- *How do the LC characteristics differ for composite and glass insulator under the same environmental conditions?*

  - A composite and glass insulator string were installed on the same tower in an inverted-V configuration. Thus, their LC levels can be reliably compared. When no rain is present and humidity is relatively low, the LC on the composite and glass insulator are similar. There is a high probability of elevated LC occurring on the

glass insulator when humidity is high and at the onset of rain. However, the composite insulator suppresses the LC surges under the same conditions. This research shows that the composite insulator outperforms the glass insulator in high humidity and rainy weather conditions, since lower LC has been measured on its surface. This is in agreement with literature that states that composite insulators have superior performance over glass insulators under dc excitation (Zhang *et al*., 2010; Engelbrecht *et al*., 2012; Abbasi *et al*., 2014; Yu *et al*., 2016).

- Statistical correlation of all climatic parameters versus LC were calculated as well. It was observed that a positive correlation exists between the composite insulator LC and the temperature (correlation coefficient of 0.48), indicating that there is a rise in LC as the temperature increases. A negative and a positive correlation existed, respectively, for the composite and glass insulator, which indicates that the composite insulator LC decreases when humidity increases and the glass insulator LC increases when humidity increases. When rain was present, the glass insulator LC exhibited a strong positive correlation indicating that the glass insulator is susceptible to rainy conditions. Throughout the year, the composite insulator LC had a slightly negative correlation with rain (correlation coefficient of -0.03), which indicates that its LC remained essentially unchanged in the presence of rain.

- *What is the relationship between LC measured at the corona cage and that of the Cahora Bassa HVDC line?*
  - An attempt was made in section 6.4.3 to linearly approximate if there was any correlation between the corona cage LC measurement results and that of the Cahora Bassa HVDC transmission line. Such an approximation will be useful to support the design of new HVDC lines, such as for South Africa's envisaged HVDC line along the Limpopo-West power corridor. A linear equation, consistent with the measurements at the corona cage and at Apollo, was derived to extrapolate the LC measured at the corona cage to what can be expected at Apollo under the same contamination conditions. This relationship is presented in Equation 6.10.

7.3 Recommendations

The following recommendations can be made regarding this research project:

- More research into the mechanical considerations of the developed sensor has to be conducted. The initial prototype for field tests has been deemed too bulky. One approach to decreasing its size is to perhaps use a smaller core to measure the ambient magnetic

field. The core can have a smaller diameter as long as its properties match that of the core being clamped around the insulator.

- Investigation of wideband time- and frequency-domain techniques can be investigated to study partial discharges in more detail.
- The development of a WiFi / GPRS module for the wireless transmission of LC data. This will be an important aspect in future as these sensors will be deployed in remote areas where it may be difficult to manually retrieve the data.
- When designing a next-generation prototype, the live line workers should be part of the discussion as they will be the end-users of it. The live line workers can give more detailed information on how exactly they expect from the sensor to perform. They can also give valuable mechanical design considerations due to their practical experiences in the field.
- Replace glass insulators with composite insulators as it improves the suppression of insulator leakage current. Over the 11-month in-situ measurement period, it has been observed that the composite insulators outperform the glass insulators on the Cahora Bassa transmission line since lower LC has been detected on it.
- Investigate the fluctuations seen on the HVDC line's current. It has been observed that the line current can vary considerably. This may cause degraded performance of the Cahora Bassa transmission line.
- Investigate the validity of the linear approximation of expected LC under HVDC conditions that was discussed in Section 6.4.2 further.
- Little has been published in literature regarding the relationship between insulator LC and USCD for HVDC insulators. Investigate further the possible adaption and augmentation of Equation 2.4 and Equation 2.5 for the HVDC insulator case, as was attempted in Equation 2.6. It was observed in Section 5.3.2 that the highest measured LC before flashover was 0.6 mA. Equation 2.4 and Equation 2.5 (400 mA and 100 mA, respectively) gave considerably higher LC values for the ac case. These equations ignored the dependency of insulator contamination, which may be an over-simplification.

7.4 Contributions

In conclusion, this thesis made unique contributions to the body of knowledge reported in the literature as follows:

- Finite element method simulations of a dc glass insulator's voltage, electric field and current density distributions, where the conductivity of the ambient air has been taken into account as well.

    - This dc physics-based model allows for satisfactory simulation and forecasting of real-life performance, which is important in the designing of new insulators and transmission lines.
- The design and development of a magnetic field-based LC sensor for in-situ insulator LC measurements.
    - The design was validated against the standard shunt resistor measurement technique and results agreed well. Although the two-core prototype was not implemented for the in-situ tests, the second core was simply removed but the compensating magnetoresistive sensor still maintained to allow for differential measurements. The ambient magnetic fields were successfully suppressed using this method.
- The probability of flashover occurring as a function of LC and contamination was determined for the glass insulators used during the laboratory experiments.
- A linear approximation has also been determined between LC measured during laboratory tests and actual HVDC field tests.
    - The linear approximation showed good consistency between the corona cage LC measurements and that of the Cahora Bassa HVDC transmission line. Such an approximation will be useful to support the design of new HVDC schemes.
- A relationship between the LC and USCD for HVDC insulators has been derived.
- Long-term monitoring of insulator LC activity of an HVDC transmission line.
    - This was the first time that such long-term LC measurements have been conducted on composite and glass insulators using an actual HVDC transmission line where these insulators experienced the same climatic conditions and the same line voltage.
    - The average LC activity of the transmission line and its associated power loss have been quantified as well. From the data collected, it is evident that the composite insulator boasts superior performance in terms of LC suppression in the presence of adverse weather conditions when compared to the glass insulator. This finding validates the South African power utilities' decision to replace all the glass insulators on the South African side of the Cahora Bassa with composite insulators.

REFERENCES

ABB. N.d. *The Cahora Bassa HVDC transmission Apollo converter station refurbishment*. http://www.abb.co.za/industries/ap/db0003db004333/ba5c7f1924f82c77c1257743003d666d.aspx [22 June 2012].

Abbasi, A., Shayegani, A., Niayesh, K. 2014. Pollution Performance of HVDC SiR Insulators at Extra Heavy Pollution Conditions. *IEEE transactions on Dielectrics and Electrical Insulation*, 21(2):721-728.

Abdus Salam, M. D., Ahmad, H., Saadom, Z., Budin, R., Tamsir, T., Buntat, Z., Piah, M. A. M. 2000. Effect of equivalent salt deposit density on flashover voltage of contaminated insulator energized by HVDC, *Proceeding of the 6th international conference on properties and applications of dielectric materials*. 21-26 June, Xi'an, 2:821-824.

Abimouloud, A., Arif, S., Korichi, D., Ale-Emran, S. D. 2018. Prediction of DC flashover voltage of cap-and pin polluted insulator. *IET Science, Measurement & Technology*, 13(2):279-286.

Advance magnetics. 2014. AD-MU Alloy Specifications. https://advancemag.com/ad-mu-specs/. [23 January 2014].

Akbar, M., Zedan, F. M., Arif Abdul-Majeed, A. 1991. Design of HV Transmission Lines to Combat Insulator Pollution Problems in the Eastern Region of Saudi Arabia. *IEEE transactions on Power Delivery*, 6(4):1912-1921.

Ali, Z., Tunio, M. A., Khokhar, S., Tunio, N. A., Mari, M. A. 2018. Modeling of High Voltage Insulator Strings through Finite Element Method. *International Journal of Computer Science and Network Security,* 18(8):65-69.

Amin, M., Amin, S., Muhammed, A. 2009. Monitoring of LC for composite insulators and electrical devices. *Review of advanced material science*, 21:75-89. www.ipme.ru/e-journals/RAMS/no_12109/amin.pdf

Ansys. 2019. *Ansys Maxwell: Low Frequency Electromagnetic Field Simulation*. https://www.ansys.com/products/electronics/ansys-maxwell [29 November 2019].

Apernathi, R., Dwivedi, V. 2015. Modeling and Analysis of Inductive Coil ELF Sensor. *TELKOMNIKA Indonesian Journal of Electrical Engineering*, 16(1):38-45.

Applied research. N.d. *Miniature super-low power three-component fluxgate magnetometer* LEMI-011.
http://www.stcu.int/documents/reports/distribution/tpf/SENSORS/hannover%2074.pdf
[7 May 2012].

Arshad, Nekahi, A., McMeekin, S. G, Farzaneh, M. 2015. Influence of Voltage Type and Polarity on Electric field distribution along a Polymeric Insulator under Contaminated Conditions. https://www.comsol.ch/paper/download/289961/arshad_paper.pdf [6 January 2020]

Arshad, Nekahi, A., McMeekin, S. G, Farzaneh, M. 2015. Effect of pollution layer conductivity and thickness on electric field distribution along a polymeric insulator. https://www.comsol.com/paper/download/289991/arshad_paper.pdf. [6 January 2020]

Arshad, Nekahi, A., McMeekin, S. G, Farzaneh, M. 2015. Effect of dry band location on electric field distribution along a polymeric insulator under contaminated conditions. *International Universities Power Engineering Conference*, 1-4 September, Stoke, UK, 1-4.

Bahrman, M. & Johnson, B., K. 2007. The ABCs of HVDC transmission technologies. *IEEE power and energy magazine*, 5(2):32-44, March-April.

Baker, A. C., Zaffanella, L. E., Anzivino, L. D., Scheider, H. M., Moran, J. H. 1989. A comparison of HVAC and HVDC contamination performance of station post insulators. *IEEE Transactions on Power Delivery*, *4*(2):1486-1491.

Banik, A., Dalai, S., Chatterjee, B. 2014. Condition Monitoring of Overhead line Insulator By measuring Surface Leakage Current. *Annual IEEE India Conference (INDICON)*, 11-13 December, Pune, India,1-5.

Banik, A., Dalai, S., Chatterjee, B. 2015. Studies the Effect of Equivalent Salt Deposit Density on Leakage Current and Flashover Voltage of Artificially Contaminated Disc Insulators. *Conference on Power, Dielectric and Energy Management at NERIST (ICPDEN*), 10-11 January, Itanagar, India, 1-6.

Banik, A., Chatterjee, B., Dalai, S. 2017. Development of a pollution flashover model for 11 kV porcelain and silicon rubber insulator by using COMSOL Multiphysics. *Electrical Engineering*, 100,533-541.

Batalovic, M., Matoruga, H., Berberovic, S., Maroruga, M. 2018. Influence of environmental stresses on high voltage polymer rod type insulator performances. *International Conference on Smart and Sustainable Technologies*, 26-29 June, Split, Croatia, 1-6

Benguesmia, H., Bakri, B., Khadar, S., Hamrit, F., M'Ziou, N. 2019. Experimental study of pollution and simulation on insulators using COMSOL® under ac voltage. *Diagnostyka*, 20(3):1-9.

Chen, W., Yao, C., Chen, P., Sun, C., Du, L., Liao, R. 2008. A new broadband microcurrent transducer for insulator LC monitoring system. *IEEE Transactions on Power Delivery*, 23(1):355-360.

Cheng, C., Li, R., Chen, J. 2013. Design of the DC Leakage Current Sensor with Magnetic Modulation-Based Scheme. *IEEE international symposium on industrial electronics*. 1-6.

Cheng, T. C., Wu, C. T., Zedan, F., Elder, G. R., Low, S. S., Rippey, J. N. 1981. EPRI - HVDC insulator studies: part i field test at the sylmar HVDC converter station. *IEEE Transactions on Power Apparatus and Systems*, 100(2): 902-909.

Chenyang Technologies. *DC Current Sensor CYCT04-xnM85B*. http://www.cy-sensors.com/CYCT04-xnM85B.pdf. [2 March 2014].

Chrzan, K. L., Vosloo, W. L., Holtzhausen, P. 2011. Leakage Current on Porcelain and Silicone Insulators Under Sea or Light Industrial Pollution. *IEEE Transactions on Power Delivery*, 26(3):2051-2052.

Clean line energy partners fact sheet. 2011. *Understanding electric and magnetic fields of HVDC lines.*

http://www.rockislandcleanline.com/Documents/SIFS_EMF%20FactSheet_FINAL.pdf [18 April 2012].

COMSOL Multiphysics. 2019. COMSOL Multiphysics reference manual. https://doc.comsol.com/5.5/doc/com.comsol.help.comsol/COMSOL_ReferenceManual.pdf [20 November 2019].

Costea, M., Baran, I. A comparative analysis of classical and composite insulators behaviour. *Science bulletin*, 2012, series C, 74(1), pp. 1-8.

de Decker, D., Perin, D., Lambeth, P. J., Lampe, W. D., Marrone, G., Naito, K., Niklasch, H., Schneider, H. M. 1992. Artificial pollution testing of HVDC insulators: Analysis of factors influencing performance. Electra, 140. 99-113.

Dias, B. A., Costa, E. G., Germano, A. D., Ferreira, T. V., Brito, K. B., Barbosa, L. A., Silva Neto, I., Silva, J. K. P., Bezerra, R. C., Silvera, S., Paiva, R. S., Mello, D. R. 2017. Impact Analysis of Biological Pollution on Glass Insulators. *The 20th International Symposium on High Voltage Engineering,* Buenos Aires, Argentina, 27 August 27 – 1 September, 1-6.

Digikey. 2015. *Hall-Effect Sensing Provides Current Measurement for the Smart Grid*. https://www.digikey.com/en/articles/techzone/2015/oct/hall-effect-sensing-provides-current-measurement-for-the-smart-grid [20 March 2016]

Douar, M. A., Mekhaldi, A., Bouzidi, M. C. 2010. Flashover Process and Frequency Analysis of the Leakage Current on Insulator Model under non-Uniform Pollution Conditions. *IEEE Transactions on Dielectrics and Electrical Insulation, 17*(4):1284-1297.

Drobik, T. n.d. *High-voltage direct current transmission lines*. eeeic.eu/proc/papers/69.pdf [24 July 2012].

El-Sayed, M., El-Refaie, M. K., Elrahman, A., Mohamed, M., K. 2018. Electric field distribution of optimized composite insulator profiles under different pollution conditions. *Ain Shams Engineering Journal*, 9:1349-1356.

El Bacha, G., Milano, S., Viola, J. 2014. *Hysteresis Mitigation in Current Sensor ICs using Ferromagnetic Cores*. https://www.allegromicro.com/en/Insights-and-Innovations/Technical-Documents/Hall-Effect-Sensor-IC-Publications/Hysteresis-Mitigation-in-Current-Sensor-ICs-Using-Ferromagnetic-Cores.aspx. [5 November 2019].

Elmatboly, O. & Homaifar, A. 2008. Novel sensing of utility currents along transmission line spans. *IEEE international symposium on industrial electronics*, Cambridge, 30 June-2 July: 1131-1137.

Elombo, A. I., Haultzhausen, J. P.,Vermeulen, H. J., Pieterse, P. J., Vosloo, W. L. 2013. Comparative evaluation of the LC and aging performance of HTV SR insulators of different creepage lengths when energised by AC, DC+, DC- in a severe marine environment. *IEEE Transactions on Dielectrics and Electrical Insulation,* 20(2):421-428.

Engelbrecht, C. S., Hartings, R., Lundquist, J. 2004. Statistical dimensioning of insulators with respect to polluted conditions. *IEEE Transactions on Generation, Transmission and Distribution,* 151(3):321-326.

Engelbrecht, C. S., Gutman, I., Hartings, R. 2005. A practical implementation of statistical principles to select insulators with respect to polluted conditions on overhead AC lines. *IEEE Transactions on Power Delivery,* 22(1):667-673.

Engelbrecht, C. S., Gutman, I., Hartings, R. 2007. A practical implementation of statistical principles to dimension AC line insulators with respect to contaminated conditions. *IEEE Russia Power Tech*, St. Petersburg, Russia, June 27-30, 1-7.

Engelbrecht, C. S. Reynders, J. P., Gutman, I., Kondo, K., Lumb, C., Pigini, A., Sklenicka, V., Wu, D. 2012. *Outdoor insulation in polluted conditions: guidelines for selection and dimensioning. Part 2: The DC case*. CIGRE working group C4.303.

Farzaneh, M., Baker, T., Brown, K., Chisholm, W. A., de Tourreil, C. Drapeau, J. F., Fikke, S., George, J. M., Gnandt, E., Grisham, T., Gutman, I, Hartings R., Kremer, R., Powell, G., Rolfseng, L., Rozek, T., Ruff, L. D., Shaffner, D., Sklenicka, V., Sundararajan, R., Yu, J. 2003. Insulator icing test methods and procedures a position paper prepared by the IEEE task force on insulator icing test methods. *IEEE Transactions on Power Delivery,* 18(4):1503-1515.

Ferreira, T. V., Germano, A. D., da Costa, E. G., Angelini, J. M. G., Nallim, F. E., Mendonca, P. 2010. Naturally aged polymeric insulators: washing and its consequences. *Modern electric power systems (MEPS)*. Wroclaw, 20-22 September:1-5.

Finite Element Method Magnetics. 2014. http://www.femm.info/wiki/HomePage [12 December 2015].

Gencoglu, M. T. The comparison of ceramic and non-ceramic insulators. *New world sciences academy*, October 2007, 2(4), pp. 1-21.

Global insulator group. 2020. *HV glass suspension insulator of U100BL type*. http://www.gig-group.com/en/catalog/izolyatory_podvesnye_standartnogo_profilya_tipa_ps/hv-glass-suspension-insulator-of-u100bl/ [20 January 2020].

Glossop, W. K. 2008. *Performance comparison of existing AC and DC transmission lines within Southern Africa with predictions for lines above 765 kv*. University of Witwatersrand, Master's thesis, Johannesburg.

Gouda, O. E., Moussa, A. Z. E. D. M., Maowed, A. E. M. 2014. Prediction of flashover voltage and dry band location for polluted ceramic insulators using dynamic open-model. *Journal of Energy and Power Sources,* 1(6):304-313.

Griffiths, D. J. 2008. *Introduction to electrodynamics*. San Francisco. Pearson Benjamin Cummings.

Guo, Y., Jiang, X., Gowri Sree, V., Sundararajan, R. 2015. AC Flashover Performance of Porcelain, Glass and Polymeric Insulators at High Altitudes, *International Conference on Properties and Applications of Dielectric Materials*, Sydney, NSW, Australia, 19-22 July 2015, 484-487.

Haus, Hermann A., and Melcher J. R. *Electromagnetic Fields and Energy*.
Englewood Cliffs, NJ: Prentice-Hall, 1989. ISBN: 9780132490207.

Heyman, A., Weimers, L., Bohl, M. n.d. *HVDC-A key solution in future transmission systems*. www.worldenergy.org/documents/congresspapers/237.pdf [24 April 2012].

Holtzhausen, J. P., Pieterse, P. J., Vermeulen, H. J., Limbo, S. 2010. Insulator aging tests with HVAC and HVDC excitation using the tracking wheel tester. *International conference on high voltage engineering and application (ICHVE),* New Orleans, LA, 11-14 October:445 - 448.

Honeywell. N.d. *1- and 2-Axis Magnetic Sensors HMC1001/1002/1021/1022.* http://www51.honeywell.com/aero/common/documents/myaerospacecatalog-documents/Missiles-Munitions/HMC_1001-1002-1021-1022_Data_Sheet.pdf [13 March 2013].

Honeywell. N.d. *Magnetic current sensing*. http://aerospace.honeywell.com/~/media/UWSAero/common/documents/myaerospacecatalog-documents/Defense_Brochures-documents/Magnetic__Literature_Application_notes-documents/AN209_Magnetic_Current_Sensing.pdf [13 March 2013].

Hu, Y., Liu, K. 2017. Transmission lines detection technology. *In Inspection and Monitoring Technologies of Transmission Lines with Remote Sensing*. 205-279. Elsevier Inc.

Hussain, M. M., Farokhi, S., McMeekin, S. G., Farnazeh, M. 2015. The Effects of Salt Contamination Deposition on HV Insulators Under Environmental Stresses. *The 11th International Conference on the Properties and Applications of Dielectric Materials*, Sydney, NSW, Australia, 19-22 July 2015, 616-619.

Ildstad, E. 2013. Challenges Arising from Use of HVDC. *Nordic Insulation Symposium - Nord-IS 13* - Trondheim, Norway, June 9 - 12, 17-20.

Jayabal, R., Vijayyarekha, K. 2017. A study on performance of 11 kv overhead polymeric and porcelain insulators under contaminated conditions. *ARPN Journal of Engineering and Applied Sciences*, 12(23):7008-7011

Jeroense, M. 2011. *New HVDC technology lights the future of power transmission*. http://www.elp.com/index/display/article-display/_saveArticle/articles/utility-products/volume-6/issue-1/product-focus/td-automation/new-hvdc-technology-lights-the-future-of-power-transmission.QP129867.adPoolId=.adLocationId=Left1.dynamicAd=no.brandLogo=.html [7 May 2012].

Jia, Z., Chen, C., Wang, X., Lu, H. 2014. Leakage current analysis on RTV coated porcelain insulators during long term fog experiments. *IEEE Transactions on Dielectrics and Electrical Insulation*, 21(4):1547-1553.

Jiang, X., Yuan, J., Shu, L., Zhang, Z., Hu, J., Mao, F. 2008. Comparison of DC Pollution Flashover Performances of Various Types of Porcelain, Glass, and Composite Insulators. *IEEE transactions on power delivery,* 23(2):1183-1189.

Jiang, X., Wang, S., Zhang, Z., Hu, J., Hu, Q. 2010. Investigation of Flashover Voltage and Non-uniform Pollution Correction Coefficient of Short Samples of Composite Insulator Intended for ±800kV UHVDC. *IEEE Transactions on Dielectrics and Electrical Insulation*, 17(1):71-79.

Jiaqe, X., Renyu, Z., Xinghai, Z. 1988. DC Flashover Characteristics of the Contaminated Insulators Under Low Atmospheric Pressure, *International Conference on Properties and Applications of Dielectric Materials*, 260-263.

Jun, Z., Zhicheng, G., Liming, W. 2003. Study on the Various Pollution Performance of the Post Insulators in Exceeding High Voltage in High Altitude Area*. International Conference on Properties and Applications of Dielectric Materials*, Nagoya, Japan, 1024-1027.

Kamel, M. Y., AbouelSaad, M., El-Wakeel, A. S., Hassan, H. A. 2008. Influences of water droplet size and pollution layer permittivity on the electric field and potential distribution on a polluted insulator surface. *International Conference on Electrical Engineering*, 1-12.

Kimoto, I., Fujimura, T., Naito, K. 1973. Performance of insulators for direct current transmission line under polluted condition. *IEEE Transactions on Power Apparatus and Systems,* 1(3):943-949.

Kontargyri, V. T., Llia, N. C., Gonos, I. F., Stathopulos, I, A. 2004. Electric field and voltage distribution along insulators under pollution conditions. https://pdfs.semanticscholar.org/2a06/270ce3754d27f6976ef53276ad07a52ee2d0.pdf?_ga=2.97079320.601486613.1582732427-88114789.1582732427. [11 December 2019].

Krile, T. K., Neuber A. A. 2004. DC Flashover of a Dielectric Surface in Atmospheric Conditions. *IEEE Transactions on Plasma Science, 32*(5):1828-1834.

Krzma, A. S., Khamaira, M. Y. 2018. Computation of the electric field and voltage distributions over the polluted surface of silicone-rubber insulators. *Elixir International Journal*, 116:50009-50012.

Krzma, A. S. 2018. Study the electrical performance of 11 kV porcelain outdoor high voltage insulators. *Libyan International Conference on Electrical Engineering and Technologies*, 3-7 March, Tripoli, Libya, 106-110.

Krzma, A. S., Khamaira, M. Y. 2018. Comparative analysis of electric field and potential distributions over porcelain and glass insulators using finite element method. *Proceedings of First Conference for Engineering Sciences and Technology*, 25-27 September, 176-184

Latham, A., 2019. *Common Mode Rejection in Coreless Hall-Effect Current Sensor ICs*. https://www.allegromicro.com/-/media/Files/Technical-Documents/AN269123-Common-Mode-Field-Rejection-in-Coreless-Current-Sensor-ICs.ashx?la=en&hash=3912858F5909DA07DF0EEDB93E27609700CB1D1E. [05 November 2019].

Lempriere, M. 2019. *China's mega transmission lines*. https://www.power-technology.com/features/chinas-mega-transmission-lines/. [05 November 2019].

Li, J., Sima, W., Sun, C. 2009. Use of Leakage Currents of Insulators to Determine the Stage Characteristics of the Flashover Process and Contamination Level Prediction. *IEEE Transactions on Dielectrics and Electrical Insulation*, 17(2):490-501.

Liang, X. D., Song, L., Zhang, F. Z., Wang, G. L., Li, R. H. 2011. Influence of Composite Insulator Profiles on Pollution Flashover Performance. 17th International Symposium on High Voltage Engineering, Hannover, Germany, August 22-26, 1-6.

Larruskain, D. M., Zamora, I., Mazon, A.J., Aberrategui, O., Monasterio, J. n.d. *Transmission and distribution networks: AC vs DC.* www.trec-uk.org.uk/reports/larruskain_HVAC_to_HVDC.pdf [20 July 2012].

Lastos, A. E. 1990. Experience from insulators with RTV silicone rubber sheds and shed coatings. *IEEE Transactions on Power Delivery*, 5(4):2030-2038.

Lastos, A. E. 1991. Peak leak current of silicone and EPDM transmission line polymeric insulator families. *The 7th International Symposium on High Voltage Engineering, Dresden, Germany*, 1-6.

Limbo, B. S. 2009. *Insulator Aging Tests with HVAC and HVDC Excitation using the Tracking Wheel Tester.* University of Stellenbosch, Master's thesis, Stellenbosch.

Long, Y., Xiao, Y., Su, Z., Wu, D., Astrom, U. n.d. *The Reliability Study of the Statistical Method on Insulator Dimensioning of (U)HVDC Lines with Regard to Pollution Conditions*. 1-5. https://library.e.abb.com/public/7c202cf3262274f3c12573d70059f85d/paper_TD_Nov_en_.pdf [30 November 2016].

Macintyre, S.A. 1999. *Magnetic field measurement*. Macintyre electronic design.

Magnetics. 1997. *Magnetic Cores for Hall Effect Devices*. https://elnamagnetics.com/wp-content/uploads/library/Magnetics-Documents/Magnetic_Cores_for_Hall_Effect_Devices.pdf. [2 June 2015].

Matandirotya, E., Cilliers, P. J., van Zyl R. R. 2014. Methods of measuring and modelling geomagnetically induced currents (GICs) in a power line. *Proceedings of SAIP2013, the 58th Annual Conference of the South African Institute of Physics*, edited by Roelf Botha and Thulani Jili (SAIP and University of Zululand), 410-415.

Matandirotya, E., Cilliers, P. J., van Zyl R. R. 2015. Differential magnetometer method (DMM) for the measurement of geomagnetically induced currents (GIC) in a power line: Technical aspects, *Journal of Electrical Engineering*, 66(7):50-53.

Mavrikakis, N., Kapellakis, M., Pylarinos, D., Sidekaris, K. 2015. A novel autonomous monitoring system for distributed LC measurements on outdoor high voltage insulators. http://trivent-publishing.eu/pdfdownload/12.NikolaosMavrikakis.pdf.

Meyer, L. H., Olibini, C. R. P., Mustafa, T. I. A. H., Almaguer, A. D., Molina, F. H., Cassel, G. 2011. A study of the correlation of LC, humidity and temperature of 25 kV insulators in urban and rural areas. *Electrical Insulation and Dielectric Phenomena Conference,* 16 - 19 October 2011, 398-402.

Mouton, G. N. J., Vermeulen, H. J. 2012. *An Evaluation of Different Material Line Insulators under High Voltage AC and Bipolar DC Excitation in a Marine Polluted Environment*. University of Stellenbosch, Master's thesis, Cape Town.

Muniraj, C., Chandrasekar, S. 2009. Analysis of leakage current on polluted polymer insulator by high resolution spectrum estimation method. *Third International Conference on Power Systems*, Kharagpur, India, 27-29 December, 1-5.

Murugan, N., Sharmila, G., Kannayeram, G. 2013. Design optimization of high voltage composite insulator using electric field computations. *International Conference on Circuits, Power and Computing Technologies*, Nagercoil, India, 20-21 March, 1-6.

Narain, S., Naidoo, V., Vajeth, R. 2012. Upgrading the performance of the Apollo – Cahora Bassa 533kV links.

http://www.cigre.org/content/download/16961/680337/version/1/file/b2_301_2012.pdf. [6 November 2015].

Netravati, N. H. M., 2016. Risk assessment of pollution on a 66 kV composite insulator using ANSYS. *International Journal of Scientific Development and Research*, 1(11):6-12.

News24. News24-21 unbelievable photos and videos of Joburg's flash floods'. https://www.news24.com/You/Archive/21-unbelievable-photos-and-videos-of-joburgs-flash-floods-20170728. [2 July 2017].

Nobrega, R. B., Costa, E. G., Germano, A. D., Silva Neto, A. I., Barbosa, H. R. 2017. Performance of alternative coatings based on RTV silicone rubber under artificial pollution tests. *The 20th International Symposium on High Voltage Engineering, Buenos Aires, Argentina*, 1-6.

Obenaus, F. 1958. Contamination flashover and creepage path length. *Deustsche Elektrochnik*, 12, 135-136.

OCLA product description. n.d. http://www.ctlab.com/downloads/all%20olca%20new.pdf [3 November 2013].

Oliveria, S. C., Fontana, E., de Melo Cavalcanti, F. 2009. Leakage Current Activity on Glass-Type Insulators of Overhead Transmission Lines in the Northeast Region of Brazil. *IEEE transactions on power delivery,* 24(2):822-827.

Othman, N. A., Piah, M. A. M., Adzis, Z., Admad, H., Admad, N. A. 2013. Simulation of voltage and electric-field distribution for contaminated glass insulator. *IEEE Student Conference on Research and Development*, 16-17 December, Putrajaya, Malaysia.

Otto, A. J. 2009. *Direct Current Conductor Corona Modelling and Metrology*. University of Stellenbosch, PhD thesis, Stellenbosch.

Otto, A. J., Reader, H. C. 2010. Wideband and narrowband HVDC conductor corona test methods for radio noise prediction. *IEEE transactions on power delivery,* 25(4):2950-2957.

Pargamin, L. 1984. Considerations of the choice of the insulators for HVDC overhead lines. *CIGRE proceedings*, Paris, France, paper 33-11.

Parus, N., Mahatho, N., Govender, T., Marshall, E., Goosen, P.V., Greyling, E., Sibilant, G.C. 2011. Glass cap-and-pin insulator strings under HVDC conditions: preliminary results of investigations into the influence of shattered discs on insulation strength. *Proceedings of the 17th international symposium on high voltage engineering, E-090, 1-6.*

Pigini, A., Cortina, R. 2011. Evaluation of the Performance of Polluted Insulators under DC: A Statistical Approach. *Proceedings of the 17th international symposium on high voltage engineering*, 1-6.

Phillips, A. J., Engelbrecht, C. S. 2005. Insulation for power frequency voltage, in Lings, R.: EPRI AC Transmission Line Reference book-200 kV and above. Third Edition, 201.

Phillips, A.J., Bologna, F.F., Major, J.M., Engelbrecht, C.S. 2009. Development and demonstration of low cost robust LC sensors for evaluating contaminated insulators. *Proceedings of the 16th international symposium on high voltage engineering, paper 5-3, 1-6.*

Pieterse, P.J., Elombo, A. I., Mouton, G. N. J., Vermeulen, H. J., Holtzhausen, J. P., Vosloo, W. L. 2011. A coastal insulator pollution test station for the evaluation of the relative ageing performance of power line insulators under AC and DC voltage. *Proceedings of the 17th international symposium on high voltage engineering,* C-007, 1-5.

PPC insulators. 2020. *PPC Transmission and Distribution Insulators*. https://gdpowernet.dk/wp-content/uploads/2020/04/PPC_ANSI_TD_US-Letter_LQ-pocelain.pdf [20 January 2020].

Pylarinos, D., Siderakis, K., Pyrgioti, E. 2011. *Measuring and analyzing LC for outdoor insulators and specimens*. Advantage study center:31-53. http://www.ipme.ru/e-journals/RAMS/no_12911/03_pylarinos.pdf [22 February 2013].

Rakov, V. A., Uman, M. A. 2003. *Lightning physics and effects*. United Kingdom: Cambridge University Press.

Reddy, S., Sultan, N. A., Monika, P. M., Pooja, B., Salma, O., Ravishankar, K. V. 2010. Simulation of potential and electric field for high voltage ceramic disc insulators. *International Conference on Industrial and Information Systems*, 29 July – 1 August, Mangalore, India, 526-531.

Reddy, S. Verma, A. R. 2014. Pollution performance of HVDC insulator strings under normal and faulted conditions. *6th IEEE Power India International Conference (PIICON)*, 5-7 December 2014, 1-6.

Rosli, H., Othman, N. A., Jamail, N. A. M., Ismail, M. N. 2017. Potential and Electric Field Characteristics of Broken Porcelain Insulator. *International Journal of Electrical and Computer Engineering*, 7(6):3114-3123.

Sudalai Shunmugam, S., Vasudev, N., Krishna Kumar, M., De Bhowmick, B. N., Rao, S. B. R. 2017. Insulator Pollution Mapping of the Northern Region of the Indian Power System. *The 20th International Symposium on High Voltage Engineering*, Buenos Aires, Argentina, August 27 - September 01, 1-8.

Sarkar, J., Patil, R. 2014. Detection of partial discharges occurring in HVDC environment. International journal of innovation science, engineering and technology, 1(4):424-428.

Schwardt, W.H., Holtzhausen, J.P., Vosloo, W. L. 2004. A Comparison between measured Leakage current and surface conductivity during salt fog tests*. Africon Conference in Africa*, 597-600.

Schwardt, W.H., Vermeulen, H. J., HoltzHausen, J. P. 2005. *Insulator pollution monitoring device: Development, Calibration and Field Evaluation*. University of Stellenbosch, Master's thesis, Stellenbosch.

Seifert, J. M., Petrusch, W., Janssen, H. 2007. A Comparison of the Pollution Performance of Long Rod amd Disc Type HVDC Insulators. *IEEE transactions on Dielectrics and Electrical Insulation,* 14(1):125-129.

Seran, E., Godefroy, M., Pili, E., Michielsen, N., Bondiguel, S. 2017. What we can learn from measurements of air electric conductivity in ^{222}Rn-rich atmosphere. *Earth and Space Science, American Geophysical Union/Wiley*, 4(2):91-106.

Siemens. 2011. *High voltage direct current transmission- proven technology for power exchange*.http://www.energy.siemens.com/hq/pool/hq/power-transmission/HVDC/HVDC_Proven_Technology_.pdf [23 March 2012].

Sierra, C. R., Oviedo-Trespalacios, O., Candelo, J.E., Soto, J. D. 2015. The influence of atmospheric conditions on the LC of ceramic insulators on the Colombian Caribbean coast. Environ Sci Pollut. Res (2015) 22: 2526. doi:10.1007/s11356-014-3729-3

Sivaraman, M., Sivadasan, J. 2014. Comparison of Pollution Flashover Performance of Various Insulators*. International Conference on Circuit, Power and Computing Technologies*, 148-152.

Siziba, E. 2011. *Evaluation of a fluxgate magnetometer for a Cubesat*. Cape Peninsula University of Technology, Master's thesis, Bellville.

Shaohua, L., Yanfeng, G., Xidong, L., Jiafu, W., Yingyan, L. 2015. Relationship Between Leakage Current and Diameter of Composite Insulators During the Early Period of Tracking Wheel Test. *The 19th International Symposium on High Voltage Engineering*, Pilsen, Czech Republic, August, 23 - 28, 1-6.

Sunitha, N. S., Ravi, K. N, Prakash, R., Pushpanjali. 2015. A study on leakage current characteristics of polymeric insulators for different pollution layers. *International Conference on Power and Advanced Control Engineering*, 384-387.

Suwarno and Parhusip, J. 2010. Effects of humidity and fog conductivity on the leakage current waveforms of ceramics for outdoor insulators. *WSEAS transactions on systems,* 4(9):442-452.

Suzuki, R., Vosloo, W. 2011*. Annex A: Measurement of ESDD and NSDD*. http://clumb.free.fr/WG11/docs/public/Milan102.pdf. [16 November 2015].

Tang, Q. J., Liu, X. D., Yang, X. L., Zhou, L. 2015. Study on Critical Conditions of the Insulator String Covered with Ice Based on the Leakage Current. The 19th International Symposium on High Voltage Engineering, Pilsen, Czech Republic, August, 23 - 28, 1-6.

TDK. 2017. Ferrites and accessories. https://www.tdk-electronics.tdk.com/download/531568/419f8df165fa780842566ab55510a8ce/pdf-generaldefinitions.pdf. [24 October 2019].

Thejane, K. V., Ntshani, M. D., Geldenhuys, H. J., Van Coller, J.M., Beutel, A. A., Mvayo, T. D., Watson, R., Vosloo, W. L., Khatri, A. 2013. Effect of insulator application on the LC performance of woodpole distribution line structures. *Proceedings of the 18th international symposium on high voltage engineering, OE3-03, 1223-1227.*

Thejane, K. V., Van Coller, J.M., Ntshani, M. D., Beutel, A. A. 2015. Leakage Current Performance Evaluation of a Woodpole Distribution Line Structure. *The 19th International Symposium on High Voltage Engineering*, Pilsen, Czech Republic, 23-28 August, 1-6.

Valagussa, C., Kuljac, N., Mazza, P., Pirovano, G. De Donà, G., Rendina R. 2009. Minimum approach distance calculation for safe live works in presence of line composite insulators according to IEC61472 criteria. *Proceedings of the 16th international symposium on high voltage engineering,* Cape Town, South Africa, paper 6-8, 24 - 28 August 2009, 1-6.

Verma, M. P., Heise, W., Lipken, H., Luxa, G. F., Schreiber, H. 1978. The criterion for pollution flashover and its application to insulation dimensioning and control*. International Conference on Large High Voltage Electric Systems,* Paris, France, 1-12.

Wang, J., Yao, C., Mi, Y., Zhang, X., Li, C. 2012. Research for the LED optical fiber sensor for the leakage current of the insulator string. *Asia-Pacific Power and Energy Engineering Conference*, Shanghai, China, 27-29 March, 1-4.

Wang, K., Zhao, C., Zhu, M., Mei, H., Wang, L., Guan, Z., Zhou, Z., Gao, S. 2015. Analysis on flashover performance of polluted porcelain insulators in high conductivity fog environment*. IEEE Conference on Electrical Insulation and Dielectric Phenomena (CEIDP),* Ann Arbor, MI, USA, 193-196.

Wang, S., Wu, Y. 2019. *Effect of salty fog on flashover characteristics of OCS composite insulators, Chinese Journal of Electrical Engineering*, 5(3):59-66.

Werneck, M. M., dos Santos, D. M., de Carvalho, C. C., de Nazare, F. V. B., Allil, R. C. S. 2014. Detection and monitoring of LCs in power transmission insulators. *IEEE sensors journal*, 1-9.

Yang, L., Hao, Y., Li, L., Zhao, Y. 2012. Comparison of Pollution Flashover Performance of Porcelain Long Rod, Disc Type, and Composite UHVDC Insulators at High Altitudes. *IEEE transactions on Dielectrics and Electrical Insulation, 19*(3):1053-1059.

Yu, X. Zhang, Q., Yang, H., Xinzhe, Y., Jun, Z., Bo, L. 2016. Leakage Current Characteristics of Long Insulator String during DC Pollution Flashover Test under Various Air Pressures. *International Conference on Condition Monitoring and Diagnosis*, Xi'an, China, 481-484.

Zchariades, C., Rowland, S. M., Cotton, I. 2013. Real-time monitoring of LC on insulating cross-arms in relation to local weather conditions. *Electrical and Insulation Conference*, Ottawa, Canada, 2 - 5 June 2013, 397-401.

Zhang, J., Farzaneh, M. 2000. Propagation of ac and dc Arcs on Ice Surfaces. *IEEE transactions on Dielectrics and Electrical Insulation,* 7(2):269-275.

Zhang, F., Yingke, M., Wang, X., Wang, L., Guan, Z. 2007. Experimental Investigation on Flashover Performance of Glass Insulator for DC Transmission Lines at High Altitudes. *Conference on Electric Insulation and Dielectric Phenomena,* Vancouver, Canada, 324-328.

Zhang, F., Zhao, J., Wang, L., Guan, Z. 2010. Experimental Investigation on Outdoor Insulation for DC Transmission Line at High Altitudes. *IEEE transactions on power delivery,* 25(1):351-357.

Zhang, Z., Jiang, X., Chao, Y., Chen, L., Sun, C., Hu, J. 2010. Study on DC Pollution Flashover Performance of Various Types of Long String Insulators Under Low Atmospheric Pressure Conditions. *IEEE transactions on power delivery,* 25(4):2132-2141.

Zhang, Z., Jiang, X., Huang, H., Sun, C., Hu, J. Wenzhong Gao, D. 2013. Study on the Wetting Process and Its Influencing Factors of Pollution Deposited on Different
Insulators Based on Leakage Current. *IEEE transactions on power delivery,* 28(2):678-685.

Zhang, C., Wang, L., Guan, Z. 2013. Pollution Flashover Performance of Full-scale ±800 kV
Converter Station Post Insulators at High Altitude Area. *IEEE transactions on Dielectrics and Electrical Insulation,* 20(3):717-726.

Zhengfa, L., Qing, Z., Wuyang, Z., Shimian, L., Gaolin, W. Jianlin, H., Maoqiang, B. 2018. Study on Leakage Current Characteristics and Influence Factors of 110kV Polluted Composite Insulators. *International Conference on the Properties and Applications of Dielectric Materials*, 896-900.

Zhicheng, G., Renyu, Z. 1990. Calculation of dc and ac Flashover Voltage of Polluted Insulators. *IEEE transactions on Electrical Insulation*, 25(4):723-729

APPENDIX A: WEEKLY LC ACTIVITY FROM AUGUST 2016 TO JUNE 2017 AS MONITORED AT THE APOLLO STATION

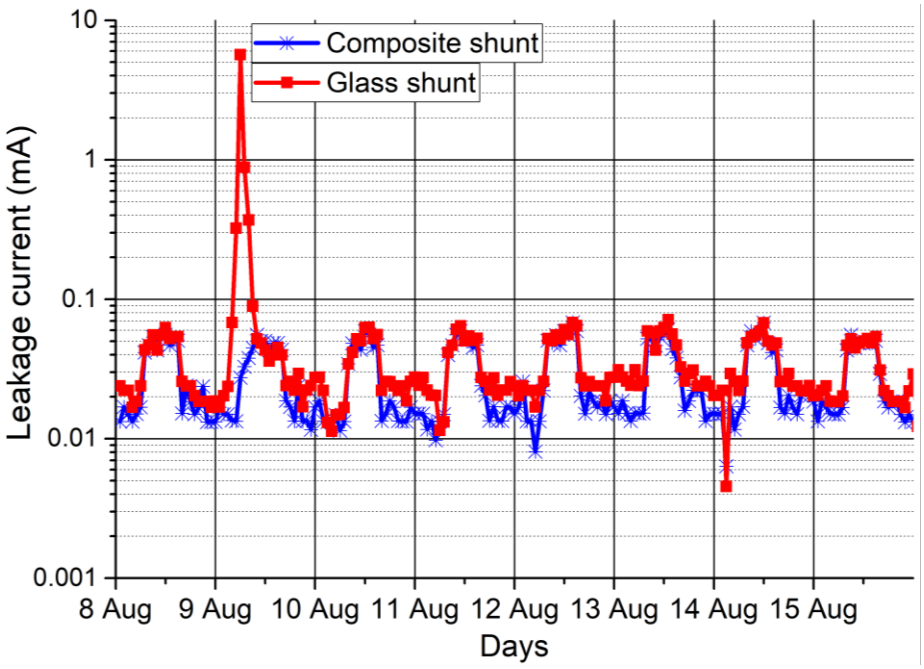

Figure A. 1: Leakage current activity: 8th - 15th of August

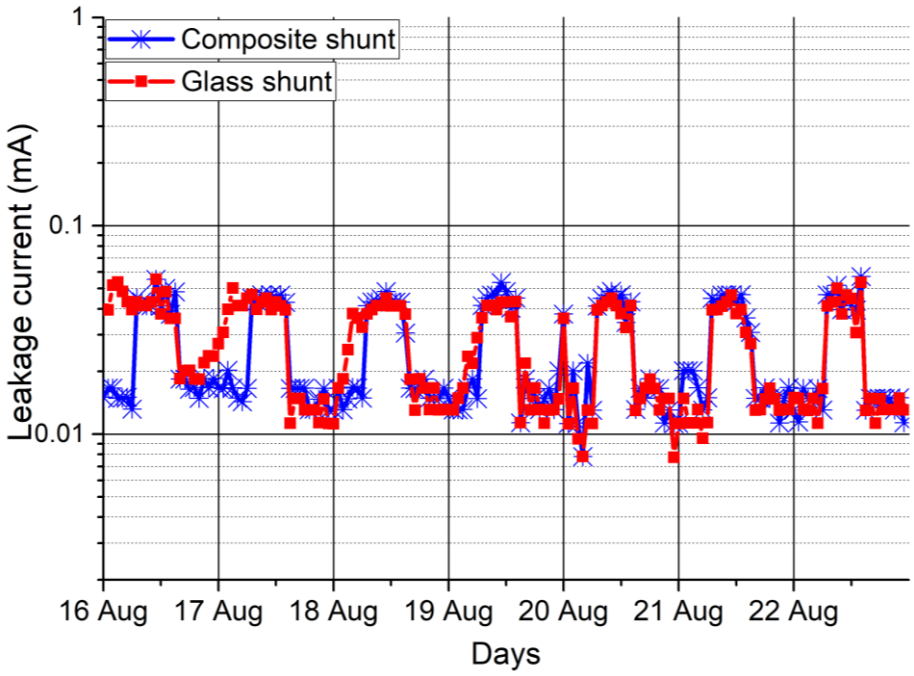

Figure A. 2: Leakage current activity: 16th - 22nd of August

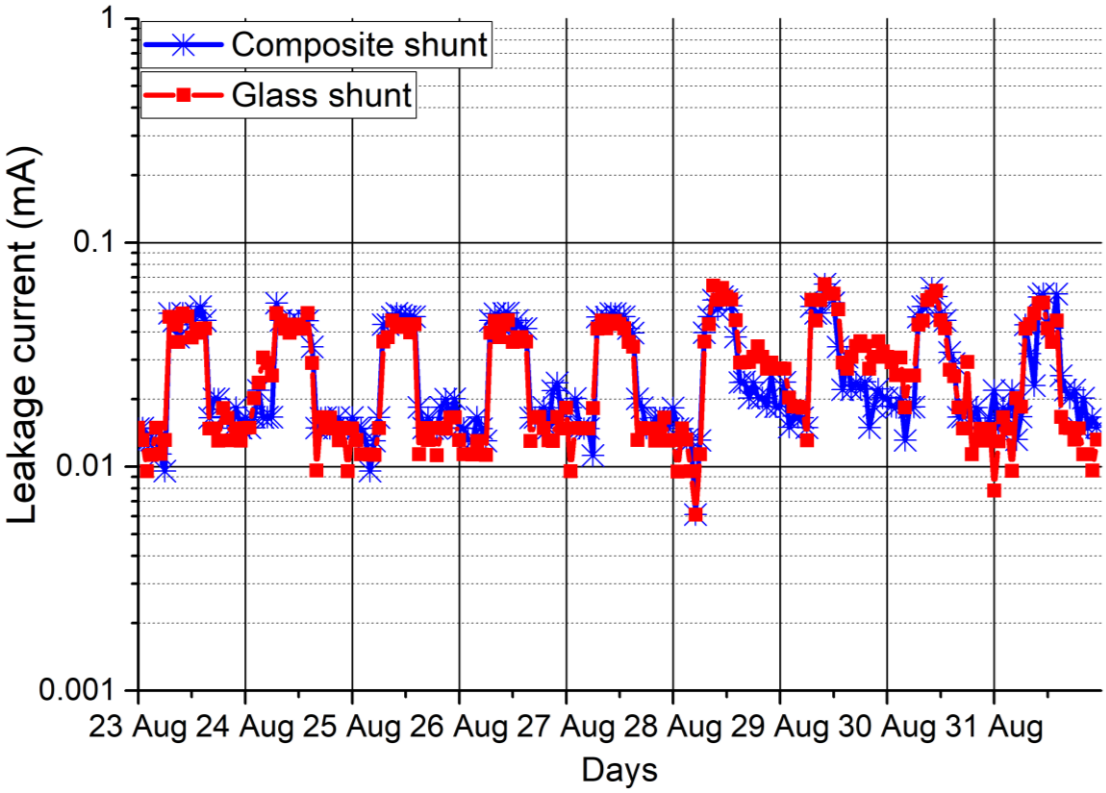

Figure A. 3: Leakage current activity: 23rd - 31st of August

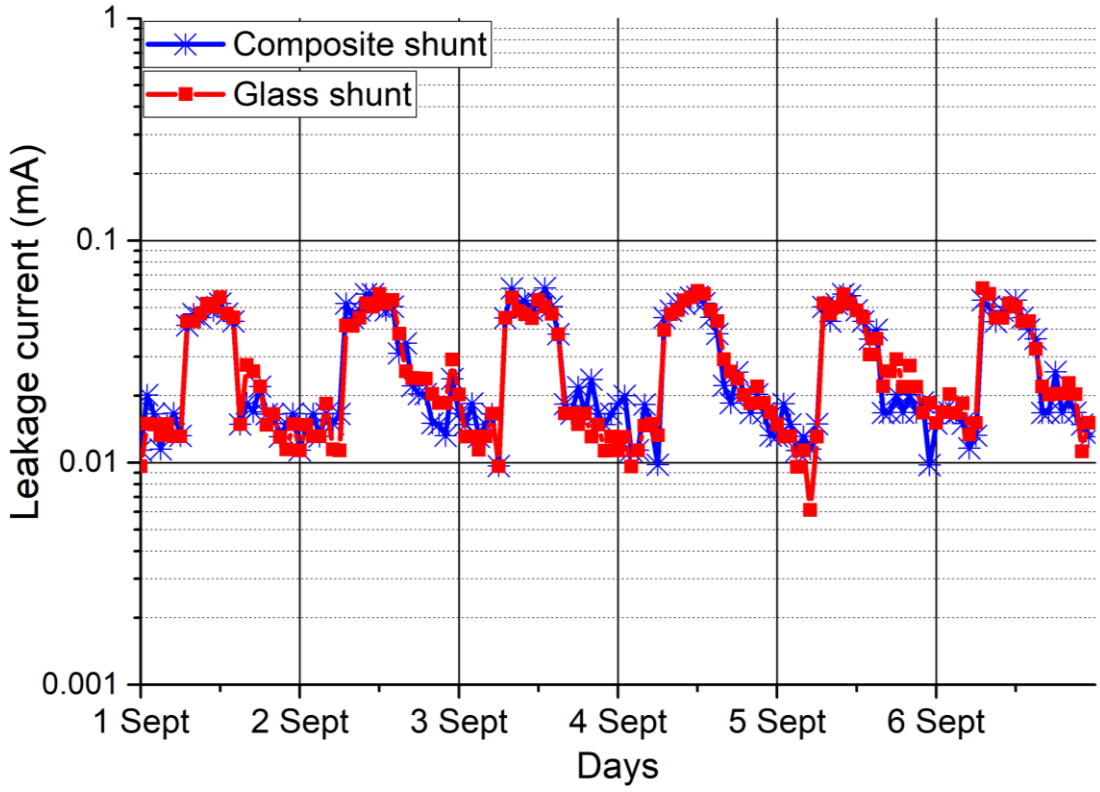

Figure A. 4: Leakage current activity: 1st - 6th of September

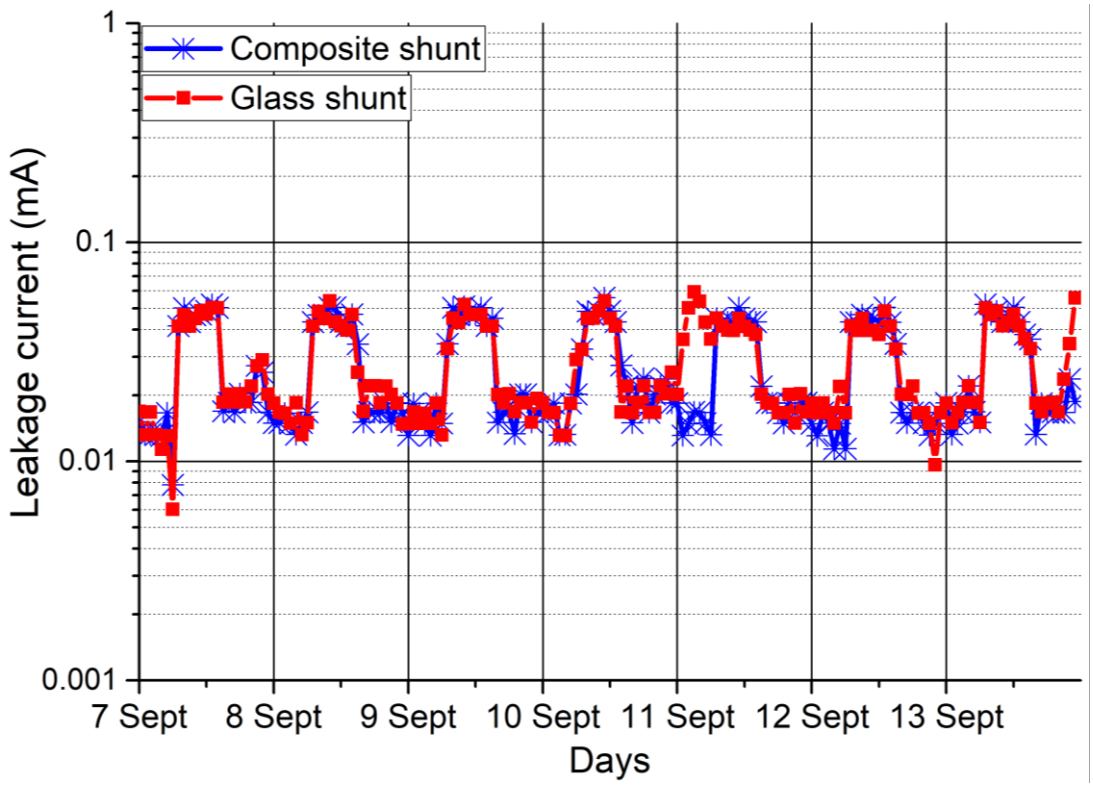

Figure A. 5: Leakage current activity: 7th - 13th of September

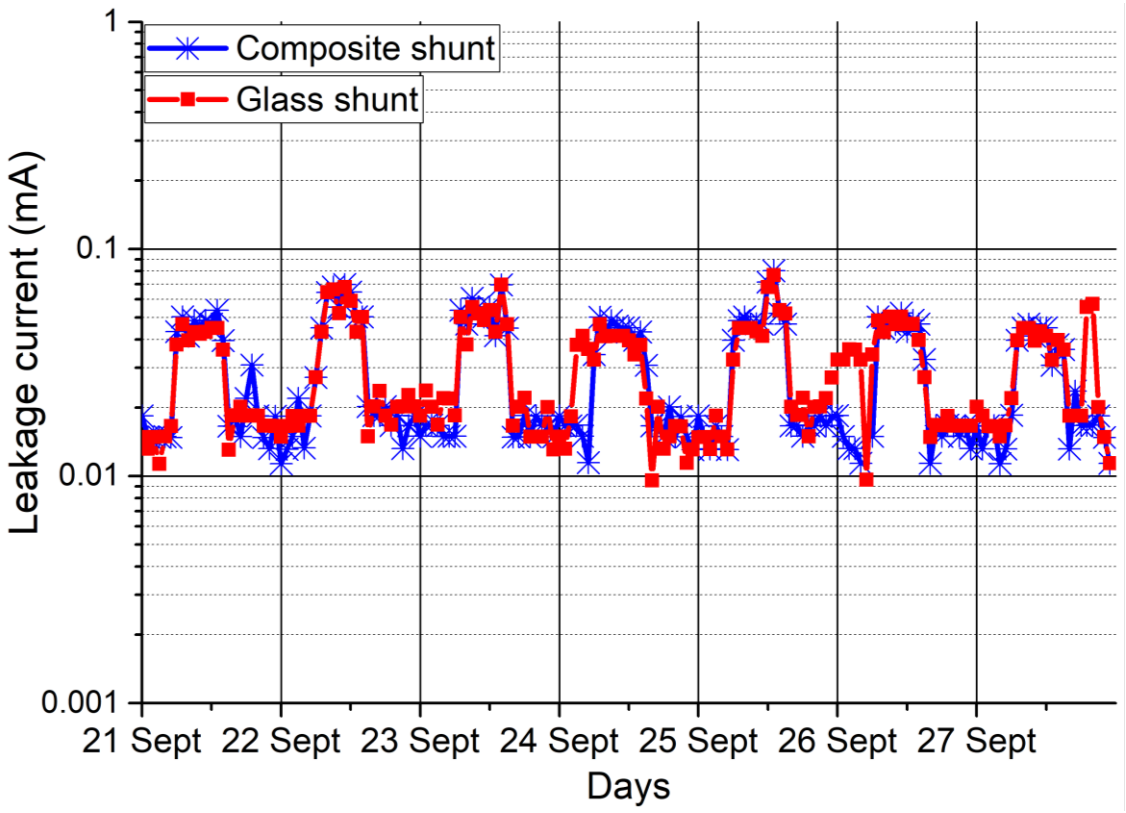

Figure A. 6: Leakage current activity: 21st - 27th of September

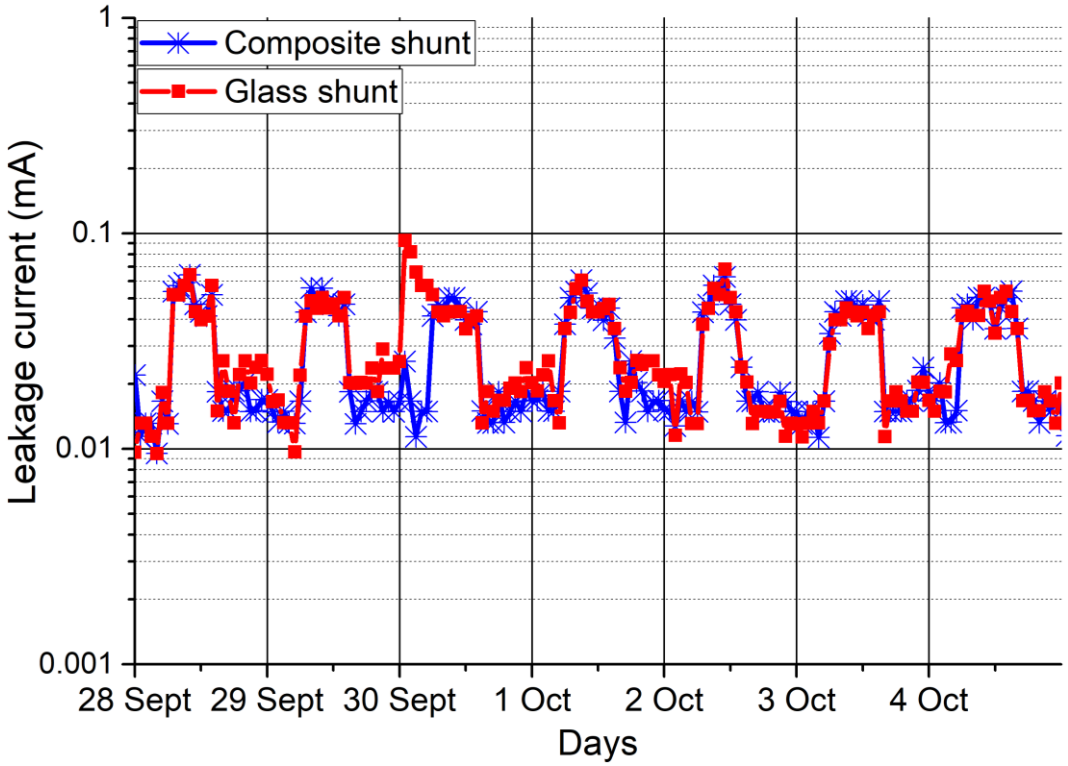

Figure A. 7: Leakage current activity: 28th of September to the 4th of October

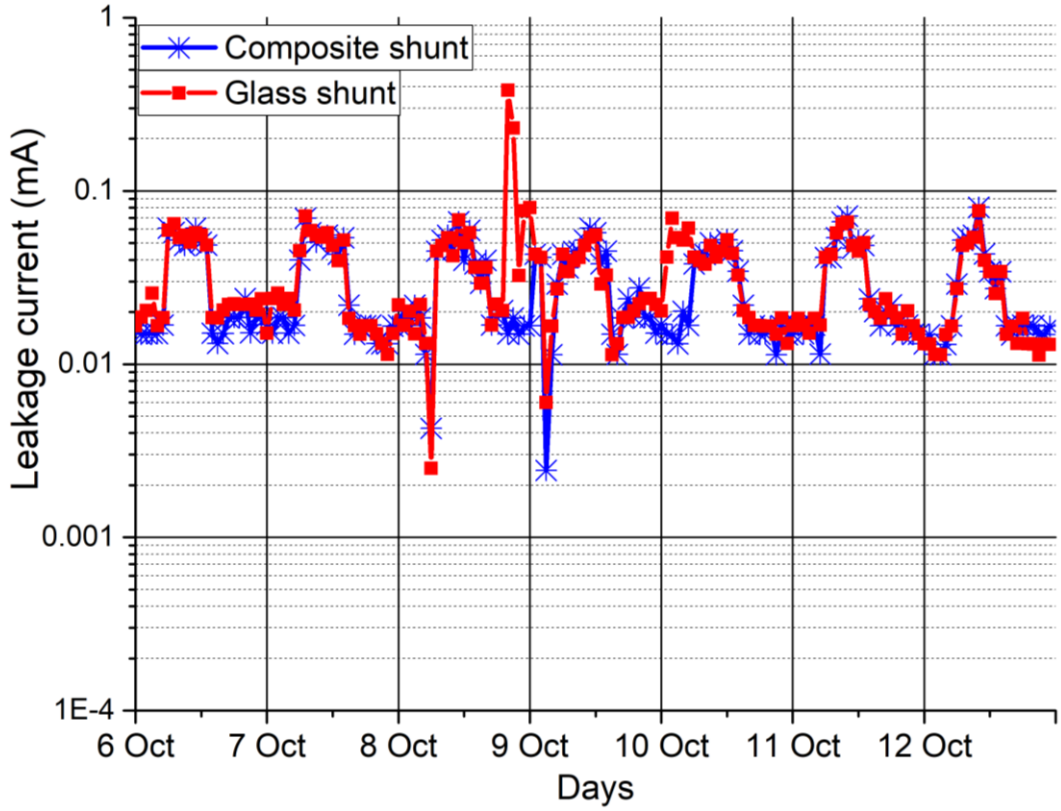

Figure A. 8: Leakage current activity: 6th - 12th of October

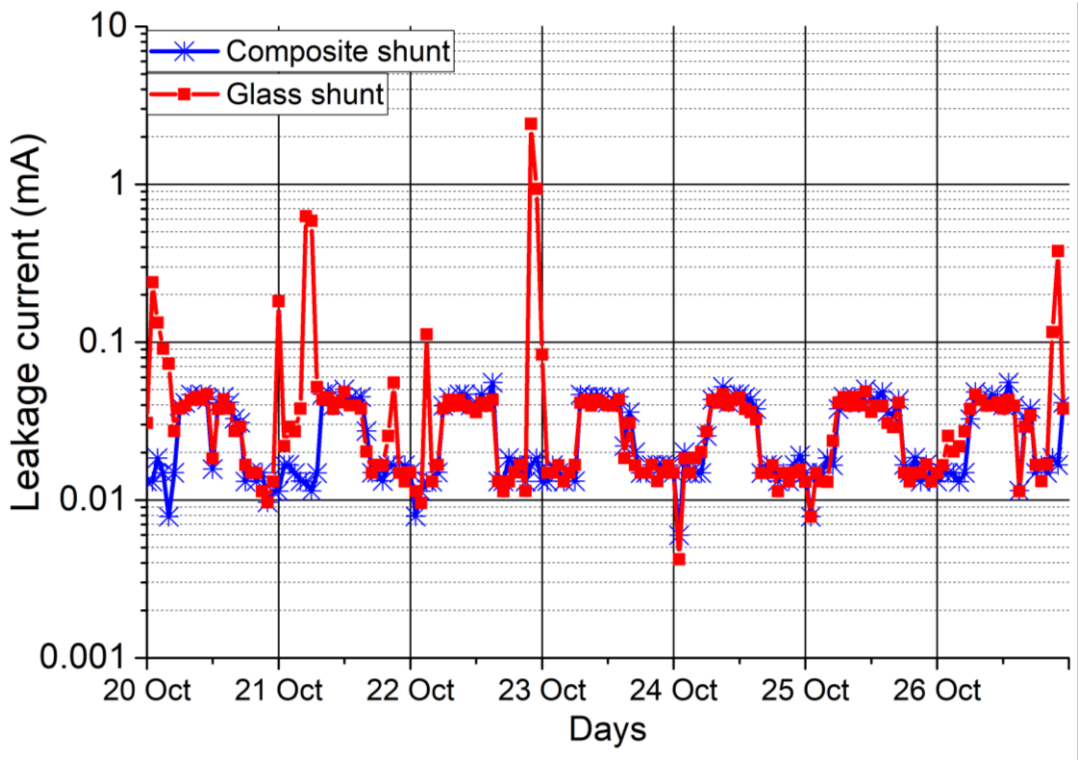

Figure A. 9: Leakage current activity: 20th - 26th of October

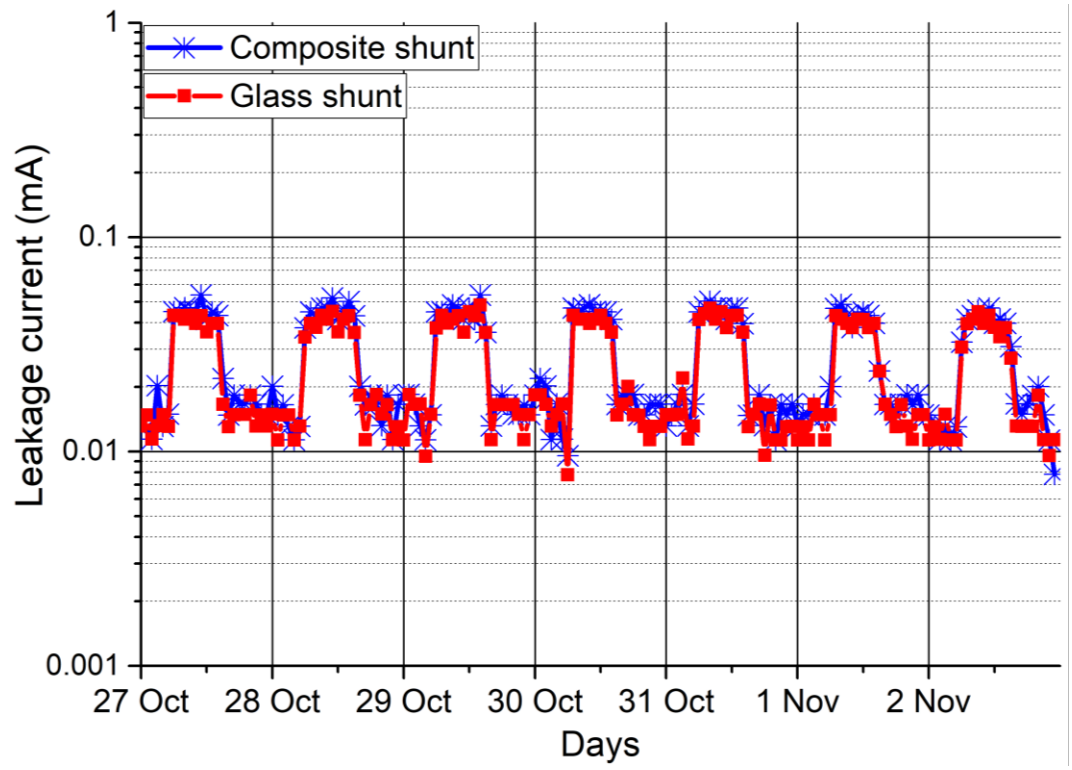

Figure A. 10: Leakage current activity: 27th of October to the 2nd of November

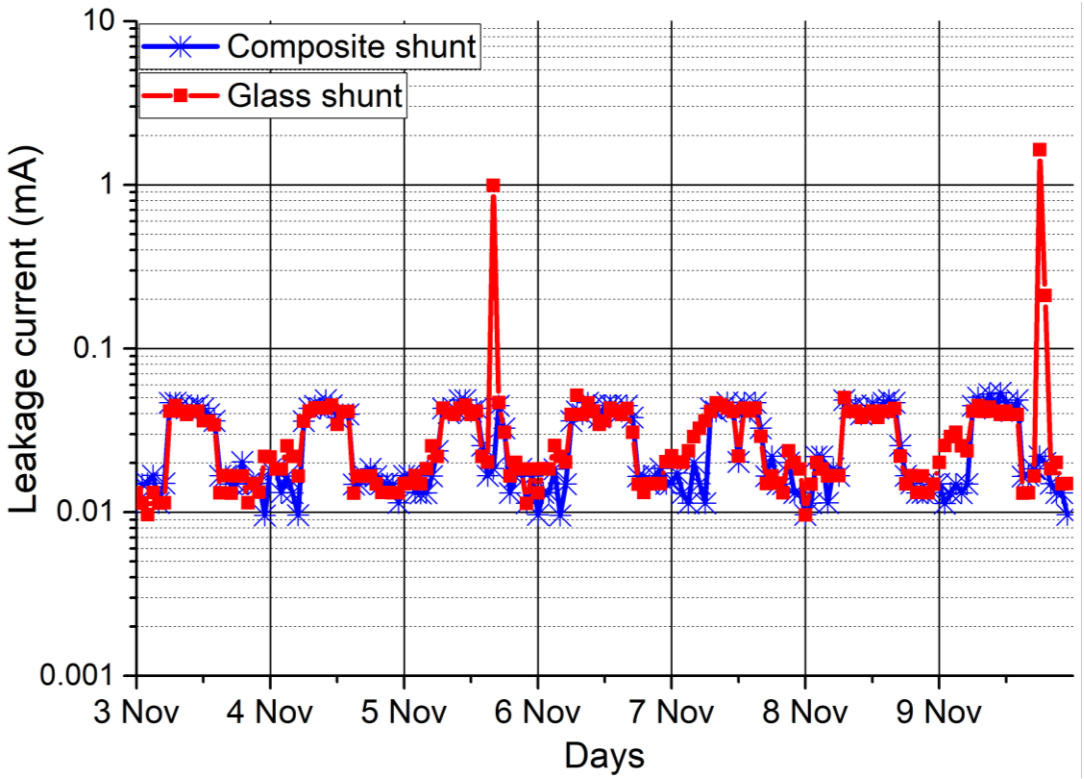

Figure A. 11: Leakage current activity: 3rd - 9th of November

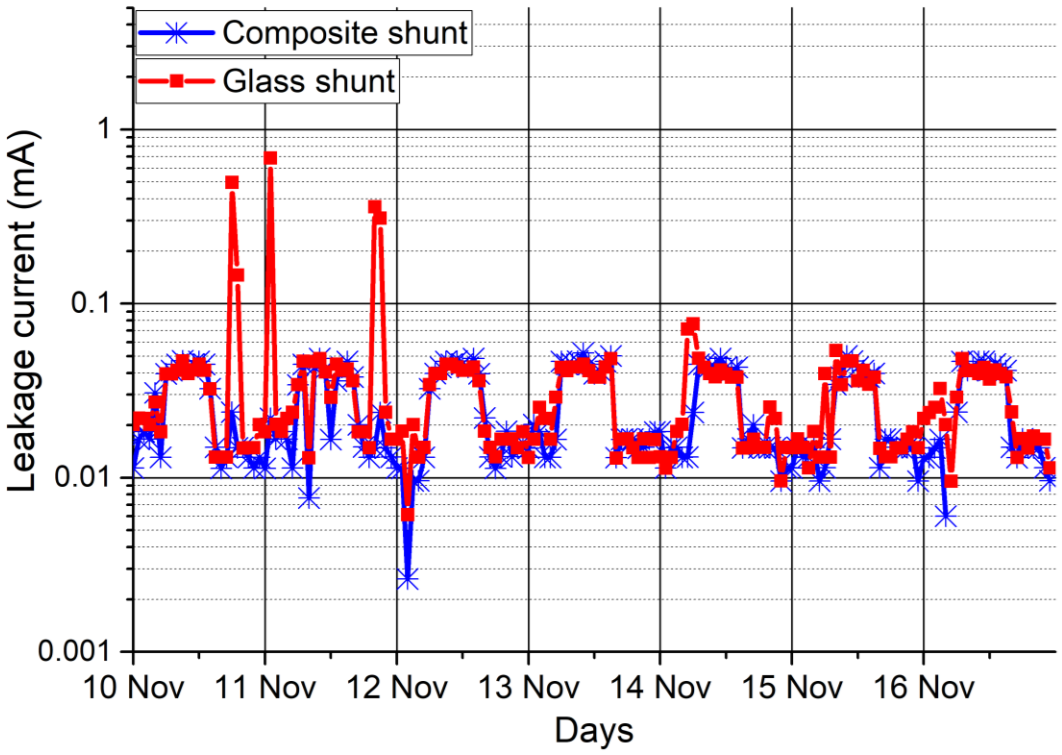

Figure A. 12: Leakage current activity: 10th - 16th of November

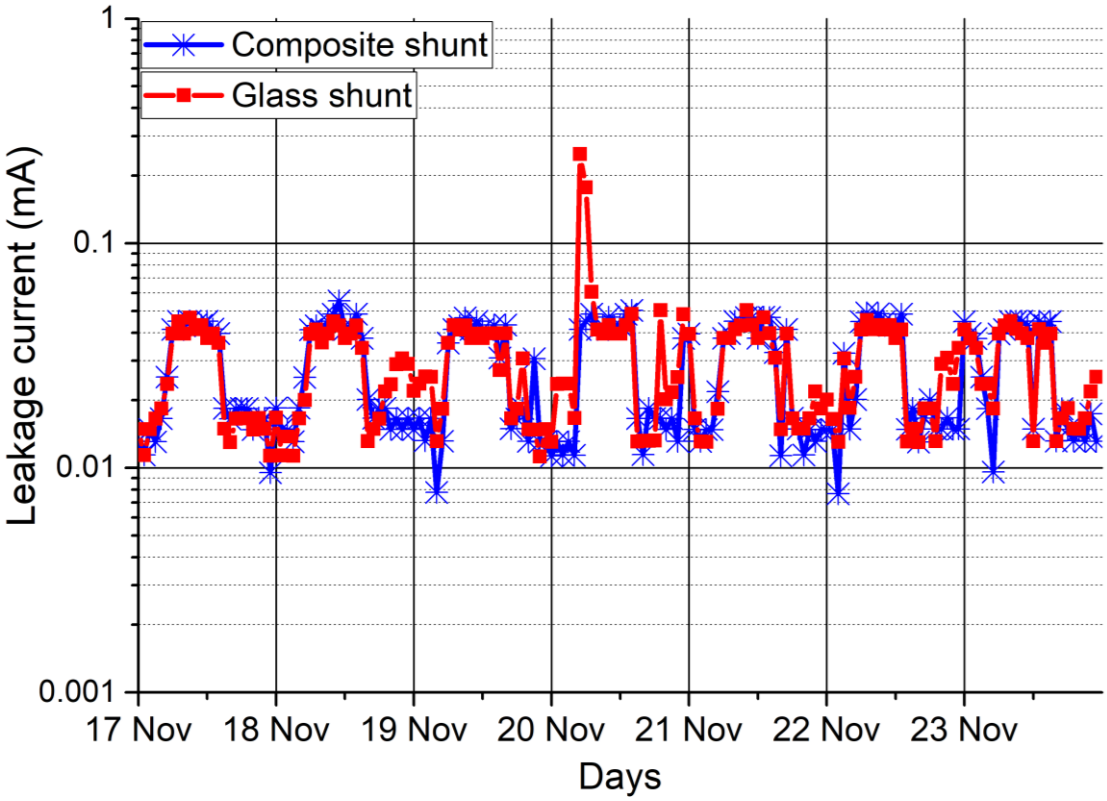

Figure A. 13: Leakage current activity: 17th - 23rd of November

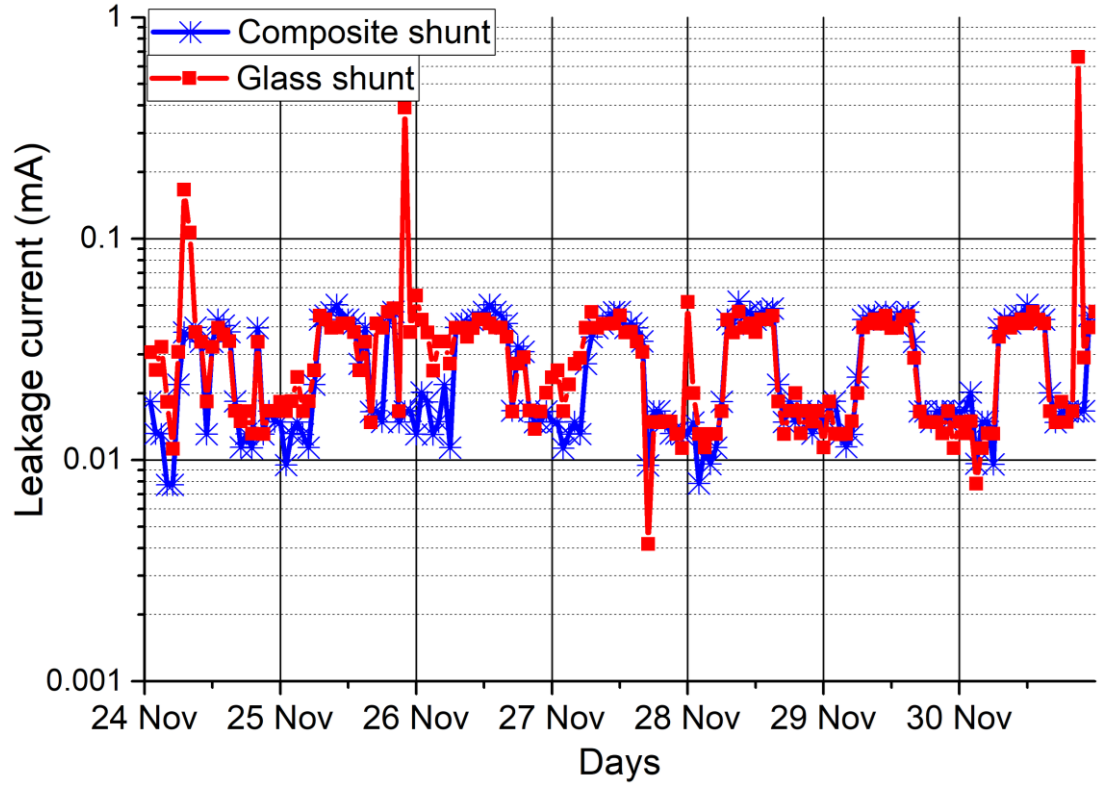

Figure A. 14: Leakage current activity: 24th - 30th of November

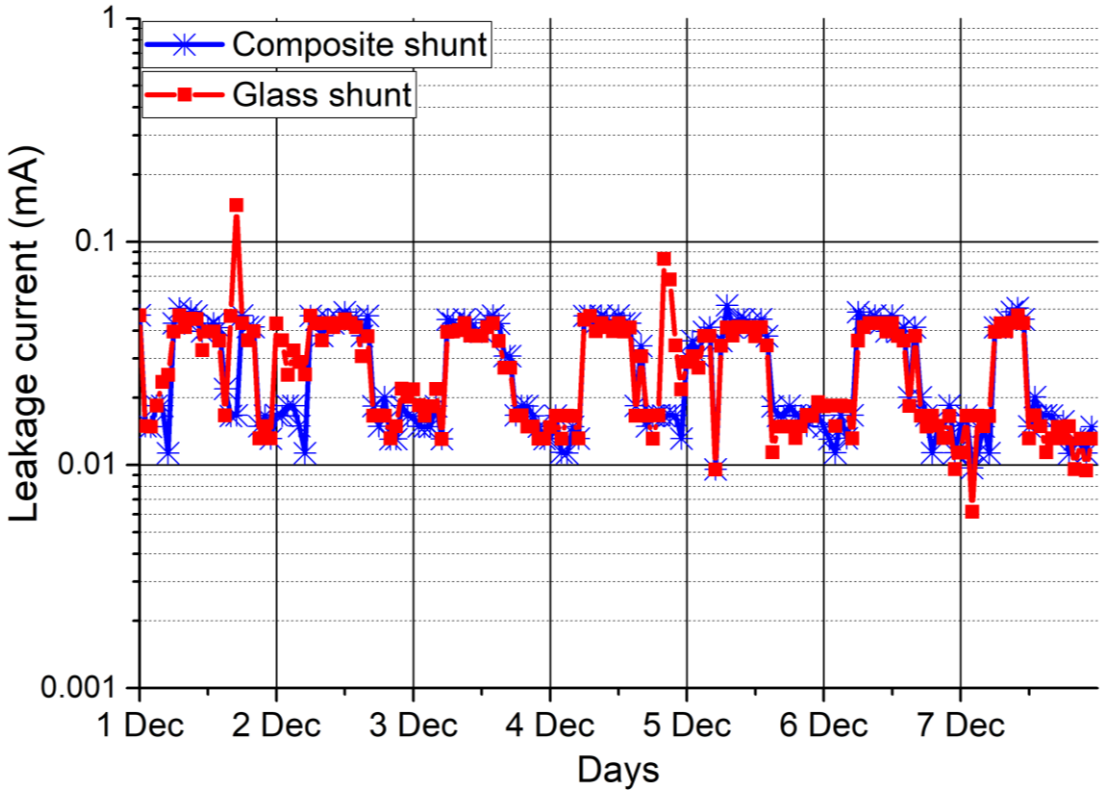

Figure A. 15: Leakage current activity: 1st - 7th of December

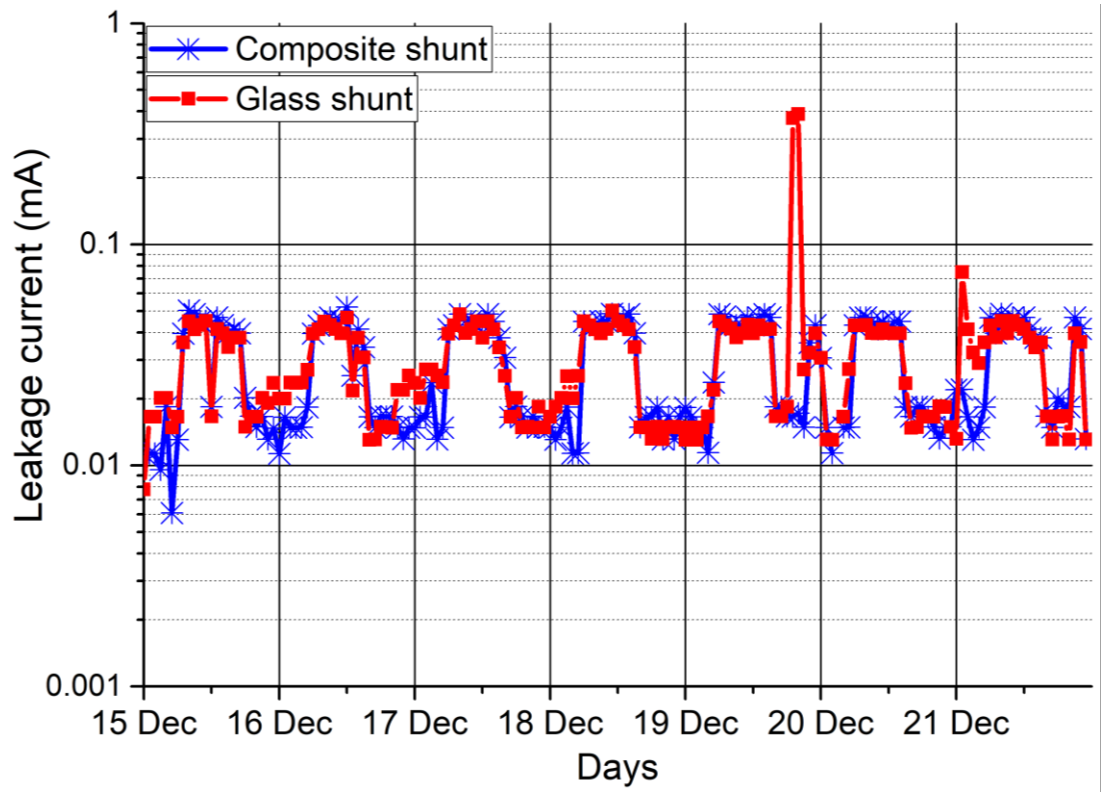

Figure A. 16: Leakage current activity: 15th - 21st of December

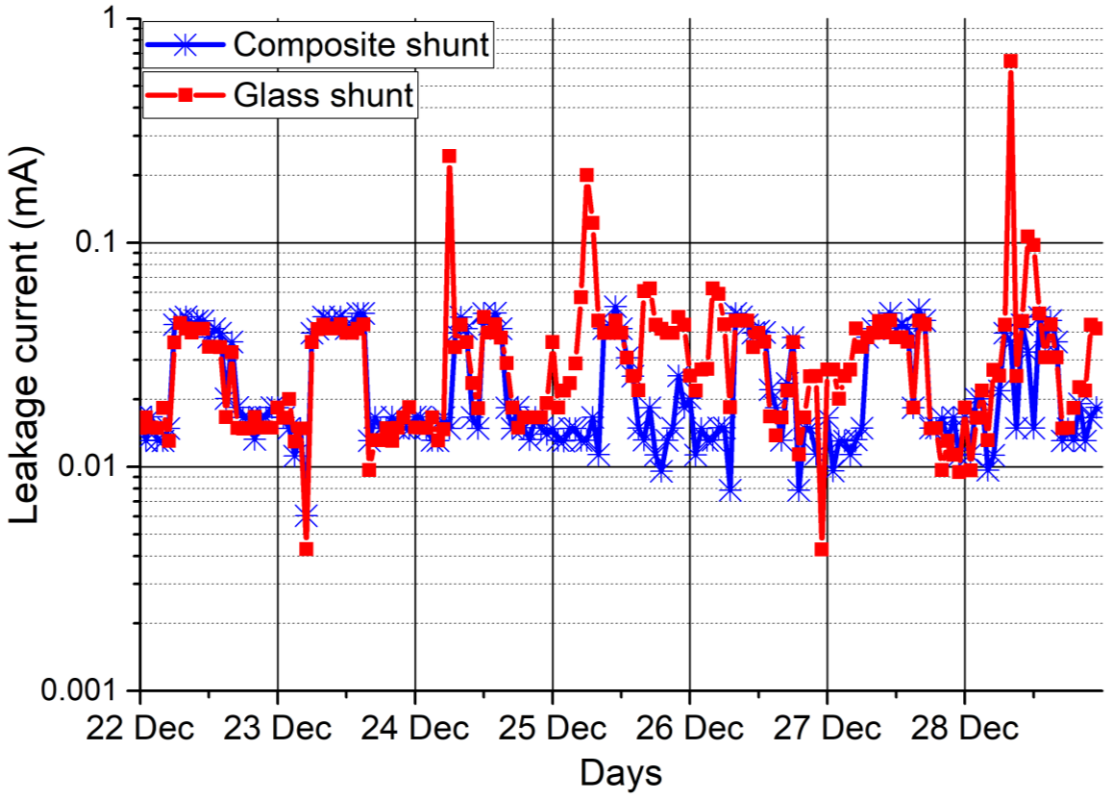

Figure A. 17: Leakage current activity: 22nd - 28th of December

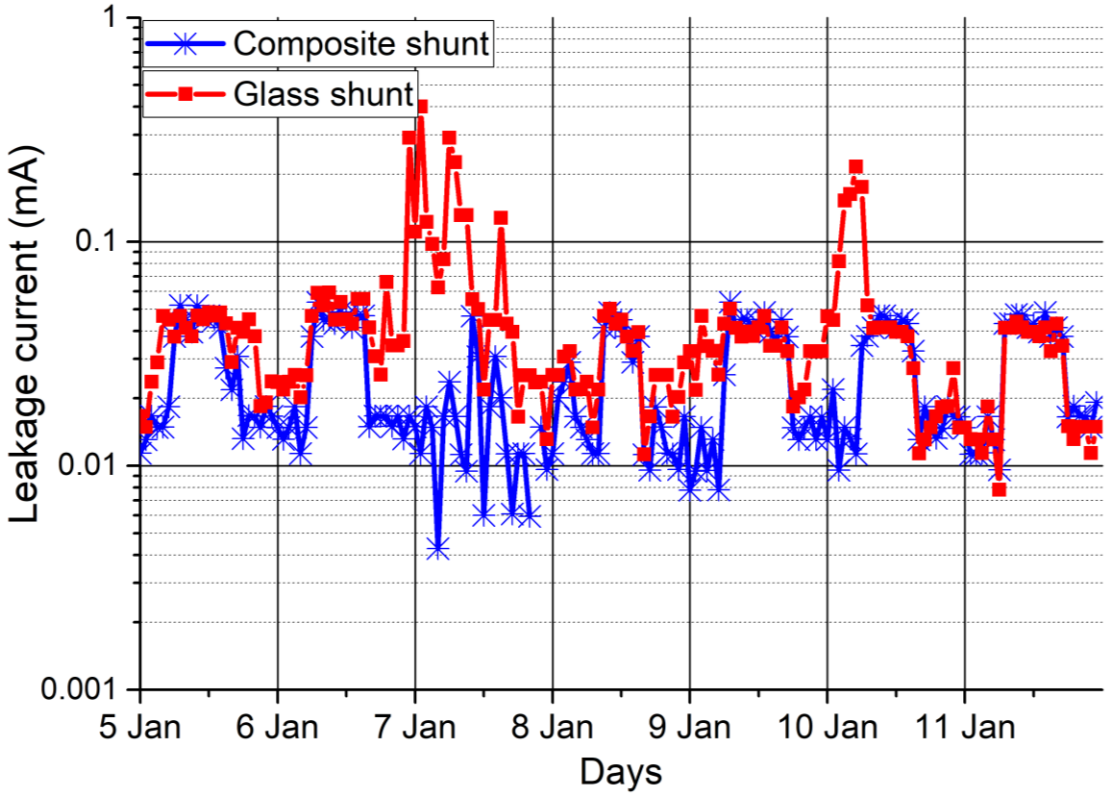

Figure A. 18: Leakage current activity: 5th - 11th of January

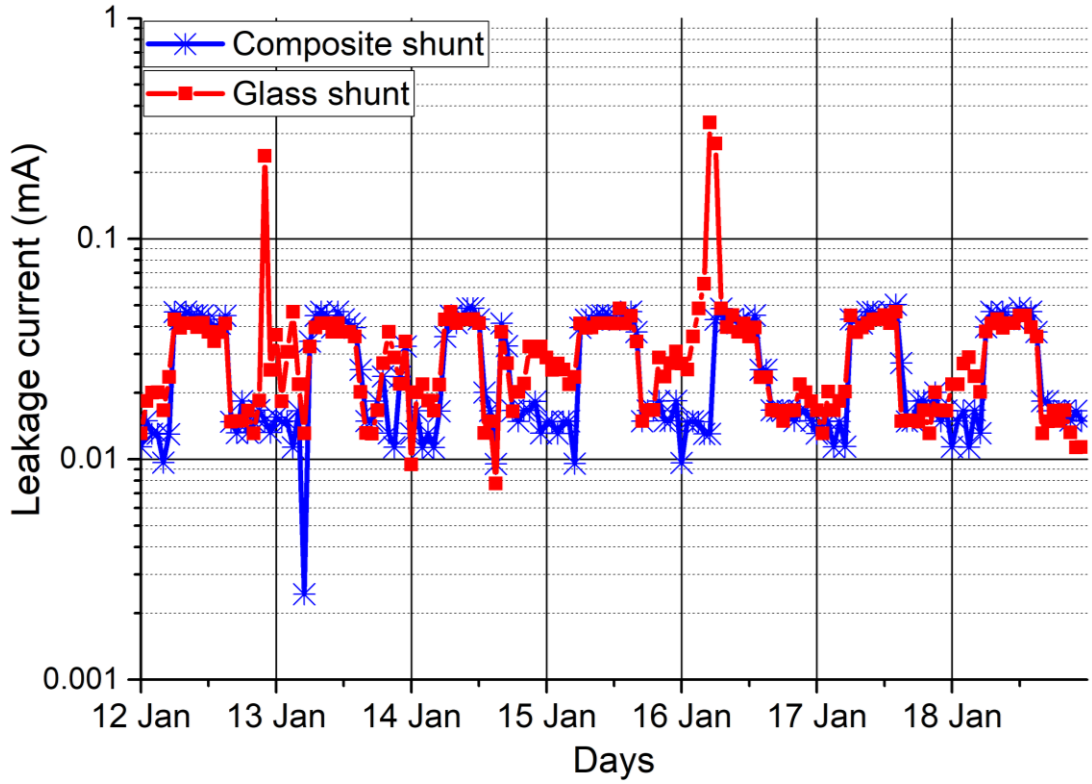

Figure A. 19: Leakage current activity: 12th - 18th of January

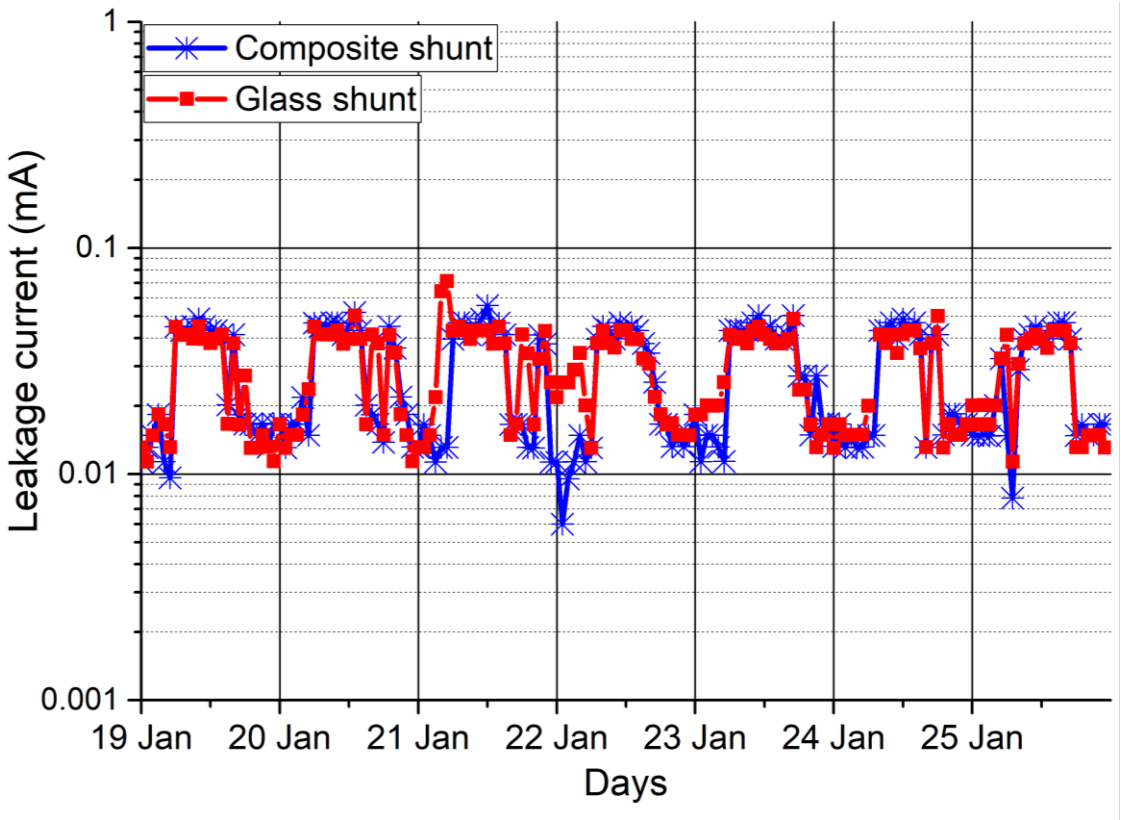

Figure A. 20: Leakage current activity: 19th - 25th of January

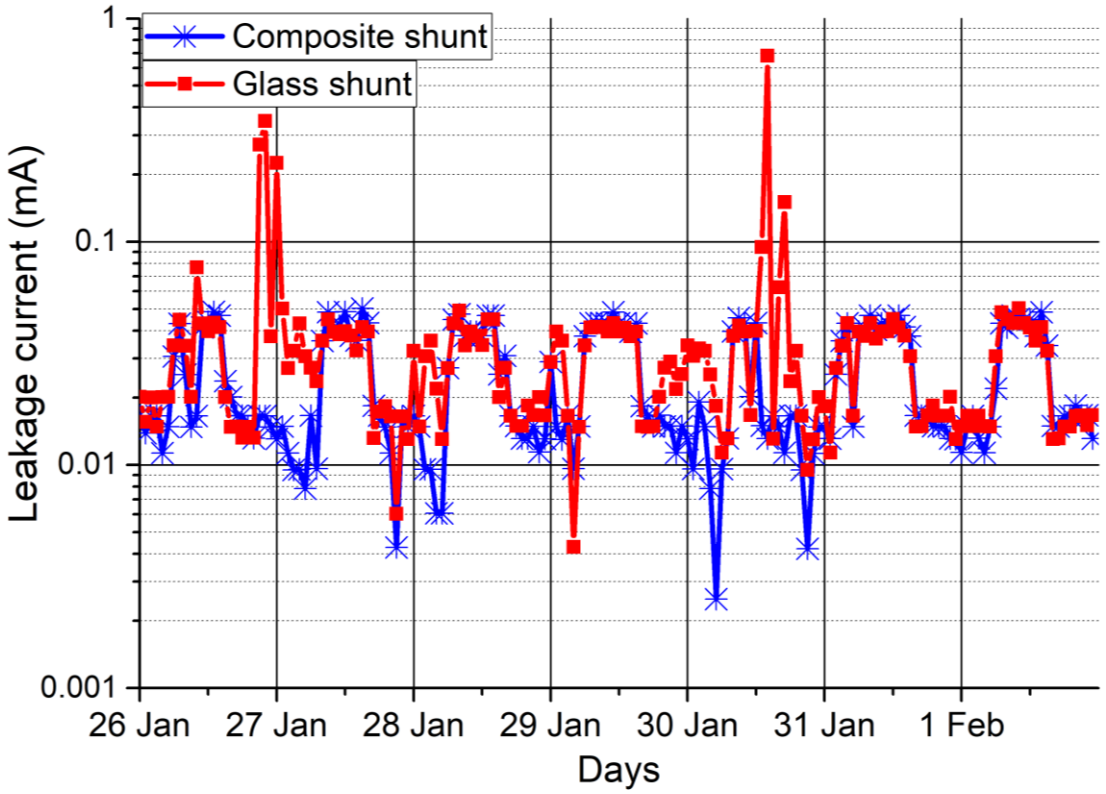

Figure A. 21: Leakage current activity: 26th of January to the 1st of February

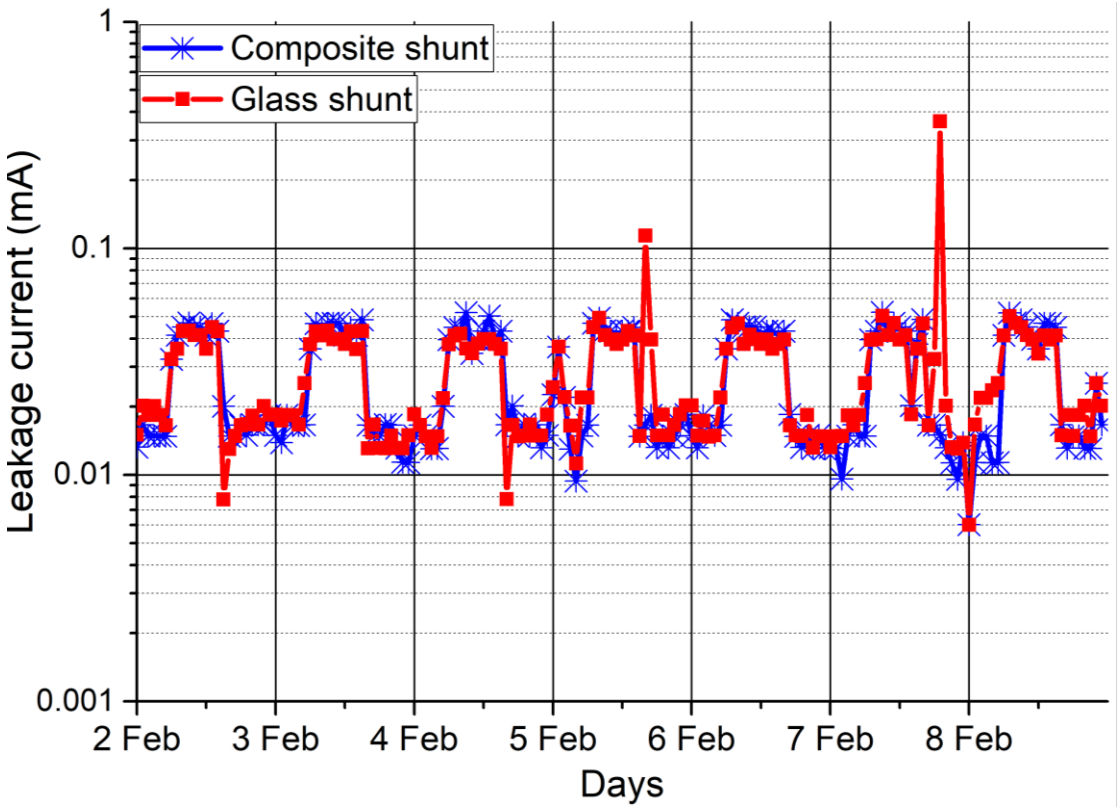

Figure A. 22: Leakage current activity: 2nd - 8th of February

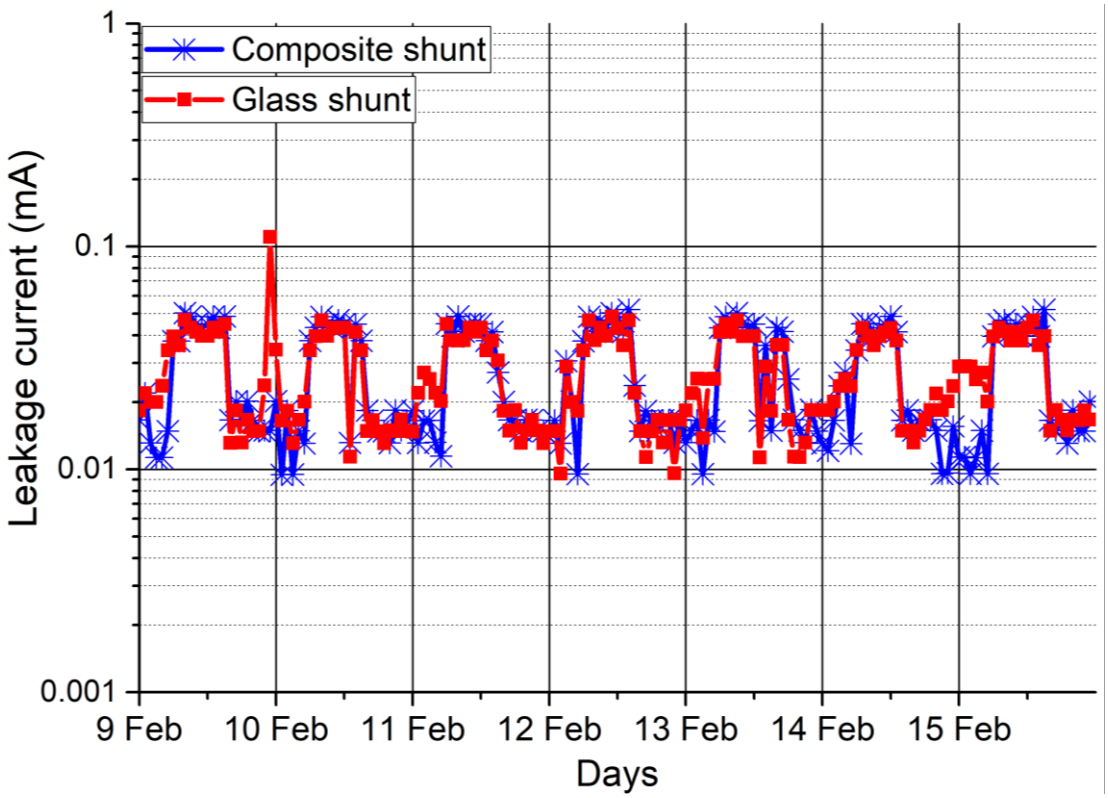

Figure A. 23: Leakage current activity: 9th - 15th of February

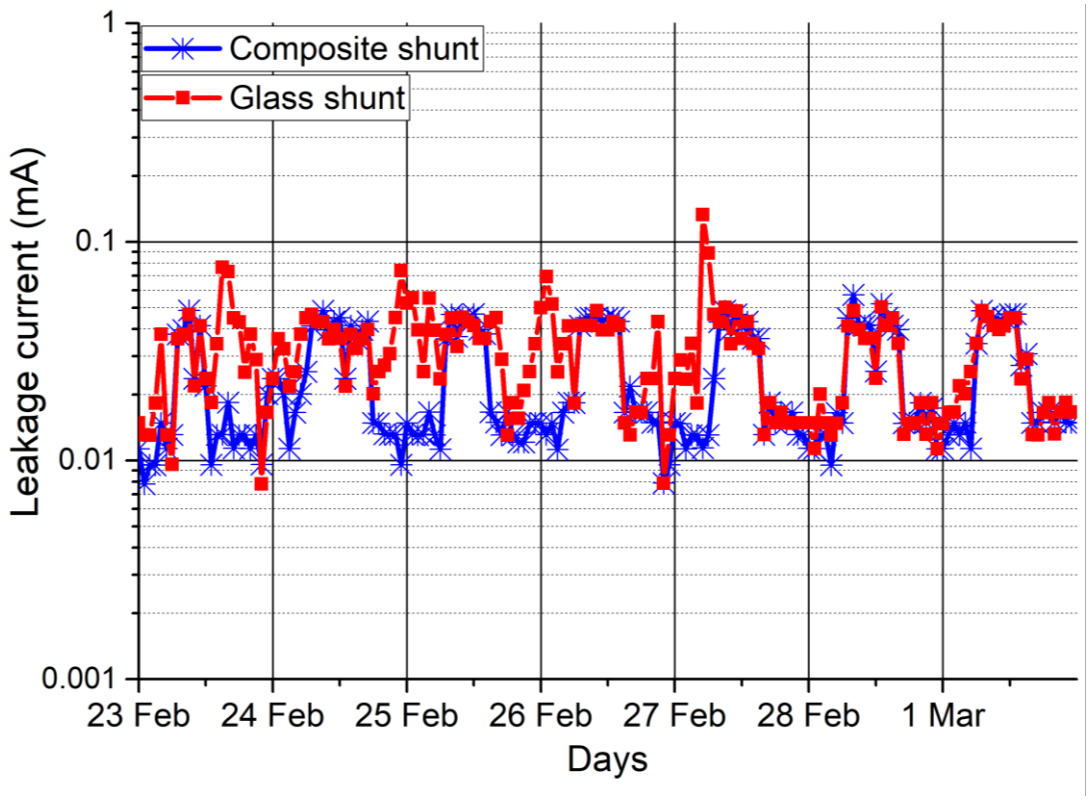

Figure A. 24: Leakage current activity: 23rd of February to the 1st of March

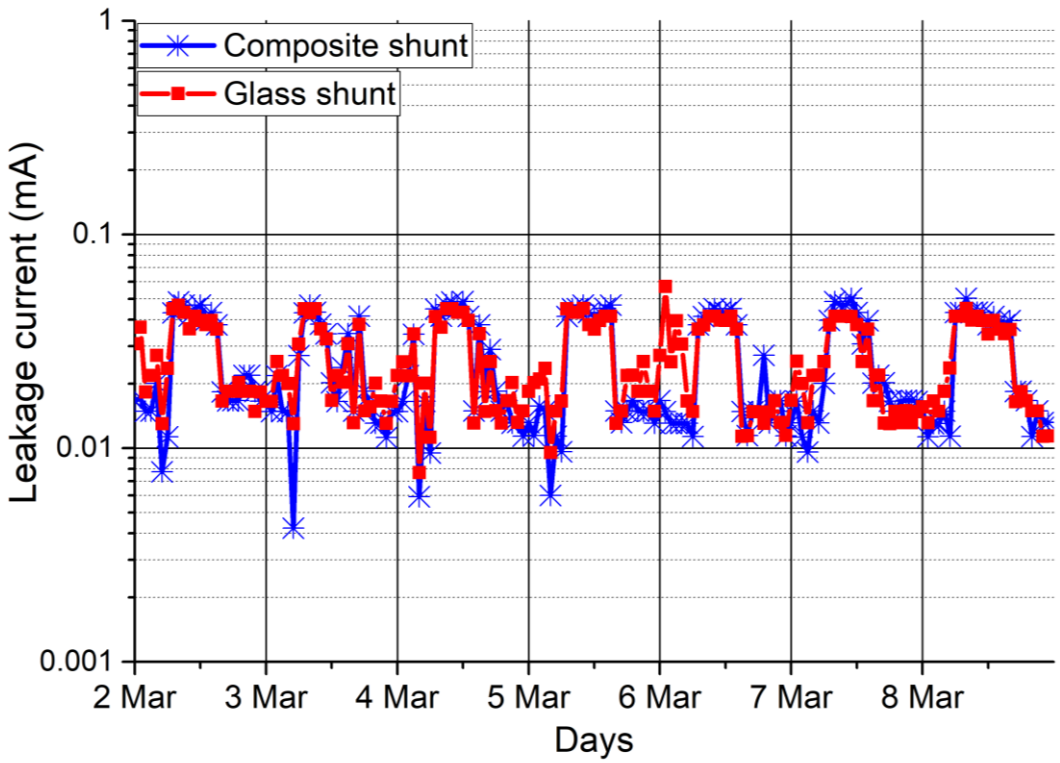

Figure A. 25: Leakage current activity: 2nd - 8th of March

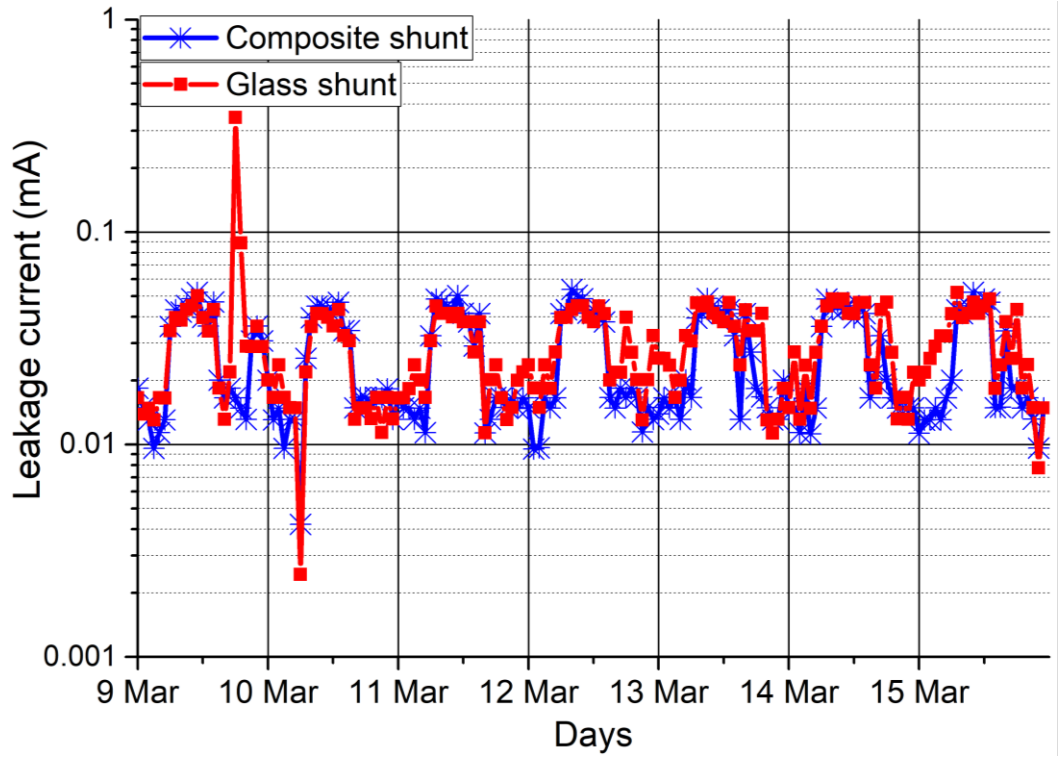

Figure A. 26: Leakage current activity: 9th - 15th of March

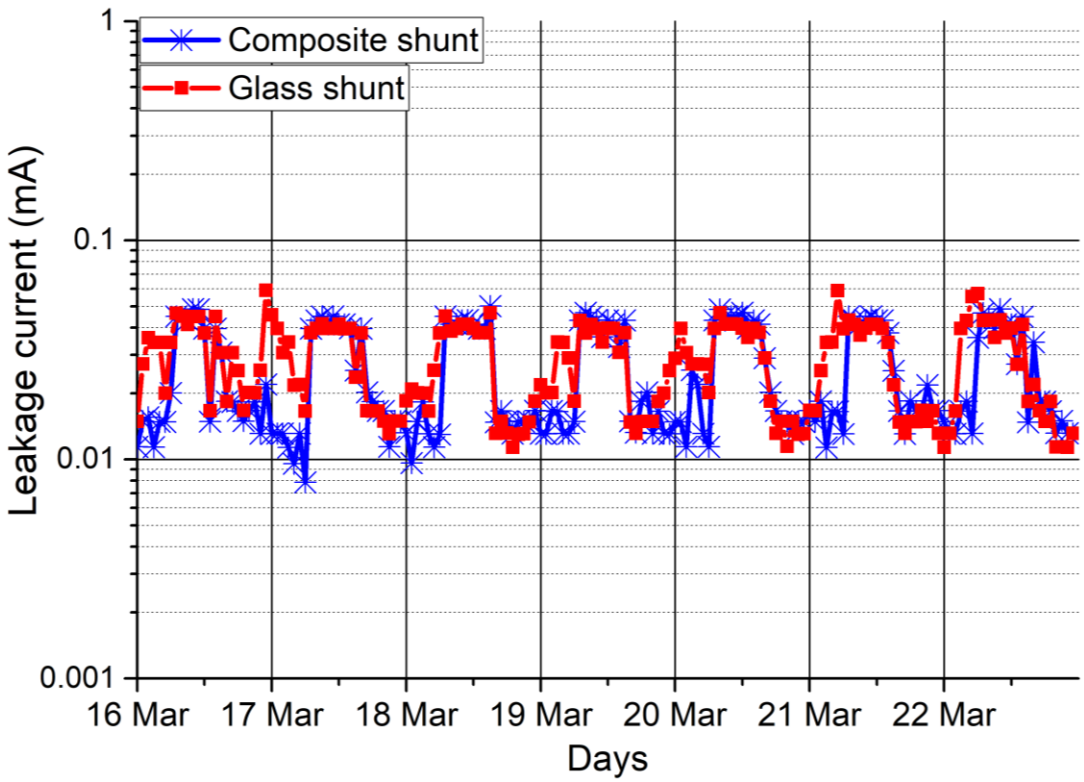

Figure A. 27: Leakage current activity: 16th - 22nd of March

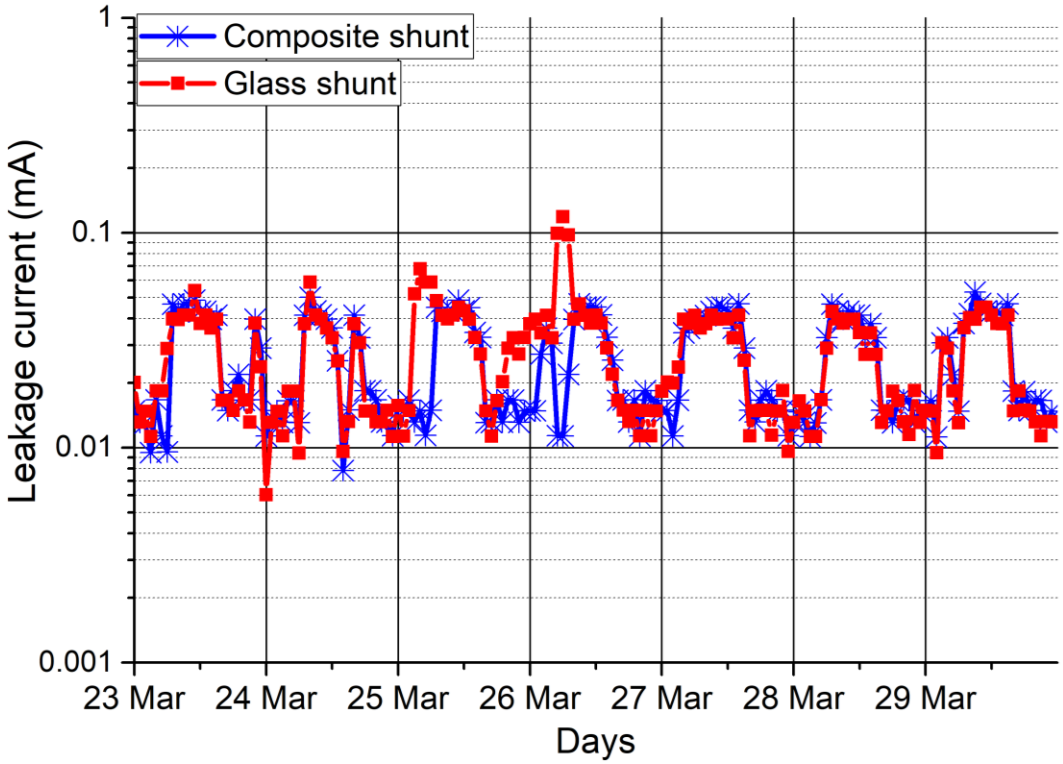

Figure A. 28: Leakage current activity: 23rd - 29th of March

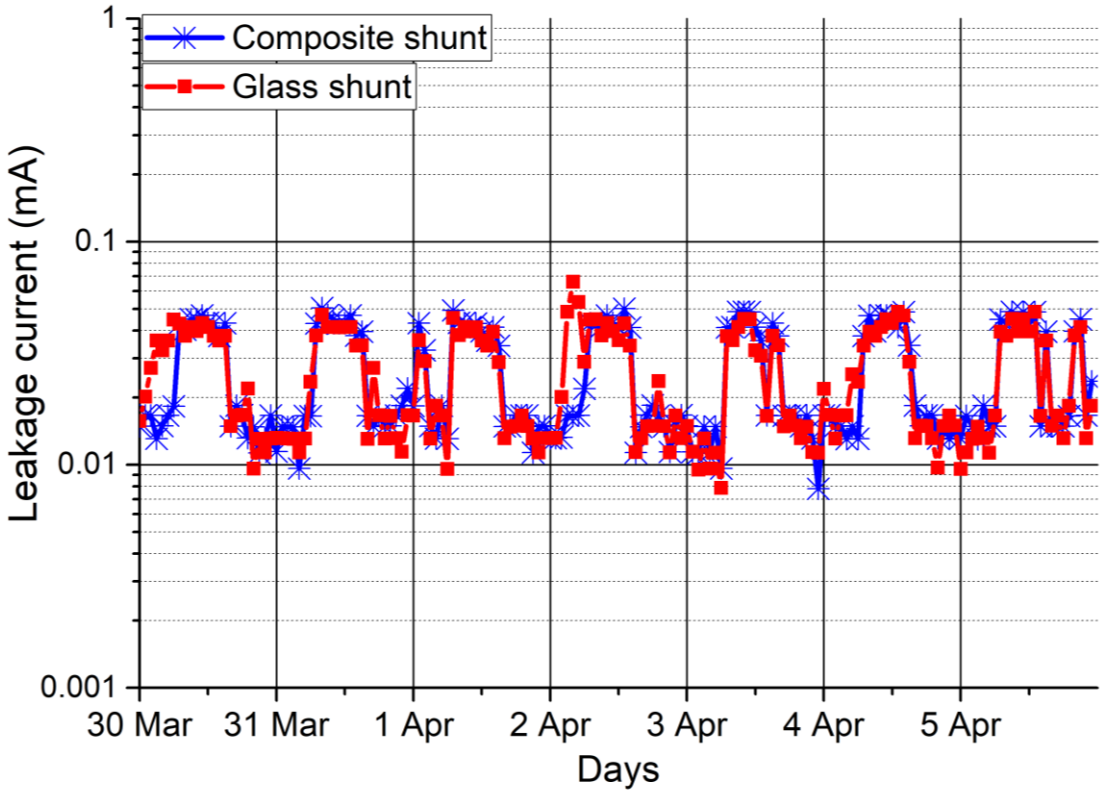

Figure A. 29: Leakage current activity: 30th of March to the 5th of April

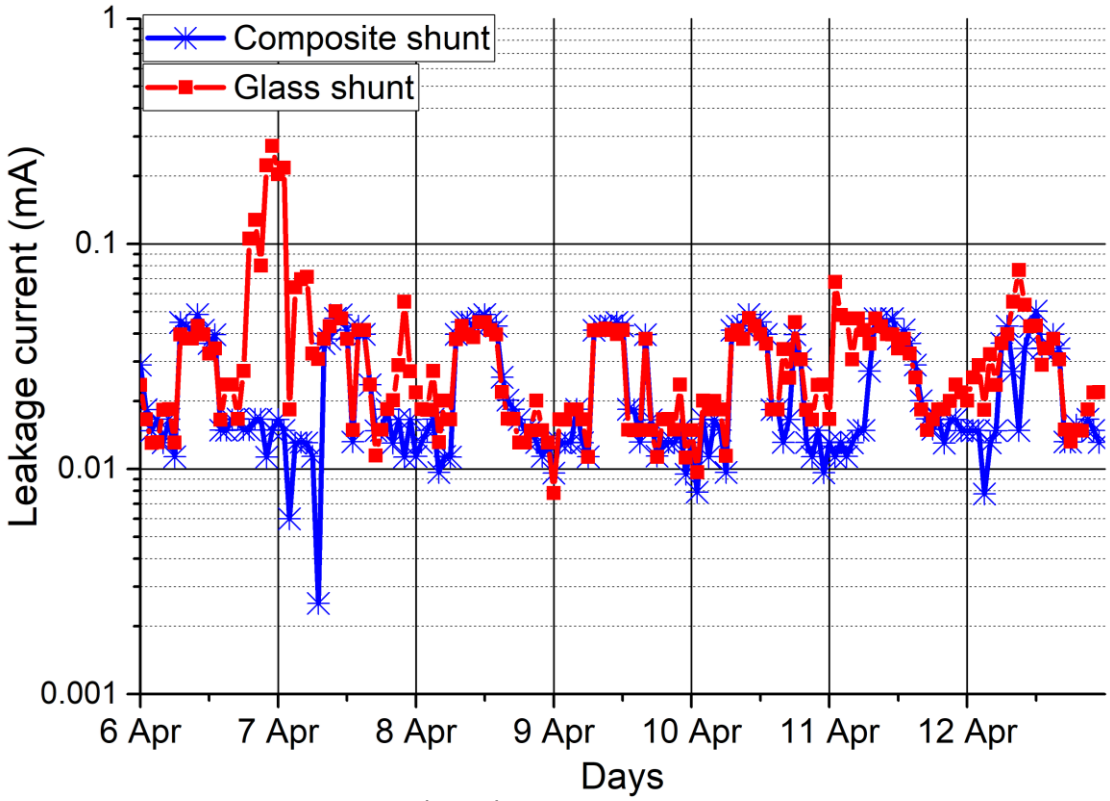

Figure A. 30: Leakage current activity: 6th - 12th of April

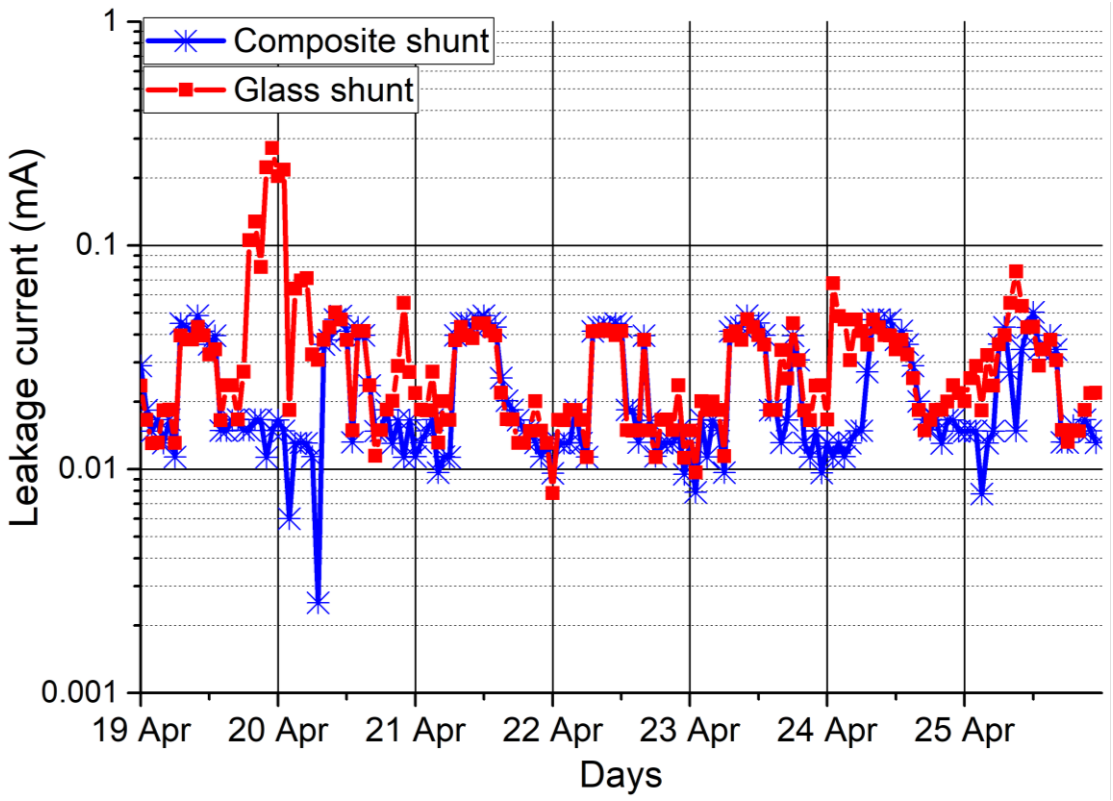

Figure A. 31: Leakage current activity: 19th - 25th of April

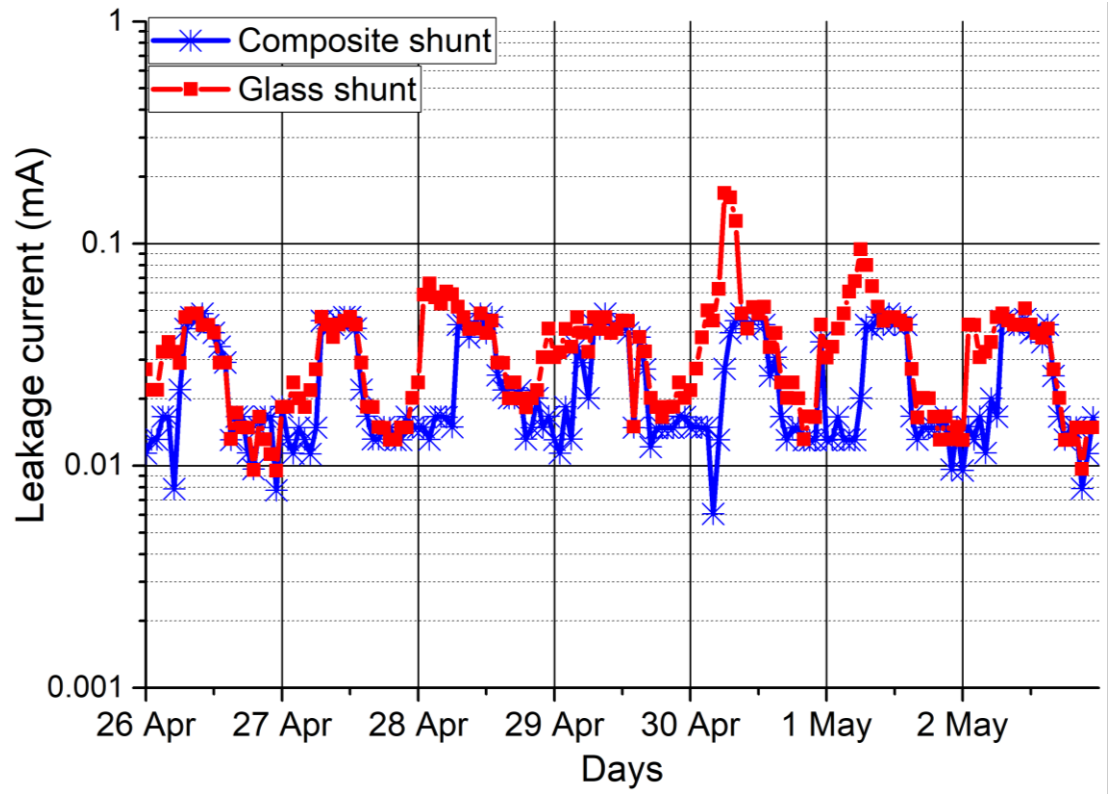

Figure A. 32: Leakage current activity: 26th of April to the 2nd of May

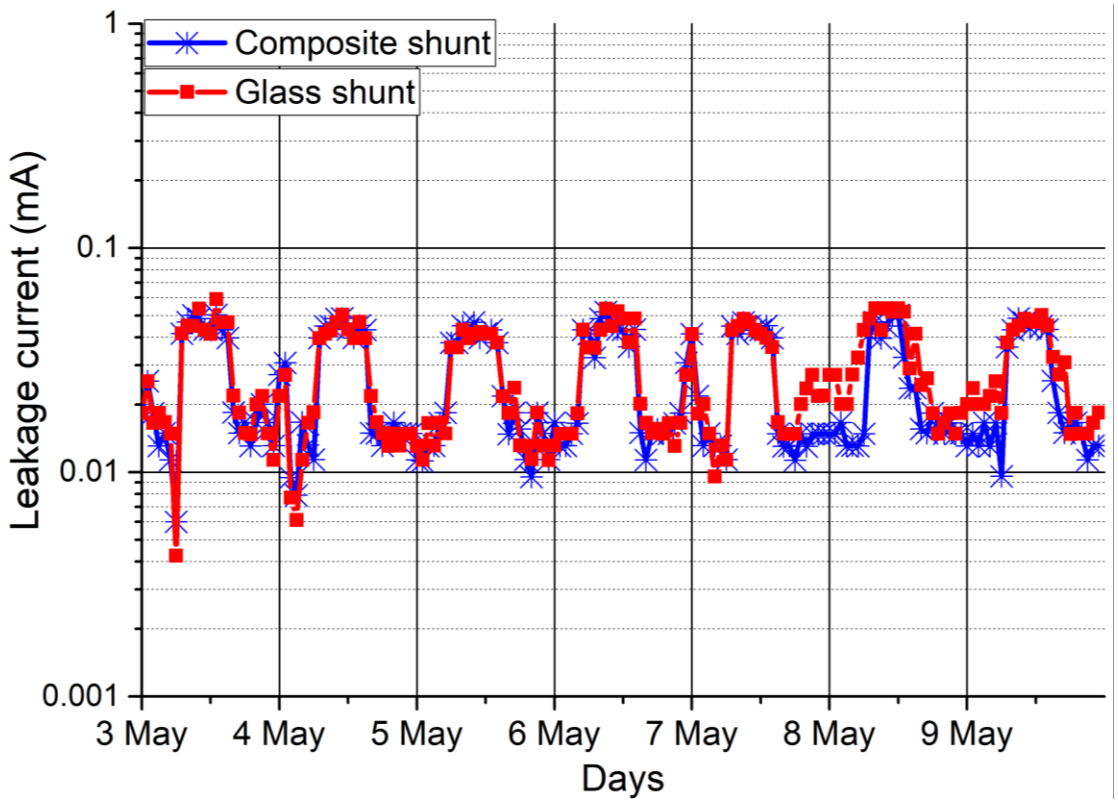

Figure A. 33: Leakage current activity: 3rd - 9th of May

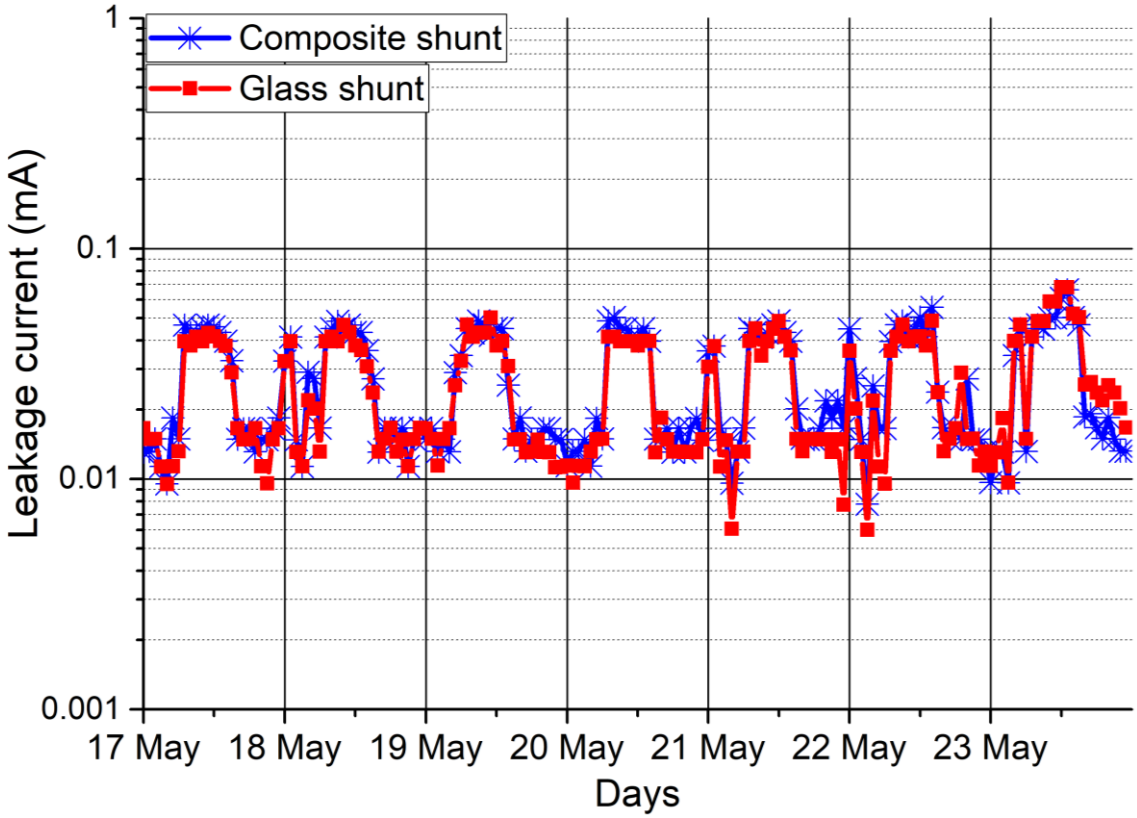

Figure A. 34: Leakage current activity: 17th - 23rd of May

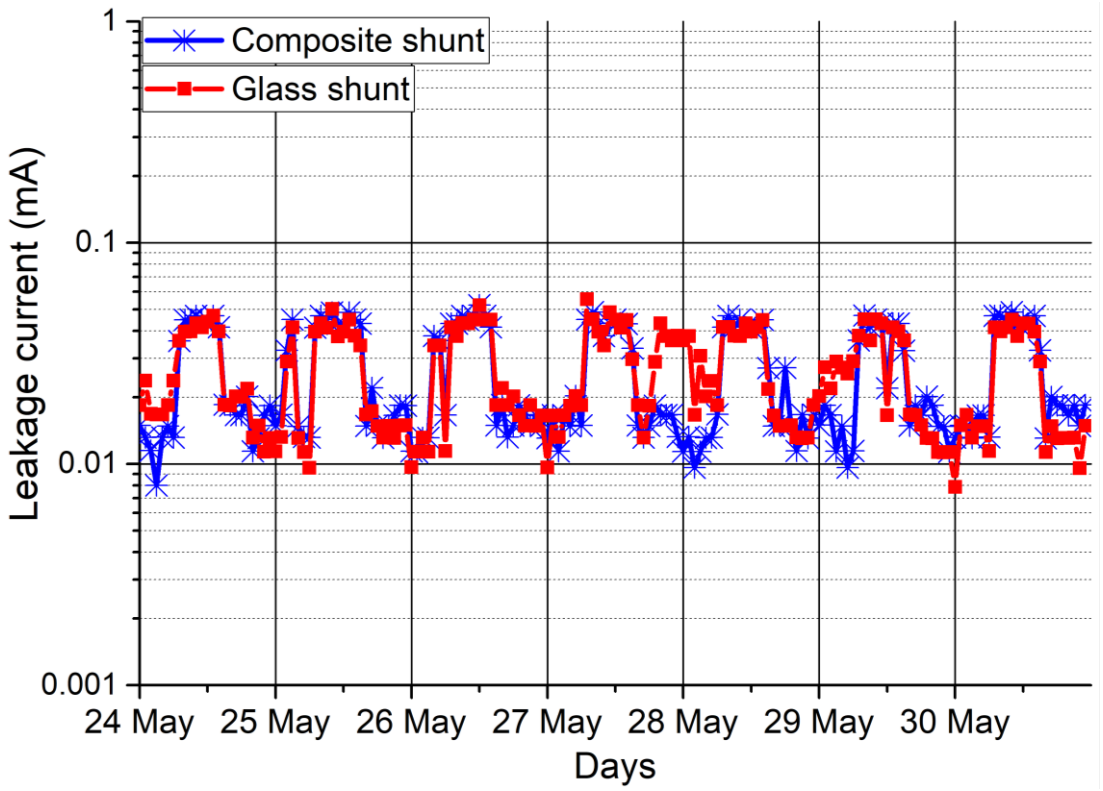

Figure A. 35: Leakage current activity: 24th - 30th of May

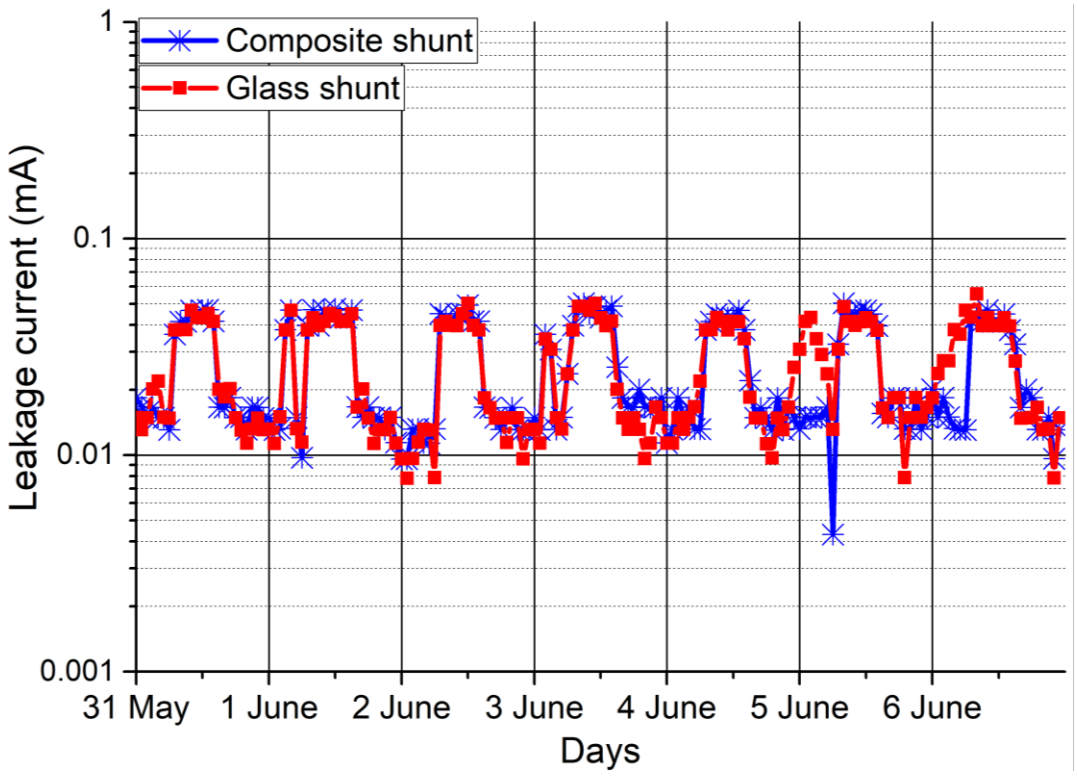

Figure A. 36: Leakage current activity: 31st of May to the 6th of June